Gravitational Waves from 3D MHD Core-Collapse Supernova Simulations with Neutrino Transport

Inauguraldissertation
zur
Erlangung der Würde eines Doktors der Philosophie
vorgelegt der
philosophisch-naturwissenschaftlichen Fakultät
der Universität Basel
von

Simon Urs Scheidegger

aus Sumiswald, BE

Basel, 2011

Genehmigt von der philosophisch-naturwissenschaftlichen Fakultät

auf Antrag von

Prof. Dr. Friedrich-Karl Thielemann, Prof. Dr. Matthias Liebendörfer und PD Dr. Jérôme Novak

Basel, den 21. September 2010

Prof. Dr. Martin Spiess

Namensnennung-Keine kommerzielle Nutzung-Keine Bearbeitung 2.5 Schweiz

---

Sie dürfen:

das Werk vervielfältigen, verbreiten und öffentlich zugänglich machen

Zu den folgenden Bedingungen:

Namensnennung. Sie müssen den Namen des Autors/Rechteinhabers in der von ihm festgelegten Weise nennen (wodurch aber nicht der Eindruck entstehen darf, Sie oder die Nutzung des Werkes durch Sie würden entlohnt).

Keine kommerzielle Nutzung. Dieses Werk darf nicht für kommerzielle Zwecke verwendet werden.

Keine Bearbeitung. Dieses Werk darf nicht bearbeitet oder in anderer Weise verändert werden.

- Im Falle einer Verbreitung müssen Sie anderen die Lizenzbedingungen, unter welche dieses Werk fällt, mitteilen. Am Einfachsten ist es, einen Link auf diese Seite einzubinden.

- Jede der vorgenannten Bedingungen kann aufgehoben werden, sofern Sie die Einwilligung des Rechteinhabers dazu erhalten.
- Diese Lizenz lässt die Urheberpersönlichkeitsrechte unberührt.

Die gesetzlichen Schranken des Urheberrechts bleiben hiervon unberührt.

Die Commons Deed ist eine Zusammenfassung des Lizenzvertrags in allgemeinverständlicher Sprache: http://creativecommons.org/licenses/by-nc-nd/2.5/ch/legalcode.de

Haftungsausschluss:
Die Commons Deed ist kein Lizenzvertrag. Sie ist lediglich ein Referenztext, der den zugrundeliegenden Lizenzvertrag übersichtlich und in allgemeinverständlicher Sprache wiedergibt. Die Deed selbst entfaltet keine juristische Wirkung und erscheint im eigentlichen Lizenzvertrag nicht. Creative Commons ist keine Rechtsanwaltsgesellschaft und leistet keine Rechtsberatung. Die Weitergabe und Verlinkung des Commons Deeds führt zu keinem Mandatsverhältnis.

Quelle: http://creativecommons.org/licenses/by-nc-nd/2.5/ch/ Datum: 3.4.2009

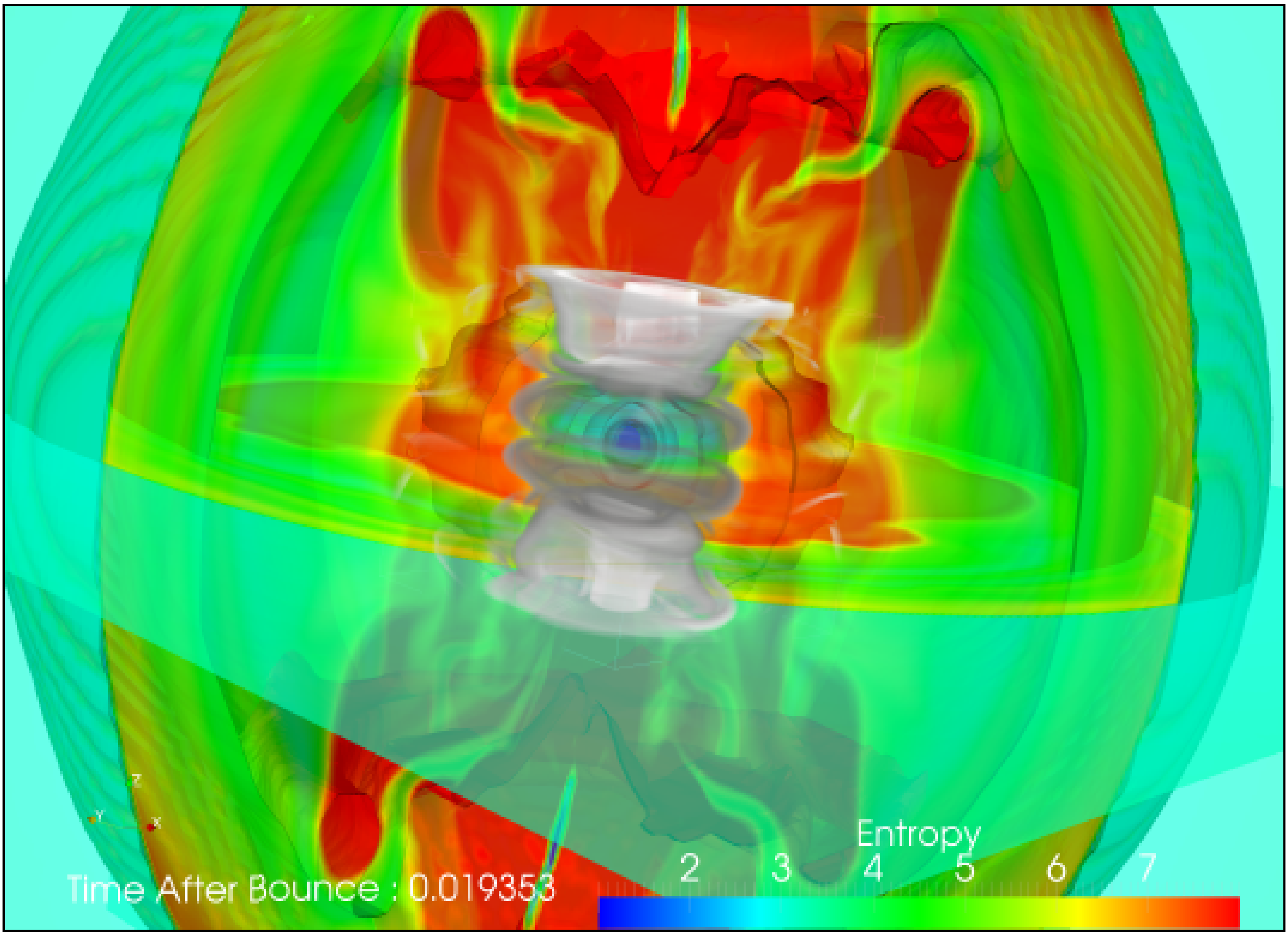
Z
Y
X
Time After Bounce : 0.019353
Entropy
2
3
4
5
6
7

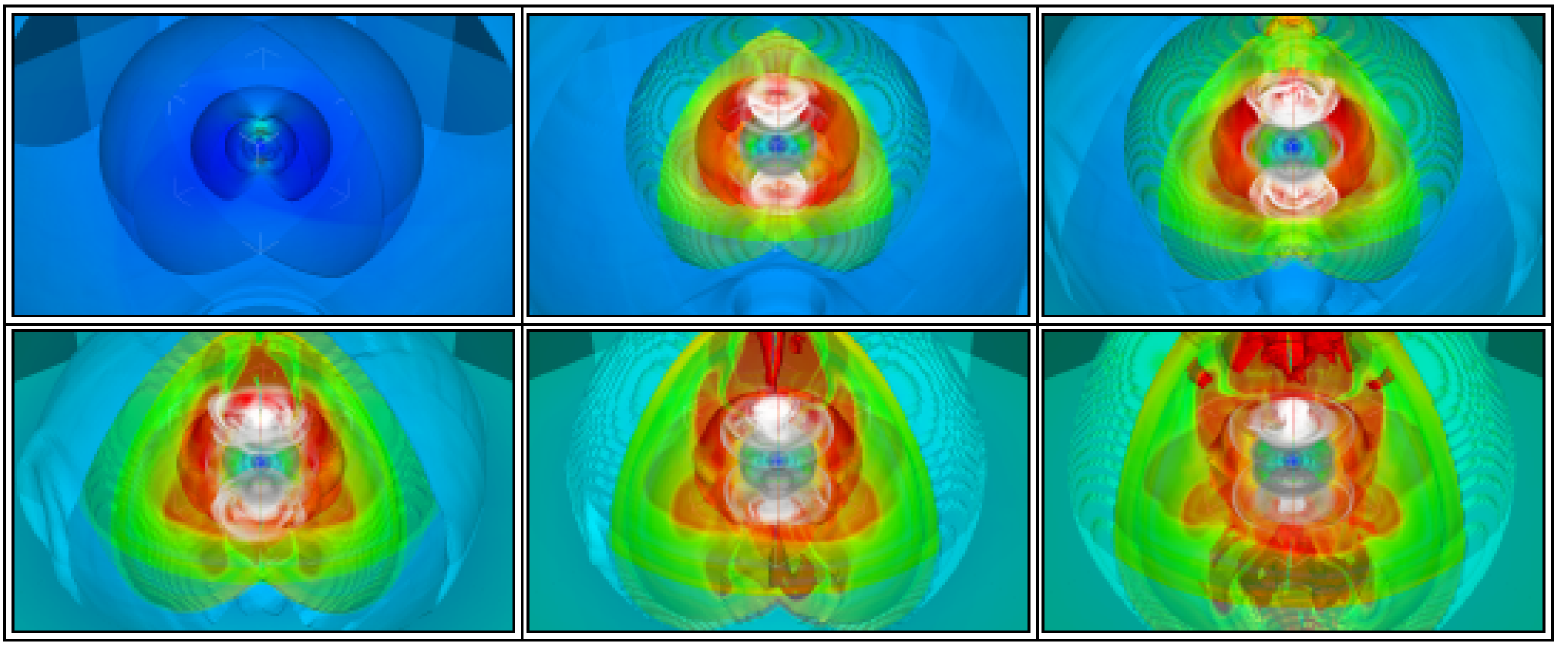

Preceding page: Rotating core-collapse 'jet' supernova simulation (model R4E1CF) at equally spaced instances during the first 20ms after core bounce. The visualization was done by J. Biddiscombe, Swiss Supercomputer Centre (CSCS).

Dedicated to my mother, Ruth

Abstract

Core-collapse supernovae (CCSNe) are among the most energetic explosions in the universe, liberating the prodigious amount of $\sim 10^{53}$ erg, the binding energy of their compact remnants, neutron stars or stellar mass black holes. While 99% of this energy is emitted in neutrinos, 1% goes into the internal and asymptotic kinetic energy of the ejecta, and it is reasonable to assume that a tiny fraction is radiated in gravitational waves (GWs).

Ever since the first experimental efforts to detect GWs, CCSNe have been considered prime sources of gravitational waves for interferometric detectors. Besides neutrinos, which have already been observed in the context of stellar core collapse of SN1987A, GWs could provide us access to the electromagnetically hidden compact inner core of some such cataclysmic events, supplying us for example with valuable information about the angular momentum distribution and the baryonic equation of state, both of which are uncertain. Furthermore, they might even help to constrain theoretically predicted SN mechanisms. However, GW astronomy strongly depends on the extensive data processing of the detector output on the basis of reliable GW estimates, which only recently have become feasible with the emerging power of supercomputers.

The work presented in this thesis is concerned with numerical CCSN models and their imprints in GWs.

I performed an extensive series of more than 30 three-dimensional magnetohydrodynamical (MHD) core-collapse simulations. My models are based on a $15M_{\odot}$ progenitor stemming from stellar evolution calculations, an effective general relativistic potential and either the Lattimer-Swesty (with three possible compressibilities) or the Shen equation of state (EoS) for hot, dense matter. Furthermore, the neutrino transport is tracked by computationally efficient algorithms for the radiative transfer of massless fermions.

I systematically investigated the effects of the microphysical finite-temperature nuclear EoS, the initial rotation rate, both the toroidal and the poloidal magnetic fields, and multidimensional gravitational potentials on the GW signature. Based on the results of these calculations, I obtained the largest – and also one of the most realistic – catalogue of GW signatures from 3D MHD stellar core collapse simulations at present.

I stress the importance of including postbounce neutrino physics, since it quantitatively alters the GW signature. Non- and slowly-rotating models show GW emission caused by prompt and protoneutron star (PNS) convection. Moreover, the signal stemming from prompt convection allows for the distinction between the two different nuclear EoS indirectly by different properties of the fluid instabilities. For simulations with moderate or even fast rotation rates, I only find the axisymmetric type I wave signature at core bounce. In line with recent results, I could confirm that the maximum GW amplitude scales roughly linearly with the ratio of rotational to gravitational energy ($T/|W|$) at core bounce below a threshold value of about 10%. Furthermore, I point out that PNS can become dynamically unstable to rotational instabilities at $T/|W|$ values as low as $\sim 2\%$ at core bounce. Apart from these two points, I show that it is generally very difficult to discern the effects of the individual features of the input physics in a GW signal from a rotating CCSN that can be attributed unambiguously to a specific model. Weak magnetic fields do not notably influence the dynamical evolution of the core and thus the GW emission. However, for strong initial poloidal magnetic fields ($\gtrsim 10^{12}$G), the combined action of flux-freezing and field winding leads to conditions where the ratio of magnetic field pressure to matter pressure reaches about unity which leads to the onset of a jet-like supernova explosion. The collimated bipolar out-stream of matter is then reflected in the emission of a type IV GW signal. In contradiction to axisymmetric simulations, I find evidence that nonaxisymmetric fluid modes can counteract or even suppress jet formation for models with strong initial toroidal magnetic fields. I emphasize the importance of including multidimensional gravitational potentials in rapidly rotating 3D CCSN simulations: taking them into account can alter the resulting GW amplitudes up to a factor of 2 compared to simulations which encounter gravity only by a monopolar approximation. Moreover, I show that the postbounce dynamics occuring in the outer layers (at radii $R \gtrsim 200$km) of models run with 3D gravity deviates vastly from the ones run with a 1D or 2D gravitational potential. The latter finding implies that both spherically symmetric and axisymmetric treatments of gravity are too restrictive for a quantitative description of the overall postbounce evolution of rapidly rotating CCSN models. The results of models with continued neutrino emission show that including deleptonization during the postbounce phase is an indispensable issue for the quantitative prediction of GWs from core-collapse supernovae, because it can alter the GW amplitude up to a factor of 10 compared to a pure hydrodynamical treatment. My collapse simulations indicate that corresponding events in our Galaxy would be detectable either by LIGO, if the source is rotating, or at least by the advanced LIGO detector, if it is not or only slowly rotating.

Contents

Overview

There's a lady who's sure all that glitters is gold
and she's buying a stairway to heaven.
When she gets there, she knows if the stores are all closed
with a word she can get what she came for.
Ooh, ooh, and she's buying a stairway to heaven.

Robert Plant, Led Zeppelin, Stairway to heaven

0.1 Preface

The major task of my PhD thesis was to study the gravitational wave signature of three-dimensional magnetohydrodynamical core-collapse supenova simulations.

The foundations of this work were laid in the spring term 2005, when as an undergraduate student I attended a proseminar held by Prof. Dr. B. Binggeli and Prof. Dr. E. K. Grebel on current issues of modern astronomy. I picked *gravitational waves* as my presentation topic. Ever since, I have happily remained chained to this very fascinating and exciting subject, as I feel that our generation might be at the dawn of gravitational wave astronomy.

In the subsequent master course, lasting from autumn 2005 to spring 2007, a joint lecture by Prof. Dr. M. Liebendörfer and Prof. Dr. F.-K. Thielemann on *numerical astrophysics* awaked my interest in computational and supernova physics. At this time, I began to collaborate with Prof. Dr. M. Liebendörfer on gravitational waves from stellar core collapse. He gave me the opportunity to take my first steps in science, supervising first my master thesis, and later also the course of my dissertation in the *Astroparticle* group of the University of Basel.

During my PhD studies from June 2007 - August 2010, I had the unique chance to delve into the very interesting but also challenging world of stellar core collapse physics. Beside carrying out my own research in Basel, I was able to visit a large number of places all over the world in order to promote scientific results and for talks (Todtmoos, Germany; Trento, Italy; Ladek Zdroj, Poland; Ringberg Castle, Germany; Paris, France; Hirschegg, Austria; Heidelberg, Germany; Potsdam, Germany; Copenhagen, Denmark; Pasadena, USA; Caen, France; Garching, Germany). I would hardly have visited all these places so early in life if it hadn't been for science! At these conferences and invited talks I profited extensively from discussions with many interesting and inspiring persons.

The process of writing this thesis was an intense and exhausting experience. However, I would do it again: the positive impressions I gained in exchange for hard work will remain.

0.2 Acknowledgements

The results obtained in this dissertation would not have been possible without the close collaboration and support of a variety of persons. My thanks go to

- Prof. Dr. M. Liebendörfer (University of Basel) for advising the course of my PhD thesis, his steady support and encouragement. To him I would like to express my sincere gratitude!
- Prof. Dr. F.-K. Thielemann (University of Basel) for co-supervising my dissertation and giving me the possibility to do this thesis in the very stimulating working environment of the Astroparticle group.
- PD Dr. J. Novak (LUTH, Meudon, France) for the newly established collaboration from which I could profit extensively. Moreover, I appreciate his willingness to be the external expert for my dissertation.
- R. Käppeli & U. Frischknecht (University of Basel) for loads of useful and useless discussions. It was a unique time of sharing with them a 'research outpost' for three years at Oetlingerstrasse 194, 4057 Basel.
- PD. Dr. A. Aste & Dr. C. von Arx (University of Basel) for proof-reading, sharing the office, discussions on theoretical foundations of human existence, and for their friendship.
- the National Science Foundation for granting financial support for my PhD project.
- Dr. T. Fischer, M. Horras, A. Perego, PD Dr. T. Rauscher, Prof. Dr. D. Trautmann, Dr. S. C. Whitehouse, C. Winteler, present and past members of the Astroparticle group of the University of Basel, for a cordial work ambiance.
- Prof. Dr. C. D. Ott (CALTECH, Pasadena, USA) for the smooth and enjoyable collaboration on the matter of merging general-relativistic supernova codes with the IDSA, and mentoring me for more than three years on issues of gravitational wave physics.
- PD Dr. Olaf Schenk (University of Basel) for his friendly and unbureaucratic support with issues concerning the PARDISO sparse matrix solver.
- Dr. S. Alam and J. Biddiscombe (Swiss Supercomputing Centre CSCS) for their support on computational issues, the visualization of simulations and related topics.
- Helen Wallimann, for proof-reading.
- CompStar, a research networking programme of the European Science Foundation.
- my family for their constant, altruistic support.

0.3 New results obtained in this dissertation

This dissertation is primarily devoted to the study of the gravitational wave emission from core-collapse supernovae.

The new results presented in this thesis and in part reported in [206, 208, 210] are my contributions to this very active field of research. Below, I list and summarize the most important findings.

An alternative formula for gravitational wave extraction

The gravitational wave signature of stellar core collapse is usually extracted via numerically convenient formulations of the ‘quadrupole approximation’ [71, 32]. However, these formulas usually do not account for the contributions of magnetic fields. Since I perform magnetohydrodynamical simulations, I extended the existing formulas to the latter case in order to calculate the contribution to the GW signal due to magnetic stresses. Following the 2D axisymmetric derivations of [170, 122], I have generalized the standard quadrupole formula to the case of a magnetized fluid in 3D Cartesian coordinates (see sec. 1.4.1).

The importance of spectral neutrino transport for the prediction of the 3D gravitational wave signal from ‘prompt’ and early protoneutron star convection

Non- and slowly rotating progenitor stars all undergo quasi-spherically symmetric core collapse. As the emission of gravitational waves intrinsically depends on dynamical processes that deviate from spherical symmetry, the collapse phase does not provide any kind of signal. However, subsequent pressure-dominated core bounce, where the collapse is halted due to the stiffening of the equation of state at nuclear density, launches a shock wave that plows through the infalling layers, leaving behind a negative entropy gradient. Moreover, as soon as the shock breaks through the neutrino sphere ~ 5ms after bounce, the immediate burst of electron neutrinos causes a negative lepton gradient at the edge of the protoneutron star. The combination of these two gradients forms a convectively unstable region according to the Schwarzschild-Ledoux criterion [127, 251], which in turn induces a gravitational wave burst due to this so-called ‘prompt’ convection.

In order to study the influence and necessity of neutrino transport on the stochastic 3D matter dynamics and the gravitational wave emission in the early supernova stages ($t \lesssim 100$ms after bounce), without having other different physical parameters interfering, I investigated comparative simulations with various degrees of neutrino transport: a) purely hydrodynamical postbounce evolution, b) a leakage scheme, and c) full spectral electron neutrino transport.

My results suggest that the primary ingredient for supernova simulations which attempt a quantitative prediction of GWs from ‘prompt’ and early protoneutron star convection ($t \lesssim 100$ms after bounce) is the accurate radial location and size of convectively unstable layers. It defines the dynamical behaviour and timescale of overturning matter in this early supernova stage (see sec. 3.4.3).

Equation of state dependence of the gravitational wave signature

The temperatures and densities inside a supernova core exceed the range that is easily accessible by terrestrial experiments. Thus, it will be impossible for the foreseeable future to construct a unique finite temperature equation of state for hot and dense matter based on experimentally verified data. In order to circumvent this problem, the information content gravitational waves carry to us from the heart of stellar core collapse might provide us with an alternative way of studying nuclear matter properties far beyond saturation. However, to tap this information, models with different nuclear input must be run and their computed wave form output can subsequently be compared with actual (future) detector data.

In order to address this task, I carried out a large parameter study in 3D, employing the Lattimer-Swesty [130] and the Shen equation of state [215].

Note that I compared for the first time ever the gravitational wave signatures resulting from the three different choices of nuclear matter compressibility provided by the Lattimer-Swesty equation of state.

My studies show that the gravitational wave signal stemming from prompt convection in slowly rotating supernova cores allows for the distinction between the two different nuclear equations of state (Lattimer-Swesty and Shen) indirectly by different properties of the fluid instabilities. I also found minor deviations in the GW characteristics for simulations which were carried out with different compressibility versions of the Lattimer-Swesty equation of state. However, the differences in the frequency domain of the GW signal are negligibly small and thus not likely to be constrained by observation (see sec. 3.4).

Furthermore, my results indicate that the particular choice of the nuclear equation of state has little influence on the gravitational wave signal from rapidly rotating core collapse. It is, among other things, degenerate with the rotation rate of the supernova core (see secs. 3.4.2 and 3.5.2).

Nonaxisymmetric rotational instabilities in the protoneutron star

Recently it has been argued, based on numerical simulations of equilibrium neutron star models or full core-collapse simulations, that differentially rotating protoneutron stars can be subject to non-axisymmetric rotational instabilities at β values ($\hat{=} T/|W|$, the ratio of rotational to gravitational energy) far below the ones known from the classical dynamical bar mode instability with a threshold of $\beta_{dyn} = 27\%$, or the secular instability, which is triggered at $\beta_{sec} \sim 14\%$ [228], leading to strong, narrow-band gravitational wave emission [51, 179, 206]. At present little is known about the true nature of the so-called low $T/|W|$ instability. Previous work has so far failed to establish (for example) an analytical instability criterion, as was pointed out by [174]. I address two relevant questions regarding the so-called 'low $T/|W|$' instability in the context of stellar core collapse: i) What is the minimum

β value required in self-consistent core-collapse simulation to trigger the onset of the instability? This is important to know, since most stars which undergo a core collapse rotate only slowly [92]; furthermore, it was pointed out by [62] that even fast rotating protoneutron stars can never accrete enough angular momentum to reach the β_{dyn} value required for the onset of the classical bar mode instability. ii) How does the inclusion of deleptonization in the postbounce phase quantitatively alter the GW signal?

My studies indicate that protoneutron stars can become dynamically unstable to rotational instabilities at $T/|W|$ values as low as $\sim 2\%$ at core bounce. Moreover, they also show that the inclusion of deleptonization during the postbounce phase is very important for the quantitative GW prediction, as it enhances the absolute values of the gravitational wave trains up to a factor of ten with respect to a lepton-conserving treatment (see sec. 3.5.3).

Effects of strong magnetic fields on the gravitational wave signature in 3D

Weak magnetic fields do not notably influence the dynamical evolution of the core and thus the GW emission. However, for strong initial poloidal magnetic fields ($\gtrsim 10^{12}$G), the combined action of flux-freezing and field winding leads to conditions where the ratio of magnetic field pressure to matter pressure reaches about unity which leads to the onset of a jet-like supernova explosion. The collimated bipolar out-stream of matter is then reflected in the emission of a type IV GW signal [170]. In contradiction to axisymmetric simulations, I find evidence that nonaxisymmetric fluid modes can counteract or even suppress jet formation for models with strong initial toroidal magnetic fields. The resulting GW signals consequently show pure hydrodynamical features (see sec. 3.5.7).

Effects of multidimensional gravitational potentials on the gravitational wave signature

Since a CCSN does not proceed in an entirely spherically symmetric way, direction-dependent gradients of the gravitational potential are likely to emerge in 3D simulations. This in turn is reflected in non-uniform matter acceleration, leading to a slightly modified temporal outcome of numerical simulations in which the dimensionality of the gravitational potential is varied while keeping the other parameters fixed.

I investigate the sensitivity of the GW signal upon the dimensionality of the gravitational potential. For this I compare rapidly rotating models which implement gravity either by a spherically symmetric (1D), axisymmetric (2D) or 3D approach. My results show that in the case of a 2D gravitational potential, the axisymmetric acceleration of the fluid due to gravity leads to a somewhat more oblate configuration of the protoneutron star around bounce and the early postbounce phase compared to models which were run with a spherically symmetric approach for gravity. This causes, as a direct consequence, considerably stronger GW emission at core bounce, with an enhancement of the maximum amplitude of $\sim 20\% - 30\%$ compared to the reference models with 1D gravity. Moreover, significant differences also occur for the GW signal from the low $T/|W|$ instability. Because the axisymmetric treatment of gravity can account better for spiral structures, this in turn leads to a faster growth of unstable modes to more prominent values, causing an earlier onset of GW emission and maximum amplitudes up to a factor of 2 larger compared to the reference models with 1D gravity (see sec. 4.2).

In case of models which implement gravity in 3D, I confirm the trends found with respect to GW emission in simulations which treat the gravitational potential in axisymmetry. This is due to the fact that in my models, the dominant contributions to the GW amplitudes are emitted at radii $R < 30$km, where the predominant deformation of the PNS is of axisymmetric nature. Moreover, I also show that the postbounce dynamics occuring in the outer layers ($R \gtrsim 200$km) of models run with 3D gravity deviates vastly from the ones run with a 1D or 2D potential. The latter finding implies that both spherically symmetric and axisymmetric treatments of gravity are too restrictive for a quantitative description of the overall postbounce evolution of rapidly rotating CCSN models.

0.4 Organisation of this Dissertation

In chaper 1, I present a general introduction to core-collapse supernova physics, gravitational wave theroy and observation. In addition, I give a short overview on previous work concerning gravitational wave signatures of core-collapse supernovae. Finally, I outline a minimal set of requirements which should be included in 3D simulations if one wants to raise a claim on the reasonable and indicative outcome of the simulations and the predicted observables.

Chapter 2 is devoted to a comprehensive and detailed description of the various components of the 3D magnetohydrodynamic codes `FISH` and `ELEPHANT`.

Chapter 3 contains an extensive discussion of the results obtained via some of today's most realistic calculations of non-rotating and rotating stellar core collapse in 3D. These calculations employ a finite-temperature equation of state, magnetic fields, an approximate treatment for deleptonization during the collapse, state-of-the-art presupernova stellar models from stellar evolutionary calculations, and computationally efficient methods for the neutrino transport. I discuss estimates for the gravitational wave signature.

In chapter 4, the influence of axisymmetric (2D) and 3D gravitational potentials on the resulting GW signatures is investigated.

In chapter 5, I conclude and summarize the work presented in this dissertation.


YOUR "TO DO" LIST
TO DO
☑ ~~WRITE TO DO LIST~~
☐ GET REIMBURSED FOR CONFERENCE EXPENSES
☐ WORK ON THESIS
TO DO
☑ ~~WRITE TO DO LIST~~
☑ ~~GET REIMBURSED FOR CONFERENCE EXPENSES~~
☐ GO TO BANK
☐ WORK ON THESIS
☑ ~~SEND SLIDES TO PROF~~ JONES
☐ SUBMIT PAPER REVIEW
☐ GRADE FINALS
☐ MEET WITH UNDERG
JORGE CHAM © 2010
☐ DENTIST?
☑ BACK UP FILES!
☑ ~~BUY MORE COFFEE!~~
TO DO
☑ ~~WRITE TO DO LIST~~
☑ ~~ORDER SUPPLIES~~
☑ ~~GET REIMBURSED FOR CONFERENCE~~
WORK ON THESIS
☑ SUBMIT PAPER REVIEW
☑ HELP LABMATE WITH RESEARCH
☑ PRINT POSTER
☐ GRADE FINALS
☐ LAUNDRY!
☑ MEET WITH UNDERG
☑ ~~CALL MOM!!~~
TO DO
☐ WRITE NEW TO DO LIST
☐ WORK ON THESIS?
SIGH...
© jorge cham
WWW.PHDCOMICS.COM

1 Introduction

> *Was einmal gedacht wurde, kann nicht mehr zurückgenommen werden.*
>
> Friedrich Dürrenmatt, Die Physiker

1.1 General and historical notes on supernovae

Supernovae (SNe) owe their name to the astronomers Baade and Zwicky who in the 1930's realized that these objects were much more luminous and by far rarer than common novae [21, 22, 262]. Their high luminosities, comparable to the integrated light of their host galaxies, broad spectral lines, and sudden occurrence in the sky led them to conclude that SNe were very energetic explosions. The two physicists even went a step further and hypothesized that *'...the super-nova process represents the transition of an ordinary star into a neutron star'* [22].
This is a very remarkable idea for its time – only a few years after James Chadwick had actually discovered the neutron (1932) [52] – and still lies at the heart of modern theoretical models for SNe that result from the gravitational collapse of the cores of massive stars.

Theorists distinguish two fundamentally different SN types, regardless of their spectroscopic appearance: *core-collapse* and *thermonuclear* SNe.
Core-collapse supernovae (CCSNe hereafter) occur near star forming regions and have never been observed in elliptical galaxies [90], which leads to the idea that their progenitors are massive stars born with more than $\sim 8M_\odot$, and are relatively short-lived (a massive star of e.g. $9M_\odot$ persists for $\lesssim 2.6\times10^7$ years in the overall dominant hydrogen burning phase, while our sun's lifespan is $\gtrsim 9.8\times10^9$ years [202,146]). Such massive stars go through all the nuclear burning stages up to iron, beyond which nuclear fusion would be endothermic (see, e.g., [47], with references therein). Hence, at the end of a massive star's thermonuclear life, it has an 'onion-skin' structure in which an oxygen-neon-magnesium core or – for stars more massive than $\sim 10M_\odot$ – even an iron core is nested within shells comprised of elements of progressively lower atomic weight at progressively lower densities and temperatures (see, e.g., [146], with references therein). A typical nesting is Fe → Si → O → He → H (see figs. 1.3 and 1.4). When nuclear burning ceases in these massive stars the core becomes unstable and gravitational collapse follows, leading to the formation of a neutron

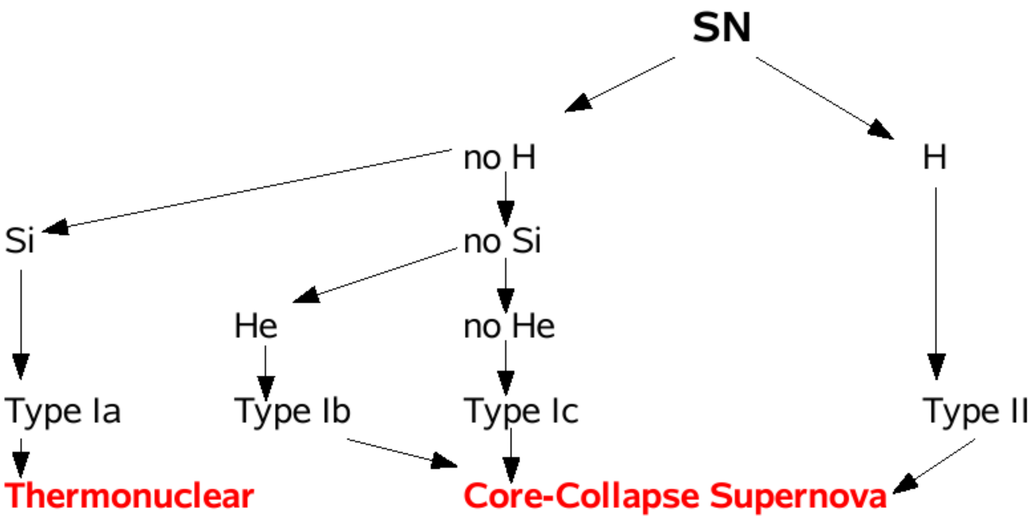

Figure 1.1: Astronomer's supernova classification [70, 90]. The two main spectroscopic types are the type II class, which comprises SNe with prominent hydrogen lines, whereas the type I class is defined by the absence of hydrogen in their spectra. Note that theorists attach less importance to the external aspects of SNe (spectra) than to their interiors (the origin of their explosion), and distinguish two fundamentally different SN types regardless of their spectroscopic appearance: core-collapse and thermonuclear SNe. In this sense, SNe Ib, Ic are thought to be physically much closer to SNe II than to SN Ia, even though SNe Ia, Ib, and Ic all share the same prefix, owing to the lack of hydrogen in their atmospheres.

star or black hole [214]. The standard paradigm is that most of the gravitational binding energy released during the collapse is liberated in neutrinos ($\mathcal{O}(10^{53})$erg) and in the kinetic energy of the explosion of the envelope ($\mathcal{O}(10^{51})$erg; 10^{51}erg $\equiv 1$ Bethe [B]).
Thermonuclear supernovae (not a subject of this PhD thesis), on the other hand, are about ten times less prevalent than CCSNe [47] and thought to arise from small carbon-oxygen white dwarfs, the end products of low-mass stellar evolution. They explode as they approach the Chandrasekhar mass ($\sim 1.4 M_{\odot}$) after a period of mass accretion from a binary companion, leaving no compact remnant behind them [214].

Astronomers use observational, not theoretical criteria to type supernovae, according to the presence or absence of certain elements in their atmospheres based on spectroscopic observations (see, e.g., [70, 90] for detailed reviews, and fig. 1.1):

- Type Ia: They are characterized by a strong absorption attributed to Si. Because all type Ia light curves (luminosity vs. time) are quite similar, they can be used as standard candles for measuring distances and probing the curvature of the universe [186].

- Type Ib: These objects are distinguished by spectra with no evident Balmer lines, weak or absent Si, and strong He.
- Type Ic: The members of this class are characterized by weak or absent hydrogen and helium lines, and no evident Si.
- Type II: These objects have prominent Balmer lines.

Note that the distinguishing feature of types Ib and Ic is the lack of conspicuous hydrogen spectral lines. Their progenitors are believed to be massive stars that lose most of their H-rich (and perhaps He-rich) envelopes via strong winds or transfer to a binary companion via Roche overflow [90]. Moreover, neutron stars have been associated with remnants of CCSNe via pulsar radio emission such as in the Crab Nebula (see [142], with references therein). Finally, it is also of great importance to point out that about a decade ago, signatures of very energetic type Ic SNe, so-called 'Hypernovae' [1], were found for the first time in the afterglows of the 'long-soft' gamma-ray bursts for the first time, thus linking nature's two grandest explosions (see [254], with references therein).

In our galaxy, i.e. at distances $\lesssim$ 10kpc, SNe are considered to be rare events. Within the last millennium, mankind has witnessed only 6 supernovae in our galaxy and one in the Large Magellanic cloud (see fig. 1.2). Among them are the recent SN 1987A (type II, located not in the Milky Way, but in the Large Magellanic cloud), the SN in the Crab Nebula (type II), and the SNe recorded by Tycho Brahe (probably type Ia) and Johannes Keppler (type Ia). Even though observers estimate that this number represents only $\sim 20\%$ of the galactic SNe that have exploded within the last 1000 years [47] (because the majority were shrouded from view by the dust that pervades the Milky Way), our generation of (gravitational wave) astronomers and astrophysicists would have to consider themselves very lucky if they could witness a SN explosion close by. Modern estimates of galactic SNe rates predict the frequency of core collapse to be $1.9(\pm 1.1)$ events per century [58]. This event rate increases drastically only when we reach out to the Virgo galaxy cluster at a distance of $\sim 10 - 20$Mpc. Then, the event rate for CCSNe is estimated to be ~ 5 per year [49]. Hence, if one wants, for instance, to use gravitational wave astronomy for regular observations of stellar core collapse with reasonable statistics, detector facilities must one day be able to provide the sensitivities required to see as far as the Virgo cluster (see sec. 1.3).

SNe were and are crucial for the dynamical and morphological development of the Universe and thus indispensable for the existence of life on earth. The 'oxygen' ejected during a CCSN for example is the dominant source of the element in the

---

[1] Detailed studies of spectra and light curves suggest that hypernovae release about 10^{52} ergs in kinetic energy, or ten times that of a typical supernova [254].

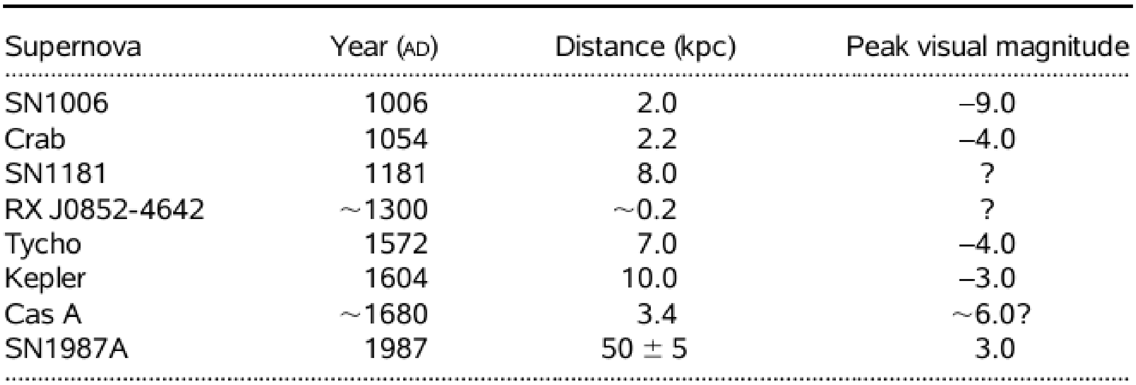

Supernova	Year (AD)	Distance (kpc)	Peak visual magnitude
SN1006	1006	2.0	–9.0
Crab	1054	2.2	–4.0
SN1181	1181	8.0	?
RX J0852-4642	~1300	~0.2	?
Tycho	1572	7.0	–4.0
Kepler	1604	10.0	–3.0
Cas A	~1680	3.4	~6.0?
SN1987A	1987	50 ± 5	3.0

Figure 1.2: Compilation of 'historical' supernovae that have exploded in our Galaxy and the Large Magellanic cloud within the past millennium. Note that these supernovae are only a fraction of the total, because the majority were probably hidden from view by the dust that pervades the Milky Way. Note also that SN 1987A exploded not in the Milky Way but in the Large Magellanic cloud (one of its nearby satellite galaxies). Astronomical magnitudes are logarithmic and are given by the formula $M_V = -2.5 \log_{10}(brightness) + constant$. For comparison, the Moon is near -12 magnitudes, Venus at peak is -4.4 magnitudes, and good eyes can see down to about $+6$ magnitudes. Note that the compilation above also contains RX J0852-4642, a supernova remnant whose very nearby birth went unrecorded (perhaps because it resides in the southern hemisphere), and Cas A, a supernova remnant that may have been recorded only in ambiguous notes. Table taken from [47].

Universe [47]. So naturally, any attempt to address human origins must begin with the understanding of CCSNe.

Finally, SNe were also of central historical and sociological importance. It is well-known that Tycho's and Kepler's SNe 1572 and 1604 (see fig. 1.2) had tremendous effects on the development of astronomy in Europe because they were used to argue against the Aristotelian idea that the universe beyond the Moon and planets was immutable [54].

1.2 The 'standard' paradigm of core-collapse supernovae

1.2.1 Stellar evolution

A star's life begins in dense parts of molecular clouds. There, in so-called star-forming regions (see, e.g. [123], with references therein), the gas collapses gravitationally via complicated interactions of turbulence, magnetic fields and radiation into balls of plasma (see, e.g., [26], with references therein).

If the initial mass of such a collapsing object is greater than about $\gtrsim 0.072 M_\odot$ [2] [214], the plasma the hydrogen ignition temperatures of $\sim 1.5 \times 10^7$K exceeds during contraction, which is the first stage of a sequence of thermonuclear burning processes. The onset of nuclear fusion leads relatively quickly to a hydrostatic equilibrium in which energy released by the core exerts a radiation pressure balancing the weight of the star's overlying matter, preventing further gravitational collapse [146]. With the exhaustion of core hydrogen, most stars proceed to shell hydrogen burning, and then on to core helium burning. The ashes of the latter are predominantly carbon and oxygen.

With the passing of each stage, the centre of the star grows hotter and more dense (see, e.g., [255]). However, low mass ($\lesssim 6 - 8 M_\odot$) stars do not proceed beyond this stage. They are not massive enough to contract to sufficiently high densities and temperatures for carbon burning. They end their lives as white dwarfs [91, 214].

More massive stars ignite carbon burning which leaves oxygen, magnesium and neon as ashes. In the case of stars with birth masses of $\sim 8 - 10 M_\odot$, the core temperatures are too low to ignite further nuclear burning. Subsequently, they either lose their envelopes and become O/Ne/Mg white dwarfs (possible progenitors of accretion-induced collapse [57,15]), or undergo a collapse of their low-mass O/Ne/Mg cores [115, 74].

For stars with masses from $\sim 10 M_\odot$ to 60-100$M_\odot$ [256] (the upper limit depends on the heavy-element/metallicity fraction at birth), the ashes of carbon burning reach temperatures sufficient to ignite, and they burn predominantly to silicon, sulphur, calcium and argon. Finally, these products ignite to produce iron-group elements. Eventually, this core of iron-group nuclei is embedded in an onion skin structure, as already mentioned in the previous sec. 1.1 and shown in figs. 1.3 and 1.4.

Note that after helium burning, the evolution is greatly accelerated by neutrino losses (see fig. 1.3). For the temperatures approaching a billion degrees or more, a large thermal population of electrons and positrons is maintained. When the electrons meet and annihilate with positrons, a neutrino-antineutrino pair is occasionally produced. These neutrinos escape the star with ease under the prevailing densities and force the burning to go faster to replenish the loss. Although the fusion of hydrogen and helium takes millions of years, the last burning stage – silicon burning – lasts only about two weeks [256].

Because the nuclear binding energy per nucleon has its maximum value for the iron group (see, e.g., [35]), no further energy can be released by nuclear fusion.

1.2.2 Core collapse and core bounce

When the iron core is formed in the centre of the massive star, it grows steadily by the ashes of the silicon shell burning. Even though the central part of the massive star is hot, the high densities and the ordered arrangement of its constituent nucleons into nuclei results in a low specific entropy. Therefore, at this low entropy the core's pressure support against gravity is derived mostly ($\gtrsim 90\%$; see [29]) from relativistic,

---

[2] Objects with a mass $\lesssim 0.072 M_\odot$ cannot fuse H to He and are called 'Brown dwarfs'. For a thorough review on Brown dwarfs, see [44], with references therein.

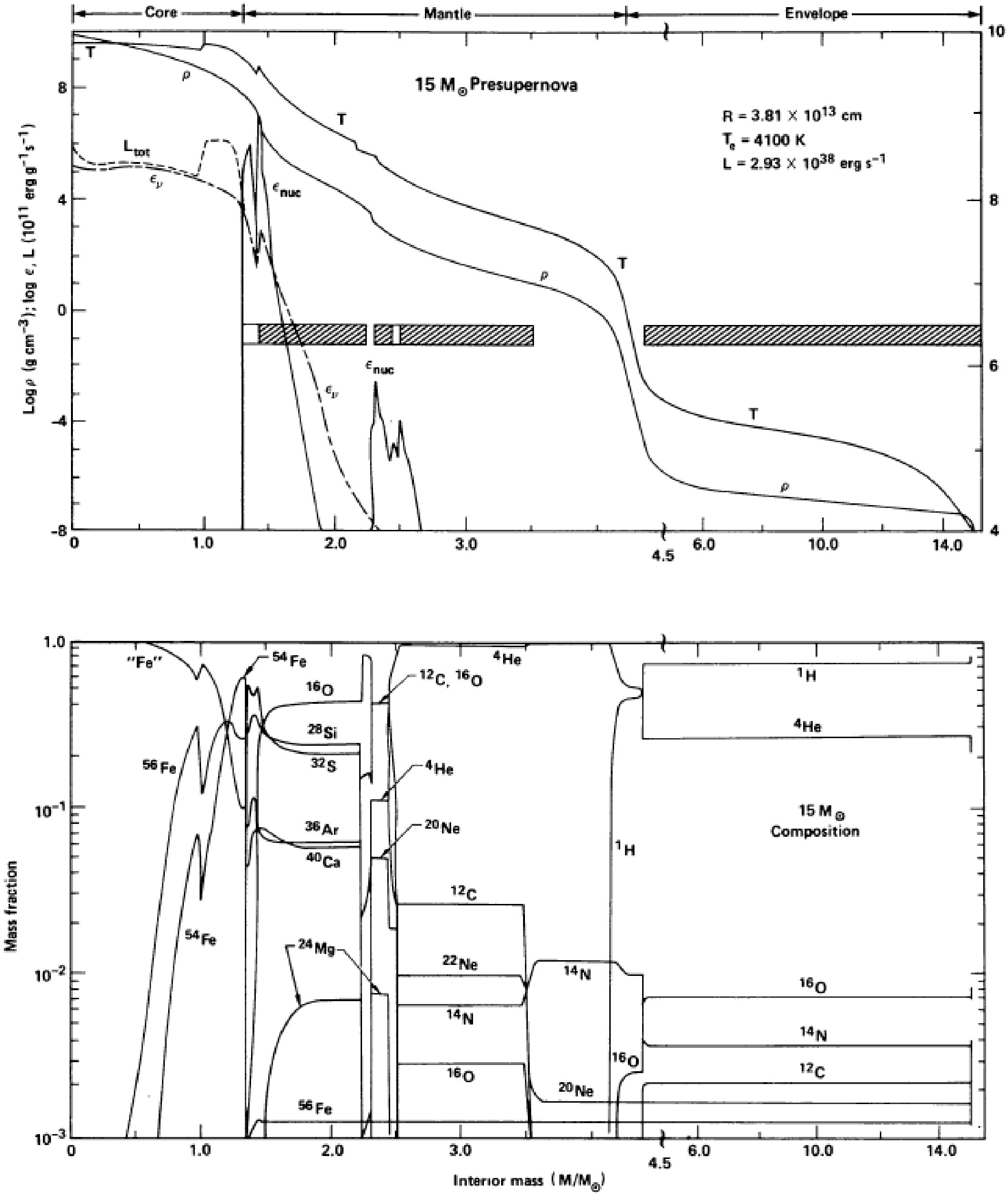

Figure 1.3: Schematic structure of a $15 M_\odot$ precollapse star, taken from [257]. The upper panel displays the temperature and the density profile. Moreover, L_{tot}, ϵ_ν and ϵ_{nuc} stand for total energy loss/luminosity and the corresponding contributions from the neutrino emission and the energy generation in nuclear reactions. The lower panel shows the composition profile, where the iron core is surrounded by shells of lighter elements. The size of the iron core is of the order 10^9 cm, while the stellar radius is larger than 10^{13} cm.

degenerate electrons [214],

$$P_e \propto Y_e^{4/3} \rho^\Gamma \,, \tag{1.1}$$

where Y_e is the number of electrons per baryon (electron fraction), ρ is the density, and Γ is the adiabatic index which assumes a value of 4/3 for the relativistic degeneracy limit [214]. For precollapse iron cores, typical values for Y_e are ~ 0.42 at the centre and ~ 0.48 at the outer edge [258]. Once the iron core is pushed over the Chandrasekhar mass limit, which is the maximum mass of a non-rotating fluid body that can be held in hydrostatic equilibrium by electron-degeneracy pressure in Newtonian gravity (see [29], with references therein),

$$M_{Ch} \approx 5.8\, Y_e^2 \left[1 + \left(\frac{s_e}{\pi Y_e} \right)^2 \right] M_\odot \ , \tag{1.2}$$

electron degeneracy pressure can no longer stabilize the core and it collapses. Note that Y_e and s_e in eq. 1.2 are average values of electron fraction and electronic entropy per baryon over the mass of the Fe core. Putting typical values ($Y_e = 0.45, s_e = 0.52$) in a $15 M_\odot$ into eq. 1.2, one gets a Chandrasekhar mass of $\sim 1.34 M_\odot$. The onset of infall is accelerated by two additional processes that rob the core's energy and pressure support: a) electron capture and b) photodissociation (see, e.g., [214]). Under the prevailing densities and temperatures, electron capture occurs on heavy Fe group nuclei and free protons via

$$\begin{aligned} {}^{56}\mathrm{Fe} + e^- &\rightarrow {}^{56}\mathrm{Mn} + \nu_e \ , \\ p + e^- &\rightarrow n + \nu_e \ , \end{aligned} \tag{1.3}$$

because the Fermi energy of electrons [214, 119],

$$\mu_e = 11.1\mathrm{MeV} \left(\frac{\rho Y_e}{10^{10}\mathrm{gcm}^{-3}} \right)^{1/3} \tag{1.4}$$

exceeds the mass difference between the nuclei, namely $m_{\mathrm{Mn}} - m_{\mathrm{Fe}} = 3.7\mathrm{MeV}$. Electron captures reduce Y_e and consequently the pressure support. Note that the electron-type neutrinos escape freely from the core before the densities reach $\sim 10^{12}$ gcm^{-3}, as will be outlined later below. Furthermore, the endothermic photodissociation of iron nuclei [214],

$$\gamma +^{56}_{26} Fe \rightarrow 13\alpha + 4n - 124.4\mathrm{MeV} \ , \tag{1.5}$$

occurs for temperatures $T \gtrsim 5 \times 10^9$K, which leads to the reduction of the additional thermal pressure support. Moreover, the internal energy produced by the core contraction is exhausted by this reaction.
Note that after the onset of the gravitational collapse, the core proceeds to contract under the pull of the self-gravitating force, unnoticed by the rest of the outer part of the star, on a free-fall time-scale which is of the order $\tau_{dyn} \sim 1/\left(G\overline{\rho}\right)^{1/2}$ (with G and $\overline{\rho}$ being the gravitational constant and the average density). This is because the density decreases steeply from the core to the surrounding shells. Hence the dynamical timescale of the core is much shorter than the one of the envelope (cf. the upper panel of fig. 1.3). As a result, the dynamics of the iron core is hardly or not, affected by the envelope. Hence, the outer shells are not moved. They are

oblivious to their impending fate until the supernova shock wave generated in the core hits and ejects them.

An important change in the physics of the collapse occurs as the densities reach $\sim 10^{12}\mathrm{gcm}^{-3}$. At this point, the scattering opacities become so large that the mean free path of the neutrinos is reduced to values much smaller than the core's size. Thus, the diffusion timescale of the neutrinos becomes large compared to the dynamical timescale of the collapse [29]. Note that during collapse, only electron neutrinos are produced copiously by electron captures. Therefore, the dominant opacity source for the neutrinos during the infall phase is coherent scattering,

$$\nu_e + A \rightarrow \nu_e + A \;, \tag{1.6}$$

by which the cross section becomes roughly A^2 times the cross section of each scattering of nucleons ($\nu_e + n/p \rightarrow \nu_e + n/p$) [37]. The trapping of neutrinos also means that β-equilibrium prevails, keeping the lepton fraction ($Y_l = Y_e + Y_{\nu_e}$) fixed [29,214,150]. After β-equilibrium is achieved, the collapse proceeds adiabatically. When neutrinos are trapped and become degenerate, the average neutrino energy increases and the core becomes optically thicker because the cross section of the coherent scattering increases as $\sigma_{coh} \propto E_\nu^2$ with the electron neutrino energy. Note as a side remark that since low-energy neutrinos can escape easily from the core, most neutrinos emitted during the collapse phase, before the trapping is active, have relatively low energy ($\lesssim$ 30 MeV; see [119], with references therein).

During the collapse, the core forms two parts: the (homologously collapsing) inner core and the (subsonically infalling) outer core. Matter inside the sonic point – the point in the star where the sound speed equals the magnitude of the infall velocity – stays in communication and collapses homologously ($v \propto r$; see [85]). On the other hand, the material outside the sonic point falls in quasi-free fall. Analytical studies by Goldreich & Weber [85] have shown that typical inner core masses scale roughly as $M_{ic} \propto Y_e^2$. The entire collapse continues on a time scale of a few 100 ms until nuclear densities, several $\times 10^{14}\mathrm{gcm}^{-3}$ [29], are reached. Now, strong repulsive nuclear forces lead to an immediate stiffening of the nuclear equation of state (EoS), which halts the collapse of the inner core on a timescale of a millisecond. The abrupt halt of the collapse of the inner core and its rebound, the so-called 'core bounce', generates a hydrodynamical shock wave as the core's outer half continues to crash down.

During the collapse of the iron core, a huge amount of gravitational binding energy, the ultimate energy source of CCSNe, is released when contracting from a radius of $\sim$ 1500km and central densities below $10^{10}\mathrm{gcm}^{-3}$ to a radius of $\sim$ 10km and densities above that in atomic nuclei (see fig. 1.4). To first order, the gravitational binding energy of the remnant neutron star is given by

$$|W| \sim \frac{3}{5}\frac{GM_{NS}^2}{R} \sim 2 - 3 \times 10^{53}\mathrm{erg} \;, \quad E_{kin} \ll E_{grav} \tag{1.7}$$

where M_{NS} is the neutron star mass and R_{NS} is its radius. Typical values are $\sim 1.4M_\odot$, $\sim$ 10km and $|W| \sim 2 - 3 \times 10^{53}$erg, respectively. 99% of this energy is liberated in form of neutrinos throughout the SN evolution and the late-time cooling of the PNS [29], as I will outline below. It is a huge amount of energy in contrast to the kinetic energy of observed SNe ($E_{kin} \sim 10^{51}$erg [29]).

1.2.3 Supernova dynamics & mechanism(s)

The core bounce with the formation of the shock wave is the starting point of a sequence of events that ultimately trigger a supernova explosion.

The shock wave which propagates into the outer core quickly loses its initial strength to the dissociation of nuclei into free nucleons at a cost of ~ 8.8MeV per nucleon [29]. At the same time, this process enables copious electron captures on the emerging free protons ($e^- + p \rightarrow n + v_e$) just behind the shock. Before the shock arrives at the neutrino sphere, electron neutrinos cannot escape on a hydrodynamical timescale, because the diffusion timescale is much longer than that for the shock propagation. However, as the shock wave moves through the neutrino sphere, the previously trapped electron neutrinos decouple from matter and begin to stream freely [232]. This sudden liberation of electron neutrinos is called the *neutronization burst*, where the peak luminosities can easily exceed 10^{53}ergs^{-1} for the duration of several ms. Hence, the combined action of dissociation and neutrino emission causes the shock to stall within $\sim 10 - 20$ms after core bounce as ‘standing accretion shock’ at radii around $100 - 200$km [138, 252] due to the large energy loss caused by dissociation and neutrino emission. Thus, all today’s state-of-the art models agree that this so-called ‘prompt’ shock is unable [3] to trigger supernova explosions (see [252], with references therein).

Meanwhile, after the core bounce, a compact remnant begins to form at the centre of the collapsing star, quickly growing through the infalling stellar material. The nascent remnant – the protoneutron-star (PNS) – will evolve to a neutron star [167] or may eventually collapse to a black hole, depending for example on whether the progenitor star had a mass below or above $\sim 25 M_\odot$ [91].

By the time the shock stalls, a hot and dense PNS has formed with an average lepton number of $Y_l \lesssim 0.3$. It contracts slowly while deleptonizing and cooling as neutrinos of all flavours – μ and τ neutrinos and antineutrinos are created by thermal processes [37] – diffuse through the optically thick regime to less dense, more transparent regions. These neutrinos are emitted on a timescale of the order of $\sim \mathcal{O}(1) - \mathcal{O}(10)$ s, which is the timescale of neutrino diffusion (see fig. 1.4, and [106], with references therein). Note that convective processes may enhance this neutrino cooling and boost the PNS luminosity (see, e.g. [56, 41]). After several tens of seconds, the compact remnant becomes transparent to neutrinos and the neutrino luminosity drops significantly [42].

Furthermore, there is accretion-driven neutrino emission from the outer layers of the PNS onto which material is accreted through the stalled shock, which is active on

---

[3] Note that it is only for very special combinations of physical parameters such as the stellar model of the progenitor or the compressibility of nuclear matter, resulting in extraordinarily small cores, that the so-called prompt explosion might work (see, e.g., [19, 95]), in which the shock wave at core bounce propagates through the outer core to produce explosions without the shock-stall.

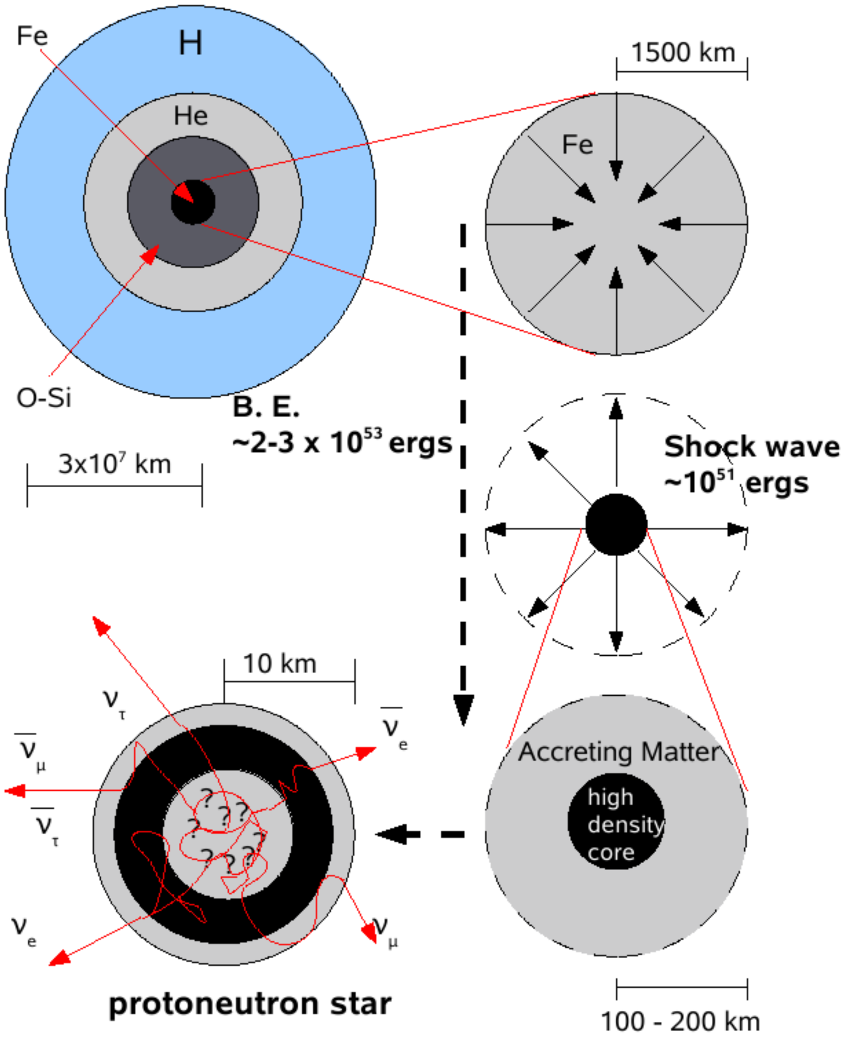

Figure 1.4: The sequence of events in the collapse of a stellar core to a nascent neutron star. It begins with a massive star with an ‘onion-skin’ structure, and goes through core implosion, to core bounce and shock wave formation, to the protoneutron-star stage before explosion, and finally to the cooling and isolated-neutron-star stage after explosion [47]. The black, straight arrows depict mass motion and the curved red arrows depict escaping neutrinos. ‘B.E.’ denotes ‘binding energy’, and ‘?’ stands for the (proto) neutron star structure and composition, which is uncertain [167].

the timescale of the order of $\mathcal{O}(100)$ ms until an explosion sets in, i.e. certain mass shells move outwards [138].

All this neutrino emission radiates, as stated previously, about $\sim 99\%$ of the released binding energy and is actually the dominant output of the event which is presumably a gravity-powered neutrino explosion. Note that a small number of neutrinos were already detected from SN 1987A and thus confirm the very basic picture of stellar core collapse [96, 97].

The question now arises how this huge reservoir of energy emitted by neutrinos can be tapped in order to 'revive' the stalled shock and turn the collapse of the rest of the star into an explosion? This part of the supernova problem has kept astrophysicists busy for more than 40 years (see, e.g., [252] and [106] for relatively recent reviews). Four SNe mechanisms are at present being discussed in literature: a) the so-called delayed, neutrino-driven explosion mechanism, b) the magneto-rotational mechanism, c) the acoustic mechanism, and d) the QCD phase transition mechanism.

a) The delayed, neutrino-driven explosion mechanism has the longest pedigree. It was already considered theoretically in the 1960's by Colgate & White [55], and then numerically 'discovered' by Bethe & Wilson [30, 250] in the 1980's. It is based on the idea that neutrinos streaming off the neutrinosphere of the PNS can revive the stalled shock wave by depositing some of their energy in the layers between the nascent neutron star and the stalled shock front by charge-current ν_e and $\overline{\nu}_e$ captures on free nucleons [30, 250]:

$$\nu_e + n \;\rightarrow\; e^- + p \tag{1.8}$$

$$\overline{\nu}_e + p \;\rightarrow\; e^+ + n\;. \tag{1.9}$$

The neutrino heating increases the pressure behind the shock and the heated layers begin to expand, creating between the shock front and the neutron star surface a region of low density but rather high temperatures, the so-called 'hot bubble'. The persistent energy input by neutrinos keeps the pressure high in this region and drives the shock outwards again, eventually leading to an SN explosion. This may take a few 100 ms and requires that during this time a small percentage of the energy radiated in electron flavour neutrinos be converted into the thermal energy of nucleons, leptons, and photons. There is also a threshold of energy that must be deposited in a short time to overcome the 'ram' pressure of the infalling matter, which is rapidly accreting [29]. The success of the delayed neutrino mechanism turned out to be sensitive to a delicate competition of neutrino cooling between the neutrinosphere and the so-called 'gain radius' on the one hand, and the neutrino heating between the gain radius and the shock on the other hand (see [106], with references therein). The gain radius is defined as the radial position where the neutrino heating rate per nucleon and the neutrino cooling rate per nucleon become equal.

However, spherically symmetric state-of-the-art simulations agree that no delayed explosions can be obtained with this mechanism in the general case [138, 134]. Only for stars with a birth mass of $\sim 8 - 10 M_\odot$ – which instead of an iron core develop a O/Ne/Mg core with a thin carbon shell, surrounded by an extremely dilute and only loosely-bound He-shell – was neutrino heating found to power explosions in one-dimensional simulations (e.g., [115, 74]).

Recent multidimensional simulations suggest that the neutrino heating mechanism might work in combination with hydrodynamical instabilities, namely convection (see, e.g., [94, 107]) and the standing-accretion-shock instability (SASI; see e.g., [40, 104, 148, 164] and [203], with references therein). Both hydrodynamic instabili-

ties combined stretch the advection time of matter accreted through the neutrino-heating layer and thus enhance the neutrino energy deposition in support of the neutrino-driven explosion mechanism [203]. Recent, computationally demanding, axisymmetric (2D) simulations by the Garching group for example produced weak explosions for $11.2M_\odot$ and $15M_\odot$ progenitor models [41, 148] in this fashion.
SASI/convection-aided neutrino driven explosions are in a sense appealing because they bear the potential to explain a variety of physical properties related to the remnants of stellar core collapse. Since they produce highly anisotropic explosions, the SASI can lead to a large recoil of the newly-born neutron star in the direction opposite to the stronger mass ejection, producing a neutron star kick up to $\sim 1000\text{kms}^{-1}$ (see, e.g., [204]), which is in agreement with the measured proper motions of young pulsars. Three-dimensional simulations have revealed the possibility of an unstable $l = 1, m = 1$ spiral SASI mode that can create a strong rotational flow in the vicinity of the accreting neutron star, thus providing a possible mechanism for the generation of neutron star spin [33]. Moreover, the globally asymmetric onset of the explosion with sizeable initial shock deformation triggers strong hydrodynamical instabilities at the composition interfaces of the progenitor when the shock propagates outwards to the stellar surface. This leads to large-scale element mixing in the exploding star, as observed in context with SN 1987A (see, e.g., [89], with references therein).
However, even though different research groups agree on the presence, necessity and functionality of the hydrodynamical instabilities mentioned, the 2D results obtained by different groups, which apply similar input physics, but different numerical methods, do not converge for the time being (cf. [148] with [45]) [4]. In addition, note that both convection as well as the SASI are genuine three-dimensional phenomena. Hence, fully self-consistent 3D calculations with sophisticated energy-dependent neutrino transport are indispensable for judging about the viability of the neutrino heating mechanism [106], but are still pending.

b) The magneto-rotational mechanism probably only works in the case of rapid rotation. Combined action of flux-freezing, field winding [151] and also of the magneto-rotational instability MRI [24] during collapse and the postbounce phase generally may lead to the growth of magnetic fields by many orders of magnitude to values where the magnetic pressure becomes comparable to matter pressure. This, in turn, triggers a collimated, bipolar jet-explosion (see, e.g., [43], and references therein) by converting magnetic energy into kinetic energy [131, 120, 43, 156, 227, 208]. Alternatively, the magnetic fields could also convert the free energy of the differential rotation of the forming compact remnant to kinetic energy of the SN ejecta by viscous heating behind the shock in addition to the energy input there by neutrinos [231]. The magneto-rotational mechanism may also be relevant in the context of long-soft gamma ray bursts (see, e.g., [254]).

c) The acoustic mechanism of Burrows at al. [45,46] requires the excitation of strong

---

[4] Note that contrary to the multi-D case, spherically symmetric state-of-the-art codes yield converging results, as was shown, for example, in a comparative study with the `Vertex` and `Agile-Boltztran` codes [134].

$l = 1$ g-mode oscillations by turbulence and SASI-modulated accretion downstreams. The large-amplitude core motions then create powerful sonic activity in the neutron star surroundings by which energy is transported to the shock, driving the explosion at relatively late times ($t \gtrsim 1$s after bounce). The source of this energy is the gravitational binding energy of the accreted gas, converted to sound by the rapidly ringing neutron star, which thus acts like a transducer. Even though this mechanism appears to be sufficiently robust to blow up even the most massive progenitor stars, it remains the most controversial mechanism. It has so far not been confirmed by other groups, and there exist even strong 'analytical' arguments against its existence [245].

d) The transition from baryonic to quark matter, a so-called QCD phase transition, may power a secondary shock wave which triggers a successful hydrodynamical explosion, as reported by [225,81], and recently also [166] and [198]. The beauty of this mechanism is that it is able to explode stars more massive than $\sim 8 - 10 M_{\odot}$ even in a spherically symmetric setup. The main drawback is that the way the explosion is triggered relies on a rather phenomenological-, and not self-consistent description of quark matter (see [198], with references therein).

Up to now, there is a consensus among theorists that there is no agreement on *the* CCSN explosion mechanism. The CCSN mechanism – if there is a unique one – may eventually involve a combination of all the outlined mechanisms, as stated e.g. in [182]. Hence, a more decisive answer with respect to the theoretically operating explosion mechanism may only be given once future 3D numerical models can incorporate all the relevant input physics known at present, i.e. full Boltzmann neutrino radiation transport, magnetic fields, general relativity, a physically well-motivated way of describing nuclear matter at 'high' densities, and multi-dimensional progenitor star models that consistently include rotation and magnetic fields.

1.3 Gravitational waves

Einstein's theory of General Relativity (GR) [64,63] teaches us that space and time are not separate entities, but join as 'spacetime'. The field equations of GR connect matter dynamics to the curvature of spacetime and describe gravity as the curvature of a four-dimensional spacetime (one temporal and three spatial dimensions) [126]. In the framework of relativity, gravity must be causal: any change to a gravitating source must be communicated to distant observers at a speed no faster than the speed of light c. This leads immediately to the idea that there must exist some notion of 'gravitational radiation' [76]. The first calculation of gravitational waves (GWs) is due to Einstein himself [65]. His final result stands today as the leading-order quadrupole formula for gravitational wave emission. This formula plays a role in the theory of gravity analogous to the dipole formula for electromagnetic radiation, showing that GWs arise from accelerated masses [157], exactly as electromagnetic waves arise from accelerated charges [105]. The quadrupole formula implies that GWs are very difficult to produce in the fabric of space-time [235] – very large masses and relativistic speeds are needed. This follows from the weakness of the gravitational interaction and coupling to matter compared to the other forces of the standard model of physics [246]. The only objects which are possibly massive and relativistic enough to emit detectable GWs are of astrophysical origin, as outlined in the review of Sathyaprakash and Schutz [39].

Due to the weakness of GWs at astronomical distances so far no one has found direct evidence of their existence. Nevertheless, Russell Hulse and Joseph Taylor found indirectly indications of their reality by observing the inspiral of the binary system PSR 1913+16, which was discovered in 1974 [101]. Several decades of observation have shown that the orbit is decaying and that the decay rate matches with very high precision GR's prediction for such decay due to loss of orbital energy and angular momentum due to GWs. For this achievement, Russell Hulse and Joseph Taylor were awarded the Nobel Prize in Physics in 1993.

However, even though their studies proved beyond a reasonable doubt that GWs exist, it still remains an open task to detect GWs directly and – even more important – exploit them as a tool for astronomy. Today, the understanding of the cosmos depends more or less entirely on the observations of electromagnetic waves, cosmic rays and marginally on neutrinos [235]. The information that GWs could carry to us would be almost orthogonal to that carried by electromagnetic waves [39]. While gravitational radiation arises from bulk matter of dense concentrations of mass and energy, ratio waves find their origin in the acceleration of individual electric charges, showing the thermodynamic state of optically thin concentrations of matter. While electromagnetic waves show us the surface of their astrophysical source (e.g. atmospheres of stars, accretion disks, clouds of interstellar gas), GWs could provide access to high density regimes such as the innermost, central part of a CCSN [174, 119], which is hidden behind a dense layer of stellar gas and whose temperatures and densities exceed the range that is easily accessible by terrestrial experiments [137].

Today, technology has brought us to the point where detectors are beginning to set interesting upper limits on the GWs of some sources (see, e.g., [14,23]), and there is reasonable hope that the first direct detection will be made in the not too far future. In this section, I will outline and review the linearized GR. Moreover, I will summarize some basic physical properties of gravitational radiation, GW generation in the weak-field, slow-motion limit by essentially-Newtonian matter sources. Moreover, I will touch on the methods for detecting GWs (see, e.g., [14, 23]). The discussion below is based on my Project- and Master Thesis ([205], with references therein), where I summarized the subject in great detail. In addition, I have used the book by Misner, Thorne & Wheeler [157], Thorne's review, published in [233], the review by Flanagan and Hughes [76] and Ott's PhD Thesis [182].
Throughout this section, I use cgs units, carrying along all factors c and G. The signature of the metric $g_{\mu\nu}$ is, as in [157], chosen to be $(-1, 1, 1, 1)$. Greek indices run from 0 to 3, Latin ones from 1 to 3, and the Einstein summation convention is followed. Partial derivatives of any tensor $T^{\alpha_1\cdots\alpha_n}$ with respect to any coordinate x^α are denoted by $T^{\alpha_1\cdots\alpha_n}{}_{,\alpha}$

1.3.1 The linearized Einstein field equations

The Einstein equations express the non-linear relation between spacetime curvature and the energy-matter fields and are given by

$$G_{\mu\nu} = \underbrace{R_{\mu\nu} \equiv \frac{1}{2} g_{\mu\nu} R}_{\text{'Geometry'}} = \underbrace{\frac{8\pi G}{c^4} T_{\mu\nu}}_{\text{'Energy'}} , \tag{1.10}$$

where all tensors are symmetric. $G_{\mu\nu}$ is the Einstein tensor, $T_{\mu\nu}$ is the stress-energy tensor describing the matter and electromagnetic components of spacetime. $R = R^{\rho}_{\rho}$ is the Ricci scalar, and $R_{\mu\nu}$ is the Ricci tensor, obtained via the contraction $R_{\mu\nu} = R^{\rho}_{\mu\rho\nu}$ of the Riemann curvature tensor which is given by

$$R^{\sigma}_{\mu\rho\nu} = \Gamma^{\rho}_{\mu\nu,\rho} - \Gamma^{\rho}_{\mu\rho,\nu} + \Gamma^{\sigma}_{\tau\rho}\Gamma^{\tau}_{\mu\nu} - \Gamma^{\sigma}_{\tau\nu}\Gamma^{\tau}_{\mu\rho} . \tag{1.11}$$

The Christoffel symbols themselves are defined in terms of the metric:

$$\Gamma^{\sigma}_{\mu\rho} = \frac{1}{2} g^{\sigma\tau} \left(g_{\rho\tau,\mu} + g_{\mu\tau,\rho} - g_{\mu\rho,\tau} \right) . \tag{1.12}$$

Note that eqs. 1.10-1.12 are covariant, which means that they are independent of the choice of coordinates. In GR, all coordinate systems and reference frames are treated as equivalent. Thus, there is no such thing as global inertial frames known in Newtonian theory. Despite the superficial simplicity of eq 1.10, the Einstein equations form a complicated set of 10 coupled non-linear partial differential equations which have closed analytical solutions only for the most idealized physical settings such as the static spherically, or the stationary axisymmetric situation: the Schwarzschild or the Kerr solutions. In most astrophysical scenarios it is thus necessary to solve the Einstein equations numerically in ways outlined for example in the review by Baumgarte and Shapiro [28].

However, in regions of spacetime where the curvature is only small, it is possible to simplify the Einstein equations by a so-called linearization. In linearized gravity, the metric $g_{\mu\nu}$ may be treated as deviating only slightly from the flat Minkowski metric $\eta_{\mu\nu} = diag(-1, 1, 1, 1)$:

$$g_{\mu\nu} = \eta_{\mu\nu} + h_{\mu\nu} , \tag{1.13}$$

demanding that

$$\| h_{\mu\nu} \| \ll 1 . \tag{1.14}$$

Here $h_{\mu\nu}$ is the metric perturbation. Note that the condition $\| h_{\mu\nu} \| \ll 1$ requires both the gravitational field to be weak and the coordinate system to be approximately Cartesian. In the linearized theory of gravity, we only keep terms linear in $h_{\mu\nu}$. Higher order terms are discarded. As a consequence, indices are raised and lowered by the flat metric $\eta_{\mu\nu}$. Note that since we use $\eta_{\mu\nu}$ to raise and lower indices, spatial indices can be written either in the 'up' position or the 'down' position without changing the value of a quantity: $f^a = f_a$. However, raising or lowering a time index switches sign: $f^t = -f_t$. The metric perturbation $h_{\mu\nu}$ thus transforms under Lorentz transformations, but not under general coordinate transformations.

In order to find the Einstein equations in the linear limit, we have to compute all the quantities which are needed to describe linearized gravity by dropping all non-linear terms in $h_{\mu\nu}$. The Christoffel coefficients are now given by

$$\Gamma^{\nu}_{\mu\rho} = \frac{1}{2}\left(h^{\nu}{}_{\mu,\rho} + h^{\nu}{}_{\rho,\mu} - h_{\mu\rho}{}^{,\nu}\right) \; . \tag{1.15}$$

Having this, the Riemann curvature tensor,

$$R_{\mu\nu\alpha\beta} = \frac{1}{2}(h_{\mu\beta,\nu\alpha} + h_{\mu\alpha,\nu\beta} - h_{\mu\alpha,\nu\beta} - h_{\nu\beta,\mu\alpha}) \; , \tag{1.16}$$

and subsequently, also the Ricci tensor,

$$R_{\mu\nu} = \frac{1}{2}\left(h^{\alpha}_{\mu,\nu\alpha} + h_{\nu\alpha,\mu}{}^{,\alpha} - \Box h_{\mu\nu} - h_{,\mu\nu}\right) \; , \tag{1.17}$$

can be constructed in linearized theory, where $h = h^{\alpha}{}_{\alpha}$ is the trace of the perturbation, and $\Box = \nabla^2 - \partial_t^2$ is the d'Alembert wave operator. Contracting once more, the Ricci scalar is given by

$$R = \left(h^{\rho}{}_{\mu}{}^{,\mu}{}_{,\rho} - \Box h\right) \; . \tag{1.18}$$

Building now the Einstein tensor from above's linearized expressions results in a unwieldy expression:

$$G_{\mu\nu} = \frac{1}{2}\left(h^{\alpha}_{\mu,\nu\alpha} + h_{\nu\alpha,\mu}{}^{,\alpha} - \Box h_{\mu\nu} - h_{,\mu\nu} - \eta_{\mu\nu} h^{\rho}{}_{\sigma}{}^{,\sigma}{}_{,\rho} + \eta_{\mu\nu}\Box h\right) \tag{1.19}$$

One can clean-up the latter eq. 1.19 by two measures. First, the trace-reversed tensor $\overline{h}$ is introduced:

$$\overline{h}_{\mu\nu} = h_{\mu\nu} - \frac{1}{2}\eta_{\mu\nu} h \; , \tag{1.20}$$

for which $\overline{h}^{\alpha}{}_{\alpha} = -h$ holds. Moreover, if one assumes secondly the Lorentz gauge conditions

$$\overline{h}^{\mu\nu}{}_{,\nu} = 0 \; , \tag{1.21}$$

and applies it in combination with eq. 1.20 to the Einstein tensor, we find that all terms but one in eq. 1.19 vanish. The linearized Einstein equations then reduce to

$$G_{\mu\nu} = \Box\overline{h}_{\mu\nu} = -\frac{16\pi G}{c^4} T_{\mu\nu} \; . \tag{1.22}$$

1.3.2 Physical properties of gravitational radiation

Wave solutions in vacuum spacetimes, GW polarizations and the transverse-traceless (TT) gauge

In vacuum ($T_{\mu\nu} = 0$ everywhere), eq. 1.22 reduces to the simple wave equation

$$\Box\overline{h}^{\mu\nu} = 0 \; , \tag{1.23}$$

and admits plane wave solutions:

$$\overline{h}^{\mu\nu} = A^{\mu\nu} \exp(ik_\lambda k^\lambda) \ , \tag{1.24}$$

with the wave vector $k^\lambda = (\omega/c, \vec{k})$. Inserting eq. 1.24 into 1.23 results in $k_\lambda k^\lambda = 0$, implying that GWs travel along the null geodesics, i.e. at the speed of light c.
Due to symmetry properties of $\overline{h}^{\mu\nu}$, the polarization tensor $A^{\mu\nu}$ has initially ten independent components. Enforcing the Lorentz gauge reduces this to six. A useful specialization of the Lorentz gauge is the so-called transverse-traceless (TT) gauge, which is obtained by choosing a special generator for the gauge transformation (ξ^μ; see [76]) with $\Box\xi^\mu = 0$. This reduces the wave field to two independent physical degrees of freedom which can be identified as polarizations:

$$A^{\mu\nu} k_\lambda = 0 \ , \qquad A^\lambda_\lambda = 0 \ , \qquad A_{\mu\lambda} U^\lambda = 0 \ , \tag{1.25}$$

with an arbitrary, light-like ($U_\nu U^\nu = 0$) unit 4-vector U^ν. From the TT gauge conditions it follows that the metric perturbation is purely spatial

$$h^{TT}_{\mu 0} = h^{TT}_{00} = 0 \ , \qquad h^{TT}_{ij,j} = 0 \ , \tag{1.26}$$

and traceless

$$h = h^i_{\ i} = 0 \ . \tag{1.27}$$

Note that since $\overline{h}^{TT}_{\mu\nu}$ is traceless, there is no distinction between $\overline{h}^{TT}_{\mu\nu}$ and $h^{TT}_{\mu\nu}$, i.e. $\overline{h}^{TT}_{\mu\nu} = h^{TT}_{\mu\nu}$. In the transverse plane, the dimensionless GW amplitude can now simply be represented by a two-dimensional matrix with only two independent elements h_+ and $h_\times$:

$$h^{TT}_{ab} = \begin{pmatrix} h_+ & h_\times \\ h_\times & -h_+ \end{pmatrix} \ . \tag{1.28}$$

If the coordinate unit basis vectors in this particular plane are $\hat{e}_x$ and $\hat{e}_y$, then we can define the basis tensors as

$$e_+ \ = \ \hat{e}_x \otimes \hat{e}_x - \hat{e}_y \otimes \hat{e}_y \tag{1.29}$$

$$e_\times \ = \ \hat{e}_x \otimes \hat{e}_x + \hat{e}_y \otimes \hat{e}_y \ , \tag{1.30}$$

where $\otimes$ is the outer product.
The dimensionless gravitational field tensor h^{TT}_{ij} of a GW propagating in the positive z-axis can then be written as a linear combination of the two independent, transverse-traceless unit tensors that correspond to the two possible polarization modes of GWs:

$$h^{TT}_{ij} = h_+ e_+ + h_\times e_\times \ . \tag{1.31}$$

If the coordinates in the transverse plane are rotated by an angle of Ψ, one obtains new amplitudes h'_+ and $h'_\times$ given by

$$h'_+ \ = \ \cos 2\Psi h_+ + \sin 2\Psi h_\times \tag{1.32}$$

$$h'_\times \ = \ -\sin 2\Psi h_+ + \cos 2\Psi h_\times \ . \tag{1.33}$$

This shows that a rotation by $\pi/4$ changes one polarization into the other (see fig. 1.5), implying that gravitational radiation possesses helicity 2 [157].

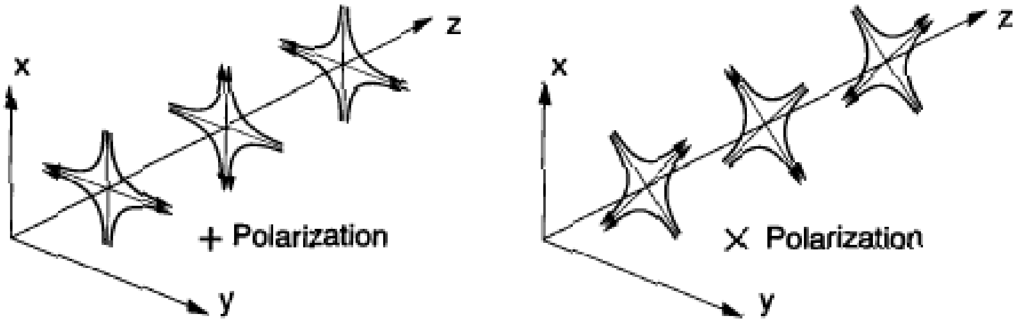

Figure 1.5: The lines of force for a purely + GW (left), and for a purely × GW (right). Note that the names are derived from the shape of the equivalent force fields that they produce. Figure taken from [16].

1.3.3 The weak-field, slow-motion limit

Gravitational waves are generated by the matter source term on the right hand side of the linearized Einstein equations (see eq. 1.22). The solution to this inhomogeneous wave equation is found in analogy to electromagnetic theory [105] via the convolution of the inhomogeneity in eq. 1.22 with a time-retarded Green's function $G(t, \vec{x}, t', \vec{x}')$. The Green's function associated with the wave operator $\Box$ is [105]

$$G(t, \vec{x}, t', \vec{x}') = -\frac{\delta(t' - |\vec{x} - \vec{x}'|/c)}{4\pi|\vec{x} - \vec{x}'|} \, , \tag{1.34}$$

where $t - |\vec{x} - \vec{x}'|/c$ is the retarded time, emphasizing the causal nature of GWs. It takes into account the lag associated with the propagation of information from events at $\vec{x}$ to position $\vec{x}'$. Applying eq. 1.34 to eq. 1.22, the solution is given by

$$h_{ij}^{TT}(t, \vec{x}) = \left[\frac{4G}{c^4} \int d^3x' \frac{T_{ij}(t - |\vec{x} - \vec{x}'|/c, \vec{x}')}{|\vec{x} - \vec{x}'|}\right]^{TT} \, . \tag{1.35}$$

Note that, as already mentioned, the radiative (physical) degrees of freedom are contained entirely in the spatial part of the metric, projected transverse and traceless.

The latter quantity (eq. 1.35) can now be evaluated at large distances from the source. Under this assumption, we may expand $|\vec{x} - \vec{x}'|^{-1} \approx r^{-1}$, where r is the distance from the observer to the source. Moreover, the source will conform to the weak-field limit ($\frac{GM}{c^2R} \ll 1$, with M, R being the mass and extent of the source) and to the slow-motion approximation ($|\vec{v}| \ll c$, where $\vec{v}$ is the velocity of internal motions of the source). In these limits and after some mathematical manipulations, this expansion (in powers of $\frac{\vec{x}}{\vec{x}'}$) yields in lowest order the so-called *quadrupole formula*

$$h_{ij}^{TT}(t, \vec{x}) = \frac{2G}{c^4 r}\left[\ddot{I}_{ij}\left(t - \frac{|\vec{x}|}{c}\right)\right]^{TT} \, , \tag{1.36}$$

where $\ddot{I}_{ij}$ is the second time derivative of the mass quadrupole moment, defined as

$$I_{ij} := \int d^3x' \rho(t, \vec{x}') x'_i x'_j \ . \tag{1.37}$$

In order to match the right hand side of eq. 1.37 with the transverse-traceless gauge conditions, we first have to subtract the trace from I_{ij}:

$$t_{ij} = I_{ij} - \frac{1}{3}\delta_{ij} I \ , \qquad I := I_{ii} \ , \tag{1.38}$$

which is the so-called *reduced mass quadrupole tensor*. Moreover, to complete the derivation, we must project out the non-TT pieces of the right-hand side of eq. 1.36. Having the projection tensor

$$P_{ijkl} = P_{ik}P_{jl} - \frac{1}{2}P_{ij}P_{kl} \ , \quad \text{where} \quad P_{ij} = \delta_{ij} - \frac{x_i x_j}{|\vec{x}|^2} \ , \tag{1.39}$$

we can write out the *standard quadrupole formula* (SQF):

$$h_{ij}^{TT}(t, \vec{x}) = \frac{2G}{c^4 r} P_{ijkl} \ddot{t}_{kl}^{TT}(t - \frac{|\vec{x}|}{c}) \ . \tag{1.40}$$

Note that higher-order terms are strongly suppressed by powers of $1/c$ and thus not considered anywhere in this thesis (see, e.g., [234, 32, 158]).
It should be clear from the TT projection operation that the emitted radiation is not isotropic: it will be stronger in some directions than others. It should also be clear from this that spherically-symmetric motions do not emit gravitational radiation; when the trace is removed, nothing remains. This fact is independent of the quadrupole approximation and known as *Birkhoff's theorem*, which states that any spherically symmetric solution of the vacuum field equations must be stationary and asymptotically flat. This means that the exterior solution must be given by the Schwarzschild metric [157]; as direct consequence, no monopolar gravitational radiation can exist. At this point, it is wort mentioning that similarly to electrodynamics, there are in principle two sets of moments in the GW expansion: moments of mass distribution ρ and moments of mass current distribution ρv [234], where v is the velocity (cf. electrodynamics, where electric and magnetic moments exist [105]). The mass-dipole moment as well as the mass-current dipole moment (the subsequent expansion terms next to the monopole term) will not produce any kind of gravitational radiation due to conservation of momentum and angular momentum in an isolated system. Thus, gravitational radiation of a leading order must be of a quadrupolar nature [157].
Note moreover that the prefactor G/c^4 in eq. 1.40 turns out to be $\mathcal{O}(10^{-50})$ – a very small number. Hence, in order to generate interesting amounts of GWs, the quadrupole moment's variation must be enormous. The only interesting sources of GWs will be those which have very large masses undergoing extremely rapid variation; even in this case, the typical GW strains we expect from such sources are tiny [39]. This reflects the fact that gravity is the weakest of the fundamental interactions [246].

Finally, there are several issues related to the SQF (eq. 1.40) and its use, which need to be mentioned:
a) The quadrupole formalism to extract the gravitational radiation is not gauge invariant and only valid in the Newtonian slow-motion limit. However, it was shown by [219] that the method above seems to be sufficiently accurate compared to more elaborate techniques, as it preserves phase while being off in amplitude by $\sim 10\%$ in neutron star pulsations.
b) GWs extracted by the SQF live only in the distant wave zone [157], that is, they are fully formed and linear. From electrodynamics [105] it is known that waves that are very close to their source do not yet have their asymptotic shape. The same is true for GWs. Moreover, since GR is a non-linear theory, GWs also interact strongly with curvature near their source. Note that there exist elaborate techniques such as post-Newtonian expansions which in principle allow for an extension of the SQF to regions of space-time where the pure weak-field slow-motion approximation breaks down [157, 76]. However, this is beyond the scope of my thesis.
c) The SQF contains second time derivatives of the mass quadrupole tensor which are numerically cumbersome, related to numerical high-frequency noise and the r^2 momentum-arm, which make the performance of a direct numerical evaluation of eq. 1.40 poor, as discussed in [71]. Therefore, in my simulations I use alternative expressions of [32] and [71] where one or both time derivatives of the quadrupole moment are transformed into hydrodynamical variables that are known from the core collapse simulation. I will outline this issue in more detail in subsection 1.4.

1.3.4 Gravitational wave detectors

Physics is after all an empirical science. The simulations I carried out during the course of my PhD studies were aimed at producing GW forms which might help to measure and/or interpret future detector output which is generated by a CCSN. Hence, in this subsection I will give an overview of the ongoing experimental efforts to observe GWs with earth-based facilities.

Interaction of gravitational waves with matter

Before I start with describing ground-based detector facilities, it is necessary to explain how GWs act on matter, since this in consequence influences the design of the experimental set-up.

In GR, the Newtonian expression of the gravitational force is replaced by the idea that freely falling bodies follow geodesics in spacetime. Given a spacetime metric $g_{\mu\nu}$ and a set of spacetime coordinates x^μ, the classical equation of motion is replaced by

$$\frac{d^2x^\mu}{d\tau^2} + \Gamma^\mu_{\nu\sigma}\frac{dx^\nu}{d\tau}\frac{dx^\sigma}{d\tau} = 0 \, , \tag{1.41}$$

where τ is the proper time measured by an observer travelling along the geodesic.

If we specialize again to linearized theory, with the non-flat part of the metric dominated by a GW in TT gauge, and assume moreover non-relativistic motions for the test body ($v \ll c$), eq. 1.41 simplifies to

$$\frac{d^2x^i}{dt^2} + \Gamma^i_{00} = 0 \ . \tag{1.42}$$

In linearized GR and the TT gauge,

$$\Gamma^i_{00} = \Gamma_{i00} = \frac{1}{2}\left(2\partial_t h^{TT}_{j0} - \partial_j h^{TT}_{00}\right) = 0 \ , \tag{1.43}$$

since $h^{TT}_{\mu 0} = 0$. Hence, we find that $d^2x^i/dt^2 = 0$. This does not mean that GWs have no effect; it simply tells that in the TT gauge the coordinate location of a slowly moving, free falling body is unaffected by the GW. In essence, the coordinates move with the waves. The proper separation between two freely falling particles on the other hand oscillates, even if the coordinate separation is constant. This can be best seen if we consider two spatial freely falling particles, located at $z = 0$, and separated on the x axis by a coordinate distance L_c [76]. For simplicity, we assume a GW in the TT gauge that propagates down the z axis, $h^{TT}_{\mu\nu}(t, z)$. The proper distance L between the two particles in presence of the GW is given by

$$L = \int_0^{L_c} ds = \int_0^{L_c} dx \sqrt{\left(1 + h^{TT}_{xx}(t, z = 0)\right)} \ , \tag{1.44}$$

where the infinitesimal line element ds is

$$ds^2 = g_{\mu\nu}dx^\mu dx^\nu = \left(\eta_{\mu\nu} + h_{\mu\nu}\right) dx^\mu dx^\nu \ . \tag{1.45}$$

Eq. 1.44 can be approximated by

$$L \approx \int_0^{L_c} dx \left[1 + \frac{1}{2}h^{TT}_{xx}(t, z = 0)\right] = L_c \left[1 + \frac{1}{2}h^{TT}_{xx}(t, z = 0)\right] \ . \tag{1.46}$$

Expression 1.46 tells that the proper separation between the two test particles oscillates with a fractional length change $\Delta L/L_c$ which is proportional to the gravitational wave strain:

$$\frac{\Delta L}{L_c} = \frac{1}{2}h^{TT}_{xx}(t, z = 0) \ . \tag{1.47}$$

Notice that although I applied the TT gauge in order to perform this calculation, the result is gauge independent [76].

Any attempt to measure GWs thus must be based on the fact that the physical distance ΔL between two point masses will undergo changes when a wave passes them, since they act tidally, stretching and squeezing space and thus any object they pass through. Figure 1.5 shows this behaviour in a more general case: the two polarizations of a GW and the lines of force associated with them.

In contrast to electromagnetic radiation, the wavelength of GWs is typically comparable or larger than the size of the radiating source. GWs are generated by the bulk dynamics of the source itself such as the motion of neutron stars in a binary system. In consequence, GWs cannot deliver an image, since the radiation simply does not resolve the generating system. However, since GWs are coherent, they probe, in analogy to sound, the two polarizations which carry a stereophonic description of the source's dynamics. Another extremely important consequence of the coherency mentioned is that the direct observable of gravitational radiation is the GW strain h^{TT}, being an amplitude, falls off by $\propto 1/r$. This contrasts with electromagnetic radiation whose observables are in most cases energy fluxes and hence fall off with $\propto 1/r^2$. This means that relatively small improvements in the sensitivity of GW detectors can have a large impact on science: doubling the sensitivity of a detector doubles the distance to which sources can be detected, increasing the volume of the Universe to which sources are measurable by a factor of 8. In contradiction to electromagnetic astronomy, which is based on deep imaging of small fields of view, GW astronomy is an all-sky affair: GW detectors have nearly a 4π steradians sensitivity to events in the sky [14]. This means on one hand that any source in the sky will be detectable, but on the other hand also that the ability of a single detector to localize a source is not good at all. However, having a network of GW observatories operating widely scattered over the globe improves the situation drastically. Sky location and the simultaneous measurement of the distance to the source follows from triangulation of time-of-flight differences between separate detectors [242,39,23,13].

From these general considerations, we now turn to more specific details. The 'known' sources of GWs cover 22 decades of frequencies, ranging from $\sim 10^{-18}$Hz (inflationary universe) up to $\sim 10^4$Hz (e.g. neutron star mergers; for a review of GW sources, see e.g., [39], with references therein). The high-frequency band, 1Hz $\lesssim f \lesssim 10^4$Hz [76,39,233], can be targeted by ground-based detectors, while lower frequencies can only be accessed via spaceborne facilities for reasons which will be given later in this subsection. Note that I will restrict myself from now on to the discussion of earth-based facilities and their performance, because the GW signature of stellar core collapse falls into this particular frequency range, as can be seen by the following simplistic, but nevertheless very useful estimates: for compact sources such as a core-collapse supernova, typical GW properties such as the GW amplitude at a given distance r, or the typical frequency of emission can be related to the source's size R and mass M by dimensional analysis and the quadrupole formula (eq. 1.40). Here, R means the length scale over which the source's dynamics vary. The 'natural' GW frequency f_{GW} of such a source, and its inverse, the dynamical timescale τ_{dyn}, can be estimated by [76,157]

$$\tau_{dyn} := \frac{\text{characteristic size R}}{\text{mean velocity}} \sim \frac{R}{\sqrt{GM/R}} = \sqrt{\frac{R^3}{GM}}\ . \tag{1.48}$$

Using the estimate of eq. 1.48 and applying the quadrupole formula (eq. 1.40), a first order-of-magnitude estimate for the dimensionless GW strain can be made [157]:

$$|h^{TT}| \sim \frac{2G}{rc^4}\frac{MR^2}{\tau_{dyn}^2}\ . \tag{1.49}$$

If we assume in eq. 1.49 values which are representative for a Galactic stellar core collapse, namely $M \sim 1M_\odot$, $R \sim 1500$km, and $r = 10$kpc, then we obtain as a

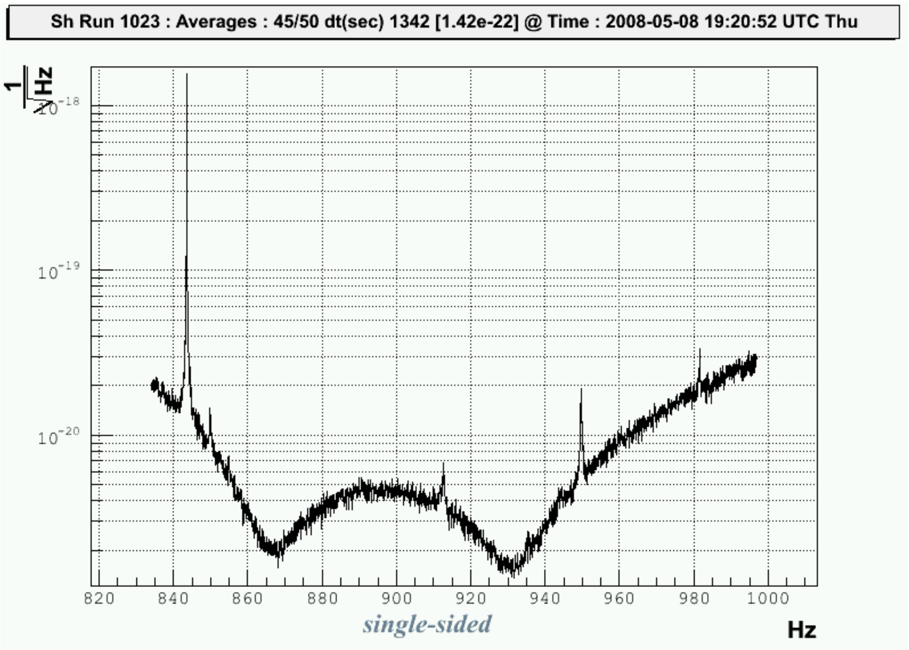

Figure 1.6: Strain sensitivity of the *AURIGA* detector (Istituto Nazionale di Fisica Nucleare [5]). The cryogenic 'bar' detector *AURIGA* is possibly the most sensitive and stable detector of this kind continuously on the air. The figure is courtesy of Massimo Cerdonio, private communication (April 2010).

rough estimate $|h^{TT}| \sim \mathcal{O}(10^{-21})$. Results which I will present later in this thesis, namely in chapters 3 and 4, verify such value as the right order of magnitude. With the aid of the simplistic arguments above, the extreme requirements upon GW detector sensitivity and the related experimental challenges become obvious: measuring a fractional change in length of order $\mathcal{O}(10^{-21})$ translates into determining the distance from earth to moon with the incredibly high precision of several atomic nuclei.

Earth-based gravitational wave detectors are divided into two classes, namely *resonant mass detectors* and *interferometric detectors*. In the following, I will outline the basic functionality and strategies of the present detector systems/classes in operation.

Resonant-mass detectors

The first attempts to detect GWs in a laboratory were made by Joseph Weber in 1960 by building two cylindrical aluminium resonant-mass detectors, operating at room temperature, a resonance frequency of $\sim$ 1660Hz, and a strain sensitivity of $\sim 10^{-15}$ [244]. Nowadays, resonant bar detectors are still constructed Weber-like; however, going to cryogenic- or even ultracryogenic temperatures has improved their sensitivities by many orders of magnitude.

A typical resonant bar detector consists of a cylinder of very high-Q [5] material such as aluminium or niobium, a length $l \sim 3$m, and a mass of $M \sim 2000$kg, and possesses a resonance frequency of ~ 1kHz (for a summary of properties of resonant-mass detectors in operation in 2005, see [48]).

As a basic principle of operation, one exploits the fact that the fundamental longitudinal frequency of such a bar is very sharply defined, allowing for the resonant driving of mechanical oscillations by incident GWs at the bar's resonant frequency and in a narrow bandwidth of ~ 100Hz around it (see fig. 1.6). A GW burst with $h \sim 10^{-21}$ will make the bar vibrate with an amplitude

$$\Delta L_{GW} \sim hL \sim 10^{-21}\text{m} \; . \tag{1.50}$$

The elastic vibrations of the mass are measured by means of a transducer that converts the displacement into an electric signal, which is then amplified [20, 233, 157].

To be able to measure this, the experimentalists have to fight against three main sources of noise [39]

1. **Thermal noise**: This is due to the Brownian motion of the detector atoms. The root mean square amplitude of this motion is

$$\langle \Delta L \rangle_{Th}^{1/2} = \left(\frac{kT}{4\pi^2 M f^2} \right)^{1/2} \; . \tag{1.51}$$

   At room temperature, the rms amplitude of the Brownian vibration is of the order of 10^{-16}m [20]. The most advanced bar detectors such as AURIGA (Legnaro, Padova, Italy) and NAUTILUS (Frascati, Rome, Italy) operate today at ultracryogenic temperatures of $T = 100$mK and very high Q-values of $Q \sim 10^6 - 10^7$ [5, 11]. Under these circumstances, the rms amplitude of vibration is lowered to $\sim 10^{-18}$m. Moreover, the fundamental mode changes its thermal amplitude of vibration in a random walk with very small steps, taking a time $Q/f \sim 1000$s to change by a full amount. For a 1ms GW burst at resonance frequency, the thermal noise will have random-walked to an expected amplitude change $(1000s/1ms)^{1/2} = Q^{1/2}$ times smaller [20, 39]:

$$\langle \Delta L \rangle_{Th,1ms}^{1/2} = \left(\frac{kT}{4\pi^2 M f^2 Q} \right)^{1/2} \; . \tag{1.52}$$

   Thus ultracryogenic resonant-mass detectors can have a thermal-noise limited strain sensitivity of $\sim 6 \times 10^{-21}$m [39].

2. **Sensor noise**: A transducer converts the bar's mechanical energy into electrical energy and an amplifier increases the electrical signal level to record it. Both components introduce noise, limiting the sensitivity to narrow regions

---

[5] Note that a high-Q (quality) factor is important, since it causes a lower rate of dissipation relative to the stored energy of the oscillator; the oscillations hence die out more slowly. Oscillators with high quality factors have low damping so that they ring longer [86].

near the resonance frequency f. However, state-of-the art transducer-amplifier units allow for resonant-mass detector bandwidths of not only 10 [48], but more than 100Hz, as displayed in fig. 1.6.

3. **Quantum noise**: The zero-point vibrations of a bar with a resonance frequency of 1kHz are given by Heisenberg's uncertainty principle [20, 39]:

$$\langle \Delta L \rangle^{1/2}_{Quant} = \left(\frac{\hbar}{2\pi M f} \right)^{1/2} \sim 4 \times 10^{-21}\mathrm{m} \ . \tag{1.53}$$

   This number is comparable to the thermal limits over 1ms. So, as detectors improve their thermal limits, they run into the quantum limit, which must be breached before a signal at 10^{-21} can be seen with such a detector.

From the discussion above, it becomes clear that bar detectors have great difficulty in achieving the sensitivity goal of 10^{-21}. Nevertheless, the excellent sensitivity of resonant detectors within their rather narrow bandwidth makes them suitable for specialized searches such as for GWs from so-called low T/|W| instabilities [243], as shown in fig. 3.22 in sec. 3.5. However, funding for bar detectors at present (2010) is very restricted, because there is a more promising detector design: laser interferometry. Currently, there are only two remaining bar detectors, NAUTILUS and AURIGA. They might eventually be shut down in the near future, when the interferometers begin operating at sensitivities clearly better than 10^{-21}. It is however important to keep them on air at least until 2014, when all the large interferometric detector systems, currently shut down due to major sensitivity upgrades [242], are back in operation. In the words of Massimo Cerdonio (April 2010): *rather be shortsighted than blind.*

Interferometric detectors

The first seeds of the idea for laser interferometer GW detectors were already planted in the 1960's and 1970's, since already at that time the limitations of bar detectors were apparent (see e.g., [82, 159, 247, 31]).

As a basic principle of operation, interferometric GW detectors use laser light to measure changes in the difference between the length of two perpendicular arms. This design is, in contrast to the bar detectors, intrinsically wide-band [16]. The experimental set up is very much like that of a two-armed Michelson Interferometer, as shown in fig. 1.7. An injected laser beam is split into two components which then travel at right angles to each other down separate arms. The beams bounce off polished test masses/mirrors at the end of each arm and return to their starting point, where they interfere with one another. The interferometer is set up so that in its default mode the laser beams interfere destructively and there is no net output. A passing GW would make one arm slightly longer and the other shorter, which induces a relative phase shift in the arm light, seen as a change in intensity at the output of the detector. In general, both the + and × polarization of incident GWs influence the test masses. A general detector output $h(t)$ can then be written as a

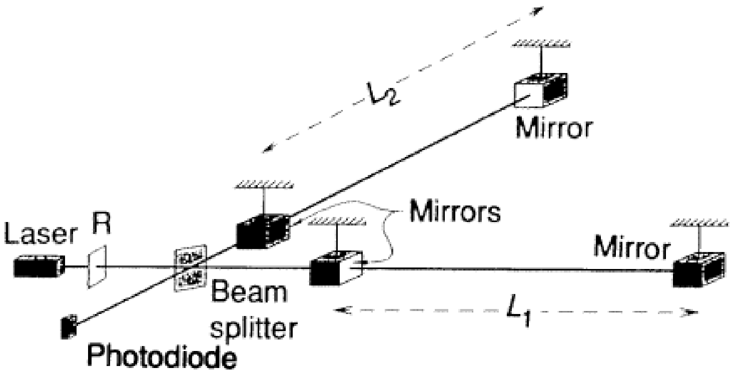

Figure 1.7: Schematic view of a laser light interferometric GW detector. Figure taken from [16].

time series:

$$\frac{\Delta L}{L} = F_+ h_+(t) + F_\times h_\times(t) + n(t) = h(t) \ , \tag{1.54}$$

where L is the detector arm length. The instrument response is a convolution of the antenna patterns $F_{+,\times}$ with the two GW polarizations. The antenna patterns depend on the frequency and sky location of the source, and $n(t)$ marks the instrument noise [233]. From astrophysical models (see eq. 1.49), we know that $h \sim 10^{-21}$ strain sensitivity is required. With the current displacement sensitivities of $\Delta L \sim 10^{-18}$m, a detector should thus have an arm length of $\sim 1 - 10$km in order to achieve the desired sensitivity. This is the actual scale of the interferometers which are in operation.

The sensitivity of the interferometer thus depends on the arm length, but also on the amount of light energy stored in the arms (see [20], with references therein). Furthermore, note that all the main interferometric optical components and beam path are enclosed in an ultra-high vacuum system ($10^{-8} - 10^{-9}$Torr) for acoustical isolation and to reduce phase fluctuations from light scattering off residual gas [14]. More detailed reviews of the interferometric detector design can be found in [233, 201, 108, 39].

Like the resonant mass detectors, interferometers are also plagued by different kinds of noise which put limits upon the sensitivity of the instrument (see fig. 1.8). The main sources of noise competing with physical signals are [20, 39]:

1. **Seismic noise**. External mechanical vibrations lead to displacements of the mirrors that are many orders of magnitude larger than the expected signal. Seismic noise is the limiting noise below ~ 10 Hz (see Fig. 1.8). Above this value, a combination of active filters (piezo-electric actuators), passive filters (alternate layers of steel and rubber) and a multi-stage pendulum suspension of the optical components allow effective filtering.

2. **Thermal noise**. As with bar detectors, Brownian motion of the mirrors and the excitation of the violin modes of the suspension can mask GWs. Thermal

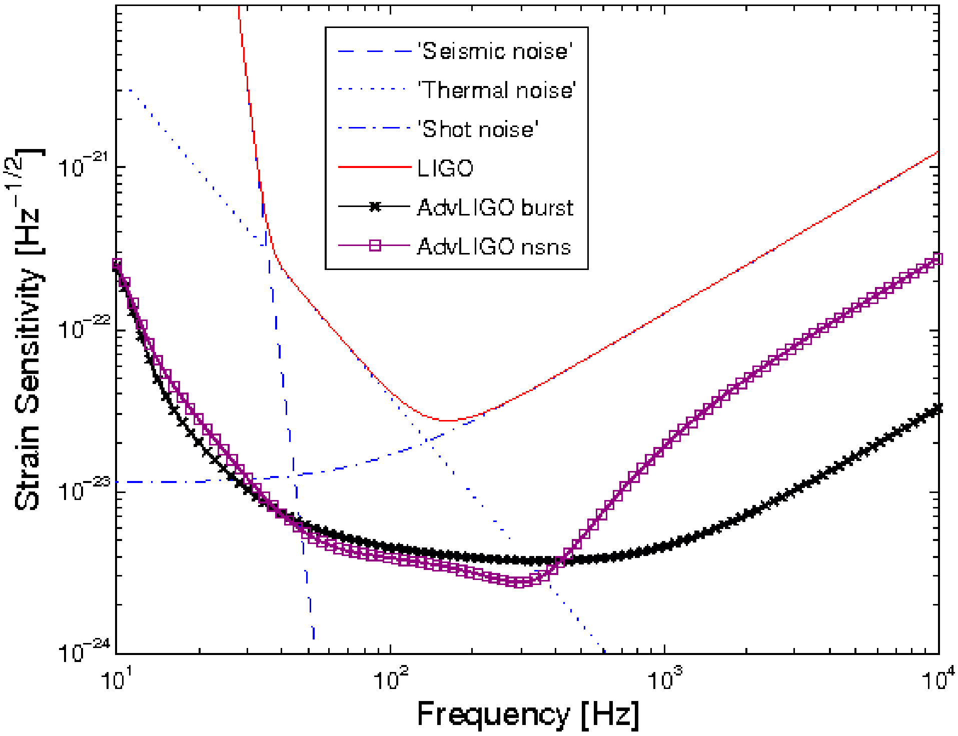

Figure 1.8: Strain sensitivity of LIGO, its limiting noise sources, and the strain sensitivity of Advanced LIGO. These curves are for unity signal to noise in strain amplitude in a one-hertz bandwidth, for a single instrument. The sensitivity curves are for an optimally incident wave in position and polarization; no averaging over position is given. Note that for Advanced LIGO, there is an adjustable frequency response, labelled as 'NSNS', which is a narrow-band tuning, and 'Burst', which corresponds to broad-band tuning. The LIGO data are courtesy of D. Shoemaker (2007).

noise is the limiting noise between 50 and 250Hz.

3. **Shot noise**. The photons that are used to do interferometry are quantized and so arrive at random and make random fluctuations in the light intensity that can look like a GW signal. The more photons one uses, the smoother the interference signal will be. As a random process, the measurement error improves with $\sqrt{N}$, where N is the number of photons. The shot noise related error displacement is given by [20]

$$\delta l_{shot} = \left(\frac{\hbar c}{2\pi} \frac{\lambda}{\eta P} \right)^{1/2} , \tag{1.55}$$

where η is the efficiency of the photodiode, λ the laser wavelength and P the circulating light power. In order to obtain $h < 10^{-22}$, $\eta P \sim 1$kW is required. Photon shot noise is the principal limitation to sensitivity for frequencies above

250Hz, as shown in fig. 1.8. Today, the interferometric detectors operate with lasers of 10W output, and the necessary high light power is obtained via resonant cavities and beam recycling [14].

4. **Quantum effects**. Shot noise is a quantum noise, and like all quantum noises there is a corresponding conjugate noise. As the laser power is increased to reduce the shot noise, the position sensing accuracy improves, and one eventually comes up against the Heisenberg uncertainty principle $\Delta x \Delta p > \hbar$. For present-day detectors, this corresponds to $h_{qu} \approx 10^{-25}$ [20].

5. **Gravity gradient noise**. Changes in the local gravitational field act like tidal forces on a GW detector. This environmental noise comes from human activities, but also from atmospheric activity such as clouds or the surf of the sea [39]. These effects become dominant at low frequencies and are the primary reason why the detection of GWs in the frequency band below 1Hz cannot be done with earth-based detectors, but must be done in space [14]. In order to be able to probe GW sources at frequencies below $\lesssim$ 1Hz, two major projects, namely the Laser Interferometer Space Antenna (LISA), a joint project of the ESA and NASA [2,102], and the Japanese DECIGO (DECi-hertz Interferometer Gravitational wave Observatory, [113]) are scheduled for launching in 2018 (LISA), or probably later, depending on the funding situation [39].

Today, the major projects for large interferometers are [39,248] (see fig. 1.9):

- **LIGO**. The Laser Interferometer Gravitational wave Observatory [14,10] consists of three operating systems: A single 4km interferometer in Livingston (Louisiana, USA), as well as a pair of interferometers (4km, 2km) in Hanford (Washington, USA).
- **VIRGO**. VIRGO is a 3km French-Italian detector near Pisa, Italy [17,7].
- **GEO600**. GEO600 is a 600m interferometer, constructed in a German-English joint project near Hannover, Germany [144,1].
- **TAMA300**. TAMA300 is a 300m interferometer operating near Tokyo [4,226].

Note that all these sites are well separated, which supports coincidence analysis. I further point out that there is also a small detector operating in Western Australia, the so-called AIGO (Australian Interferometric Gravitational Observatory [8]). At the moment, it is not clear if a large detector might also be funded. From the point of view of extracting information from observations, however, it would be very desirable to have a large-scale detector in Australia too, because of its very long baselines to the USA and Europe [39].

Within the past few years, the first generation of these interferometers have got very close to or even reached design sensitivity and collected partially coincident data, as discussed in [14]. Lately, the two 4km LIGO detectors were upgraded to sensitivities increased by a factor of 2-3 (enhanced LIGO, see [191]) and resumed observations in 2009 for the S6 science run [10]. S6 is expected to continue until

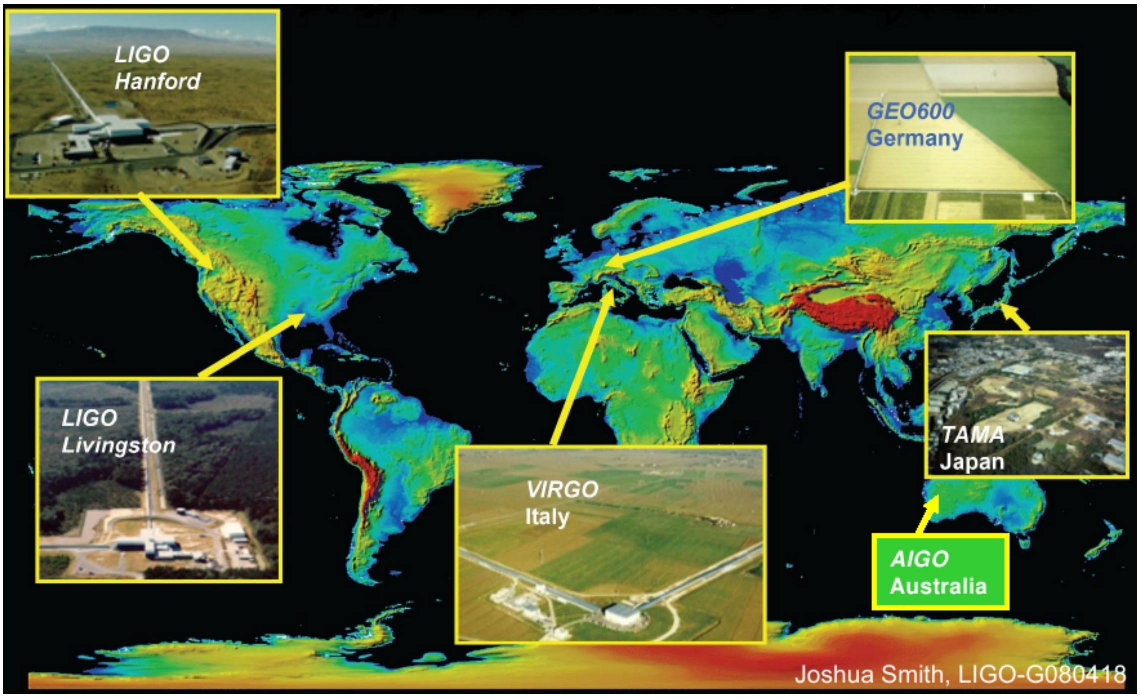

Figure 1.9: The interferometric GW projects spread around the globe. Figure taken from [242].

the end of 2010, when the interferometers will be shut down and disassembled in preparation for the installation of Advanced LIGO. Moreover, VIRGO, also, will undergo major upgrades at the same time [242]. The installation of the advanced detectors is expected to be completed by 2014 [10]. This will increase the observable volume by a factor of ~ 1000. Operating at such a high level of precision, 1 year of initial LIGO data taking will correspond to $\lesssim 1$ day of Advanced LIGO [242].

1.4 Gravitational wave extraction in HD- and MHD simulations

In sec. 1.3.3 I introduced and discussed the basics of the linearized GW theory. As pointed out there, I extract the GWs from my magnetohydrodynamical simulations via the quadrupole approximation (eq. 1.40). For relatively weak fields ($\frac{G}{c^2}\frac{M}{R} \sim 0.1$), and motions ($v \sim 0.1 - 0.2c$) encountered in CCSNe, this method works reasonably well, as pointed out in [219] (see sec. 1.3.3). However, since the SQF (eq. 1.40) is numerically cumbersome [71], I will now present expressions for GW extraction which I implemented because they are directly applicable to astrophysical problems. Note that for purposes of convenience, I have slightly changed the notation in the following subsection as compared to subsections 1.3.3-1.3.1.

1.4.1 Alternative formulations of the Standard Quadrupole Formula

As a reminder, I start again with the two independent polarisations of the dimensionless gravitational wave field $h_{\mu\nu} = g_{\mu\nu} - \eta_{\mu\nu}$, which in the transverse-traceless gauge are given by

$$h_{ij}^{TT}(\mathbf{X}, t) = \frac{1}{r}(A_+ e_+ + A_\times e_\times) \; . \tag{1.56}$$

The spatial indices i, j run from 1 to 3 [157]; r is the distance from the source to the observer. Since stellar core collapse proceeds in good approximation spherically, I choose a source-local spherical coordinate frame (r, θ, ϕ) to describe the two possible GW polarizations. Hence, this time I give the unit polarisation tensors e_+ and $e_\times$ in Spherical and not Cartesian coordinates:

$$\begin{aligned} e_+ &= e_\theta \otimes e_\theta - e_\phi \otimes e_\phi & (1.57) \\ e_\times &= e_\theta \otimes e_\phi + e_\phi \otimes e_\theta \; . & (1.58) \end{aligned}$$

In the slow-motion limit [157,71], the amplitudes A_+ and $A_\times$ are linear combinations of the second time derivative of the transverse-traceless mass quadrupole tensor t_{ij}^{TT}, as shown in sec. 1.3.3. In Cartesian coordinates, the quadrupole tensor is expressed as

$$t_{ij}^{TT} = \frac{G}{c^4} \int dV \rho \left[x_i x_j - \frac{1}{3}\delta_{ij}(x_1^2 + x_2^2 + x_3^2) \right]^{TT} \; . \tag{1.59}$$

The polarisation modes can be obtained explicitly from a coordinate transformation, for example for the $\theta\theta$-component:

$$t_{\theta\theta} = t_{ij}^{TT} \frac{\partial x^i}{\partial \theta} \frac{\partial x^j}{\partial \theta} . \tag{1.60}$$

This leads to the following non-vanishing components [173]:

$$\begin{aligned} t_{\theta\theta} &= (t_{xx}^{TT} \cos^2\phi + t_{yy}^{TT} \sin^2\phi + 2t_{xy}^{TT} \sin\phi\cos\phi)\cos^2\theta \\ &+ t_{zz}^{TT} \sin^2\theta - 2(t_{xz}^{TT}\cos\phi + t_{yz}^{TT}\sin\phi)\sin\theta\cos\theta \\ t_{\phi\phi} &= t_{xx}^{TT}\sin^2\phi + t_{yy}^{TT}\cos^2\phi - 2t_{xy}^{TT}\sin\phi\cos\phi \\ t_{\theta\phi} &= (t_{yy}^{TT} - t_{xx}^{TT})\cos\theta\sin\phi\cos\phi + t_{xy}^{TT}\cos\theta(\cos^2\phi \\ &- \sin^2\phi) + t_{xz}^{TT}\sin\theta\sin\phi - t_{yz}^{TT}\sin\theta\cos\phi. \end{aligned}$$

For convenience I evaluate below the GW amplitudes along the polar axis ($\theta = \phi = 0$, denoted as subscript I)

$$\begin{aligned} A_{+\mathrm{I}} &= \ddot{t}_{xx}^{TT} - \ddot{t}_{yy}^{TT} \; , & (1.61) \\ A_{\times\mathrm{I}} &= 2\ddot{t}_{xy}^{TT} \; , & (1.62) \end{aligned}$$

and in the equatorial plane ($\theta = \frac{\pi}{2}$, $\phi = 0$, denoted as II)

$$\begin{aligned} A_{+\mathrm{II}} &= \ddot{t}_{zz}^{TT} - \ddot{t}_{yy}^{TT} \; , & (1.63) \\ A_{\times\mathrm{II}} &= -2\ddot{t}_{yz}^{TT} \; . & (1.64) \end{aligned}$$

Note that in axisymmetry, $A_{+\mathrm{I}}, A_{\times\mathrm{I}}$, and $A_{\times\mathrm{II}}$ all vanish, leaving only $A_{+\mathrm{II}}$ [234]. Since a direct evaluation of eq. 1.59 is numerically problematic, as discussed e.g. in [71] and [32], we apply alternative reformulations of the standard quadrupole formula, in which one or both time derivatives are replaced by hydrodynamic variables using the continuity and momentum equations.

In the *first moment of momentum density formula* [71], one can get rid of one time derivative by making use of the continuity equation [127]:

$$\frac{\partial \rho}{\partial t} + \frac{\partial \left(\rho v_i\right)}{\partial x_i} = 0 \; . \tag{1.65}$$

Inserting eq. 1.65 into eq. 1.40 and integrating by parts, the first time derivative of the quadrupole moment is then

$$\dot{t}_{ij}^{TT} = \frac{G}{c^4} \int dV \rho \left[v_i x_j + v_j x_i - \frac{2}{3} \delta_{ij} \left(v_1 x_1 + v_2 x_2 + v_3 x_3 \right) \right]^{TT} \; . \tag{1.66}$$

This first moment of momentum density (eq. 1.66) already greatly reduces the numerical noise in the extracted GW signal [71]. In order to obtain my GW forms numerically, I compute the single remaining time derivative via finite differences in a postprocessing step.

One can even go a step further and additionally apply the Newtonian equation of momentum conservation [127],

$$\frac{\partial \left(\rho v_i\right)}{\partial t} + \frac{\partial \left(\rho v_i v_j + p \delta_{ij}\right)}{\partial x_i} = -\rho \frac{\partial \Phi}{\partial x_i} \; , \tag{1.67}$$

in order to get rid of the second time derivative [32]. In eq. 1.67, p stands for the fluid pressure. By virtue of eqs. 1.67 and 1.66, the so-called *stress formulation* [32], $\ddot{t}_{ij}^{TT}$ is given by

$$\ddot{t}_{ij}^{TT} = \frac{G}{c^4} \int dV \rho \left(2 v_i v_j - x_i \partial_j \Phi - x_j \partial_i \Phi \right)^{TT} \; , \tag{1.68}$$

where Φ is the Newtonian gravitational potential. Note that in the simulations I carried out, an effective, GR corrected gravitational potential Φ_{eff} is used, which then replaces Φ in eq. 1.68 (see [147] and sec. 2.2.2).

I applied both ways of computing the GW signal and compared them by computing the overlap [83] of the resulting waveforms via

$$O(h_1, h_2) = \frac{\langle h_1 | h_2 \rangle}{\sqrt{\langle h_1 | h_1 \rangle \langle h_2 | h_2 \rangle}} \; , \tag{1.69}$$

$$\langle h_1 | h_2 \rangle = 4 \Re \int_0^{\infty} df \frac{\hat{h}_1(f) \hat{h}_2(f)}{S_h(f)} \; . \tag{1.70}$$

where $\hat{h}$ is the Fourier transform of h, $S_h(\nu)$ [Hz^{-1}] is the power spectral density of the strain noise from a given detector, e.g. LIGO, which was kindly provided by D. Shoemaker (2007, private communication). The results show good agreement with

Model	$\Omega_{c,i}$ [rads^{-1}]	Overlap
R1E1AC$_L$	0.3	96%
R3E1AC$_L$	2π	92%
R4E1AC$_L$	3π	97%

Table 1.1: Overlap of GW trains from representative models R1E1CA$_L$, R3E1CA$_L$ and R4E1FC$_L$ (see chap. 3, and [206]).

numerical deviations of a few percent, as displayed in tab. 1.1. There, I computed the overlap of GW trains from the representative models R1E1CA$_L$, R3E1CA$_L$ and R4E1FC$_L$ (see chap. 3, and [208]), extracted by using eqs. 1.66 and 1.68. I assume optimal orientation of detector and source as well as the GW to be emitted along the polar axis.

In [122], it was pointed out that magnetic fields as strong as $\mathcal{O}(10^{17})$G can affect the GW amplitude considerably. Thus, in order to calculate the contribution to the GW signal due to 'strong' magnetic stresses (see e.g. [170, 208, 122], and sec. 3.5), I generalized eq. 1.68, taking into account contributions from the magnetic field. Following the 2D axisymmetric derivations of [120] and [170], I accounted for the magnetic field in the SQF by applying the equation of motion of a magnetized fluid [105, 124],

$$\frac{\partial\left(\rho v_i\right)}{\partial t}+\frac{\partial\left(\rho v_i v_j+P_\star\delta_{ij}-b_i b_j\right)}{\partial x_i}=-\rho\frac{\partial\Phi}{\partial x_i}\ , \tag{1.71}$$

to eq. 1.68. In eq. 1.71, the total pressure is composed of the fluid and magnetic pressure, $P_\star = p+\frac{b^2}{2}$, where $b_i = B_i/\sqrt{4\pi}$ are the normalized Cartesian components of the magnetic field. The Cartesian quadrupole gravitational wave amplitude in the MHD case, published in [208], then becomes:

$$\ddot{t}_{ij}^{TT}=\frac{G}{c^4}\int dV\left[2f_{ij}-\rho\left(x_i\partial_j\Phi+x_j\partial_i\Phi\right)\right]^{TT}\ , \tag{1.72}$$

where $f_{ij} = \rho v_i v_j - b_i b_j$.

Below, I apply eq. 1.66 *if not stated otherwise.* Given our spherically-symmetric effective GR approach to the solution of the Poisson equation in most models I computed (cf. chap. 3 and [206, 210, 208]), this expression is best motivated physically, since it does not depend on spatial derivatives of the gravitational potential.

Note that the radiative quadrupole moment is a measure of asphericity of the core's density distribution. It was pointed out by [170] in the purely 'axisymmetric' case that the quadrupole moment is positive for a very prolate core, and negative in the limit of a very oblate core. Its first time derivative measures the asphericity of the mass-flux and momentum distribution of the core, and its second time derivative, $A_{+\mathrm{II}}$, is a measure of the asphericity of the forces acting on the fluid. As a rule of thumb, a prolate mass-flux or a prolate momentum distribution (e.g. bipolar jet-like outflow along the rotational axis) gives rise to a positive value of the first time derivative of the quadrupole moment. Forces that act on the core in a way to make it more oblate, such as centrifugal forces, will give rise to a negative contribution to the total amplitude.

1.4.2 Total energy emission and spectral energy density

The energy carried away by gravitational radiation can be calculated by the following expression [157]:

$$\begin{aligned} E_{GW} &= \frac{c^3}{5G}\int \left[\frac{d}{dt}\left(I_{ij} - \frac{1}{3}\delta_{ij}I_{ll}\right)\right]^2 dt \qquad (1.73) \\ &= \frac{2c^3}{15G}\int dt \Big[\dot{I}_{xx}^2 + \dot{I}_{yy}^2 + \dot{I}_{zz}^2 \\ &\quad -\dot{I}_{xx}\dot{I}_{yy} - \dot{I}_{xx}\dot{I}_{zz} - \dot{I}_{yy}\dot{I}_{zz} \\ &\quad + 3(\dot{I}_{xy}^2 + \dot{I}_{xz}^2 + \dot{I}_{yz}^2)\Big] \ , \end{aligned}$$

where $I_{ij} = \ddot{t}_{ij}^{TT}$. The equivalent frequency integral yields [161]

$$\begin{aligned} E_{GW} &= \frac{4c^3}{15G}\int_0^\infty \nu^2 d\nu \Big[\hat{I}_{xx}^2 + \hat{I}_{yy}^2 + \hat{I}_{zz}^2 \\ &\quad -\hat{I}_{xx}\hat{I}_{yy} - \hat{I}_{xx}\hat{I}_{zz} - \hat{I}_{yy}\hat{I}_{zz} \\ &\quad +3\left(\hat{I}_{xy}^2 + \hat{I}_{xz}^2 + \hat{I}_{yz}^2\right)\Big] \ , \qquad (1.74) \end{aligned}$$

where $\hat{I}_{ij}(\nu)$ is the Fourier transform of the quadrupole amplitude $I_{ij}(t)$.

1.4.3 Characteristical GW strain

In order to assess the question of detectability of a certain model, I estimate the signal-to-noise ratios (SNR) for optimal filtering searches according to [75]:

$$\left(\frac{S}{N}\right)^2 = 4\int \frac{|\hat{h}(\nu)|^2}{S_h(\nu)} d\nu = 4\int \frac{|\hat{h}_+(\nu)|^2 + |\hat{h}_\times(\nu)|^2}{S_h(\nu)} d\nu \ , \qquad (1.75)$$

where $\hat{h}(\nu)$ is the Fourier transform of the gravitational wave amplitude and $S_h(\nu)$ is the power spectral density of strain noise in the detector. For numerical results, I always assume the source to be located at the Galactic centre at $R = 10$kpc. Moreover, I assume optimal orientation of detector and source. Note also that the Fourier spectra were normalized according to Parseval's theorem.

1.5 Additional analysis tools

Gravitational waves are a result of bulk matter motion [157]. Below, I therefore define a number of quantities and analysis tools which I extracted from my simulation data in order to help me to specify a particular model and allow me to monitor the development of the collective matter dynamics.

1.5.1 The β-parameter

A variable commonly used to quantify the dynamics of rotating, Newtonian fluid bodies (see, e.g., [228]) is the dimensionless parameter β,

$$\beta := \frac{T}{|W|} \ , \tag{1.76}$$

which is the ratio of rotational kinetic (T) to gravitational binding energy ($|W|$). The rotational kinetic energy is given by [86]

$$T = \frac{1}{2} \int \Omega_z (x j_y - y j_x) d^3x \ , \tag{1.77}$$

where $j_i = \rho v_i$ is the specific angular momentum.
Moreover, based on $\vec{\Omega} = \frac{\vec{r} \times \vec{v}}{r^2}$, the z-component of the angular velocity can be computed via

$$\Omega_z = \frac{x v_y - y v_x}{x^2 + y^2} \ . \tag{1.78}$$

1.5.2 The β_{mag}-parameter

In order to track the growth, strength and influence of the magnetic fields on the fluid, I monitor the quantity β_{mag}

$$\beta_{mag} := \frac{E_{mag}}{|W|} \ , \tag{1.79}$$

which is the ratio of magnetic

$$E_{mag} = \frac{|\vec{B}|^2}{8\pi} = \frac{B_x^2 + B_y^2 + B_z^2}{8\pi} \tag{1.80}$$

to gravitational binding energy ($|W|$).

1.5.3 Nonaxisymmetric structures

A commonly used way to monitor the growth of nonaxisymmetric structures is to examine the azimuthal Fourier components in the density distribution (see [182], and references therein):

$$\rho(R, z, \phi) = \sum_{m=-\infty}^{\infty} C_m(R, z) e^{im\phi} \ , \tag{1.81}$$

where R is the radius orthogonal to the rotational z-axis. The Fourier components C_m correspond to the azimuthal modes m and are defined by

$$C_m = \frac{1}{2\pi} \int_0^{2\pi} \rho(R, z, \phi) e^{-im\phi} \mathrm{d}\phi \ . \tag{1.82}$$

Furthermore, it is useful to define the normalized amplitudes

$$A_m = |C_m|/C_0 = \frac{1}{C_0}\sqrt{\Re(C_m)^2 + \Im(C_m)^2}, \tag{1.83}$$

where $C_0(R, z) = \overline{\rho}(R, z)$ is the mean density in a ring with radius R, and

$$|C_m| = \sqrt{\Re C_m^2 + \Im C_m^2}\ . \tag{1.84}$$

In practice, I implemented eq. 1.82 by interpolating the density on discrete rings in the equatorial plane and then performed a Fourier analysis of $m \in \{1, 2, 3, 4\}$. Following [182], I used 180 angular zones for 2π radians and performed the analysis for radii between 5km and 100km from the rotational axis, taking steps of 5km. Note that the confinement of the analysis to the equatorial $z = 0$ plane is motivated by the assumption that globally unstable modes are only weakly dependent on the z coordinate inside the PNS [200].

Additional insight into the azimuthal structure of each mode m can be gained by the mode phase angle

$$\Phi_m(R, z) = \tan^{-1}\left(\Im C_m/\Re C_m\right)\ . \tag{1.85}$$

If a given mode m is globally dominant, this is reflected in a radial variation of the phase angle that corresponds to the global structure of the mode [182]. For a spiral-type mode, Φ_m should exhibit a spiral structure, while a pure bar should result in a bar-like structure [183, 181]. In the situation where a mode m becomes global, one can write the phase angle as

$$\Phi_m = \sigma_m t\ , \tag{1.86}$$

where σ_m is the eigenfrequency of the $m-$th mode. The mode pattern speed σ_p is then given by

$$\sigma_p = \frac{1}{m}\frac{d\Phi}{dt} = \frac{\sigma_m}{m}\ . \tag{1.87}$$

Unfortunately, the direct determination of Φ_m via eq. 1.85 and its time derivative proves to be rather difficult numerically, not least because of the coarse temporal resolution of the post-processing based analysis, as also stated by [182]. An alternative way of obtaining σ_m introduces itself from the physical interpretation that the oscillation period of mode m, $P_m = 2\pi/\sigma_m$, is equivalent to the time it takes the real or imaginary parts of C_m to complete a full cycle from a positive to a negative value, then back to a positive value [183]. In this way, σ_m can be read off directly from the mode amplitudes in time intervals during which they show clear temporal behaviour.

1.6 Gravitational waves as messengers of stellar core collapse

Constraining the core-collapse supernova mechanism via astronomical observations is difficult. The intricate pre-explosion dynamics of the SN core deep inside the supergiant presupernova star is inaccessible by the traditional means of astronomy.

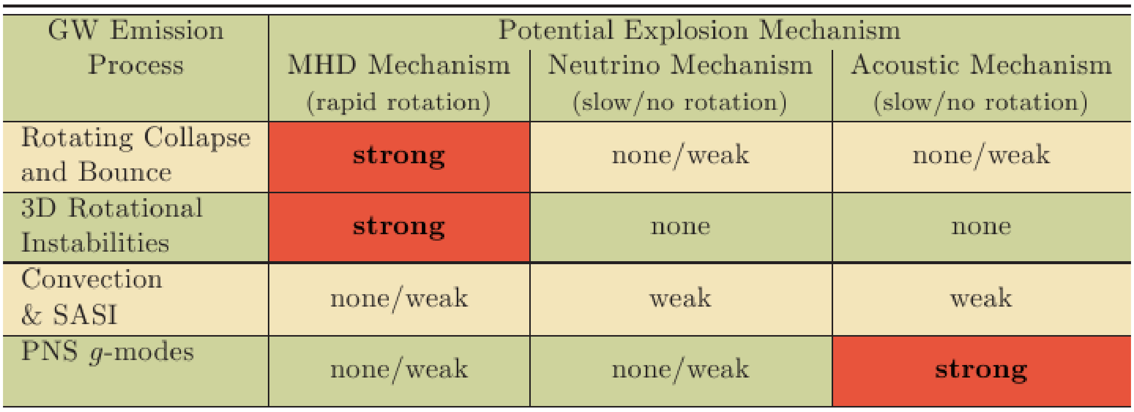

GW Emission Process	Potential Explosion Mechanism		
	MHD Mechanism (rapid rotation)	Neutrino Mechanism (slow/no rotation)	Acoustic Mechanism (slow/no rotation)
Rotating Collapse and Bounce	**strong**	none/weak	none/weak
3D Rotational Instabilities	**strong**	none	none
Convection & SASI	none/weak	weak	weak
PNS g-modes	none/weak	none/weak	**strong**

Figure 1.10: Compilation of the prominent GW emission processes in core-collapse SNe and their possible emission strength in context of the magneto-rotational (see [43], with references therein), the neutrino (see, e.g. [148], with references therein) and the acoustic SN mechanism [45]. For a galactic SN, 'strong' corresponds to 'probably detectable by initial and advanced LIGO', 'weak' means 'probably marginally detectable by advanced LIGO', and 'none' means 'absent or probably not detectable by advanced LIGO'. The three considered explosion mechanisms are likely to have mutually exclusive GW signatures and could be distinguished by the mere detection or non-detection of a GW signal without the solution of the full inverse problem. Figure taken from [174].

Theoretical models of the SN mechanism can currently be tested via secondary observables only, including asymptotic explosion energy, ejecta morphology, nucleosynthesis products [78], compact remnant mass and proper motion, and pulsar spin/magnetic fields (see sec. 1.2.3, and references therein).

Gravitational waves and neutrinos are the only messengers with the potential of delivering first-hand information on the physical processes leading to explosion: both are emitted deep inside the supernova core and travel to observers on Earth practically without interaction with intervening material.

Besides neutrinos, which have already been observed in the context of stellar core collapse of SN1987A [97], GWs could provide access to the electromagnetically hidden compact inner core of some such cataclysmic events. As strong indications both from theory and observations exist that CCSNe show aspherical, multidimensional features (see [94, 132], and sec. 1.2), there is reasonable hope that a tiny amount of the released binding energy will be emitted as GWs which could then provide us with valuable information about the angular momentum distribution [62] and the baryonic equation of state (EoS) [149], both of which are uncertain. Furthermore, they might help to constrain theoretically predicted SN mechanisms, as suggested by Ott [174] (see sec. 1.2, and fig. 1.10). However, GWs from astrophysical sources are weak and notoriously difficult to detect, as outlined in sec. 1.3.4. Hence, in order to disentangle an astrophysical GW signal from the mostly overwhelming detector noise, GW astronomy not only requires sensitive detectors, but also extensive processing and analysis of the detector output on the basis of reliable theoretical estimates for the GW signals presently expected from astrophysical sources. The latter must in most cases, such as for CCSNe, be obtained via detailed numerical modelling of the dynamics responsible for the GW emission in a given source.

The broad majority of GW sources can be subdivided into two classes: (i) mathematically well-posed events such as BH-BH coalescence and (ii) scenarios that involve matter. The first category of sources can be modelled accurately, the waveform can be calculated with high precision, and thus a matched-filter analysis can be applied. On the other hand, the latter kind of GW sources can only be modelled imperfectly, as matter effects carry large physics uncertainties and open up a huge parameter space for initial conditions. Moreover, even if there were 'perfect' models, there is still a turbulent, stochastic element in some GW emission mechanisms that makes it strictly impossible to compute templates. As a result, more general, un-modelled burst analysis techniques are used, as summarized in [14] and references therein. One of the scenarios where burst data analysis must be applied is the stellar core collapse, where in addition to the matter effects even the fundamental explosion mechanism is not fully settled, as outlined in sec. 1.2.

Until today, GW emission from CCSNe was suggested to arise from i) axisymmetric rotational core collapse and bounce (e.g., [261,122,61,62,208]) ii) prompt, neutrino-driven postbounce convection and anisotropic neutrino emission (e.g., [161,145,118, 149,165,116,117]), iii) protoneutron star (PNS) g-mode oscillations [175] and iv) nonaxisymmetric rotational instabilities (e.g., [199,243,181,183,180,179,206,207, 210,208]). A more detailed discussion will follow in sec. 1.7; recent reviews with a more complete list of references are [119,174,53]. However, only i) can be considered as being well understood as far as the physics of the collapse is concerned, since only theses models incorporate all relevant input physics known at present [62] (there are, though, still large uncertainties with respect to the progenitor star, e.g. rotation profiles, magnetic fields, and inhomogenities from convection). The predictions of all other suggested emission scenarios (ii-iv) still neglect, to a certain extent, dominant physics features due to the diversity and complexity of the CCSN problem on the one side and restrictions of available computer power on the other side. Hence, the computational resources have so far either been spent on highly accurate neutrino transport (e.g. [133,176,149]) while neglecting other physical degrees of freedom such as magnetic fields, or focus on a general relativistic treatment and/or 3D fluid effects such as accretion funnels, rotation rate and convection, but approximate or even neglect the important micro physics. Only recently have detailed 3D computer models of CCSNe become feasible with the emerging power of tens of thousands of CPUs unified in a single supercomputer. Such detailed simulations are absolutely indispensable for the reasons already implied above: a) GW astronomy requires not only very sensitive detectors, but also depends on extensive data processing of the detector output on the basis of reliable GW estimates [14]. b) The temperatures and densities inside a supernova core exceed the range that is easily accessible by terrestrial experiments (see fig. 1.11).

Thus, it will be impossible for the foreseeable future to construct a unique finite temperature equation of state (EoS) for hot and dense matter based on experimen-

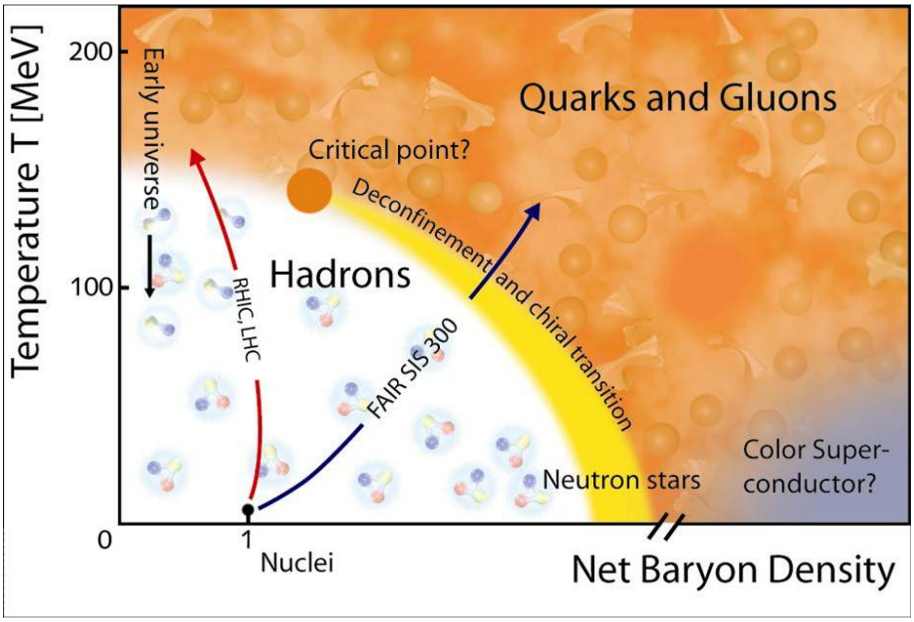

Figure 1.11: Illustration of the matter conditions which are or will be explored in the near future by the LHC [3], RHIC [6], and FAIR [9]. Although all of them will explore a different section of the nuclear matter phase diagram, they hardly reach the typical matter conditions which are present in supernova cores, namely 'low' temperatures and very high densities (see, e.g., [137]). Figure taken from [9].

tally verified data. Therefore, models with different parameter settings must be run and their computed wave form output can then be compared with actual detector data. Hence, modelling will bridge the gap between theory and measurement and allow the use of CCSNe as a laboratory for exotic nuclear and particle physics [137].

1.7 A brief survey on possible GW emission mechanisms from core-collapse supernovae

In this section, I want to provide a short overview of the different GW emission processes at present expected to occur in the context of stellar core collapse. However, this section is not meant as a review, but rather to prepare the stage for chapters 3 and 4, where I will discuss the resulting GW emission of my models in detail. Nevertheless, I hope to provide sufficient preparatory insight regarding the subject with the material provided here. Note also that I will cover neither the GW characteristics from the very massive population III stars [223] nor the accretion-induced collapse of white dwarfs [15]. For thorough review articles with complete lists of references on the GW emission processes of CCSNe, I refer to [174, 119, 53].

1.7.1 Gravitational waves from rotating core collapse and core bounce

During the past three decades probably most attention has been paid to rotational core collapse and bounce dynamics. In this particular phase, the core spins up due to angular momentum conservation, resulting in an oblate ($l = 2$) and time-dependent quadrupole deformation that leads to strong GW emission [160, 158, 107, 261, 195, 121, 122, 170, 177, 179, 180, 59, 61, 62, 206]. The steady improvement of the models (e.g. the inclusion of GR, a microphysical EoS, treatment of neutrino physics) recently led to a theoretically well understood single and generic, purely axisymmetric [179, 206, 208], so-called type I waveform which is characterized by a large negative peak at core bounce, followed by ring-down oscillations that damp quickly (see, e.g., [179, 180, 61, 62, 208], with detailed references therein). Despite the reduction to a single waveform, the combined information of the GW amplitude and the location of the narrow peak of the GW spectral energy density in frequency space contains information that makes it still possible to constrain progenitor and postbounce rotation, but can barely distinguish between different finite-temperature EoS (see, e.g., [62], who used the EoS of [130] and [216]).

1.7.2 Gravitational waves from postbounce convection, SASI and anisotropic neutrino emission

Current state-of-the-art stellar evolution calculations [93] tell us that iron cores of stars generally lose most of their angular momentum during their evolution due to magnetic torques. Therefore, they cannot become subject to strong rotationally-induced asphericities. However, anisotropic neutrino emission, convection and SASI-driven deviations from spherical symmetry which can lead to the emission of GWs of sizable amplitudes are likely to occur inside the PNS and the post-shock gain region and last for probably hundreds of ms [161,145,118,149,165,116,117,208,210]. Although there is qualitative consensus among the different core-collapse supernova groups about the aforementioned features being emitters of stochastic broad-band signals, their detailed quantitative character still remains quite uncertain, since self-consistent 3D simulations with proper long-term neutrino transport were not carried out so far, but would in principle be required. The most recent, very elaborate 2D simulations in that context were performed by [149]. Their numerical setup includes long-term multi-flavour neutrino transport, an effective relativistic potential and two different EoS. The first 100ms of after bounce they observed GWs from early prompt postbounce convection, peaking somewhat around or below 100Hz, depending on the employed EoS. After this early episode, the GW emission in their models is dominated by a growing negative amplitude related to anisotropic neutrino emission at frequencies $\lesssim$ 200Hz, while the GW signal associated with non-radial mass motions stems from density regimes $10^{11} - 10^{13}\mathrm{gcm}^{-3}$ and peaks in the frequency range of $300 - 800$Hz, highly sensitive to the nuclear EoS.

1.7.3 Gravitational waves from magnetorotational core collapse

GWs from magneto-rotational collapse were considered in 2D in detail by [122, 218] and [170], and recently also by myself [208] in 3D. As main differences compared to simulations which do not include magnetic fields it was found by these groups that only in the very special case of precollapse fields as strong as $\gtrsim 10^{12}$G the overall dynamics can be influenced. As [93] have argued, such strong fields are unlikely to occur in standard core-collapse supernova progenitors. The GW amplitude is then affected by i) time-dependent magnetic fields, which contribute considerably to the overall energy density, and ii) by bipolar magnetohydrodynamic jet outflows which give rise to a so-called type IV signal with memory [170]. Physically, such a memory effect in the GW signal arises from the temporal history of asymmetric matter outflow, leaving behind a constant offset in the amplitude [233]. The systematics of such GW memory can be best understood by considering an outflow of mass m in the z-direction with slowly changing velocity. In this case, the contribution to the GW signal by the outflow is $|h_{out}| \propto 2mv_z^2$ [218]. Once the outflow has reached quasi-steady state, the mass ejection rate can be assumed to stay roughly constant, hence the mass in the outflow increases linearly [218, 43].

1.7.4 Gravitational waves from nonaxisymmetric Instabilities at low $T/|W|$

Recently it has been argued through numerical simulations of equilibrium neutron star models or full core-collapse simulations that PNSs with a high degree of differential rotation can be subject to nonaxiymmetric rotational instabilities at low values of β, leading to strong narrow-band GW emission [199, 243, 181, 200, 183, 180, 51, 179, 206, 208, 210]. In most cases the bar-like $m = 2$ mode is dominant and one then frequently speaks of a 'barmode instability'. In analogy to the textbook example of GWs being emitted by a spinning bar [15], the self-consistent computations deliver a GW signature where the $+$ and $\times$ polarisations are shifted by a quarter cycle, and the dominant GW emission occurs at a frequency of $2f$, with f being the rotation rate of the deformed, innermost part of the protoneutron star.

However little is known about the true nature of the instability at present. Previous work has failed to establish an analytical instability criterion, and the dependence of the instability on PNS rotation rate and degree of differential rotation is still unclear, as was pointed out by [174].

1.7.5 Gravitational waves from protoneutron star pulsations

In the core-collapse scenario, PNS pulsations can provide another mechanism for GW emission. Ott et al. [175] pointed out that in the context of the acoustic mechanism [45, 46] excited core g-mode oscillations might emit very strong GWs. The GW signal is due to the nonlinear quadrupole components of the pulsations that, at least initially, are of $l = 1$ g-mode character [175].

1.8 Minimal requirements on 3D core-collapse supernova simulations

The lack of computational power at present does not allow theoreticians to include *all* the physics known to be relevant to CCSNe in a 'complete' form in 3D computer models (see chap. 2, and references therein). Nevertheless, three-dimensional models are indispensable because state-of-the-art simulations of stellar collapse and postbounce supernova evolution strongly suggest that multi-D dynamics is crucial for the CCSN mechanism to succeed in massive stars (see sec. 1.2.3, and references therein). Until 'complete' 3D modelling of CCSNe is feasible on high-performance clusters, the only way to deal with the problem is to apply pragmatic approaches, which mimic the dominant physics in a computationally efficient way.

For the time being, the list below represents a minimal set of requirements which should be included in 3D simulations if one wants to claim a reasonable and indicative outcome of the simulations (Matthias Liebendörfer, private communication (April 2010)):

- **Spectral transport of $\nu_e, \overline{\nu}_e$:** The reactions of the ν_e and $\overline{\nu}_e$ neutrinos with matter are the dominant ones in the context of CCSN dynamics, because they interact with their surrounding material via both charged and neutral current reactions, while the other neutrino species can only interact neutrally (see sec. 1.2.3, and references therein).

  Spectral treatment of ν_e and $\overline{\nu}_e$ is essential because several crucial quantities to which the SN dynamics is very sensitive, such as optical depth, neutrino cross-sections and so forth, are energy-dependent [37, 29, 106].

- **Finite-temperature nuclear EoS:** Any set of magnetohydrodynamical equations must be closed by an EoS. Moreover, in the context of stellar core collapse, a finite-temperature nuclear EoS is also a prerequisite for any kind of neutrino transport treatment, since the crucial compositional information as well as chemical potentials must be derived from a microphysical EoS (see sec. 2.3, and references therein).

- **Estimate for the flux factor:** The flux factor can be understood as a ratio of the neutrino energy flux, $L_\nu/(4\pi r^2)$, to neutrino energy density times c. Typically, it is close to 0.25 near the neutrino sphere for ν_e and $\overline{\nu}_e$ and approaches unity when the neutrino distributions get more and more forward-peaked in the limit of free-streaming with increasing distance from the neutrinosphere [106]. Usually, angle-dependent transport, i.e., solving the Boltzmann transport equation, is necessary to accurately determine the spectral and angular distribution of the neutrinos. However, as we want to apply, for example, different, computationally efficient neutrino transport approximations for different physical regimes (see sec. 2.4), it is essential to have a physically well-founded estimate for the flux factor at hand. This can help to reduce the computational time considerably.

- ν_μ, ν_τ **cooling:** Any quantitative 3D calculation of stellar core collapse should incorporate cooling processes via the emission of ν_μ and ν_τ. Spherically symmetric state-of-the-art simulations have shown that their inclusion changes the 'long-term' core-collapse dynamics (hundreds of ms after bounce) considerably, as their emission alters the hydrodynamical quantities such as entropy and electron fraction (e.g. [230, 194, 138]. The position of the stalled shock after several hundreds of ms for example, is located at considerably smaller radii compared to simulations which ignore the emission of ν_μ and ν_τ.

  The inclusion of ν_μ and ν_τ cooling in a multidimensional code is somewhat easier compared to the electron-flavour neutrinos, because i) of the limited number of relevant reactions, ii) of the sub-dominant role of μ and τ neutrinos (compared to the electron flavour neutrinos) in CCSN simulations, and iii) because of the negligible effect of their heating. Hence, a μ/τ leakage scheme, which depends on the local thermodynamical conditions only, can be implemented 'relatively' easy (Albino Perego, private communication (July 2010)). Even a simple and 'grey' [155] leakage scheme can fit the results of detailed neutrino transport calculations quite well such as position and energy of the shock.

- **Radial GR effects:** The inclusion of radial GR effects is essential in CCSN simulations, as they can influence the SN dynamics considerably. Compared to simulations in Newtonian gravity, general relativistic simulations result for example in smaller shock radii, higher neutrino luminosities and rms energies, and deeper potential wells which lead to higher central densities (see, e.g., [138, 38]).

- **Magnetic fields:** During core collapse and the early postbounce evolution of the PNS, even initially weak magnetic fields eventually grow to values where they can influence the dynamics of the SN plasma notably and thus can no longer be neglected (see sec. 2.2, and references therein).

  Moreover, as there is observational evidence that magnetorotational effects may play a dominant role in stellar core collapse such as e.g. in the GRB scenario [254], magnetic fields should be taken into account in simulations for a consistent picture of the core-collapse theory.

- **HRSC – High-resolution shock-capturing schemes:**

  In any hydrodynamical calculation, the fluid flow can be split into regions of smooth flows and regions of shock waves, where flows show sharp, discontinuous changes in flow variables such as pressure, temperature, density, and velocity across the shock. Modern hydrodynamical CCSN simulations must be able to handle both within the same framework, as the initially smooth density, velocity and internal energy distributions of the progenitor star lead to the formation of the SN shock wave at core bounce (see sec. 1.2, and references therein).

Thus, the applied, multidimensional hydrodynamical framework must rely on a reconstruction procedure for the cell-interface data that retains conservation. Moreover, it must not introduce spurious oscillations [84].

These requirements are usually met in a modern hydrodynamical schemes, which are constructed to have the following properties: i) stable and sharp discrete shock profiles; ii) high accuracy in smooth regions of the flow.

Schemes with these characteristics are usually known as *high-resolution shock-capturing* (HRSC) schemes. They avoid the use of artificial viscosity terms when treating discontinuities (see, e.g., sec. 2.2, and [238], with references therein).

In the following chapter, I will outline how the Basel 3D CCSN code tries to satisfy several of these prerequisites.

2 3D MHD Core-Collapse Simulations: Implementation

> *Ich behaupte aber,*
> *dass in jeder besonderen Naturlehre nur so viel eigentliche*
> *Wissenschaft angetroffen werden könne,*
> *als darin Mathematik anzutreffen ist.*
>
> Immanuel Kant, Metaphysische Anfangsgründe der Naturwissenschaft, A VIII

In this chapter I give an overview of the numerical methods and tools that I have used to perform the simulations on which my research on gravitational waves is based. This includes the discussion of `FISH` and `ELEPHANT`, the 3D magnetohydrodynamics (MHD) codes of the Basel supernova group of M. Liebendörfer (see, e.g., [111, 136, 141, 140]), which are primarily designed for performing astrophysical simulations such as CCSNe. Moreover, I will detail the underlying microphysical input of the core-collapse simulations such as the microphysical equation of state, neutrino transport schemes as well as the initial model configuration.

Note that during the course of my dissertation, I was involved in the technical code developement of `FISH`, including implementing a 'hybrid' parallelization scheme to the MHD part of the codes (see sec. 2.2.1) and multidimensional solvers for the gravitational potential (see sec. 2.2.2).

2.1 Ideal magnetohydrodynamics

Astrophysical problems such as CCSNe involve collisional problems where the mean free path is much smaller than all length scales of interest. Hence, one can adopt a fluid description of matter. Furthermore, since there is observational evidence that magnetorotational effects may play a dominant role in stellar core collapse such as in the collapsar-GRB (see [254], with references therein), magnetic fields must be taken into account [1].

The theoretical framework to describe a magnetized fluid is delivered by *magnetohydrodynamics* (see, e.g., [124, 105], with references therein). The simplest form of MHD, *ideal* MHD, assumes that the fluid has so little resistivity that it can be treated as a perfect conductor. For conditions prevailing in CCSNe, this way de-

---

[1] In the collapsar-GRB scenario, a black hole with stellar-mass accretion in combination with magnetorotational effects and/or neutrino-antineutrino pair creation and annihilation drive a baryon-poor ultra-relativistic GRB jet [253].

scribing the fluid is a good approximation of reality [124].

The equations of ideal MHD describe the movement of a compressible, conducting fluid subject to magnetic fields. In ideal MHD, all dissipative processes are neglected. This means that the fluid possesses no viscosity and its conductivity is assumed to be infinite. The ideal MHD equations read [105, 127]:

$$\begin{aligned}
\frac{\partial \rho}{\partial t} + \nabla \cdot (\rho \mathbf{v}) &= 0 && (2.1)\\
\frac{\partial \rho \mathbf{v}}{\partial t} \nabla \cdot (\mathbf{v} \rho \mathbf{v} - \mathbf{b}\mathbf{b}) + \nabla P &= -\rho \nabla \Phi && (2.2)\\
\frac{\partial E}{\partial t} + \nabla \cdot [(E + P)\mathbf{v} - \mathbf{b} \cdot (\mathbf{v} \cdot \mathbf{b})] &= -\rho \mathbf{v} \cdot \nabla \Phi && (2.3)\\
\frac{\partial \mathbf{b}}{\partial t} - \nabla \times (\mathbf{v} \times \mathbf{b}) &= 0\ , && (2.4)
\end{aligned}$$

expressing the conservation of mass, momentum, energy and magnetic flux, respectively. ρ stands for mass density, $\mathbf{v}$ is the velocity vector and $E = \rho e + \frac{\rho}{2} v^2 + \frac{b^2}{2}$ the total energy (the sum of internal, kinetic and magnetic energy). The magnetic field is given by $\mathbf{B} = \sqrt{4\pi}\mathbf{b}$ and the total pressure by $P = p + \frac{b^2}{2}$ (the sum of gas and magnetic pressure). The MHD equations are evolved from an (initial) condition

$$\nabla \cdot \mathbf{b} = 0\ , \tag{2.5}$$

which remains true, consistent with the physical observation that magnetic monopoles have never been observed. The right hand side of eqs. 2.2 and 2.3 take into account the effect of gravitational forces on the magnetohydrodynamical variables. The gravitational potential Φ obeys the Poisson equation

$$\Delta \Phi = 4\pi G \rho\ . \tag{2.6}$$

2.2 Numerical solution of the MHD equations: The `FISH` & `ELEPHANT` codes

The set of nonlinear partial differential equations (eqs. 2.1-2.4) generally have no analytic solution and must therefore be solved numerically. In this section, I will briefly present the 3D MHD Basel code `FISH` (Fast and Simple Ideal magneto-Hydrodynamics), which numerically evolves these hyperbolic [190] equations at second order accuracy in time and space. The entire code documentation can be found in Käppeli et al. [111]. `FISH` is based on the publicly available serial version of a cosmological hydrodynamics code of Pen et al. (see [185], with references therein), which was further improved, parallelized with MPI (Message Passing Interface, e.g. [249]) and adapted to the requirements of core-collapse supernova simulations by M. Liebendörfer [139]. Moreover, `FISH` provides the foundation for the implementation of multidimensional neutrino transport schemes (see sec. 2.4) in the

`ELEPHANT` code (ELegant and Efficient Parallel Hydrodynamics with Approximate Neutrino Transport).

Equations 2.1-2.4 are the differential form of the MHD equations. Their hydrodynamical part[2] can be expressed in a very compact notation by defining a column vector $\boldsymbol{u}$ of conserved variables and flux vectors $\boldsymbol{F}, \boldsymbol{G}, \boldsymbol{H}$ in the x, y and z directions, respectively, and a vector $\boldsymbol{S}$ of source terms:

$$\frac{\partial \boldsymbol{u}}{\partial t} + \frac{\partial \boldsymbol{F}}{\partial x} + \frac{\partial \boldsymbol{G}}{\partial y} + \frac{\partial \boldsymbol{H}}{\partial z} = \boldsymbol{S} \, , \tag{2.7}$$

where the vector $\boldsymbol{u} = (\rho, \rho v_x, \rho v_y, \rho v_z, E)^T$ denotes the conserved fluid variables, $\boldsymbol{F}$ is given by

$$\boldsymbol{F} = \begin{bmatrix} \rho v_x \\ \rho v_x^2 + P - b_x^2 \\ \rho v_x v_y - b_x b_y \\ \rho v_x v_z - b_x b_z \\ (E+P) v_x - b_x \boldsymbol{b} \cdot \boldsymbol{v} \end{bmatrix} , \tag{2.8}$$

$\boldsymbol{G}$ by

$$\boldsymbol{G} = \begin{bmatrix} \rho v_y \\ \rho v_y v_x - b_y b_x \\ \rho v_y^2 + P - b_y^2 \\ \rho v_y v_z - b_y b_z \\ (E+P) v_y - b_y \boldsymbol{b} \cdot \boldsymbol{v} \end{bmatrix} , \tag{2.9}$$

and $\boldsymbol{H}$ by

$$\boldsymbol{H} = \begin{bmatrix} \rho v_z \\ \rho v_z v_x - b_z b_x \\ \rho v_z v_y - b_z b_y \\ \rho v_z^2 + P - b_z^2 \\ (E+P) v_z - b_z \boldsymbol{b} \cdot \boldsymbol{v} \end{bmatrix} . \tag{2.10}$$

In the context of core-collapse simulations, the source term $\boldsymbol{S}$ takes into account only gravity [3] and reads

$$\boldsymbol{S} = \begin{bmatrix} 0 \\ -\rho \partial \Phi / \partial x \\ -\rho \partial \Phi / \partial y \\ -\rho \partial \Phi / \partial z \\ -\rho \boldsymbol{v} \cdot \nabla \Phi \end{bmatrix} . \tag{2.11}$$

The `FISH` code solves eqs. 2.7 numerically by applying so-called *finite volume methods* [190, 189] and *operator splitting* (see [111], and references therein), which I will now outline briefly.

---

[2] Note that the procedure to update of the magnetic fields will be discussed later in this section.

[3] Note that the general form is $\boldsymbol{S} = (0, \rho f_x, \rho f_y, \rho f_z, \rho \boldsymbol{v} \boldsymbol{f})^{\mathrm{T}}$, where $\boldsymbol{f}$ can by any external force.

In the framework of FISH, eqs. 2.7 are decomposed into two sub-problems, a homogeneous and an inhomogeneous one:

$$\text{Problem A:} \qquad \frac{\partial \boldsymbol{u}}{\partial t} + \frac{\partial \boldsymbol{F}}{\partial x} + \frac{\partial \boldsymbol{G}}{\partial y} + \frac{\partial \boldsymbol{H}}{\partial z} = 0 \tag{2.12}$$

$$\text{Problem B:} \qquad \frac{\mathrm{d}\boldsymbol{u}}{\mathrm{d}t} = \boldsymbol{S} \tag{2.13}$$

Let us consider the homogeneous system A first (eq. 2.12), where the source term vanishes. Since eqs. 2.7 need to be solved numerically, we have to discretize the problem. Time is discretized into steps Δt^n and space into finite volumes or cells $V_{i,j,k}$ where n labels the different time levels and the triple (i, j, k) denotes a particular finite volume or cell. This is a so-called finite-volume method. In practice, one stores the cell averaged values for the solution vector $\boldsymbol{u}$ (for each component separately) at cell centres:

$$\boldsymbol{u}_{i,j,k} = \frac{1}{V_{i,j,k}} \int_{V_{i,j,k}} \boldsymbol{u}\left(\boldsymbol{x}, t\right) \mathrm{d}x\mathrm{d}y\mathrm{d}z, \tag{2.14}$$

where the cell volume $V_{i,j,k} = \Delta x \Delta y \Delta z$ is given by the cell dimensions $\Delta x = x_{i+1/2} - x_{i-1/2} = x_{i'} - x_{i'-1}$, $\Delta y = y_{j+1/2} - y_{j-1/2} = y_{i'} - y_{i'-1}$, $\Delta z = z_{k+1/2} - z_{k-1/2} = z_{i'} - z_{i'-1}$ which are assumed to be constant. Half-integer indices are indicated by a prime $i' = i + 1/2$, $j' = j + 1/2$, $k' = k + 1/2$ and denote the inter-cell boundary. Note that in this introductory paragraph, the cell centred notation is kept for clarity. Further down, I switch to the more elegant ‘prime’ notation.

Let us furthermore denote $F^n_{i+1/2,j,k}$ as flux per area of $\boldsymbol{u}$ through the cell boundary $x_{i+1/2,j,k}$ at a time t^n which we assume constant over the respective cell surface. Analogously for $G^n_{i,j+1/2,k}$ and $H^n_{i,j,k+1/2}$. Then, the net flux of $\boldsymbol{u}$ in x-direction is

$$\int_{S(i+1/2)} \boldsymbol{F} \mathrm{d}y\mathrm{d}z - \int_{S(i-1/2)} \boldsymbol{F} \mathrm{d}y\mathrm{d}z = \Delta y \Delta z \left(F^n_{i+1/2,j,k} - F^n_{i-1/2,j,k}\right) . \tag{2.15}$$

If we now integrate A (eq. 2.12) numerically, a discrete time step can be written as

$$\begin{aligned} \frac{u^{n+1}_{i,j,k} - u^n_{i,j,k}}{\Delta t} \Delta x \Delta y \Delta z \quad &+ \quad \Delta y \Delta z \left(F^n_{i+1/2,j,k} - F^n_{i-1/2,j,k}\right) && (2.16)\\ &+ \quad \Delta x \Delta z \left(G^n_{i,j+1/2,k} - G^n_{i,j-1/2,k}\right) && (2.17)\\ &+ \quad \Delta x \Delta y \left(H^n_{i,j,k+1/2} - H^n_{i,j,k-1/2}\right) = 0 . && (2.18) \end{aligned}$$

The discrete temporal update for $\boldsymbol{u}$ is then

$$\begin{aligned} u^{n+1}_{i,j,k} = u^n_{i,j,k} \quad &- \quad \frac{\Delta t}{\Delta x} \left(F^n_{i+1/2,j,k} - F^n_{i-1/2,j,k}\right) \\ &- \quad \frac{\Delta t}{\Delta y} \left(G^n_{i,j+1/2,k} - G^n_{i,j-1/2,k}\right) \\ &- \quad \frac{\Delta t}{\Delta z} \left(H^n_{i,j,k+1/2} - H^n_{i,j,k-1/2}\right) . \end{aligned} \tag{2.19}$$

Note that eq. 2.19 is the so-called conservative form of the fluid part of ideal MHD equations, exhibiting the conservation of $\boldsymbol{u}$ over the whole (numerical) domain. It

expresses the fact that the flux coming out of one cell is added to the neighbouring cells which share the same boundary. For an isolated system, summing up the fluxes for the whole domain gives zero. Thus, conservation is ensured [189].
In a full operator-splitting scheme as used in `FISH`, one now applies one-dimensional solving operators in each coordinate direction. Note that the major advantage of the operator splitting technique is that permits the use of efficiently designed methods for each type of sub-problem.
If we consider, for simplicity, the pure hydrodynamical case first and forget for a moment about magnetic fields (and gravity), a splitted scheme then solves the 1D equation

$$\frac{\partial \boldsymbol{u}}{\partial t} + \frac{\partial \boldsymbol{F}}{\partial x} = 0 \tag{2.20}$$

for the x-direction, followed by analogous expressions for $\boldsymbol{G}$ and $\boldsymbol{H}$. So $\boldsymbol{u}$ is updated according to eq. 2.19 by splitting it for each direction as follows:

$$\begin{aligned}
\mathrm{L}_x : u^{n+1/3}_{i,j,k} &= u^{n}_{i,j,k} - \frac{\Delta t}{\Delta x}\left(F^{n}_{i+1/2,j,k} - F^{n}_{i-1/2,j,k}\right) \ , \\
\mathrm{L}_y : u^{n+2/3}_{i,j,k} &= u^{n+1/3}_{i,j,k} - \frac{\Delta t}{\Delta y}\left(G^{n+1/3}_{i,j+1/2,k} - G^{n+1/3}_{i,j-1/2,k}\right) \ , \\
\mathrm{L}_z : u^{n+1}_{i,j,k} &= u^{n+2/3}_{i,j,k} - \frac{\Delta t}{\Delta z}\left(H^{n+2/3}_{i,j,k+1/2} - G^{n+2/3}_{i,j,k-1/2}\right) \ ,
\end{aligned} \tag{2.21}$$

where the L_i are the solution operators for the coordinate considered. However, operator splitting is not exact. Applying the solution operators as in eqs. 2.21 is only first-order accurate in time. Nevertheless, it can be shown that applying the directional solution operators L_i twice, once in the forward and once in the backward order, makes the splitting second-order accurate every second time step [220]:

$$L_x L_y L_z L_z L_y L_x \boldsymbol{u}^{n}_{i,j,k} = L_x L_y L_z \boldsymbol{u}^{n+1}_{i,j,k} = \boldsymbol{u}^{n+2}_{i,j,k} + \mathcal{O}(\Delta t^2) \ . \tag{2.22}$$

Note that in the literature, applying a solution operator L_i is often called the $x-, y-, z-$ sweep in the respective directions. The combination $L_z L_y L_x$ is called the forward sweep, and $L_x L_y L_z$ the backward sweep.
If we turn our view now back to the more general case A (eq. 2.12), the solution algorithm of `FISH` to the ideal, homogeneous MHD equations can be summarized as

$$\boldsymbol{u}^{n+2} = L_{\text{forward}} L_{\text{backward}} \boldsymbol{u}^{n} + \mathcal{O}(\Delta t^2) \ , \tag{2.23}$$

where

$$\begin{aligned}
L_{\text{forward}} &= L_x\left(\Delta t\right) B^{yz}_{x}\left(\Delta t\right) L_y\left(\Delta t\right) B^{xz}_{y}\left(\Delta t\right) L_z\left(\Delta t\right) B^{xy}_{z}\left(\Delta t\right) \\
L_{\text{backward}} &= L_z\left(\Delta t\right) B^{xy}_{z}\left(\Delta t\right) L_y\left(\Delta t\right) B^{xz}_{y}\left(\Delta t\right) L_x\left(\Delta t\right) B^{yz}_{x}\left(\Delta t\right)
\end{aligned} \tag{2.24}$$

are the forward and backward operators for one time step. The operators $L_{x,y,z}$ evolve the fluid and account for the source terms, while the B operators evolve the magnetic field [4]. Note that during the fluid update, the magnetic field is held

---

[4] $L_{x,y,z}$ account for a further sub-splitting with gravity in the following way: $L_{x,y,z} = \frac{G_{x,y,z}}{2} L^{HD}_{x,y,z} \frac{G_{x,y,z}}{2}$; a detailed explanation will be given in subsection 2.2.

constant, while during the magnetic field advection, all quantities other than the magnetic field are held constant. Note also that the numerical solution algorithm to the MHD equations is explicit. Hence we are restricted by the Courant, Friedrich and Lewy (CFL) condition [192]. Therefore we impose the following time step

$$\Delta t^n = k \cdot \min_{i,j,k} \left(\frac{\Delta x}{C^{n,x}_{i,j,k}}, \frac{\Delta y}{C^{n,y}_{i,j,k}}, \frac{\Delta z}{C^{n,z}_{i,j,k}} \right) \tag{2.25}$$

where

$$C^{n,d}_{i,j,k} = \max \left(v^n_{d,i,j,k} + c^n_{F\ i,j,k} \right) \tag{2.26}$$

is the maximum speed at which information can travel in the entire computational domain in direction $d = x, y, z$. It is the sum of the velocity component in d-direction and the speed of the fast magnetosonic waves c_F, i.e. the fastest wave propagation speed supported by the equations of ideal MHD. $c_F = \sqrt{c_s^2 + v_A^2}$, where c_s is the speed of sound and v_A is the Alfvén velocity [124].
In our simulations, we typically set the CFL number k to 0.75.

Updating the fluid MHD equations: The $L_x^{HD}(\Delta t)$ update

In this subsection, I will outline how `FISH` performs the purely hydrodynamical $L_x^{HD}(\Delta t)$-update of the fluid variables $\boldsymbol{u}$ in x-direction. The y- and z-coordinates are treated analogously.
Integrating eq. 2.20 over a cell $V_{i,j,k}$ gives

$$\frac{\partial \boldsymbol{u}_{i,j,k}}{\partial t} + \frac{1}{\Delta x} \left(\boldsymbol{F}_{i',j,k} - \boldsymbol{F}_{i'-1,j,k} \right) = 0 \tag{2.27}$$

where the definition of the cell averaged values has been substituted and Gauss' theorem has been used. The numerical flux $\boldsymbol{F}_{i',j,k}$ represents an average flux of the conserved quantities through the surface $S_{i',j,k}$

$$\boldsymbol{F}_{i',j,k} = \frac{1}{S_{i',j,k}} \int_{S_{i',j,k}} \boldsymbol{F}(\boldsymbol{x}, t) \,\mathrm{d}y\mathrm{d}z \tag{2.28}$$

at given time t. Today, the evaluation of systems like eq. 2.27 are generally performed by Godunov-type [84] methods which now split into two parts:

- Reconstruction of the data at the cell interfaces. Based on the known cell averages $\boldsymbol{u}_{i,j,k}$ (see eq. 2.14), the data at the cell boundaries in smooth parts of the flow can be reconstructed to any required accuracy in space. In the vicinity of shocks the accuracy is dropped to first order to avoid spurious oscillations [84].

- Solution of the local Riemann problem at the cell interfaces.

The algorithm of Pen et al. [185] which is applied in `FISH` addresses these issues by a relaxation scheme of Jin and Xin [109]. For detailed information on this type of method, I refer to [109], with references therein.

The basic solution steps which the `FISH` code takes are the following:
a) A first-order upwind scheme [189] according to [109] is applied to reconstruct the total flux at the intercell boundaries:

$$\boldsymbol{F}_{i'} = \frac{1}{2}\left(\boldsymbol{F}_i + \boldsymbol{F}_{i+1}\right) - \frac{1}{2}D\left(\boldsymbol{u}_{i+1} - \boldsymbol{u}_i\right) \ . \tag{2.29}$$

For D we choose $D = d \cdot I$ to be a diagonal matrix, where

$$d = \max\left(d_i, d_{i+1}\right) \tag{2.30}$$

and d is the so-called freezing speed [109]. Inside a cell, it is chosen to be

$$d_i = |v_x| + c_F \ . \tag{2.31}$$

b) For smooth regions of flow, the first-order accurate reconstruction (see eq. 2.29), which corresponds to a piece-wise constant approximation of the flux, is 'upgraded' to second order accuracy by a slope-limited total variation diminishing (TVD) scheme (see, e.g., [238]). The total variation (TV) of $\boldsymbol{u}$ is defined by

$$TV(u) := \sum_{i=-\infty}^{\infty} |u_i - u_{i-1}| \ . \tag{2.32}$$

Second order accuracy of the flux is obtained by adding a piece-wise linear approximation ($\hat{=}$ slope) to a constant one:

$$\boldsymbol{F}(x,t) \approx \boldsymbol{F}_i + \phi \left.\frac{\partial \boldsymbol{F}}{\partial x}\right|_i (x - x_i) \ . \tag{2.33}$$

At discontinuities, a so-called slope limiter is set to zero ($\phi = 0$) which assures that piecewise constant reconstruction is recovered, while away from discontinuities, the second-order form is obtained. Thus, a slope limiter ϕ is then built so that the total variation of the solution does not increase in time:

$$TV(u^{n+1}) \leq TV(u^n) \ . \tag{2.34}$$

In `FISH`, the total second-order accurate numerical flux is constructed according to [109] as follows:

$$\boldsymbol{F}_{i'} = \underbrace{\frac{1}{2}\left(\boldsymbol{F}_i + \boldsymbol{F}_{i+1}\right) - \frac{1}{2}D\left(\boldsymbol{u}_{i+1} - \boldsymbol{u}_i\right)}_{1st-\text{order}} + \underbrace{\frac{\Delta x}{2}\left(\Delta\boldsymbol{F}_i^{+} - \Delta\boldsymbol{F}_{i+1}^{-}\right)}_{2nd-\text{order}} , \tag{2.35}$$

where

$$\begin{aligned} \Delta\boldsymbol{F}_i^{+} &= \phi\left(\Delta\boldsymbol{F}_i^{+,L}, \Delta\boldsymbol{F}_i^{+,R}\right) & (2.36) \\ \Delta\boldsymbol{F}_{i+1}^{-} &= \phi\left(\Delta\boldsymbol{F}_{i+1}^{-,L}, \Delta\boldsymbol{F}_{i+1}^{-,R}\right) \ . & (2.37) \end{aligned}$$

$\boldsymbol{F}^{+} = (\boldsymbol{w} + D\boldsymbol{u})/2$ denotes the right-travelling waves and $\boldsymbol{F}^{-} = (\boldsymbol{w} - D\boldsymbol{u})/2$ the left-travelling waves, and $\boldsymbol{w} = \boldsymbol{F}(\boldsymbol{u})$. Moreover, the 'left' and 'right' handed first order flux differences of the waves are given by

$$\left.\frac{\partial \boldsymbol{F}^{+}}{\partial x}\right|_{i} = \begin{cases} \Delta \boldsymbol{F}_{i}^{+,L} = \left(\boldsymbol{F}_{i}^{+} - \boldsymbol{F}_{i-1}^{+}\right)/\Delta x \\ \\ \Delta \boldsymbol{F}_{i}^{+,R} = \left(\boldsymbol{F}_{i+1}^{+} - \boldsymbol{F}_{i}^{+}\right)/\Delta x \end{cases} \tag{2.38}$$

and

$$\left.\frac{\partial \boldsymbol{F}^{-}}{\partial x}\right|_{i+1} = \begin{cases} \Delta \boldsymbol{F}_{i+1}^{-,L} = \left(\boldsymbol{F}_{i+1}^{-} - \boldsymbol{F}_{i}^{-}\right)/\Delta x \\ \\ \Delta \boldsymbol{F}_{i+1}^{-,R} = \left(\boldsymbol{F}_{i+2}^{-} - \boldsymbol{F}_{i+1}^{-}\right)/\Delta x \end{cases} . \tag{2.39}$$

In core-collapse simulations performed with `FISH`, we use the *Van Leer* limiter [240, 241] in the subsonic flow regions and the *minmod* limiter in supersonic regions (see [111], and references therein). The very diffusive minmod limiter is defined as

$$\phi(a,b) = \mathrm{minmod}(a,b) = \frac{1}{2}\left(\mathrm{sign}(a) + \mathrm{sign}(b)\right)\min(|a|,|b|) \; . \tag{2.40}$$

It compares the magnitude of the upwind slope with that of the downwind slope and picks the one that is smaller in magnitude, or, in the case of a local extremum where the two slopes have different signs, returns 0. The Van Leer limiter is defined by

$$\phi(a,b) = \frac{1}{2}\left(\mathrm{sign}(a) + \mathrm{sign}(b)\right)\frac{2ab}{a+b} \; . \tag{2.41}$$

It provides considerably sharper resolution of discontinuities while still preserving the TVD property.

For the time integration of eq. 2.27, a two-step predictor-corrector method [189] is applied. As predictor, half a time step with the first order fluxes (see eq. 2.29) is computed. We regard the freezing speed in the predictor step as a parameter varying between $d = 0$ and $d = \max\left(d_i, d_{i+1}\right)$ to regulate the numerical dissipation. Note that in all the core-collapse simulations I performed, the choice was $d = 0$. Hence we vary the predictor between a first-order scheme and a second-order centred difference scheme depending on the application. In the corrector step we then use the calculated values from the predictor step $\boldsymbol{u}^{n'}$ to compute the second order TVD fluxes (see eq. 2.35):

$$\boldsymbol{u}_{i}^{n+1} = \boldsymbol{u}_{i}^{n} - \frac{\Delta t}{\Delta x}\left(\boldsymbol{F}_{i'}^{n'} - \boldsymbol{F}_{i'-1}^{n'}\right) . \tag{2.42}$$

Hence a second order update in time and space of the fluid variables is obtained. For more technical details and derivations, I refer to [111, 112], with references therein.

Advection of the magnetic field: The $B_x^{yz}\left(\Delta t\right)$ update

In this subsection, I will quickly outline the procedure of updating the magnetic field in x-direction $B_x^{yz}\left(\Delta t\right)$. The operators for the update in the other spacial directions follow the same strategy.

During the $B_x^{yz}(\Delta t)$ update, the quantities other than the magnetic field are held constant. Thus, the update is governed by the induction equation [105]

$$\frac{\partial \boldsymbol{b}}{\partial t} - \nabla \times (\boldsymbol{v} \times \boldsymbol{b}) = 0 \ . \tag{2.43}$$

The main numerical difficulty here is to fulfill and maintain the physical constraint $\nabla \boldsymbol{b} = 0$ within machine precision. Ordinary discretization of eq. 2.43 can only guarantee that the divergence of the magnetic field is of the order of the truncation error [189]. Thus, at flow discontinuities, the discrete divergence may become large, leading to errors which may accumulate during the simulation. The problem with this fact is that a non-vanishing divergence of the magnetic field can produce an 'unphysical' acceleration of the magnetized fluid parallel to the field lines [110]. There are several clever algorithms which circumvent this particular problem by construction, as summarized in [239] and references therein.

`FISH` employs one particular method, the so-called *constrained transport* of Evans & Hawley [69], to guarantee the divergence-preserving time evolution of the magnetic field. The basic trick of this scheme is that it maintains the initial value $\nabla \boldsymbol{b} = 0$ by construction during every instant of the simulation. The starting point of the constrained transport is to write the induction equation in integral form. Integrating eq. 2.43, for example, over the surface $S_{i',j,k}$ of cell $V_{i,j,k}$ and using Stoke's theorem yields

$$\frac{\partial}{\partial t}\left(b_x\right)_{i',j,k} = \int_{\partial S_{i',j,k}} \boldsymbol{v} \times \boldsymbol{b} \cdot d\boldsymbol{x} \ , \tag{2.44}$$

where $\partial S_{i',j,k}$ denotes the contour of $S_{i',j,k}$, i. e. the edges of the cell-face at i'. The cell face-averaged magnetic field components at time t are given by

$$\left(b_x\right)_{i',j,k} = \frac{1}{S_{i',j,k}} \int_{S_{i',j,k}} b_x\left(\boldsymbol{x}, t\right) dydz \ , \tag{2.45}$$

where $S_{i',j,k} = \Delta y \Delta z$ denotes the cell face of cell $V_{i,j,k}$ located at $x_{i'}$ and spanned by the zone increments Δy and Δz. $\left(b_y\right)^n_{i,j',k}$ and $\left(b_z\right)^n_{i,j,k'}$ are defined analogously. The integral form then naturally suggests one to choose the normal projections of the magnetic field at faces of the cell $V_{i,j,k}$ and the normal projections of the electric field $\boldsymbol{E} = \boldsymbol{v} \times \boldsymbol{b}$ at the cell edges as primary variables. This positioning leads directly to the jump conditions of electric and magnetic fields [105] and therefore mimics Maxwell's equations at the discrete level (see fig. 2.1). The actual update of the magnetic field in `FISH` is split into two advection steps and one constraint step [185]. In x-direction, this means that the y and z components of the magnetic field need to be updated as

$$\begin{aligned}
\frac{\partial}{\partial t}\left(b_y\right)_{i,j',k} &= -\frac{1}{\Delta x}\left[\left(v_x b_y\right)_{i',j',k} - \left(v_x b_y\right)_{i'-1,j',k}\right] \\
\frac{\partial}{\partial t}\left(b_z\right)_{i,j,k'} &= +\frac{1}{\Delta x}\left[\left(v_x b_z\right)_{i',j,k'} - \left(v_x b_z\right)_{i'-1,j,k'}\right] \ ,
\end{aligned} \tag{2.46}$$

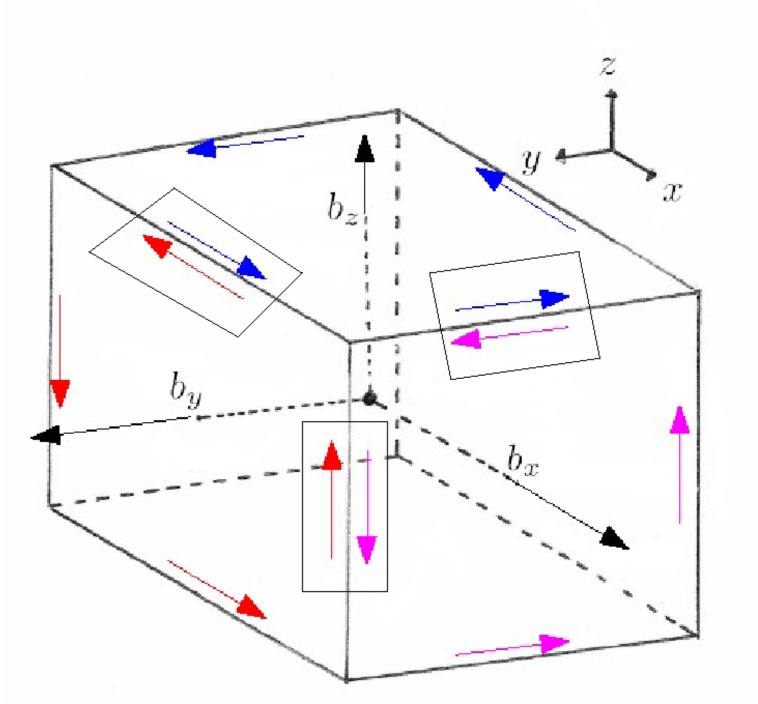

Figure 2.1: Schematic view of a 3D computational cell. The magnetic fields are placed on cell faces. The physical constraint $\nabla \boldsymbol{b} = 0$ can also be expressed by $\sum_{faces} \Phi_S = 0$, where Φ_S is the magnetic flux through a cell face. This formulation is equivalent to the fact that each electromotoric force $\boldsymbol{E}$ appears twice, but with opposite sign, as shown by the arrows inside the black squares. Hence, they cancel out by construction, guaranteeing a divergence-preserving time evolution of the magnetic field. The figure is courtesy of R. Käppeli.

and the x component of the magnetic field has to be updated as

$$\begin{aligned} \frac{\partial}{\partial t} (b_x)_{i',j,k} = &+ \frac{1}{\Delta y} \left[(v_x b_y)_{i',j',k} - (v_x b_y)_{i',j'-1,k} \right] \\ &- \frac{1}{\Delta z} \left[(v_x b_z)_{i',j,k'} - (v_x b_z)_{i',j,k'-1} \right] . \end{aligned} \tag{2.47}$$

The fluxes in eq. 2.46 need to be upwinded for stability, since they represent the two advection modes [111]. To maintain $\nabla \cdot \boldsymbol{b} = 0$ within machine precision, the same fluxes used to update b_y and b_z in eq. 2.46 need to be used in eq. 2.47 for the b_x update. To update $(b_y)_{i,j',k}$, the following steps are taken: The velocity v_x needs to be interpolated to the same location as $(b_y)_{i,j',k}$, i. e. to the cell face $S_{i,j',k}$. In `FISH`, a stable manner of doing so is averaging in x-direction [111]

$$(v_x)_{i,j',k} = \frac{1}{4} \left[(v_x)_{i+1,j',k} + 2\,(v_x)_{i,j',k} + (v_x)_{i-1,j',k} \right] \tag{2.48}$$

A first-order accurate upwinded flux is given by

$$(v_x b_y)_{i',j',k} = \begin{cases} (v_x b_y)_{i,j',k} & , \quad (v_x)_{i',j',k} > 0 \\ \\ (v_x b_y)_{i+1,j',k} & , \quad (v_x)_{i',j',k} \leq 0 \end{cases} \tag{2.49}$$

where the velocity average is

$$(v_x)_{i',j',k} = \frac{1}{2}\left[(v_x)_{i,j',k} + (v_x)_{i+1,j',k}\right] . \tag{2.50}$$

Note that again second order accuracy in space and time is achieved in the same fashion as for the fluid updates: a first-order predictor combined with a second order corrector with a piece-wise linear TVD approximation to the fluxes. For further details about implementation of the magnetic field evolution, I refer to Käppeli et al. [111], sec. 2.4, and [185].

Incorporation of gravity: The G_x operator

In this subsection, I will sketch how the integration of the gravity source term (see eq. 2.13) of the MHD equations (eqs. 2.7 and 2.11) is performed in `FISH` (see eq. 2.24). Again, I will outline the update in x-direction. The other dimensions are treated in similar manner.

In our operator-split framework, the gravity update is merged with the hydrodynamical update as $L_x = G_x\left(\frac{\Delta t}{2}\right) L_x^{HD} G_x\left(\frac{\Delta t}{2}\right)$, where $G_x\left(\frac{\Delta t}{2}\right)$ denotes the gravity update for half a time step, taken before and after the hydrodynamical update in the corresponding dimension [111]. As a reminder:

$$G_x(\Delta t): \quad \frac{\mathrm{d}\boldsymbol{u}}{\mathrm{d}t} = \boldsymbol{S}_x \tag{2.51}$$

$$L_x^{HD}: \quad \frac{\partial \boldsymbol{u}}{\partial t} + \frac{\partial \boldsymbol{F}}{\partial x} = 0 \, , \tag{2.52}$$

where

$$\boldsymbol{S_x} = \begin{bmatrix} 0 \\ -\rho \partial\Phi/\partial_x \\ 0 \\ 0 \\ -\rho v_x \partial\Phi/\partial_x \end{bmatrix} . \tag{2.53}$$

Note that, in principle, one could avoid source terms by adding gravity to the total energy $E = \rho e + \frac{\rho}{2}v^2 + \Phi$. However, this is usually not done in core-collapse simulations because of the overwhelming dominance of the gravitational energy over the sum of the other energies contained in the simulated system, and the finite precision of computers.

In the simulations I carried out, the differential equation 2.51 was discretized and integrated via a first order explicit scheme:

$$\boldsymbol{u_i^{n+1}} = \boldsymbol{u_i^n} + \Delta t \boldsymbol{S}_i^n \, . \tag{2.54}$$

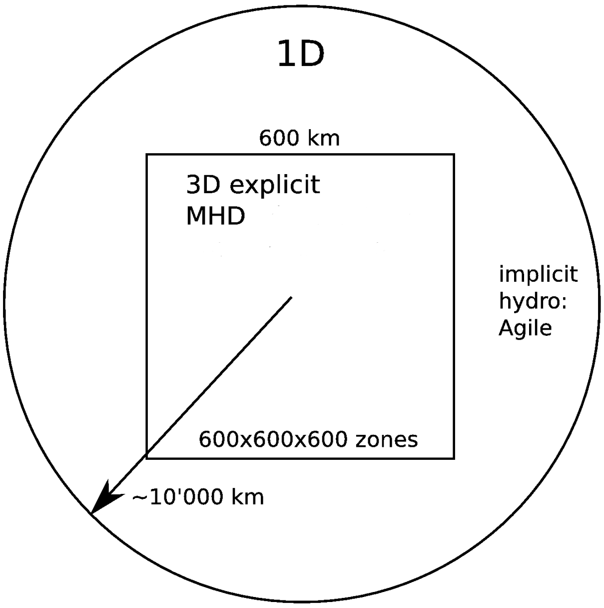

Figure 2.2: Schematic description of the code set-up: the 3D computational domain is embedded in a larger spherically symmetric domain. Figure adopted from M. Liebendörfer.

Meanwhile, centred differences for the gravitational potential are used:

$$\left(\frac{\partial \Phi}{\partial x}\right)_i^n = \frac{\Phi_{i+1}^n - \Phi_{i-1}^n}{2\Delta x} \,. \tag{2.55}$$

I point out that the operator G_x only updates the fluid momentum and the total energy while keeping the density fixed. The total energy is computed by summing up internal, magnetic and kinetic energy and given as input to the L_x^{HD} operator. Therefore, the total energy change due to the source term is implied from the updated momentum field. Note also that there are more sophisticated higher-order methods to incorporate gravity in `FISH`. These are outlined in [111, 193].

2.2.1 Code set-up and performance

In the simulations I carried out (see chap. 3 and 4), the 3D computational domain consists of a central cube of either 600^3 or 1000^3 cells, treated in equidistant Cartesian coordinates with a grid spacing of 1km or 0.6km, respectively. It is, as explained in [206] and shown in fig. 2.2, embedded in a larger spherically symmetric computational domain that is treated by the time-implicit hydrodynamics code 'Agile' [135].

A computational problem of the size $\mathcal{O}(10^9)$ grid points and another $\mathcal{O}(10)$ variables per grid point can nowadays not be handled by the resources of a single computer/CPU and thus needs to be parallelized. In a more casual formulation, one would say that *to pull a bigger wagon, it is easier to add more oxen than to grow a gigantic ox* [249].

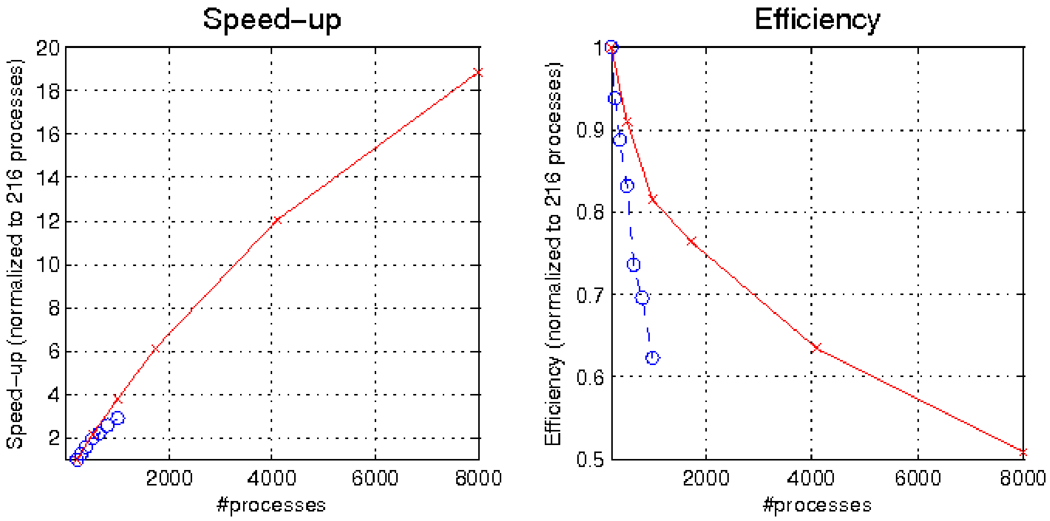

Figure 2.3: The figure shows 'strong scaling' of `FISH`. The test was performed on the ROSA system (Cray XT-5, nodes with 2 quad-core AMD Opteron 2.4 GHz Shanghai processors, SeaStar 2.2 communications processor with 2 GBytes/s of injection bandwidth per node) at the Swiss National Supercomputer Center (CSCS), and consisted of 50 time steps at the onset of the collapse. The problem size was kept constant at 600^3 cells. The speedup, normalized to 216 processes, is shown on the left hand side. The efficiency is displayed on the right hand side. The dashed lines with data points taken at the circles refer to a parallelization that uses only MPI. The solid lines with data points taken at the crosses refer to a hybrid parallelization with MPI between nodes and Open MP within nodes.

Hence, the 3D computational domain is split into several smaller sub-problems by a so-called 'cubic domain decomposition' [190]. `FISH` then solves the decomposed problem by means of a hybrid parallelization scheme, i.e. with MPI (distributed memory parallelization; see [249]) between nodes and Open MP (shared memory parallelization; see [25]) within nodes. With this setup, the code scales nicely to at least 8000 parallel processes, as displayed in fig 2.3. Note that as the number of processors is increased, the ratio of buffer zones to volume zones increases as well. In this case it is the evaluation of the physics equations on the buffer zones that limits the efficiency. However, fig. 2.3 also shows that `FISH` scales very nicely to of $\mathcal{O}(10000)$ processors in the hybrid MPI/Open MP. This scaling can be achieved because the parallelization with Open MP does not increase the number of buffer zones.

For further information about details on the parallelization, I refer the reader to [111], sec. 3.

2.2.2 Treatment of gravity

This subsection is devoted to methods for numerically solving the elliptic, linear and non-homogeneous second-order Poisson Equation (see eq. 2.6) with Dirichlet boundary conditions in one, two and three dimensions [190].

Solving the Poisson equation efficiently within a 3D MHD code carries severe difficulties. The hyperbolic MHD part of the code is, as pointed out previously, solved locally for a bunch of fluid zones with a minimum of communication between the computational nodes when exchanging the data contained in the buffer zones, because the propagation of physical information is limited by the fastest speed in the system (see eq. 2.26). The Poisson equation on the other hand is acausal, i.e. not restricted by any signal speed. Thus, whenever one tries to integrate eq. 2.6, the information of the density distribution of the entire computational domain must be accessible at once, which consequently involves data exchange via 'expensive' collective MPI routines [249]. For a problem size of $\mathcal{O}(10^9)$ computational zones, attempts to solve the Poisson equation thus must avoid massive data transfer as 'well' as possible in order to prevent the simulation from getting inefficient due to huge amounts of idle time.

Below, I will outline several ways how the Poisson equation for gravity can be solved reasonably efficiently in a 3D MHD core-collapse simulation. Note that these methods – like the neutrino transport approximations (see sec. 2.4) – are aimed at capturing only the dominant physical features and are not meant as final answers to the problem.

Gravity in (1D) spherical coordinates and general relativistic corrections

In most of the simulations I carried out, namely the ones published in [206,207,209], gravity was treated in spherical symmetry.

As a first approximation, this is reasonably good for non- and slowly rotating stars, as long as they do not undergo strong deformation by centrifugal forces [228].

The corresponding, spherically symmetric Poisson equation in principle yields

$$\frac{1}{r^2}\frac{\partial}{\partial r}\left(r^2\frac{\partial\Phi}{\partial r}\right) = 4\pi G\rho(r) \; , \tag{2.56}$$

which is integrable within a negligible amount of CPU time (< 1%) compared to the overall time consumption of a purely hydrodynamical simulation. However, as pointed out in sec. 1.8, the pure Newtonian approach to gravity is too simplistic, as it underestimates the net gravitational potential (see fig. 2.4) compared to the GR case, leading to physically 'wrong' infall velocities, neutrino luminosities, too 'flat' derivatives of the gravitational potential and so forth (see [38, 138]).

Therefore, it is important to include an appropriate approximation to radial general relativistic effects in our Newtonian MHD codes `FISH` and `ELEPHANT`. We meet this requirement by implementing the gravitational potential via a spherically symmetric mass integration that includes general relativistic corrections [147]. In this approach, the Newtonian gravitational potential Φ is replaced by an effective potential Φ_{eff}

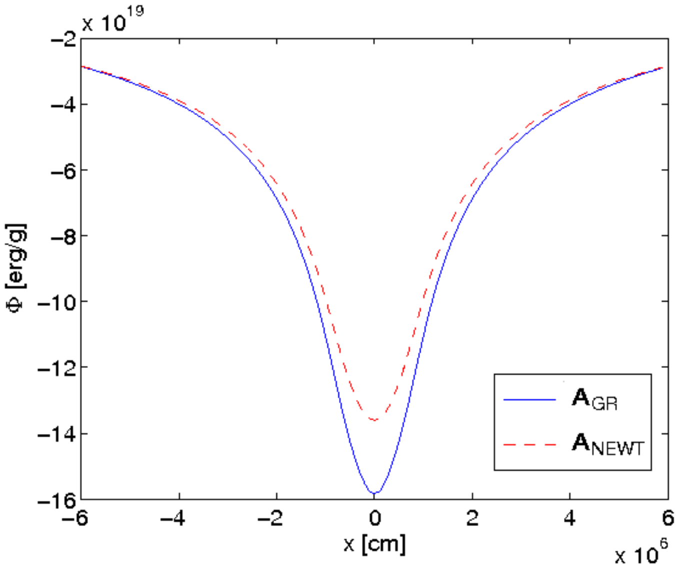

Figure 2.4: Comparison of the gravitational potential of the rotating models A$_{GR}$ (detailed initial conditions described in sec. 3.5, where the model is denoted as A) and A$_{NEWT}$ in the $y = z = 0$ plane, 64 ms after bounce. Model A$_{GR}$ was carried out applying the GR corrected potential of Marek et al. [147], while A$_{NEWT}$ was computed in pure Newtonian gravity.

('case A' potential; see [147]),

$$\Phi_{eff}(r) = \int_r^\infty \frac{dr'}{r'^2}\left[\frac{m_{eff}}{4\pi} + r'^3 \cdot (p + p_\nu)\right] \cdot \frac{1}{\Gamma^2}\left(\frac{\rho + e + p}{\rho}\right) \ , \tag{2.57}$$

with p being the gas pressure, p_ν the neutrino pressure and e the internal energy density. The effective mass is given by

$$m_{eff}(r) = 4\pi \int_0^r dr' r'^2 \left(\rho + e + E\right) \ , \tag{2.58}$$

where E is the neutrino energy density. The metric function Γ is given by

$$\Gamma = \sqrt{1 + v_r^2 - \frac{2m_{eff}}{r}} \ . \tag{2.59}$$

where v_r is the radial fluid velocity. Note that [162] also proposed an effective relativistic gravitational potential for rapidly rotating configurations. However, since it would have added another degree of freedom to my model parameters, I did not consider it in my PhD studies.

Note that in order to calculate the effective relativistic potential for multi-dimensional flows it is sensible to substitute the 'spherical contribution' $\overline{\Phi}(r)$ to the multi-dimensional Newtonian gravitational potential with the GR corrected potential $\overline{\Phi}_{eff}$. In the case of 3D Cartesian coordinates x, y, z for example, this results in

$$\Phi_{eff}(x, y, z) = \Phi(x, y, z) - \overline{\Phi}(r) + \overline{\Phi}_{eff}(r) \ . \tag{2.60}$$

Here, $\overline{\Phi}_{eff}$ is calculated according eq. 2.57. However, the hydrodynamic quantities ρ, e, p, v_r and the neutrino quantities E, p_ν must be replaced by their corresponding angular averaged values. Moreover, note that v_r in eqs. 2.58 and 2.59 in the multi-D case refers to the radial component of the velocity, only.

Gravity in (2D) axisymmetry and cylinder coordinates

Massive stars which rotate at the onset of core collapse undergo a considerable spin-up due to angular momentum conservation during the infall phase [119]. During this process, the initial rotation rate easily grows by a factor of order $\mathcal{O}(10^3)$ [62]. The configuration of the gravitational potential therefore is more naturally described by a two-dimensional axisymmetric approach compared to a spherical one [228].
The Poisson equation for the gravitational potential $\Phi(r, z)$ in (axisymmetric) cylindrical coordinates reads [105]

$$\frac{1}{r}\frac{\partial}{\partial r}\left(r\frac{\partial \Phi}{\partial r}\right) + \frac{\partial^2 \Phi}{\partial z^2} = 4\pi G\rho(r, z) \ . \tag{2.61}$$

The second-order $\mathcal{O}(h_r^2 + h_z^2)$ finite differencing analog of eq. 2.61 yields [27]:

$$\begin{aligned} \Phi_{k,j+1}\left[1 + \frac{1}{2(j-1)}\right] - 2\Phi_{k,j}\left[1 + \frac{h_r^2}{h_z^2}\right] + \Phi_{k,j-1}\left[1 - \frac{1}{2(j-1)}\right] \\ + \Phi_{k+1,j}\left[\frac{h_r^2}{h_z^2}\right] + \Phi_{k-1,j}\left[\frac{h_r^2}{h_z^2}\right] = 4\pi G\rho_{k,j}h_r^2 \ , \end{aligned} \tag{2.62}$$

where h_r and h_z is the grid spacing along the corresponding coordinate axis (see fig. 2.5). For the purpose of 3D MHD core-collapse simulations, a data set where the density distribution is averaged over cylinders rotating about the $z-$axis is constructed on the fly at every time step of the simulation (the interpolation routine to jump back and forth between the 2D and 3D grid was kindly provided by R. Käppeli). Note that in production mode, the cylindrical grid usually consists of 300 data points in r-direction and 600 in z-direction. The grid resolution was chosen to be $h_r = h_z = 1$ km. Moreover, I impose Dirichlet boundary conditions [190],

$$\Phi = g \text{ on } \partial\Omega \ . \tag{2.63}$$

Assuming $r \in [0, R_{max}]$ and $z \in [z_{min}, z_{max}]$, the outer three of the four the boundary section of our axisymmetric problem at $\Phi(r, z_{min})$, $\Phi(r, z_{max})$, and $\Phi(R_{max}, z)$ are prescribed by $\Phi(r')$, where $\Phi(r')$ is the spherically symmetric solution of the Poisson equation at the particular adjacent spherical radius r'. At $\Phi\left(0, z\right)$, a difficulty occurs since one has to circumvent a singularity at $r = 0$ (see eq. 2.61). This is done by choosing the grid cell-centered, i. e. r never becomes zero. The remaining boundary condition is fixed with *mirror* boundary conditions [105], $\Phi\left(r_{j=1/2}, z\right) = \Phi\left(r_{j=-1/2}, z\right)$. Technically, this is achieved by copying $\Phi\left(r_{j=1/2}, z\right)$ over the value of $\Phi\left(r_{j=-1/2}, z\right)$ after each iteration within the Poisson solver (the module which handles these boundary conditions was kindly provided by R. Käppeli).

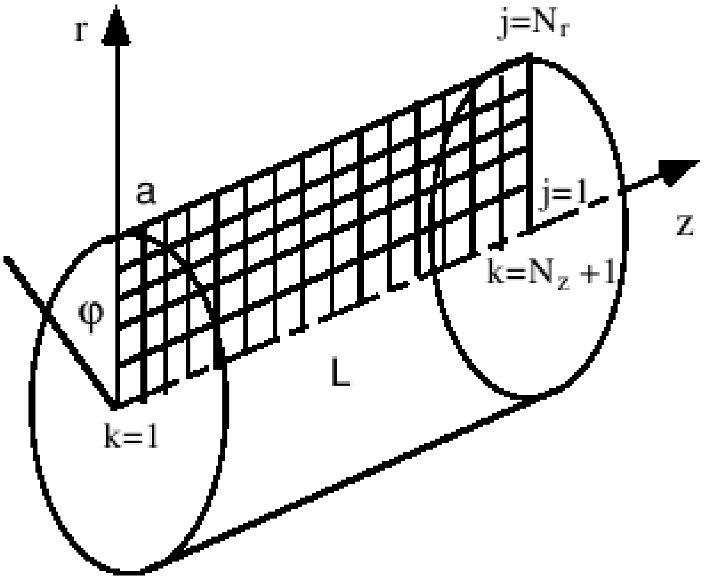

Figure 2.5: Discretization of the Poisson equation in cylindrical coordinates. Axisymmetry is assumed. Figure taken from [27].

A problem size of 300×600 points (instead of 600^3 for the entire, unreduced problem) brings the major advantage that it can easily be solved on one single compute node locally due to relatively low memory requirements. Any algorithm to solve the Poisson problem thus will not require multiple calls to collective MPI 'send' and receive' routines [249], but only one before and one after the actual solution of eq. 2.62. Reasonable speed-up of a factor of ∼8-10 (see tab. 2.2) can then be gained by parallelizing it locally via Open MP [25], since the architecture of modern high-performance cluster such as the CRAY-XT5 at CSCS, Manno, Switzerland incorporates 12 or more CPU cores per node (status: spring 2010).

The discretized version of the Poisson equation (eq. 2.62) obviously leads to a system of linear equations [189,18]. The main difficulty in solving linear problems arises from the large size of the algebraic system. Even though the matrix is sparse, the nonzero elements are usually not confined to positions next to the diagonal (see fig. 2.7). Hence, it is not easy to use the sparseness of the matrix to improve the efficiency of the direct methods for solving a system of linear equations. The most popular way of solving such systems efficiently are so-called iterative methods like the 'multigrid', or the 'successive over-relaxation' (SOR) algorithm [189, 18]. Such iterative solvers start with an initial guess for the solution $\vec{x}$ and compute the residuals $\vec{r} = A\vec{x} - \vec{b}$. Changes are then made in the solution via a certain prescription in order to reduce some component of the residual to zero. This process is repeated until all residuals have been reduced to an acceptable level. If the initial guess is 'good', i.e. close to the solution, these methods converge quickly. Moreover, such solvers bear the following advantages over the direct methods: a) The iterative methods require little

memory compared to direct methods, which need to store a significant fraction of the matrix elements in the computer memory. b) The methods are relatively easy to implement, as the main iteration loop usually contains only few lines of code.
For our axisymmetric target application (eq. 2.62), I have chosen to implement the SOR algorithm [189, 18] over a direct matrix solver or the multigrid method for the following reasons: i) A sparse matrix solver is hardly applicable together with the imposed mirror boundary conditions; therefore, I have to choose some sort of iterative solver. ii) The applicability of the SOR is more flexible than a standard multigrid iterative method. The latter solver usually requires $2^n + 1$ grid points in each spatial direction in order to be able to perform its coarsening and prolongation operations [189]. If the finite-difference grid is not square, but has different size sides (i.e. 600×300), interpolation to fill up the missing points becomes necessary. Thus, although the multigrid method in principle provides better scaling behaviour with number of stencils compared to the SOR [189, 18] the interpolation process in practice slows the multigrid down, making the running times presumably comparable. Note, however, that a test of this handwaving statement remains to be carried out.

I now specify the basic idea of SOR [189]. Suppose we wish to solve the elliptic equation

$$\mathcal{L}u = \rho \ , \tag{2.64}$$

where $\mathcal{L}$ represents some elliptic operator such as the *Laplacian*, and ρ is the source term. Now, the trick of an iterative method is to rewrite eq. 2.64 as a diffusion equation,

$$\frac{\partial u}{\partial t} = \mathcal{L}u - \rho \ . \tag{2.65}$$

An initial distribution u relaxes to an equilibrium solution as $t \to \infty$. This equilibrium has all time derivatives vanishing. Therefore it is the solution of the original elliptic problem. If I rewrite eq. 2.65 in finite differences, the algorithm to update $u_{j,l}^{n+1}$ reads [189]

$$u_{j,l}^{n+1} = u_{j,l}^{n} + \Delta t \left(\mathcal{L}_{FD} u^n - \rho^n \ \right) \ . \tag{2.66}$$

This procedure, the building block of any relaxation method, is then iterated until convergence, i.e. the equilibrium solution is reached.
Let us now turn our attention on a general, second-order elliptic equation in 2D, finite differenced as for our Poisson equation 2.62. It can generally be expressed by [189, 18]

$$a_{j,l}u_{j+1,l} + b_{j,l}u_{j-1,l} + c_{j,l}u_{j,l+1} + d_{j,l}u_{j,l-1} + e_{j,l}u_{j,l} = f_{j,l} \ . \tag{2.67}$$

For our target application (see eq. 2.62), we had for example $a = b = \left[\frac{h_r^2}{h_z^2}\right]$, $c = \left[1 + \frac{1}{2(j-1)}\right]$, $d = \left[1 - \frac{1}{2(j-1)}\right]$, $e = 2\left[1 + \frac{h_r^2}{h_z^2}\right]$, and the quantity $f = 4\pi G\rho(r,z)$ is proportional to the source term.

The iterative procedure of the SOR to solve for a certain $u_{j,l}^{new}$ is, in analogy to eq. 2.66, defined by the following steps: First, we solve eq. 2.67 for $u_{j,l}$:

$$u_{j,l}^{\star} = \frac{1}{e_{j,l}} \left(f_{jl} - a_{j,l} u_{j+1,l} - b_{j,l} u_{j-1,l} - c_{j,l} u_{j,l+1} - d_{j,l} u_{j,l-1} \right) . \tag{2.68}$$

Then the updated $u_{j,l}^{new}$ is a weighted average

$$u_{j,l}^{new} = \omega u_{j,l}^{\star} + (1-\omega)\, u_{j,l}^{old} . \tag{2.69}$$

This second step makes an *overcorrection* to the values of $u_{j,l}^{new}$, anticipating future corrections with the *overrelaxation parameter* ω [189, 18].
Numerically, we compute $u_{j,l}^{new}$ as follows: The residual at any stage is

$$\xi_{j,l} = a_{j,l} u_{j+1,l} + b_{j,l} u_{j-1,l} + c_{j,l} u_{j,l+1} + d_{j,l} u_{j,l-1} + e_{j,l} u_{j,l} - f_{j,l} , \tag{2.70}$$

and the SOR algorithm (eq. 2.69) is

$$u_{j,l}^{new} = u_{j,l}^{old} - \omega \frac{\xi_{j,l}}{e_{j,l}} , \tag{2.71}$$

where the residual vector $\xi_{j,l}$ can be used for terminating the iteration.
Note the following points [18, 189]: i) If $\omega = 1$, the SOR translates into the Gauss-Seidel method. ii) The SOR method is convergent only for $0 < \omega < 2$. If $0 < \omega < 1$, we speak of *underrelaxation*. Under certain mathematical restrictions, generally satisfied by matrices arising from finite differencing, only $1 < \omega < 2$ can give faster convergence than the Gauss-Seidel iteration. iii) There are several ways of choosing ω 'optimally': either empirically or by automated schemes [189]. In my numerical tests, I found fastest convergence by fixing it manually to $\omega = 1.7$.

I tested the SOR solver with a broad range of analytical problems and boundary conditions in order to measure its capabilities. One exemplary analytical test which I performed is the following:

$$\Delta\Phi(x,y) = x^2 + y^2 . \tag{2.72}$$

In the interval $x, y \in [0,1]$, mapped onto 100^2 grid points, I imposed as boundary conditions:

$$\Phi(x,0) = 0 \tag{2.73}$$

$$\Phi(x,1) = \frac{1}{2}x^2 \tag{2.74}$$

$$\Phi(0,y) = \sin(\pi y) \tag{2.75}$$

$$\Phi(1,y) = \exp(\pi x)\sin(\pi y) + \frac{1}{2}y^2 \tag{2.76}$$

The analytical solution of this problem is

$$\Phi(x,y) = \exp(\pi x)\sin(\pi y) + \frac{1}{2}(xy)^2 . \tag{2.77}$$

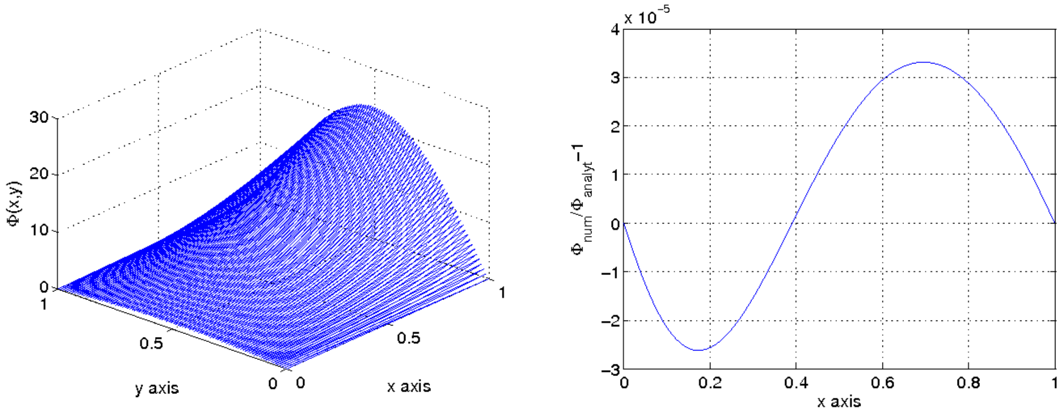

Figure 2.6: **Left panel:** Numerical solution eq. 2.72. **Right panel:** Relative error $\Phi_{num}(x, 0.5)/\Phi_{analyt}(x, 0.5) - 1$ along the x-axis.

The result of this test is shown in fig. 2.6. Note that in this computation I have chosen the residual to be $< 10^{-6}$ as abord criterion for the SOR iteration.
In the production mode of purely hydrodynamical simulations of size of 600^3 zones, $\sim 5\%$ of the overall CPU time is spent on the axisymmetric SOR solver (see sec. 4.2).

Gravity in 3D: sparse matrix solver

It is almost certain that core-collapse dynamics relies on features which are genuine 3D, as I outlined in sec. 1.2. Hence, in order to be consistent, gravity should be treated in a non-restrictive way, i.e. in 3D. This must, for the same reasons as stated in the previous subsection, be done in an efficient way.
In order to meet this requirement, I plan to solve the 3D Poisson equation only for the innermost $\sim 100^3$ to 120^3 zones in dynamical simulations. From the phyiscal point of view, this approach is reasonable, as more than $\gtrsim 99\%$ of the mass treated in such computations are contained in this central volume, thus making the dominant contribution to gravity. Moreover, in this way I can solve the 3D Poisson problem on one single node and therefore suppress again several time-consuming calls to collective MPI routines [249].

In 3D Cartesian coordinates, the Poisson equation for the gravitational potential reads

$$\Delta\Phi(x, y, z) = \left(\frac{\partial^2}{\partial x^2} + \frac{\partial^2}{\partial y^2} + \frac{\partial^2}{\partial z^2}\right)\Phi = 4\pi G\rho(x, y, z) \ . \tag{2.78}$$

The discretized version of eq. 2.78 (assuming a uniform spatial discretization) on an $m \times n \times k$ grid yields the following formula:

$$\begin{aligned}\Phi_{i-1,j,k} + \Phi_{i,j-1,k} + \Phi_{i,j,k-1} - 6\Phi_{i,j,k} + \\ \Phi_{i+1,j,k} + \Phi_{i,j+1,k} + \Phi_{i,j,k+1} = 4\pi G h^2 \rho(x, y, z) \ ,\end{aligned} \tag{2.79}$$

where h is the grid spacing. Equation 2.79 can be casted into a matrix notation, representing an $mnk \times mnk$ linear system of the general form

$$A\vec{\Phi} = \vec{\rho}\,. \tag{2.80}$$

For a 3 × 3 × 3 (m = 3, n = 3, k=3) grid with all the boundary nodes fixed (set to be zero), the matrix A of the system would look as displayed in fig. 2.7. In our notation, the entries of the vectors $\vec{\Phi}$ and $\vec{\rho}$ are defined as follows:

$$\vec{\Phi} = \begin{pmatrix} \Phi_{111} \\ . \\ . \\ . \\ \Phi_{11k} \\ \Phi_{121} \\ . \\ . \\ . \\ \Phi_{1nk} \\ \Phi_{211} \\ . \\ . \\ . \\ \Phi_{mnk} \end{pmatrix} \quad ; \qquad \vec{\rho} = 4\pi G h^2 \begin{pmatrix} \rho_{111} \\ . \\ . \\ . \\ \rho_{11k} \\ \rho_{121} \\ . \\ . \\ . \\ \rho_{1nk} \\ \rho_{211} \\ . \\ . \\ . \\ \rho_{mnk} \end{pmatrix} \quad , \tag{2.81}$$

where $\rho_{i,j,k}$ is the original density field. In the framework of the linear system (eq. 2.80), Dirichlet boundary conditions can easily be included by shifting them to the vector $\vec{\rho}$ via subtraction. In order to clarify the procedure, I give an example in 1D (cf. eq. 2.79). Let us assume a discrete Poisson equation in 1D Cartesian coordinates, having m stencils (i $\in [1, m]$), and boundary values at $i = 0$ and $i = m + 1$. At $i = 1$, the Poisson equation then reads.

$$\Phi_0 - 2\Phi_1 + \Phi_2 = 4\pi G h^2 \rho_1 \tag{2.82}$$

The lower boundary condition Φ_0 is now shifted to the other side of the equation:

$$-\,2\Phi_1 + \Phi_2 = 4\pi G h^2 \rho_1 - \Phi_0\;. \tag{2.83}$$

The upper boundary at $i = m$ is treated in analogy:

$$\Phi_{m-1} - 2\Phi_m = 4\pi G h^2 \rho_m - \Phi_{m+1}\;. \tag{2.84}$$

Subsequently, the same recipe is followed in 3D whenever one of the three running indices i, j, k reaches its minimum or maximum value.

The sparse matrix A (see fig. 2.7) can be solved via direct matrix inversion by means of a 'sparse matrix solver' (see, e.g., [18]). However, the main difficulty in solving linear problems arises because of the large size of the algebraic system. Even though the matrix is sparse, as already stated above, the nonzero elements are usually not

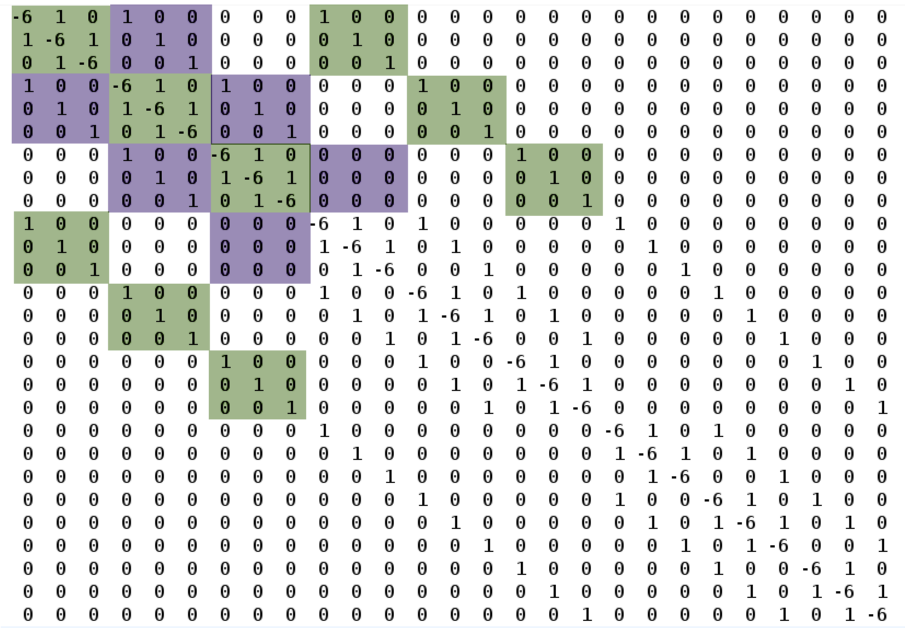

$$
\begin{array}{ccccccccccccccccccccccccccc}
-6&1&0&1&0&0&0&0&0&1&0&0&0&0&0&0&0&0&0&0&0&0&0&0&0&0&0\\
1&-6&1&0&1&0&0&0&0&0&1&0&0&0&0&0&0&0&0&0&0&0&0&0&0&0&0\\
0&1&-6&0&0&1&0&0&0&0&0&1&0&0&0&0&0&0&0&0&0&0&0&0&0&0&0\\
1&0&0&-6&1&0&1&0&0&0&0&0&1&0&0&0&0&0&0&0&0&0&0&0&0&0&0\\
0&1&0&1&-6&1&0&1&0&0&0&0&0&1&0&0&0&0&0&0&0&0&0&0&0&0&0\\
0&0&1&0&1&-6&0&0&1&0&0&0&0&0&1&0&0&0&0&0&0&0&0&0&0&0&0\\
0&0&0&1&0&0&-6&1&0&0&0&0&0&0&0&1&0&0&0&0&0&0&0&0&0&0&0\\
0&0&0&0&1&0&1&-6&1&0&0&0&0&0&0&0&1&0&0&0&0&0&0&0&0&0&0\\
0&0&0&0&0&1&0&1&-6&0&0&0&0&0&0&0&0&1&0&0&0&0&0&0&0&0&0\\
1&0&0&0&0&0&0&0&0&-6&1&0&1&0&0&0&0&0&1&0&0&0&0&0&0&0&0\\
0&1&0&0&0&0&0&0&0&1&-6&1&0&1&0&0&0&0&0&1&0&0&0&0&0&0&0\\
0&0&1&0&0&0&0&0&0&0&1&-6&0&0&1&0&0&0&0&0&1&0&0&0&0&0&0\\
0&0&0&1&0&0&0&0&0&1&0&0&-6&1&0&1&0&0&0&0&0&1&0&0&0&0&0\\
0&0&0&0&1&0&0&0&0&0&1&0&1&-6&1&0&1&0&0&0&0&0&1&0&0&0&0\\
0&0&0&0&0&1&0&0&0&0&0&1&0&1&-6&0&0&1&0&0&0&0&0&1&0&0&0\\
0&0&0&0&0&0&1&0&0&0&0&0&1&0&0&-6&1&0&0&0&0&0&0&0&1&0&0\\
0&0&0&0&0&0&0&1&0&0&0&0&0&1&0&1&-6&1&0&0&0&0&0&0&0&1&0\\
0&0&0&0&0&0&0&0&1&0&0&0&0&0&1&0&1&-6&0&0&0&0&0&0&0&0&1\\
0&0&0&0&0&0&0&0&0&1&0&0&0&0&0&0&0&0&-6&1&0&1&0&0&0&0&0\\
0&0&0&0&0&0&0&0&0&0&1&0&0&0&0&0&0&0&1&-6&1&0&1&0&0&0&0\\
0&0&0&0&0&0&0&0&0&0&0&1&0&0&0&0&0&0&0&1&-6&0&0&1&0&0&0\\
0&0&0&0&0&0&0&0&0&0&0&0&1&0&0&0&0&0&1&0&0&-6&1&0&1&0&0\\
0&0&0&0&0&0&0&0&0&0&0&0&0&1&0&0&0&0&0&1&0&1&-6&1&0&1&0\\
0&0&0&0&0&0&0&0&0&0&0&0&0&0&1&0&0&0&0&0&1&0&1&-6&0&0&1\\
0&0&0&0&0&0&0&0&0&0&0&0&0&0&0&1&0&0&0&0&0&1&0&0&-6&1&0\\
0&0&0&0&0&0&0&0&0&0&0&0&0&0&0&0&1&0&0&0&0&0&1&0&1&-6&1\\
0&0&0&0&0&0&0&0&0&0&0&0&0&0&0&0&0&1&0&0&0&0&0&1&0&1&-6
\end{array}
$$

Figure 2.7: The figure displays the matrix A (see eq. 2.80) of the discrete 3D Poisson equation in Cartesian coordinates for a $3 \times 3 \times 3$ problem.

confined to positions close to the diagonal. Hence, it is not easy to use the sparseness of the matrix to improve the efficiency of the direct methods for solving a system of linear equations. However, with significant developments in direct solutions of sparse matrices [189], the scene is changing in favour of direct methods.

One of the most powerful, memory-efficient, and publicly available sparse matrix solver is PARDISO [5] [211,212,168,169], which I apply to solve the 3D Poisson equation for gravity. It is shared-memory parallelized and solves sparse $n \times n$ matrices with a complexity of $\mathcal{O}(n^{\alpha}(\tau + n \log n))$, with n being the number of equations, τ the number of matrix entries, and $\alpha < 1$ for matrices arising from finite-difference or finite-element discretizations [169]. However, I point out that I use the PARDISO solver as a black box. The mathematically sophisticated algorithms which are applied are beyond the scope of this dissertation. Below, I will therefore only report on the results obtained with PARDISO.

I tested the PARDISO solver with a broad range of analytical problems and boundary conditions in order to measure its capabilities and its speed. One exemplary analytical test which I performed is the problem case

$$\Delta\Phi(x, y, z) = f(x, y, z) = -48\pi^2 \sin(4\pi x) \sin(4\pi y) \sin(4\pi z) \; . \qquad (2.85)$$

In the interval $x, y, z \in [0, 1]$, mapped onto 100^3 grid points, I imposed Dirichlet boundary conditions $\partial\Omega = 1$. The analytical solution of eq. 2.85 reads

$$\Phi(x, y, z) = \sin(4\pi x) \sin(4\pi y) \sin(4\pi z) \; . \qquad (2.86)$$

The result and the relative error are displayed in fig. 2.8. Excellent agreement

---

[5] PARDISO can be freely downloaded at $http://www.pardiso-project.org/$

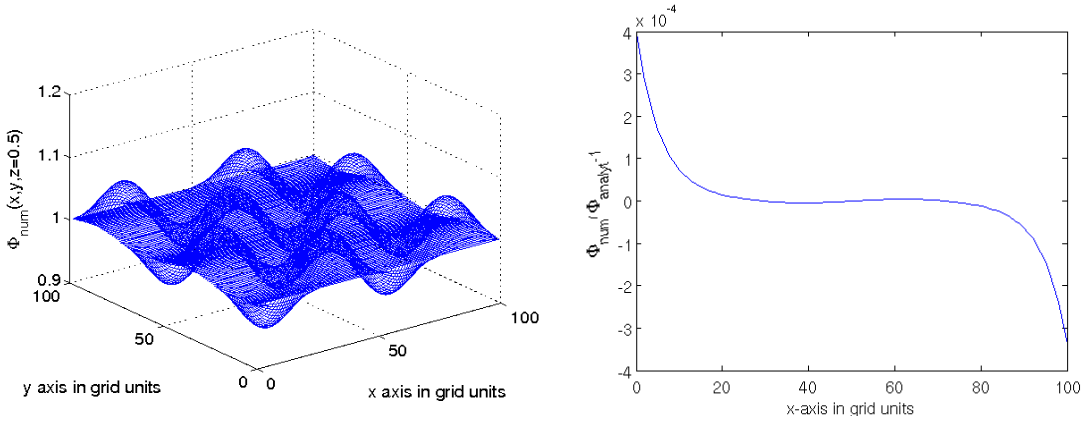

Figure 2.8: **Left panel:** Numerical solution of eq. 2.85 in the $z = 0.5$ plane. **Right panel:** Relative error $\Phi_{num}(x, 0.5, 0.5)/\Phi_{analyt}(x, 0.5, 0.5) - 1$ along the x-axis.

# CPU	elapsed time [sec]
1	11.72
2	5.92
4	3.29
8	2.01
12	1.38

Table 2.1: Scaling test of the PARDISO sparse matrix solver on one of CSCS's Cray XE6 ('Palu'; 2.1GHz, 12-core AMD Opteron (aka Magny-Cours)) nodes. The problem size considered here is 100^3 zones.

between the numerical and the exact solution was found, having a residual of $\lesssim 10^{-12}$.

Solving the Poisson equation for gravity in 3D should, as previously stated in this subsection, not consume more CPU time than one hydro time step, as the 3D MHD code else would become very inefficiently. Thus, I carried out a scaling test for 100^3 zones, the results of which are summarized in tab. 2.1.

Gravity in 3D: spectral methods

An alternative efficient approach to solve the 3D Poisson equation is presumably provided by *spectral methods* (see [190, 188], with references therein). In close collaboration with Jérôme Novak (he provided all the necessary routines), we adjusted a spectral Poisson solver from the open-source code library LORENE [6] (Langage Objet pour la RElativité NumériquE) to the context of `FISH` and `ELEPHANT`.

For the sake of consistency, I outline the basic functionality of spectral methods and the spectral Poisson solver, but omit technical and mathematical details. For a fine-grained introduction to the method, I point the reader to [190, 188].

---

[6] The URL to download LORENE is http://www.lorene.obspm.fr/

In contrast to finite-difference methods, spectral methods represent a function f not by its values on a finite number of grid points, but by using coefficients $\{c_i\}_{i=0..N}$ in a finite basis of known, smooth functions $\{\Phi_i\}_{i=0..N}$, so-called *trial functions*. Let us take, for example, a function $f : [-1,1] \to \mathbb{R}$. It can be approximated as

$$f(x) \approx \sum_{i=0}^{N} c_i \Phi_i(x) \ . \tag{2.87}$$

Spectral methods are, as in our target application, often based on orthogonal polynomials. In order to define orthogonality, one must define the scalar product of two functions on an interval, in our example $[-1,1]$. Let us consider a positive function w on $[-1,1]$ called the measure [77]. The scalar product of f and g with respect to this measure is defined as

$$(f,g)_w := \int_{x\in[-1,1]} f(x)g(x)w(x)dx \ . \tag{2.88}$$

A basis $P_{\mathbb{N}}$ is then set of $N+1$ polynomials $\{p_n\}_{n=0...N}$. p_n is of the degree n and the polynomials are orthogonal: $(p_i,p_j)_w = 0$ for $i \neq j$. The projection $P_N f$ of a function f on this basis is then

$$P_N f = \sum_{n=0}^{N} \hat{f}_n \, p_n \ , \tag{2.89}$$

where the coefficients of the projection are given by

$$\hat{f}_n = \frac{(f,p_n)}{(p_n,p_n)} \ . \tag{2.90}$$

The difference between f and its projection goes to zero when N increases:

$$\|f - P_N f\|_\infty \to 0 \quad \text{for} \quad N \to \infty \ . \tag{2.91}$$

At first sight, the projection seems to be an interesting mean of numerically representing a function. However, in practice, this is not the case, because for determining the projection of a function, one needs to compute the integrals in eq. 2.90, which require the evaluation of f at a large number of points, making the whole scheme impractical [188].

To circumvent this difficulty, the idea of the spectral methods is to approximate the coefficients of the projection by making use of the Gaussian quadrature, which states that, given a measure w, there exist $N+1$ positive real numbers w_n and $N+1$ real numbers $x_n \in [-1,1]$ such that:

$$\forall f \in \mathbb{P}_{2N+1} \ : \int_{x\in[-1,1]} f(x)w(x)dx = \sum_{n=0}^{N} f(x_n)w_n \ . \tag{2.92}$$

The x_n are so-called collocation points. Thus, one can define the interpolant of a function f by

$$I_N f = \sum_{n=0}^{N} \tilde{f}_n p_n(x) \ , \tag{2.93}$$

where

$$\tilde{f}_n = \frac{1}{\gamma_n} \sum_{i=0}^{N} f(x_i) p_n(x_i) w_i \quad \text{and} \quad \gamma_n = \sum_{i=0}^{N} p_n^2(x_i) w_i \ . \tag{2.94}$$

The $\tilde{f}_n$ exactly coincide with the coefficients $\hat{f}_n$ (see eq. 2.90) if the Gaussian quadrature is applicable for computing eq. 2.90, that is, for all $f \in \mathbb{P}_{2N+1}$. So, in general, $I_N f \neq P_N f$. The advantage of using $\tilde{f}_n$ is that they are computed by estimating f at $N+1$ collocation points only. However, one can show that $I_N f$ and f coincide at the collocation points: $I_N f(x_i) = f(x_i)$ so that I_N interpolates f on the grid, whose nodes are the collocation points.

Having laid out these first principles of the spectral methods, I now turn my attention back to the Poisson equation. In the current set-up, I solve it inside a 3D spherical volume of radius R (typically $\sim$ 60km) with Dirichlet boundary conditions at radius R, which are prescribed either by a spherically symmetric or an axisymmetric solution (cf. chap. 4).
The steps taken to obtain the solution are the following:

- interpolate the 3D density distribution from the finite difference grid (FD) to the spectral mesh (SM),
- solve the Poisson equation to obtain the 3D gravitational potential, and
- make a spectral summation of the field from the spectral to the FD grid.

Schematically:

$$\rho_{FD} \quad \longrightarrow \quad \rho_{SM} \underbrace{\longrightarrow}_{\Delta^{-1}} \quad \Phi_{SM} \quad \longrightarrow \quad \Phi_{FD} \tag{2.95}$$

Inside the spherical volume, our gravitational field Φ is expressed in spherical coordinates (r, θ, ϕ). Then, it is decomposed in a basis of spherical harmonics [105]:

$$\Phi(r, \theta, \phi) = \sum_{\ell, m} f_{\ell m}(r) Y_\ell^m(\theta, \phi) \tag{2.96}$$

where $l \in [0, \ell_{max}]$, and $m \in [-\ell, \ell]$. The same is also done with the source term $s(r, \theta, \phi)$ of the Poisson equation (note that here I omit the prefactor $4\pi G$ for simplicity):

$$s = \sum_{\ell, m} s_{\ell m}(r) Y_\ell^m(\theta, \phi) \ . \tag{2.97}$$

Because spherical harmonics are eigenfunctions of the angular part of the Laplace operator, the Poisson equation $\Delta\Phi = s$ can be equivalently solved as a set of ordinary differential equations (ODEs) for each tuplet (ℓ, m), in terms of the coordinate r:

$$\forall(\ell, m) \ : \quad \frac{d^2 f_{\ell m}}{dr^2} + \frac{2}{r}\frac{df_{\ell m}}{dr} - \frac{[\ell(\ell+1)]}{r^2} f_{\ell m} = s_{\ell m} \ . \tag{2.98}$$

This collection of ODEs is solved using a multi-domain spectral technique (see [188], chapters 1.3 and 2.6 for the technical details), where one maps a certain part of the physical domain $[R_{min}, R_{max}] \mapsto [-1,1]$, and the radial coordinate $r \mapsto \xi$. Note that in our application, we use 5 domains.

We then decompose each field in a (finite) basis of Chebyshev polynomials $\{T_{i=0\ldots N}\}$:

$$s_{\ell m}(\xi) = \sum_{i=0}^{N} c_{i\ell m} T_i(\xi) \ , \tag{2.99}$$

$$f_{\ell m}(\xi) = \sum_{i=0}^{N} a_{i\ell m} T_i(\xi) \ . \tag{2.100}$$

The Chebyshev polynomials T_i are eigenfunctions of a singular Sturm-Liouville problem [86, 188]. Given that $T_0 = 1$ and $T_1 = x$, the higher-order polynomials can be obtained by making use of the recurrence relation

$$T_{n+1} = 2xT_n - T_{n-1} \ . \tag{2.101}$$

They are orthogonal on $[-1,1]$ with respect to the measure $w = 1/\sqrt{1-x^2}$, and the scalar product of two polynomials is

$$(T_n, T_m) = \int_{-1}^{1} \frac{T_n T_m}{\sqrt{1-x^2}} dx = \frac{\pi}{2}(1+\delta_{0n})\delta_{mn} \ . \tag{2.102}$$

The derivatives are given by

$$\forall n > 1 \ : \quad \frac{dT_{n+1}(x)}{dx} = 2(n+1)T_n(x) + \frac{n+1}{n-1}\frac{dT_{n-1}(x)}{dx} \ . \tag{2.103}$$

The adapted grid for the computation of the spectral coefficients is equidistant in angular directions (9 points for θ, 16 for ϕ in our code version); moreover, we compute Chebyshev-Gauss-Lobatto collocation points (33 in our case) for the radial direction. The positions of the latter and the weights are given by analytic formulae

$$x_i = \cos\left(\frac{\pi i}{N}\right) \qquad w_0 = w_N = \frac{\pi}{2N} \quad \text{and} \quad w_i = \frac{\pi}{N} \ . \tag{2.104}$$

The coefficients can now be obtained by performing a Fast Fourier Transform (FFT, [189]). Having these, each function $f_{\ell m}$ (see eq. 2.100) can thus be regarded as column-vector $A_{\ell m}$ of its $N+1$ coefficients $a_{i\ell m}$ in its basis; the linear differential operator on the left-hand side of eq. 2.98 is then a matrix $L_{\ell m}$ acting on the vector (cf. the previous subsection on the sparse matrix solver method)

$$L_{\ell m} A_{\ell m} = S_{\ell m} \ , \tag{2.105}$$

with $S_{\ell m}$ being the vector of the $N+1$ coefficients $c_{i\ell m}$ of $s_{i\ell m}$.

The matrix $L_{\ell m}$ can be computed from the recurrence relations fulfilled by the Chebyshev polynomials and their derivatives. Once the boundary conditions are incorporated in eqs. 2.105 (see [188], sec. 2.5.2), these linear systems can be inverted for each tuplet of values (ℓ, m) with coefficients of the source term on the right-hand side. The idea therefore is to invert something like $\mathcal{O}(30^2)$ ODEs, and for each one to invert a $\sim 30 \times 30$ matrix per domain. In view of the fact that for spectral methods, the error decays as $e^{-\ell_{max}} \cdot e^{-N}$ [88], machine round-off accuracy can already be reached with $\ell_{max} \sim N \sim 30$, which makes the matrix inversions very cheap in terms of CPUh and the whole method affordable in terms of memory usage. These are the two main advantages of using spectral methods [188]. Note that for the time being, the first and last step (see eq. 2.95), on which most of the CPU time is spent during the solution procedure ($\sim 99\%$), are currently OpenMP parallel [25]. In the more distant future, a hybrid parallelization scheme might also be applied, where, in addition, each of the 5 domains will be distributed to separate MPI processes.

# CPU	elapsed time [sec]
1	10.44
2	5.43
4	3.73
8	2.05
12	1.52

Table 2.2: Scaling test of the Poisson solver on one of CSCS's Cray XT-5 ('Rosa') nodes. The problem size was a 3D sphere of radius $R = 60$km and with a grid spacing of 1km in the Cartesian domain. Note that the test volume treated here is $\sim 10\%$ smaller than the one considered in tab. 2.1 with the sparse matrix solver. The elapsed time includes the interpolation process from the FD grid onto the spectral grid, the solution of the Poisson equation itself, and the spectral summation from the spectral back to the FD grid (see eq. 2.95).

One central issue when computing the gravitational potential via spectral methods is that no mass should get lost when interpolating back and forth between the spectral and Cartesian grid. In our case, the interpolation conserves mass very well, with a relative error smaller than $\lesssim \mathcal{O}(10^{-8})$, as displayed in fig. 2.9.

Comparison of methods: spherical mass integration vs. spectral solver vs. sparse matrix solver

Figure 2.10 displays comparisons of both 3D poisson solvers with the spherically symmetric mass integration and each other. As test data, I have chosen a density distribution of model A$_{NEWT}$ (see tab. 3.5), 64 ms after bounce. The comparison of both 3D Poisson solvers shows that they deliver a comparable solution for the gravitational potential, with an agreement of $\sim \mathcal{O}(10^{-3})$. Moreover, the comparison of both 3D solvers with the spherically symmetric solution shows a certain discrepancy at the origin. This is because the 1D poisson equation owns a singularity at $r = 0$ (cf. eq. 2.56), which is circumvented by assuming a constant value for $\Phi_{\text{spherical, int}}$ according to the mass contained inside the central zone. This procedure leads to a somewhat deeper gravitational well compared to the 3D solutions.

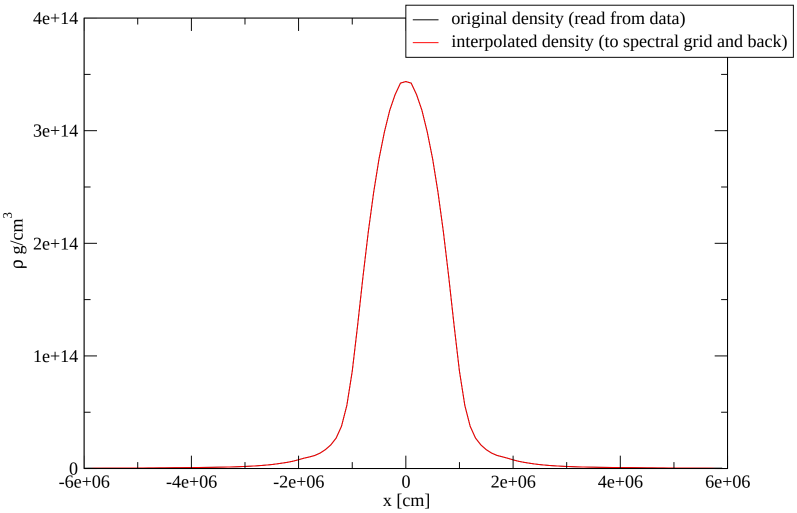

Figure 2.9: The figure displays two density distributions of a test data set. The first one (black) is taken from the original data, while the second one (red) is an interpolated distribution which resulted after having been sent to the spectral grid and back to the Cartesian grid. It becomes clear that the interpolation hardly introduces numerical errors, as the two lines cannot be distinguished. The test data were taken from density distribution of model A_{NEWT} (see tab. 3.5) 64 ms after bounce. The figure is courtesy of Jérôme Novak.

2.3 Equations of state

The system of the MHD equations (eqs. 2.1-2.4) must be closed by an equation of state (EoS) which provides the pressure as well as other thermodynamic quantities as a function of density, temperature (or specific internal energy), and composition/electron fraction. In core-collapse simulations, the inclusion of a ‘realistic’ EoS, which is built from a microphysical finite-temperature model is crucial, as an EoS must be able to capture the stiffening of nuclear matter around nuclear matter density. Moreover, such a sophisticated EoS is also a prerequisite for any kind of neutrino transport treatment, since the crucial compositional information as well as chemical potentials must be derived from a microphysical model (see sec. 2.4).

In core-collapse supernova simulations, an EoS has to handle several different regimes. For temperatures below ∼0.5MeV, the presence of nuclei and time-dependent nuclear processes dominate the internal energy evolution. For simplicity, an ideal gas of Si-nuclei is assumed, which, for our GW studies (see chap. 3 and 4), is sufficiently accurate to describe the low baryonic pressure contribution at low densities in the outer core (T. Fischer (2009), private communication). At higher temperatures, where matter is in nuclear statistical equilibrium (NSE), we employ two alternative EoS: The Lattimer & Swesty EoS ([130], LS EoS) and the one by Shen et al. [215]. Note that such microphysical EoS are too complicated to be computed on the fly in a simulation and are used in tabulated form with interpolation.

The Basel 3D MHD codes run with tables based on the thermodynamically independent variables (ρ, s, Y_e), which in their final form consist of $100 \times 100 \times 100$

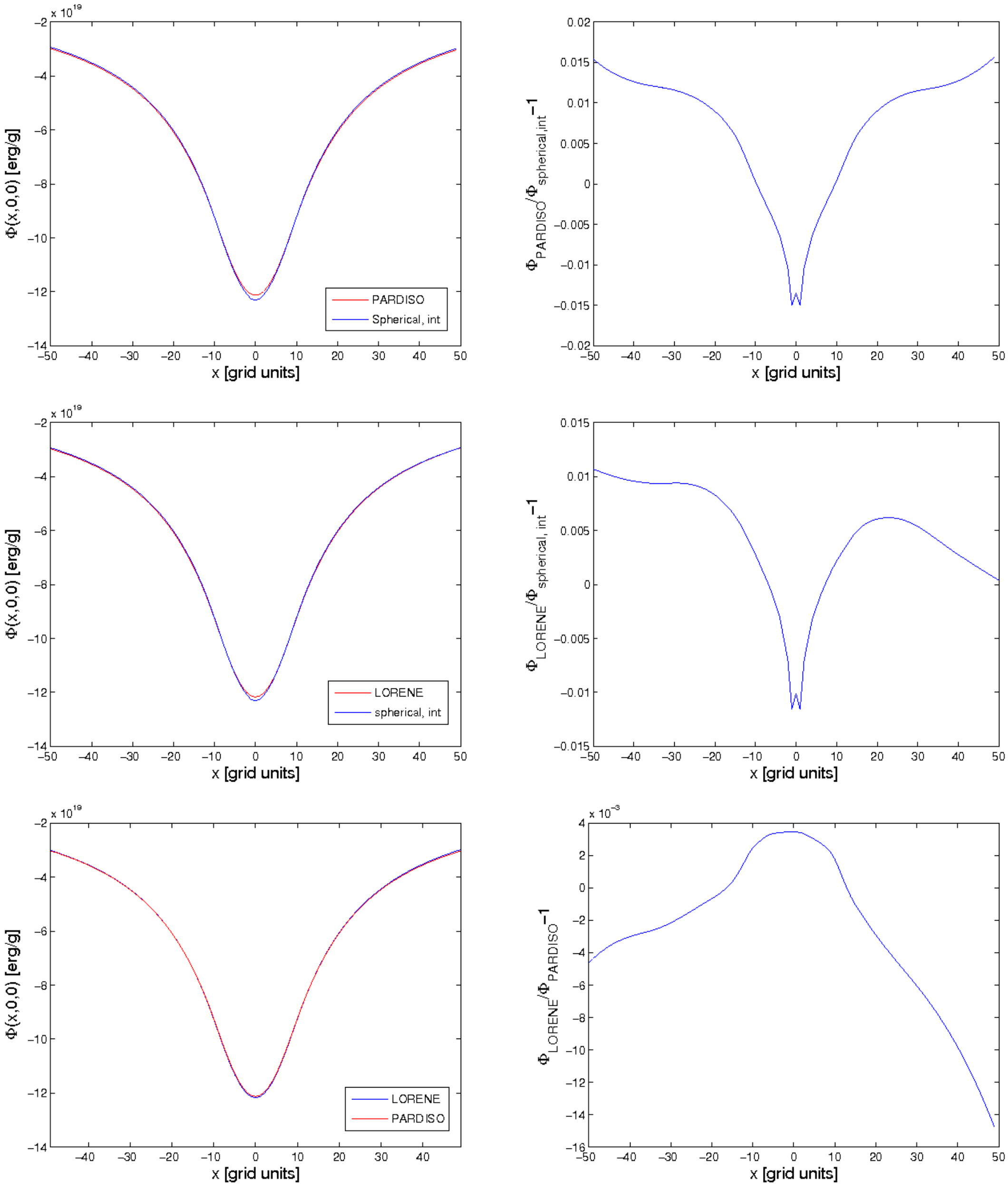

Figure 2.10: **Upper left panel**: Comparison of the gravitational potential Φ along the x-axis, obtained either via a spherically symmetric mass integration, or a solution of the 3D Poisson equation via the PARDISO solver. **Upper right panel**: Relative difference $\Phi_{PARDISO}(x,0,0)/\Phi_{spherical,int}(x,0,0) - 1$ along the x-axis. **Middle left panel:** Comparison the the spherically symmetric mass integration with the 3D spectral solver. **Middle right panel:** Relative difference $\Phi_{LORENE}(x,0,0)/\Phi_{spherical,int}(x,0,0) - 1$ along the x-axis. **Lower left panel:** Comparison of the two 3D Poisson solvers. **Lower right panel:** Relative difference $\Phi_{PARDISO}(x,0,0)/\Phi_{LORENE,int}(x,0,0) - 1$ along the x-axis.

equidistant points in $\log_{10}\rho$, $\log_{10}s$, and Y_e, respectively (T. Fischer, private communication (2010)).

2.3.1 Lattimer-Swesty EoS

The Lattimer-Swesty EoS [130] is based on a phenomenological, finite-temperature compressible liquid drop model; it also includes surface effects as well as electron-positron and photon contributions. The LS EoS assumes a nuclear symmetry energy of 29.3MeV and I will perform simulations (see chap. 3) with three choices of the nuclear compressibility modulus K (180, 220, 375MeV) as provided by [130]. Since variations in K affect the stiffness of the nuclear component of the EoS, this enables us to probe the effects of variations in stiffness while keeping the general EoS model fixed.

The variants of the LS EoS used in this work are provided by M. Liebendörfer and T. Fischer. The table ranges are

$$\begin{aligned} 1.66\times10^{7}\mathrm{gcm}^{-3} &< \rho < 10^{15}\mathrm{gcm}^{-3}\ , \\ 0.5\mathrm{k}_B &< s < 50\mathrm{k}_B\ , \\ 0.05 &< Y_e < 0.56\ . \end{aligned}$$

In between the data points of the table, bisection is applied. Note that wherever this method fails to generate a numerical value, a relativistic electron-positron gas is assumed.

2.3.2 Shen EoS

The pure baryon EoS of Shen et al. [215] has a compressibility of K=281MeV and a symmetry energy of 36.9MeV. It is based on relativistic mean field theory and the Thomas-Fermi approximation. For matter in non-NSE ($T < 0.44$ MeV), the Shen EoS is coupled to the ideal Si-gas and electron-positron EoS given in [236] and [237]. It employs an ideal gas for the nuclei and additionally includes contributions from ion-ion correlations and photons. The variant of the Shen EoS used in this work is provided by T. Fischer. The table ranges are

$$\begin{aligned} 10^{5.1}\mathrm{gcm}^{-3} &< \rho < 10^{15.46}\mathrm{gcm}^{-3}\ , \\ 0.1\mathrm{MeV} &< T < 50\mathrm{k}_B\ , \\ 0.01 &< Y_e < 0.56\ . \end{aligned}$$

2.4 Neutrino transport & transport approximations

The inclusion of neutrino physics is an essential ingredient of core-collapse supernova simulations, as ∼99% of the released binding energy is converted into neutrinos of all flavours. Their complex interactions with matter are believed to drive the supernova explosion dynamics in the outer layers as well as deleponizing the PNS to its compact

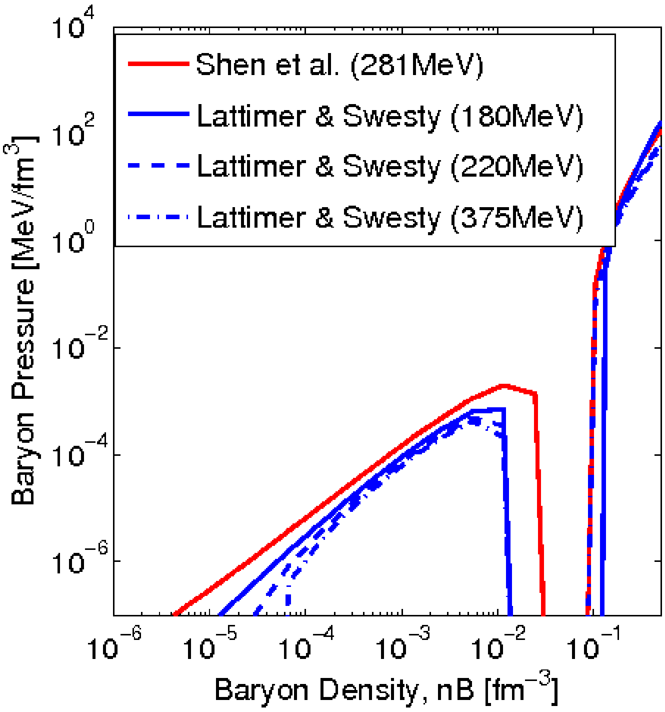

Figure 2.11: Comparison of the Lattimer-Swesty EoS (it comes with three different compressibilities K=180, 220, 375MeV) with the Shen EoS (K=281MeV) for a typical PNS configuration: specific entropy $s = 1k_B$/baryon and the electron fraction $Y_e = 0.3$. Shown is the *pure* baryonic pressure component with respect to the baryon number density. Note that a) in the regions of negative baryonic pressure, electron and positron pressure prevails, and b) the essential difference in the compressibilities comes across only in the region of high densities, i. e. homogeneous nuclear matter. The figure is courtesy of T. Fischer.

final stage as a neutron star (see sec. 1.2, and references therein). The neutrinos travelling through the postshock region in a postbounce supernova core are not in thermal equilibrium with the baryonic matter [29, 106]. Thus, they should ideally be treated with full kinetic theory, describing the neutrino distributions and their temporal distribution with the Boltzmann transport equation [155].

The Boltzmann equation describes the time t evolution of the distribution function *f(x,v,t)* in a one-particle phase space, where x and v are position and velocity, respectively. In Cartesian coordinates, the classical Boltzmann equation for particles reads [155]

$$\left(\frac{\partial f}{\partial t}\right) + v^i \left(\frac{\partial f}{\partial x^i}\right) + a^i \left(\frac{\partial f}{\partial v^i}\right) = \left(\frac{Df}{Dx^i}\right)_{coll} . \tag{2.106}$$

From eq. 2.106 it can be seen that Boltzmann transport is in its most general form a 7-dimensional problem: the 6D neutrino phase space (usually split into 3D spatial coordinates, neutrino energy, and 2 angular degrees of freedom) and time. Additionally, there are up to 6 neutrino types (3 particle flavours, and their antiparticles [187]) to deal with.

Due to the complexity of the problem (see, e.g., [138, 133], and references therein), the Boltzmann neutrino transport equation can still only be solved numerically in a complete form in spherical symmetry on today's supercomputers [152]. In order to solve the Boltzmann equation in 3D in a closed manner, a single fluid element would contain at least 4 neutrino types ($\nu_e, \overline{\nu}_e, \nu_{\mu,\tau}, \overline{\nu}_{\mu,\tau}$) × 20 energy bins × 100 angles = 8000 variables. For an entire 3D domain with a typical size of $\sim 1000^3$ zones, this translates to a requirement of 64 TB memory per time step, which is still beyond the range of resources available on HPC systems.

Multidimensional core-collapse supernova simulations must therefore rely on more or less severe approximations of the neutrino physics. In state-of-the-art 2D simulations, one way to approach the Boltzmann transport is the so-called 'ray-by-ray plus scheme' [40]. It solves the full transport problem in separate 1D angular segments, where the neighbouring rays are coupled. Other groups rely on multi-group flux-limited diffusion (MGFLD, [176, 224]). MGFLD treats all neutrinos in separate energy groups, drops the momentum space angular dependence of the radiation field and evolves the zeroth moment of the specific intensity instead of the specific intensity itself. In three dimensions, simulations have been performed using 'grey' flux-limited diffusion [79], which oversimplifies the important neutrino spectrum. It is, however, essential to resolve at least the electron-flavour neutrino spectrum, since the charge-current interaction rates go with the square of the neutrino energy (see secs. 1.2 and 1.8).

In the following subsections, I will outline the basic principles of two neutrino transport schemes which the Basel supernova group applies in 3D simulations during the collapse and the postbounce phase. More details about these schemes can be found in Liebendöfer et al. [136, 140], on which the discussion below is based. Prior to this, however, I will review the 'standard' neutrino interactions which are commonly considered in stellar core-collapse simulations; this discussion is primarily based on Bruenn [36].

2.4.1 Neutrino interactions

A 'standard' set of neutrino interactions which is included in at present-days state-of-the-art 1D numerical core-collapse simulations is listed below (see, e.g., [260,37,72]):

$$
\begin{aligned}
\nu_e + n &\rightleftarrows e^- + p && (2.107)\\
\overline{\nu}_e + p &\rightleftarrows e^+ + n && (2.108)\\
\nu_e + A &\rightleftarrows e^- + A' && (2.109)\\
\nu + N &\rightleftarrows \nu + N && (2.110)\\
\nu + A &\rightleftarrows \nu + A && (2.111)\\
\nu + e^- &\rightleftarrows \nu + e^- && (2.112)\\
e^- + e^+ &\rightleftarrows \nu + \overline{\nu} && (2.113)\\
\nu + e^+ &\rightleftarrows \nu + e^+ && (2.114)\\
N + N &\rightleftarrows N + N + \nu + \overline{\nu} && (2.115)\\
\nu_e + \overline{\nu}_e &\rightleftarrows \nu_{\mu/\tau} + \overline{\nu}_{\mu/\tau}\ , && (2.116)
\end{aligned}
$$

where the particles are denoted as follows: n = free neutrons, p = free protons, N = free neutrons or protons, A = nuclei, ν_e = electron-type neutrinos, ν = any type of neutrinos, $\overline{\nu}$ = antiparticle of particle ν, e^- = electrons, and e^+ = positrons. Moreover, A' in eq. 2.109 denotes a nucleus $(A, Z+1)$ with an atomic mass number A and charge $Z+1$, which decays via electron capture into a nucleus $A = (A, Z)$. Note that an important correction that must/should be incorporated in eq. 2.111 results from ion-ion correlations [103]. These tend to increase the neutrino mean free paths, particularly at low energies. Including them in core-collapse simulations is important, particularly during the infall phase when the core is cold and made up mainly of heavy nuclei. Their inclusion results in a substantial increase of the core deleptonization.
Currently, the Basel code version of `Agile-Boltztran` [133] (1D GR) incorporates the reactions 2.107-2.113 according to Bruenn [37]. Process 2.115 is implemented according to Thompson and Burrows [229]. Interaction 2.114 was implemented by T. Fischer [72], following [260]. Finally, the emission of μ/τ-pairs via the annihilation of trapped electron neutrino pairs (process 2.116) as well as contributions from nucleon recoil and weak magnetism [100] are taken into account in a fashion outlined in Fischer et al. [74]. Note that the 3D MHD code `ELEPHANT` applies only a reduced set of neutrino reactions, as will be explained in the subsequent two sections 2.4.2 and 2.4.3. However, before that I will now briefly summarize the reaction rates of processes 2.107-2.113 [37], since they play a dominant role in the core-collapse simulations I carried out. Note that I will not go into the details of their derivations, but rather give the expressions which are applied in the different core-collapse codes of the Basel supernova group.

Following Bruenn ([37], with references therein), I denote the occupation probability of a neutrino species by f defined as such that $dn = f(t, r, \mu, \omega) dV d\Omega[\omega^2 d\omega/(2\pi\hbar c)^3]$ is the mean number of neutrinos at time t within a volume dV at r, having a propagation direction within a solid angle $d\Omega$ at μ, and within an energy $d\omega$ at ω. Here, r is a *Lagrangian* coordinate (distance from the centre of the star of a given spherically symmetric fluid element), $\mu = cos(\theta)$ is the cosine of the angle between the propagation direction of the neutrino and the outward radial direction, and ω is the neutrino energy. For notational convenience, I suppress from now on for the rest of this subsection the dependence of these terms on r and t [e.g. $f(\mu,\omega) \equiv f(t,r,\mu,\omega)$]. The distribution function of particles of type i, denoted by $F_i(E_i)$. is assumed to be Fermi-Dirac, i.e.,

$$F_i(E_i) = 1/\left\{1 + \exp\left[\beta(E_i - \mu_i)\right]\right\} \ , \tag{2.117}$$

where μ_i is the chemical potential including rest mass of type i particles (μ_i^0 without the rest mass included) and $\beta = 1/k_B T$, where T is the fluid temperature. Hereafter, the index $i = e^-, e^+, p, n, N, A$ refers to electrons, positrons, protons, neutrons, nucleons, and nuclei, respectively.

- *Interaction I (2.107):* $\nu_e + n \rightleftarrows e^- + p$ (electron-type neutrino absorption on neutrons)

  The ν_e absorptivity $\chi = 1/\lambda(\omega)$ (where $\lambda(\omega)$ is the neutrino absorption mean free path) is given by

$$\chi(\omega) = \frac{G^2}{\pi}\eta_{np}\left(g_{\mathrm{V}}^2 + 3g_A^2\right)\left[1 - F_{e^-}(\omega+Q)\right](\omega+Q)^2\left[1 - \frac{M_e^2}{(\omega+Q)^2}\right]^{1/2} \ , \tag{2.118}$$

  where $Q = M_n - M_p = 1.2935\mathrm{MeV}$ is the mass difference between the neutron and proton rest energies. g_{V} and g_A are form factors resulting from virtual strong interaction processes. In the zero momentum transfer limit, i.e. under the assumption, that no momentum is transferred between the neutrinos and the nucleons (and the nucleons are non-relativistic), $g_{\mathrm{V}} = 1$ and $g_{\mathrm{A}} = 1.23$. η_{np} in eq. 2.118 takes into account nucleon final-state blocking and reads

$$\eta_{np} = (n_p - n_n)/\left(\exp\left[\beta(\mu_p^0 - \mu_n^0\right] - 1\right) \ . \tag{2.119}$$

  The neutrino emissivity in process 2.107 can be described by

$$j(\omega) = \frac{G^2}{\pi}\eta_{pn}\left(g_{\mathrm{V}}^2 + 3g_A^2\right)F_{e^-}(\omega+Q)\,(\omega+Q)^2\left[1 - \frac{M_e^2}{(\omega+Q)^2}\right]^{1/2} \ . \tag{2.120}$$

  The factor G^2 in the expressions 2.118 and 2.120 is the Fermi constant with the value

$$G^2 = 5.18 \times 10^{-44}\mathrm{MeV}^{-2}\mathrm{cm}^2 \ . \tag{2.121}$$

  Note that nucleon recoil and thermal motions were neglected in the derivation of the expressions of interaction I.

- *Interaction II (2.108):* $\bar{\nu}_e + p \rightleftarrows e^+ + n$ (electron-type anti-neutrino absorption on protons)

  The absorption in this process is given by

$$\chi(\omega) = \frac{G^2}{\pi}\eta_{pn}\left(g_{\mathrm{V}}^2 + 3g_A^2\right)\left[1 - F_{e^+}(\omega - Q)\right](\omega - Q)^2\left[1 - \frac{M_e^2}{(\omega - Q)^2}\right]\Theta(E - Q - M_e)\ , \tag{2.122}$$

  and the emissivity is

$$j(\omega) = \frac{G^2}{\pi}\eta_{np}\left(g_{\mathrm{V}}^2 + 3g_A^2\right)F_{e^+}(\omega - Q)\,(\omega - Q)^2\left[1 - \frac{M_e^2}{(\omega - Q)^2}\right]\Theta(\omega - Q - M_e)\ , \tag{2.123}$$

  where the threshold of $\omega = Q + M_e$ for the anti-neutrino absorption and emission by free nucleons is incorporated in the Θ-function:

$$\Theta(x) = \begin{cases} 0 & \text{for} \quad x < 0 \\ 1 & \text{for} \quad x > 0 \end{cases} . \tag{2.124}$$

  As in interaction I, nucleon recoil and thermal motions were neglected.

- *Interaction III (2.109):* $\nu_e + A' \rightleftarrows e^- + A$ (neutrino absorption on nuclei)

  In the approach we apply, electron capture on heavy nuclei is dominated by the Gamow-Teller transition from the single-particle $1f_{7/2}$ level to the single-particle level $1f_{f_{5/2}}$ unless the reaction is blocked by the absence of neutron holes, which, in the standard picture, occurs for $N \geq 40$ [80]. Thus, the rates of [37] for electron capture I apply do not include electron capture on nuclei with $N \geq 40$.

  However, I point out that recent results from Langanke et al. [129] and Hix et al. [99], obtained via nuclear shell model calculations, show that thermal unblocking and other effects lead to significant electron capture rates even on nuclei with $N \geq 40$. As a consequence, this leads to the insight that electron capture on nuclei dominates the one on free protons throughout the entire collapse of the stellar core. This in turn lowers Y_e by roughly $\sim 5-10\%$ at core bounce, which then is reflected in smaller inner core masses (see, e.g., [150]).

  If we denote N_p as the number of protons in the single $1f_{f_{7/2}}$ level and N_h the number of neutron holes in the single-particle $1f_{f_{5/2}}$ level, the applied zero-order shell model predicts

$$N_p(Z) = \begin{cases} 0, & Z < 20 \\ Z - 20, & 20 < Z < 28 \\ 8, & Z > 28\ , \end{cases} \tag{2.125}$$

$$N_h(N) = \begin{cases} 6, & N < 34 \\ 40 - N, & 34 < N < 40 \\ 0, & N > 40\ . \end{cases} \tag{2.126}$$

In the case of neutrino absorption on neutrons in nuclei, the emissivity is given by

$$j(\omega) = \frac{G^2}{\pi} n_{\mathrm{A}} g_{\mathrm{A}}^2 \frac{2}{7} N_p(Z) N_Z(Z) F_{e^-}(\omega + Q')\,(\omega + Q')^2 \left[1 - \frac{M_e^2}{(\omega + Q')^2}\right]^{1/2}\ , \tag{2.127}$$

where

$$Q' = M^*_{A'} - M_A = M_{A'} - M_A + \Delta \approx \mu_n - \mu_p + \Delta\ , \tag{2.128}$$

and A is the mean nucleus. The quantity $\Delta = M^*_{A'} - M_{A'}$ is the energy of the neutron $1f_{5/2}$ state above the ground state. In [37] its value is estimated to be about $\sim$ 3MeV for all nuclei.

The resulting absorptivity yields

$$\chi(\omega) = \frac{G^2}{\pi} n_{\mathrm{A}} \exp(\beta[\mu_n - \mu_p - Q']) g_{\mathrm{A}}^2 \frac{2}{7} N_p(Z) N_n(N) \cdot \\ [1 - F_{e^-}(\omega + Q')]\,(\omega + Q')^2 \left[1 - \frac{M_e^2}{(\omega + Q')^2}\right]^{1/2}\ . \tag{2.129}$$

The derivations of expressions 2.127 and 2.129 neglect nuclear recoil and thermal motions.

- *Interaction IV (2.110):* $\nu + N \rightleftarrows \nu + N$ (isoenergetic neutrino-nucleon scattering, where N is a neutron or proton).

Neutrino-nucleon scattering proceeds via the exchange of a neutral Z boson only. In this process, the different neutrino or anti-neutrino flavours will not be distinguished, since the reaction rate is the same for all types. Note that in the derivation of this process, the nucleon recoil and thermal motions were neglected. Expanding the isoenergetic ($\omega = \omega'$) scattering kernel in terms of a Legendre series, it yields (approximated by the first two Legendre coefficients):

$$R_{IS}(\omega, \omega, \cos(\Theta))^{\left\{ {in \atop out} \right\}} = \frac{1}{2}\Phi_{0,IS}(\omega) + \frac{3}{2}\Phi_{1,IS}(\omega)\cos(\Theta)\ , \tag{2.130}$$

where $cos\Theta$ is the cosine of the relative angle between the incoming neutrino and the outgoing neutrino directions. The zeroth and first moments of the scattering functions are given by

$$\Phi^N_{0,IS}(\omega) = 4\pi G^2 \eta_{NN} \left[(h^N_{\rm V})^2 + 3(h^N_A)^2\right] \ , \tag{2.131}$$

$$\Phi^N_{1,IS}(\omega) = \frac{4\pi}{3} G^2 \eta_{NN} \left[(h^N_{\rm V})^2 - (h^N_A)^2\right] \ , \tag{2.132}$$

where η_{NN} accounts for the nucleon final-state blocking,

$$\begin{aligned}\eta_{NN} &= \int \frac{2d^3p_N}{(2\pi)^3} F_N(E_N)\left[1 - F_N(E_N)\right] \\ &= \frac{1}{\beta}\frac{\partial n_N}{\partial \mu_N} \ .\end{aligned} \tag{2.133}$$

The quantities $h^N_{\rm V}$ and $h^N_{\rm A}$ are the neutral nucleon current form factors in the limit of zero-momentum transfer:

$$h^p_{\rm V} = \frac{1}{2} - 2\sin^2\theta_{\rm W} \ , \tag{2.134}$$

$$h^p_{\rm A} = \frac{1}{2} g_A \ , \tag{2.135}$$

$$h^n_{\rm A} = -\frac{1}{2} \ , \tag{2.136}$$

$$h^n_{\rm A} = -\frac{1}{2} g_A \ , \tag{2.137}$$

$$\tag{2.138}$$

where $\sin^2\theta_{\rm W} \approx 0.23$ and Θ_W the Weinberg angle. The constant G^2 here takes the value

$$G^2 = 1.2 \times 10^{-65} {\rm MeV cm^3 s^{-1}} \ . \tag{2.139}$$

- *Interaction V (2.111):* $\nu + A \rightleftarrows \nu + A$ (Coherent scattering of neutrinos on nuclei)

In the derivation of this process, nuclear recoil and thermal motions were neglected. The isoenergetic scattering kernel (see eq. 2.130) is again expressed by the zeroth and first moments of the scattering functions which are given by:

$$\Phi^A_{0,IS}(\omega) = 2\pi G^2 n_A A^2 \left(C_{\rm V0} + \frac{1}{2}\frac{N-Z}{A} C_{\rm V1}\right)^2 \cdot \frac{2y - 1 + e^{-2y}}{y^2} \ , \tag{2.140}$$

and

$$\Phi^A_{1,IS}(\omega) = 2\pi G^2 n_A A^2 \left(C_{\mathrm{V}0} + \frac{1}{2}\frac{N-Z}{A} C_{\mathrm{V}1} \right)^2 \cdot \\ \frac{2-3y+2y^2-(2+y)e^{-2y}}{y^3} \ , \quad (2.141)$$

where $y = b\omega^2$ and $b \approx 4.8 \times 10^{-6} A^{2/3}\mathrm{MeV}^{-2}$. Moreover, $C_{x0} = \frac{1}{2}(h^p_x + h^n_x)$ and $C_{x1} = (h^p_x - h^n_x)$, where $x = V$ (*'Vector'*) or A (*'Axial'*). The constant G is given by eq. 2.139.

- *Interaction VI (2.112):* $\nu + e^- \rightleftarrows \nu + e^-$ (neutrino electron scattering NES)

I first consider the electron-type neutrinos. The first two Legendre coefficients of the scattering kernel,

$$R^{\left\{\begin{smallmatrix} in \\ out \end{smallmatrix}\right\}}_{NES}(\omega, \omega', \cos(\Theta)) \approx \frac{1}{2}\Phi^{\left\{\begin{smallmatrix} in \\ out \end{smallmatrix}\right\}}_{0,NES}(\omega, \omega') + \frac{3}{2}\Phi^{\left\{\begin{smallmatrix} in \\ out \end{smallmatrix}\right\}}_{1,NES}(\omega, \omega')\cos(\Theta) \quad (2.142)$$

are then given by

$$\begin{aligned} \Phi^{\left\{\begin{smallmatrix} in \\ out \end{smallmatrix}\right\}}_{l,NES}(\omega, \omega') &= \frac{G^2}{\pi\omega^2\omega^{2'}} \int dE_e F_e(E_e)\left[1 - F_e(E_e + \omega - \omega')\right] \cdot \begin{Bmatrix} \exp[-\beta(\omega-\omega')] \\ 1 \end{Bmatrix} \\ &\times \left[(C_\mathrm{V} + C_\mathrm{A})^2 H^\mathrm{I}_l(\omega, \omega', E_e) + (C_\mathrm{V} - C_\mathrm{A})^2 H^\mathrm{II}_l(\omega, \omega', E_e) \right] \ , \quad (2.143) \end{aligned}$$

where $C_\mathrm{V} = \frac{1}{2} + 2\sin^2(\Theta_\mathrm{W})$ and $C_\mathrm{A} = \frac{1}{2}$. The constant G^2 in eq. 2.143 has the value

$$G^2 = 1.55 \times 10^{-33}\mathrm{cm}^3\mathrm{MeV}^{-2}\mathrm{s}^{-1}. \quad (2.144)$$

The functions H^I_l and H^{II}_l for $l = 0$ and $l = 1$ are given by relatively large expressions. For details, we refer the reader to [260], appendix A.

The NES for $\overline{\nu}_e$ can be obtained from eq. 2.143 by replacing C_A by $-C_\mathrm{A}$. The NES for ν_μ and ν_τ can be obtained by replacing C_V and C_A in eq. 2.143 by $C_\mathrm{V} - 1$ and $C_\mathrm{A} - 1$, respectively. Finally, the NES for $\overline{\nu}_\mu$ and $\overline{\nu}_\tau$ neutrinos is obtained by replacing C_V and C_A in eq. 2.143 by $C_\mathrm{V} - 1$ and $C_\mathrm{A} - 1$, respectively, and then changing the sign of $C_\mathrm{A} - 1$.

- *Interaction VII (2.113):* $e^- + e^+ \rightleftarrows \nu + \overline{\nu}$ (pair creation and annihilation)

The thermal production (TP) and absorption kernels of absorption/annihilation (a) and production/creation (p) processes are given by

$$R^{\left\{\begin{smallmatrix} p \\ a \end{smallmatrix}\right\}}_{TP}(\omega, \omega', \cos(\Theta)) \approx \frac{1}{2}\Phi^{\left\{\begin{smallmatrix} p \\ a \end{smallmatrix}\right\}}_{0,TP}(\omega, \omega') + \frac{3}{2}\Phi^{\left\{\begin{smallmatrix} p \\ a \end{smallmatrix}\right\}}_{1,TP}(\omega, \omega')\cos(\Theta) \quad (2.145)$$

The l-th moment $\Phi^{\left\{\begin{smallmatrix} p \\ a \end{smallmatrix}\right\}}_{l,TP}$ is given by an expressions of the form

$$\Phi^{\left\{\begin{smallmatrix} p \\ a \end{smallmatrix}\right\}}_{l,TP} = \alpha^2_1 j^{I\left\{\begin{smallmatrix} p \\ a \end{smallmatrix}\right\}}_{l,TP}(\omega, \omega') + \alpha^2_2\, j^{II\left\{\begin{smallmatrix} p \\ a \end{smallmatrix}\right\}}_{l,TP}(\omega, \omega') \ . \quad (2.146)$$

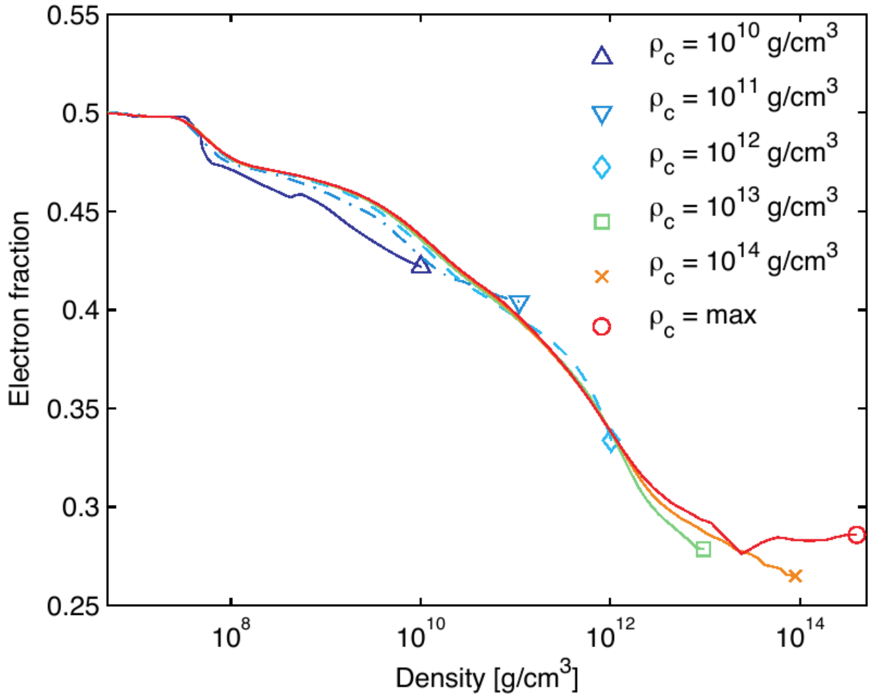

Figure 2.12: Electron fraction (Y_e) profiles at varying central densities during collapse in model G15 of Liebendörfer et al. [134]. As shown, $Y_e(\rho, t)$ is only a weak function of time. Figure taken from [136].

The very large expressions for the zeroth and first moments of the absorption and production functions for the different neutrino species can be found in [37], eqs. (C66) - (C74).

2.4.2 Neutrino parametrization scheme

Stellar core collapse proceeds, as outlined previously in sec. 1.2, by an imbalance between the self-graviting forces of the inner core and its fluid pressure. At the onset of the collapse, a degenerate electron gas provides the dominant contribution to the pressure. The electron fraction Y_e is therefore the fundamental quantity for stability of the inner core, as the electron pressure scales as $P_e \propto Y_e^{4/3}$ (see sec. 1.2, with references therein). The electron fraction evolves during the collapse of the iron core by electron capture on protons (eq. 2.107) and on protons bound in nuclei (eq. 2.109). These reactions lead to a reduction of the electron fraction Y_e. The electron neutrinos ν_e produced in these charged-current weak interactions either (1) directly escape at low densities, (2) thermalize and eventually escape, or (3) are trapped for longer than the dynamical timescale (see, e.g., [29, 106]). As in cases (1) and (2) the core loses leptons, one commonly refers to electron capture during collapse as *deleptonization*. Case (3) is encountered above neutrino trapping densities $\sim 10^{12}$gcm^{-3}, when the opacities for neutrino scattering become large enough such that the neutrinos can leave the core only on a diffusion timescale, which is much larger than the dynamical timescale. In this regime, the total lepton fraction $Y_l = Y_e + Y_\nu$ is conserved and the neutrinos are in β-equilibrium. ν_μ and ν_τ neutrinos and their antiparticles are not yet present in this supernova stage, as the material does not provide the high temperatures needed for the pair-production processes.

Thus, during the collapse phase until core bounce, a consistent numerical treatment of deleptonization is important, as a reduction of Y_e leads to a reduction of pressure support below nuclear densities. This in turn reduces the size of the homologous inner core [259] which rebounds coherently and that defines the size of the inner core and the initial energy that is imparted to the shock. The latter scales roughly as $\propto Y_e^{10/3}$ (see [37], with references therein). This is also one of the reasons why core-collapse simulations that do not include a treatment of deleptonization almost always produce 'prompt' explosions, while computations that do take into account deleptonization hardly explode [138].

Taking deleptonization properly into account is also very important in the context of the GW emission from CCSNe: In quickly spinning core collapse, one of the strongest GW signals is expected to come from the matter dynamics at core bounce (see sec. 3.5, and for a review [174]). The size of the inner core is the dynamically relevant quantity for the emission of GWs at core bounce (see [62], with references therein). Hence, for reliable estimates of the GW signature of rotating iron core collapse, it is essential to fully capture the bounce dynamics and include deleptonization which – in combination with the EoS and centrifugal effects – controls the mass of the inner core.

As full 3D Boltzmann neutrino transport is, as outlined above, computationally not yet feasible on today's HPC machines [152], the Basel code `ELEPHANT` encounters the deleptonization during the collapse phase with a simple and computationally efficient Y_e vs. ρ parametrization scheme of Liebendörfer [136]. It is based on data from detailed 1D radiation-hydrodynamics calculations [136].

The deleptonization scheme is based on the observation that the $Y_e(\rho, t)$ is only very weakly dependent on time during the collapse phase of the iron core, as shown in fig. 2.12. A microphysically consistent Y_e can be obtained during collapse in a hydrodynamical simulation with high precision from a tabulated [7], time-independent $\overline{Y}_e(\rho) = Y_e(\rho, t = t_b)$ that is based on computationally expensive radiation hydrodynamics calculations in spherical symmetry. Moreover, Liebendörfer [136] has shown that in spherical symmetry such a parametrization yields microphysical and thermodynamical conditions at core bounce to within $\sim 5\%$ of those obtained with a detailed radiation-hydrodynamics simulation. Note that the parametrization of the deleptonization during the collapse relies much more on the local density evolution than on the global geometry. Hence, applying the Y_e parametrization for rotating models as well is likely to be almost as accurate as for spherically symmetric models. However, note that the applicability of the scheme in highly asymmetric situations has not been numerically investigated up to now, because their assessment would require corresponding reference simulations with multidimensional neutrino

---

[7] Alternatively, a fitting formula which may replace a Y_e-table is provided in [136].

transport [136].
Following [136], the implementation of an electron fraction evolution along $\overline{Y}_e$ is achieved by

$$\frac{\delta Y_e}{\delta t} = \frac{\min\left(0, \bar{Y}_e\left(\rho\left(t+\delta t\right)\right) - Y_e\left(t\right)\right)}{\delta t}, \tag{2.147}$$

where $\delta/\delta t$ denotes a Lagrangian change in a fixed mass element, and where $\overline{Y}_e\left(\rho(t+\delta t)\right)$ is the parametrized Y_e interpolated in $\log_{10}\rho$ to update the density at $t+\delta t$. The minimum function guarantees that the electron fraction decreases monotonously even if transient instances occur in which the parametrized $\overline{Y}_e$ is larger than the actual $Y_e(t)$. This happens, as can be seen in fig. 2.12, at the beginning of Liebendörfer's computation. The deleptonization sets in slowly after a short time of adiabatic compression during which the original electron fraction profile moves to the right in the $\rho - Y_e$ plane to join the bounce profile, $\overline{Y}_e$. Note that eq. 2.147 is implemented in an operator-splitted manner from the 3D MHD update.

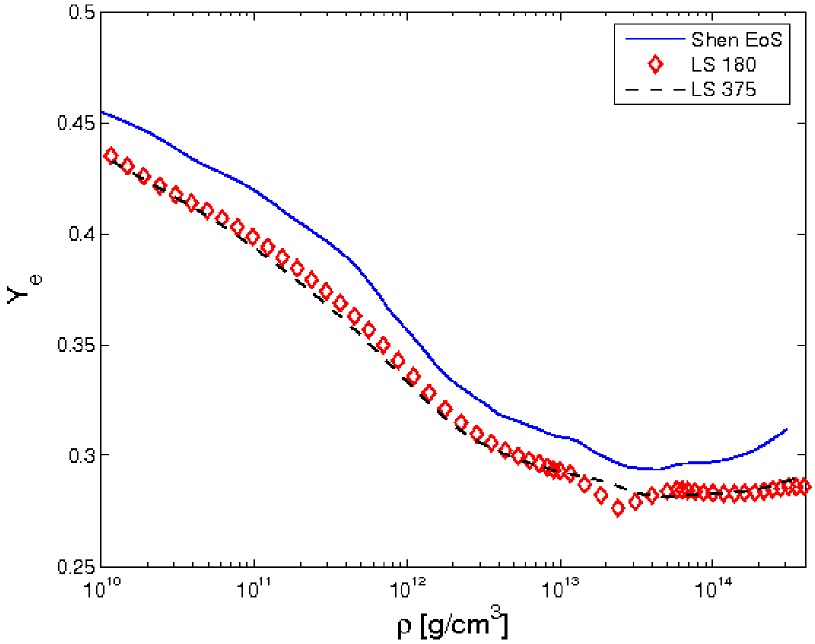

Figure 2.13: Electron fraction Y_e as a function of density, obtained from detailed general relativistic, spherically symmetric three-flavour Boltzmann neutrino transport. The calculations were carried out using a $15M_\odot$ progenitor from [258] a finite temperature EoS of either [130] or [215], and the `Agile-Boltztran`-code [133]. In the figure, we denote the LS EoS version with a compressibility of 180MeV as LS180, the one carried out with 375MeV as LS375. The Shen EoS is named as such.

For the computations I carried out and which are presented in chap. 3 and 4, I use Y_e-tables obtained with the `Agile-Boltztran` code [134], including either the Lattimer-Swesty [130] or the Shen EoS [215] and the electron capture rates from [36] (processes 2.107-2.113) plus the reactions 2.114 and 2.115 (T. Fischer (2010), private communication). Exemplary $Y_e(\rho)$ profiles from the Lattimer-Swesty [130] and the Shen EoS [215] are shown in fig. 2.13. The offset between the Y_e profiles from the LS- and the Shen EoS is consistent with the different asymmetry energies of the two EoS. This in turn is reflected in different neutrino reaction rates and thus a different Y_e at a given density. These effects have been discussed in [222] and [74] for massive progenitor stars in the range of 40-50$M_\odot$.

Entropy changes during the collapse phase

Electron capture during collapse not only reduces Y_e, but also affects matter entropy. The baryons are in NSE and the electrons in thermal equilibrium. Changes in the entropy per baryon (δs) are then determined by the chemical potentials μ_n, μ_p and μ_e of neutrons, protons and electrons, respectively. The resulting energy transfer between matter and neutrinos, δq, has to be taken into account (see, e.g., [29, 37]):

$$T\delta s = -\delta Y_e \left(\mu_e - \mu_n + \mu_p\right) + \delta q \; , \tag{2.148}$$

where T is the fluid temperature. Depending on matter density and the energy, produced neutrinos can, as pointed out earlier, either (1) escape freely without further interactions, (2) thermalize and escape, or (3) be trapped for longer than the dynamical timescale. In regime (1), which prevails at densities $\lesssim 10^{11}$ gcm^{-3} [29], the energy transfer is $\delta q = \delta Y_e \left\langle E_\nu^{escape}\right\rangle$, where $\left\langle E_\nu^{escape}\right\rangle$ is the average energy of the freely escaping neutrino [29]. Thus,

$$T\delta s = -\delta Y_e \left(\mu_e - \mu_n + \mu_p - \left\langle E_\nu^{escape}\right\rangle\right) . \tag{2.149}$$

Since $\left\langle E_\nu^{escape}\right\rangle > \mu_e - \mu_n + \mu_p$, the entropy of the fluid decreases in regime (1). However, since the energy of the escaping neutrinos is only marginally larger than $\mu_e - \mu_n + \mu_p$ due to the average Q-value of the nuclei at $\sim$ 3MeV (see, e.g., [37] and eq. 2.128), the resulting entropy change is small and thus neglected here in case (1). In regime (2), between $\sim 2 \times 10^{11}$gcm^3 and the density threshold for neutrino trapping around $\sim 2 \times 10^{12}$gcm^3, the neutrino mean free path is reduced by coherent scattering off heavy nuclei. The increasing matter density causes the electron chemical potential to rise, resulting in the production of neutrinos at higher energies compared to regime (1). Since the neutrino mean free path scales as E_ν^{-2}, thermalization to low energies provides the fastest way of escape. This thermalization process leads to a mean final escape energy of the order of $\sim$ 10MeV [150]. For the parametrization of the entropy changes, Liebendörfer suggests using $E_\nu^{escape} = 10$ MeV as a constant parameter that defines where regime (2) begins, namely when the inequality $\mu_e - \mu_n + \mu_p - E_\nu^{escape} > 0$ holds true. Hence, the entropy increases according to

$$\frac{\delta s}{\delta t} = -\frac{\delta Y_e}{\delta t} \frac{\mu_e - \mu_n + \mu_p - E_\nu^{escape}}{T} , \tag{2.150}$$

where $\delta Y_e / \delta t$ is given by eq. 2.147. At even higher densities in regime (3), the neutrinos are no longer able to escape before the postbounce neutronization burst. Hence, β-equilibrium prevails (the neutrinos are in equilibrium with the fluid) and δq in eq. 2.148 can be determined by the neutrino chemical potential $\delta q = \delta Y_e \mu_\nu$ [136].

Since $\mu_e + \mu_p = \mu_n + \mu_\nu$ in β-equilibrium, δs follows. Thus, in regime (3), no further entropy changes are taken into account. Note again that the entropy changes are updated in an operator-splitted manner.

Neutrino stress and neutrino pressure

In the optically thick regime (3), the neutrinos are trapped inside the PNS and their diffusion timescale is longer than the hydrodynamical timescale [134, 150]. The neutrinos now form a normal (Fermi-) gas component without transport abilities within the fluid, giving the pressure

$$p_\nu = \frac{4\pi}{3\left(hc\right)^3} \left(kT\right)^4 F_3\left(\frac{\mu_\nu}{kT}\right) , \tag{2.151}$$

where the neutrino chemical potential is given by $\mu_\nu = \mu_e - \mu_n + \mu_p$. $F_n\left(\eta\right) = \int_0^\infty x^n \left(e^{x-\eta} + 1\right)^{-1} dx$ is the Fermi-Dirac function of order n. F_3 then is given by the expression of [196]:

$$F_3\left(\eta\right) \simeq \frac{1}{4}\left(\eta^4 + 2\pi^2\eta^2 + \frac{7\pi^4}{15}\right) - \frac{7\pi^4}{120}e^{-\eta} , \tag{2.152}$$

where $\eta = \mu/kT$. Note that eq. 2.151 considers only the pressure originating from electron neutrinos. In principle, both electron and anti-electron neutrinos should be considered in this stage of the collapse. This would require a term $\left[F_3\left(\eta\right) + F_3\left(-\eta\right)\right]$ instead of $F_3\left(\eta\right)$ [8]. However, as the anti-electron neutrino fraction is several orders of magnitudes smaller than the electron neutrino fraction during collapse and bounce, we may neglect their contribution. The neutrino stress then is approximately given by the gradient of the neutrino pressure,

$$\frac{d\mathbf{v}}{dt} = -\frac{\nabla p_\nu}{\rho} = -4\pi r^2 \frac{\partial p_\nu}{\partial m} , \tag{2.153}$$

where $d\mathbf{v}/dt$ is the Lagrangian time derivative of the velocity, the term in the middle the general expression, and the term on the right the spherically symmetric limit based on enclosed mass $m(r)$ at radius r.

In the optically semi-transparent and transparent regimes ($\rho < \rho_{trap}$), the procedure to calculate the neutrino stress is computationally more intensive and less straightforward than in regime (3). Thus, I outline only how the neutrino stress is computed. For details of the derivation, I refer to Liebendörfer [136].

At $\rho < \rho_{trap}$, a first-order estimate for the neutrino stress relies on arguments based on the neutrino number luminosity, spherical symmetry, the assumption that neutrinos leave isotropically and without time delay from the locations of deleptonization, and the requirement of lepton conservation. With all these assumptions, the neutrino stress (in spherical symmetry) can be expressed by

$$\frac{dv}{dt} = \frac{CL}{4\pi r^2} \max\left[\left(kT\right)^3 \frac{F_5\left(\frac{\mu_\nu}{kT}\right)}{F_2\left(\frac{\mu_\nu}{kT}\right)}, \left(E_\nu^{escape}\right)^3 \frac{F_2^2\left(0\right) F_5\left(0\right)}{F_3^3\left(0\right)}\right] , \tag{2.154}$$

---

[8] In β-equilibrium, electron and anti-electron neutrinos have equal chemical potentials with the opposite sign.

where r, T, $\mu_\nu \equiv \mu_e - \mu_n + \mu_p$ and the neutrino number luminosity L represent the local values at the point where dv/dt is evaluated. An estimate of L (in spherical symmetry) is given by

$$L(r) = -\int_0^{m(r)} \frac{\delta Y_e}{\delta t} N_A dm \ , \tag{2.155}$$

where Avogadro's number is denoted by N_A and $\delta Y_e/\delta t$ is given by eq. 2.147. The constant C is defined such that it attaches regime (3) to regime (2):

$$C = -4\pi r^2 \frac{\partial p_\nu}{\partial m} \left[(kT)^3 \frac{F_5(\mu_\nu/kT)}{F_2(\mu_\nu/kT)} \frac{L}{4\pi r^2} \right]^{-1} . \tag{2.156}$$

In eq. 2.156, r, $\partial p_\nu/\partial m$, T, μ_ν, and L are evaluated at the transition density ρ_{trap}. Finally, the Fermi integrals F_3 and F_5 can be evaluated by [196]:

$$\begin{aligned} F_3(\eta) &\simeq \frac{1}{4}\left(\eta^4 + 2\pi^2\eta^2 + \frac{7\pi^4}{15}\right) - \frac{7\pi^4}{120} e^{-\eta} \ , \\ F_5(\eta) &\simeq \frac{1}{6}\left(\eta^6 + 5\pi^2\eta^4 + 7\pi^4\eta^2 + \frac{31\pi^6}{21}\right) - \frac{31\pi^6}{252} e^{-\eta} \ . \end{aligned} \tag{2.157}$$

As the expressions for the neutrino stress in the optically thin regime is only valid in spherical symmetry, Liebendörfer [136] recommends for multi-D simulations to use spherically averaged conditions of the multidimensional configurations to evaluate the neutrino stress. This approach is justified by the fact that neutrino pressure contributions are already small at the transition density ($\lesssim 5 - 10\%$ of the fluid pressure).

Limitations of the parametrization scheme

There is a minor i) and a major ii) limitation of the parametrization scheme: i) The present deleptonization scheme cannot capture the slight increase of Y_e around core bounce (see fig. 2.12), which is due to increasing neutron degeneracy at very high densities. In the density regime where neutrinos are trapped and β-equilibrium prevails, Y_l is conserved/constant; hence, Y_e should be obtained by a weak equilibrium calculation. A parametrization of the lepton fraction Y_l instead of the electron Y_e fraction would improve this, as it allows for a more consistent Y_e at nuclear densities. However, such a treatment would also lead to a significant increase in the computational complexity of the scheme [136]. The major limitation ii) of the parametrization is its inability to capture any postbounce neutrino effects such as the neutronization burst (see fig. 2.14), which occurs when the shock reaches the electron-neutrinosphere.

2.4.3 The isotropic diffusion source approximation IDSA

Around core bounce, the neutrino parametrization scheme, described above, breaks down as it cannot model the neutronization burst (see fig. 2.14). After core bounce, the neutrino transport is tracked via a partial (i.e., a leakage scheme) or a full

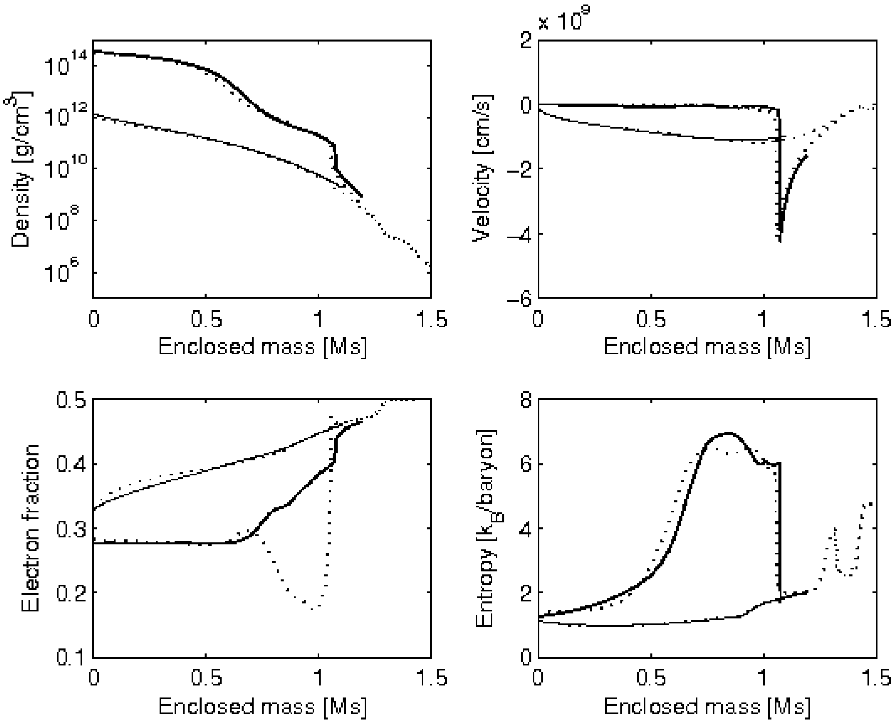

Figure 2.14: The figure shows the comparison of the almost non-rotating 3D model R1E1CA (see sec. 3.2) with the spherically symmetric model G15 (see Liebendörfer et al. [134]), which is based on general relativistic three-flavour Boltzmann neutrino transport. From the upper left to the lower right we compare as a function of enclosed mass: the density, the velocity, the Y_e, and the entropy profiles. The solid lines show the results of model R1E1CA (cf. chap. 3) and the dotted lines the results of model G15. The thin lines represent a time instance at 5ms before bounce and the thick lines represent a time instance at 5ms after bounce. Excellent agreement is found in all four quantities – with one exception. The parametrised neutrino leakage scheme cannot model the neutronization burst, which causes a prominent Y_e-dip and additional cooling in the G15 data.

implementation of the so-called Isotropic Diffusion Source Approximation (IDSA) [140]. Note that the IDSA, contrary to the parametrization scheme outlined above, is a general concept of radiative transfer, applicable to all sorts of problems where matter interacts with radiation or transported particles. However, as our target application is the neutrino transport in stellar core collapse, we will only discuss the IDSA in this particular context.

As a basic concept, the IDSA decomposes the distribution function f of a given neutrino species into two components, an isotropic, trapped component f^t and a streaming component f^s, representing neutrinos of a given species and energy which find the local zone opaque or transparent, respectively. The total distribution function is the sum of the two components, $f = f^t + f^s$. One particle species (in the current implementation either the ν_e or $\overline{\nu}_e$ neutrino) is allowed to have a component that evolves in the hydrodynamical limit, while another component of the same particle species is treated by radiative transfer techniques. Moreover, the two components are coupled by a *diffusion source* term Σ. The source term Σ converts trapped particles into streaming particles and vice versa. It can be determined from the requirement that the temporal change of f^t has to reproduce the diffusion limit within the limit of a small mean free path.

The Boltzmann transport equation can then be written in terms of a linear operator $D\,()$ describing particle propagation, $D\,(f = f^{\mathrm{t}} + f^{\mathrm{s}}) = C$, where $C = C^{\mathrm{t}} + C^{\mathrm{s}}$ is a suitable decomposition of the collision integral according to the coupling to the trapped (C^{t}) or streaming (C^{s}) particle components. Consequently, we have to solve the following set equations for the individual components in a operator-split manner:

$$
\begin{aligned}
D\left(f^{\mathrm{t}}\right) &= C^{\mathrm{t}} - \Sigma &\quad (2.158)\\
D\left(f^{\mathrm{s}}\right) &= C^{\mathrm{s}} + \Sigma. &\quad (2.159)
\end{aligned}
$$

Application of the IDSA to the $\mathcal{O}(v/c)$ Boltzmann transport equation in spherical symmetry

For the time being, in our current implementation of the IDSA the linear operator $D\,()$ in eqs. 2.158 and 2.159 represents the $\mathcal{O}(v/c)$ Boltzmann transport equation (cf. eq. 2.106) of massless fermions in spherical symmetry (see [50, 153]). It reads

$$
\begin{aligned}
\frac{df}{cdt} &+ \mu\frac{\partial f}{\partial r} + \left[\mu\left(\frac{d\ln\rho}{cdt} + \frac{3v}{cr}\right) + \frac{1}{r}\right]\left(1-\mu^2\right)\frac{\partial f}{\partial \mu}\\
&+ \left[\mu^2\left(\frac{d\ln\rho}{cdt} + \frac{3v}{cr}\right) - \frac{v}{cr}\right]E\frac{\partial f}{\partial E}\\
&= \underbrace{j\,(1-f)}_{emission} - \underbrace{\chi f}_{absorption} + \frac{E^2}{c\,(hc)^3}\\
&\times \left[\underbrace{(1-f)\int Rf'd\mu'}_{isoenergetic\quad \text{`}inscattering'} - \underbrace{f\int R\,(1-f')\,d\mu'}_{isoenergetic\quad \text{`}outscattering'}\right] \qquad (2.160)
\end{aligned}
$$

and describes the propagation of massless fermions at the speed of light c, with respect to a compressible background with a rest mass density ρ. Note that in this subsection, for sake of simplicity, I follow the conventions used by Liebendörfer et al. [140], who uses for energy the variable E instead of ω (cf. sec. 2.4.1).

The particle distribution function $f\,(t, r, \mu, E)$ depends on the time, t, radius, r, and the momentum phase space spanned by the angle cosine, μ, of the particle propagation direction with respect to the radius and the particle energy, E. The momentum phase space variables are measured in the frame co-moving with the background matter, which moves with velocity v with respect to the laboratory frame. The Lagrangian time derivative (see, e.g. [127]) in the co-moving frame is denoted by df/dt. The derivatives $\partial f/\partial \mu$ and $\partial f/\partial E$ in eq. 2.160 are also taken co-moving with a fluid element. On the right hand side of eq. 2.160, a particle emissivity, j, and a particle absorptivity, χ, as well as an isoenergetic scattering kernel, R, are included. All blocking factors $(1-f)$ in eq. 2.160 are explicitly written out to ease the identification of in-scattering and out-scattering terms. The abbreviation f' refers to $f(t, r, \mu', E)$, where μ' is the angle cosine over which the integration is performed. Note that currently the inelastic scattering process is neglected. Furthermore, note that the current implementation only considers ν_e and $\overline{\nu}_e$ neutrinos. The particle density is given by an integration of the distribution function over the momentum phase space,

$$n(t, r) = 4\pi/(hc)^3 \int f(t, r, \mu, E)\, E^2 dE d\mu, \qquad (2.161)$$

where h denotes Plancks constant.

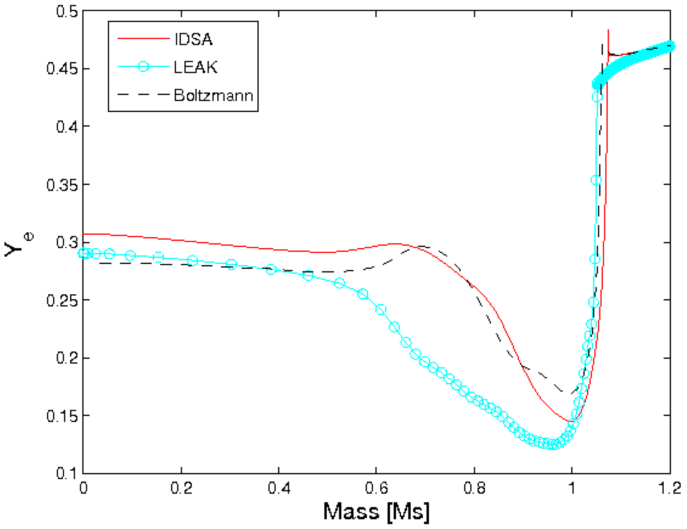

Figure 2.15: Comparison of the spherically averaged Y_e profiles of models R0E1CA$_L$ (circled line, '$LEAK'$', see sec. 3.2), R0E1CA$_{IDSA}$ (solid line, '$IDSA'$', see sec. 3.2) with the spherically symmetric model G15 (dashed line, '$Boltzmann'$') as a function of the enclosed mass at 5ms after bounce. Model G15 is based on general relativistic three-flavour neutrino transport [134]. Note that our leakage scheme significantly overestimates the deleptonization in and around the neutrinosphere region, as it neglects any absorption of transported neutrinos by discarding the streaming component ($f^s = 0$).

Time-evolution of the trapped and the streaming particle distributions

We assume that the 'trapped' and the 'streaming' particle components of the neutrino distribution function $f = f^{\mathrm{t}} + f^{\mathrm{s}}$ evolve separately according to eq. 2.160, coupled by a source term Σ. Hence, the evolution of the trapped particle component f^t can be written as

$$\begin{aligned}\frac{df^{\mathrm{t}}}{cdt}+\mu\frac{\partial f^{\mathrm{t}}}{\partial r} &+ \left[\mu\left(\frac{d\ln\rho}{cdt}+\frac{3v}{cr}\right)+\frac{1}{r}\right]\left(1-\mu^2\right)\frac{\partial f^{\mathrm{t}}}{\partial\mu}\\ &+ \left[\mu^2\left(\frac{d\ln\rho}{cdt}+\frac{3v}{cr}\right)-\frac{v}{cr}\right]E\frac{\partial f^{\mathrm{t}}}{\partial E}\\ &= j-\left(j+\chi\right)f^{\mathrm{t}}-\Sigma\\ &+ \frac{E^2}{c\left(hc\right)^3}\left[\int Rf^{\mathrm{t}\prime}d\mu'-f^{\mathrm{t}}\int Rd\mu'\right]. \qquad (2.162)\end{aligned}$$

Since we assume that $f^{\mathrm{t}}=f^{\mathrm{t}}\left(t,r,E\right)$, and the source function, $\Sigma=\Sigma\left(t,r,E\right)$, are isotropic, an angular integration of eq. 2.162 over μ simplifies this equation to

$$\frac{df^{\mathrm{t}}}{cdt}+\frac{1}{3}\frac{d\ln\rho}{cdt}E\frac{\partial f^{\mathrm{t}}}{\partial E}=j-\left(j+\chi\right)f^{\mathrm{t}}-\Sigma\,. \qquad (2.163)$$

In the hydrodynamical limit, i.e. fast-moving particles with a very short transport mean free path, the trapped particle distribution function f^{t} has to reproduce the diffusion limit [140]. In the framework of the IDSA, the diffusive drain (or replenishment) of trapped particles is accounted by means of a source term Σ. Comparing 2.163 with the diffusion limit of the Boltzmann equation [154,140] yields the following source term:

$$\Sigma=\frac{1}{r^2}\frac{\partial}{\partial r}\left(\frac{-r^2\lambda}{3}\frac{\partial f^{\mathrm{t}}}{\partial r}\right)+\left(j+\chi\right)\frac{1}{2}\int f^{\mathrm{s}}d\mu\,, \qquad (2.164)$$

where $\lambda=1/\left(j+\chi+\phi\right)$ is the mean free path and ϕ the opacity. Note that isoenenergetic scattering enters eq. 2.164 only implicitly via ϕ. The additional term $\left(j+\chi\right)/2\int f^{\mathrm{s}}d\mu$ in eq. 2.164 accounts for the absorption of streaming particles in matter; its necessity is visualized in fig. 2.16.

Note that the IDSA does not allow for the possibility of a direct emission of matter into the streaming particle component. This can be tracked more easily by a large conversion rate Σ of trapped particles. Moreover, Liebendörfer et al. [140] suggest accounting the streaming particles that are absorbed by matter in the manner represented by the arrow labelled by $\left(j+\chi\right)f^{\mathrm{s}}$ in fig. 2.16. In the diffusion limit, the net particle exchange of the fluid element with its environment, $\Sigma-\left(j+\chi\right)/2\int f^{\mathrm{s}}d\mu$, must then correspond to the diffusion term (cf. [140], their eq. A10). This is the case for the choice of Σ in eq. (2.164).

In order to guarantee that eq. 2.164 delivers consistent, ‘physical’ particle fluxes in the entire computational domain, limiters must be applied. As a limit in the transparent region, the diffusion source is thus set to $\Sigma\leq j$. If the diffusion source and emissivity reach equality, the matter absorptivity $-\left(j+\chi\right)f^{\mathrm{t}}$ removes remaining trapped particles while all newly emitted ones are directly converted to streaming particles that escape the fluid element. With this limit imposed, the net interaction of particles with matter in fig. 2.16 has the correct limit for large mean free paths, $j-\left(j+\chi\right)f^{\mathrm{s}}$. The lower boundary is chosen to fulfill the requirement

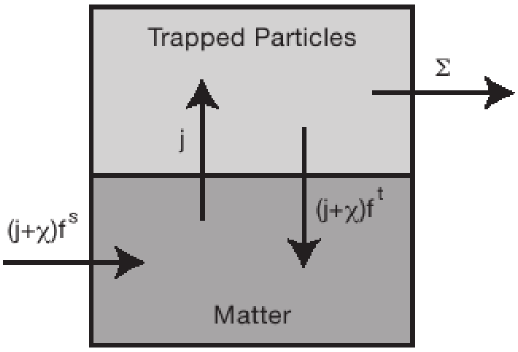

Figure 2.16: The shaded box schematically represents a fluid element in the diffusion source approximation. It contains matter (lower part) and trapped radiation particles (upper part). The interaction with other fluid elements can only occur through the exchange of streaming particles or the combined hydrodynamics of matter and trapped particles. Thus, streaming particles can be absorbed in matter at the rate $(j+\chi)\, f^{\mathrm{s}}$ and trapped particles are converted to streaming particles at the rate Σ. Within the fluid element, matter emits trapped particles at the rate j and absorbs trapped particles at the rate $(j+\chi)\, f^{\mathrm{t}}$. The emissivity in the absorption term originates from the identity $j\,(1-f)-\chi f = j-(j+\chi)\, f$, which hides the Pauli blocking factor in the absorption term. Figure taken from [140].

$f^{\mathrm{t}} \leq j/\,(j+\chi)$, where $j/\,(j+\chi)$ represents the equilibrium distribution function. This in consequence leads to the requirement $\Sigma \geq 0$. Therefore, the net absorption of particles in a fluid element cannot exceed $(j+\chi)\, f^{\mathrm{s}}$ (cf. fig. 2.16).
In a compact notation, the diffusion source is limited as follows:

$$\begin{aligned} \Sigma &= \min\left\{\max\left[\alpha+(j+\chi)\,\frac{1}{2}\int f^{\mathrm{s}}d\mu, 0\right], j\right\} \\ \alpha &= \frac{1}{r^2}\frac{\partial}{\partial r}\left(\frac{-r^2}{3\,(j+\chi+\phi)}\frac{\partial f^{\mathrm{t}}}{\partial r}\right). \end{aligned} \tag{2.165}$$

Having discussed the time evolution of the trapped particle distribution component, we now turn our attention to the evolution of the streaming component f^{s}. The starting point for its temporal evolution is again eq. 2.160:

$$\begin{aligned} \frac{df^{\mathrm{s}}}{cdt} &+ \mu\frac{\partial f^{\mathrm{s}}}{\partial r}+\left[\mu\left(\frac{d\ln\rho}{cdt}+\frac{3v}{cr}\right)+\frac{1}{r}\right]\left(1-\mu^2\right)\frac{\partial f^{\mathrm{s}}}{\partial\mu} \\ &+ \left[\mu^2\left(\frac{d\ln\rho}{cdt}+\frac{3v}{cr}\right)-\frac{v}{cr}\right]E\frac{\partial f^{\mathrm{s}}}{\partial E} \\ &= -\,(j+\chi)\, f^{\mathrm{s}}+\Sigma+\frac{E^2}{c\,(hc)^3}\left[\int R f^{\mathrm{s}\prime}d\mu'-f^{\mathrm{s}}\int R d\mu'\right]. \end{aligned} \tag{2.166}$$

By design of the IDSA, the particle density of the streaming component is small compared to the trapped one in regions where scattering dominates the interactions. Hence, the scattering integrals on the right hand side of eq. 2.166 can be neglected. For reason of convenience, eq. 2.166 is transformed into the laboratory frame. Then, the temporal evolution of f^{s} reads

$$\frac{\partial \hat{f}^{\mathrm{s}}}{c\partial \hat{t}} + \hat{\mu}\frac{\partial \hat{f}^{\mathrm{s}}}{\partial r} \quad + \quad \frac{1}{r}\left(1-\hat{\mu}^2\right)\frac{\partial \hat{f}^{\mathrm{s}}}{\partial \hat{\mu}} = -\left(\hat{j}+\hat{\chi}\right)\hat{f}^{\mathrm{s}} + \hat{\Sigma}\,, \tag{2.167}$$

where the quantities carrying a hat are measured in the laboratory frame. Furthermore, it is assumed that the fluxes of free streaming particles reach stationary values much faster than the dynamical time scale of interest. Thus, the time-derivative can be dropped in the first term in eq. 2.167. If the source on the right hand side is assumed to be known from a consistent solution of eqs. 2.163 and 2.165, the integration of eq. 2.167 over angles leads to a Poisson equation for a potential ψ, whose gradient represents the particle flux:

$$\begin{aligned} \frac{\partial \psi}{\partial r} &= \frac{1}{2}\int \hat{f}^{\mathrm{s}}\hat{\mu}\, d\hat{\mu} \\ \frac{1}{r^2}\frac{\partial}{\partial r}\left(r^2\frac{\partial \psi}{\partial r}\right) &= \frac{1}{2}\int \left[-\left(\hat{j}+\hat{\chi}\right)\hat{f}^{\mathrm{s}} + \hat{\Sigma}\right] d\hat{\mu}\,. \end{aligned} \tag{2.168}$$

Finally, the streaming particle flux and particle density are, as suggested in [133], related by an expression which assumes that all particles of a given energy group are emitted isotropically at their corresponding scattering sphere:

$$\frac{1}{2}\int \hat{f}^{\mathrm{s}}(E)\, d\hat{\mu} = \frac{2\frac{\partial \psi}{\partial r}(E)}{1+\sqrt{1-\left(\frac{R_\nu(E)}{\max(r,R_\nu(E))}\right)^2}}\,, \tag{2.169}$$

where $R_\nu(E)$ is the radius of the monochromatic scattering sphere, i. e. the neutrinosphere, that depends on the particle energy E. The radial position of the neutrinosphere is usually defined as the surface where the neutrino's optical depth reaches

$$\tau(r, E_\nu) = \int_{R_\nu(E)}^{\infty} \frac{dr}{\lambda_{\nu,E_\nu}} = \frac{2}{3}. \tag{2.170}$$

The neutrinosphere is the effective radiating surface for neutrinos, in analogy to the 'photosphere' of normal light emitting surfaces. Note that its position differs from neutrino species to species and is dependent on the neutrino energy. Moreover, note also that τ is used to discriminate between f^{t} and f^{s} at the neutrinosphere.

In order to solve for both the trapped and the streaming particle component, the quantities must be Lorentz-boosted from the laboratory frame to the co-moving frame and vice versa . However, in the current implementation of the IDSA, where we run our simulations in the Newtonian limit, the required transformations are neglected. Hence, we refer the reader to [140] and [155], where the details of the necessary Lorentz transformation can be found in their full glory.

The coupling of the IDSA with hydrodynamics

The neutrino distribution function must be somehow coupled to the dynamics of the background matter. The latter can be described by the conservation laws of hydrodynamics (see sec. 2.2, and [155]). In spherical symmetry for example, this set of equation results in

$$\frac{\partial}{\partial t}U + \frac{\partial}{r^2 \partial r}\left(r^2 F\right) = 0 \; , \tag{2.171}$$

where U is a vector of primitive variables and F a vector of fluxes.
In the IDSA, the following approach is taken: since the characteristic timescale of the local reactions between the transported particles is faster than the diffusion timescale, which is of order [155]

$$t_{diff} \sim \frac{l^2}{2c\lambda} \; , \tag{2.172}$$

(where λ is the mean free path, l characteristical length, i. e. the size of a computational domain, and c the speed of light), the neutrino spectrum can be approximated by a thermal spectrum:

$$\begin{aligned} Y^{\mathrm{t}} &= \frac{m_{\mathrm{b}}}{\rho}\frac{4\pi}{(hc)^3}\int f^{\mathrm{t}} E^2 dE d\mu \\ Z^{\mathrm{t}} &= \frac{m_{\mathrm{b}}}{\rho}\frac{4\pi}{(hc)^3}\int f^{\mathrm{t}} E^3 dE d\mu \; , \end{aligned} \tag{2.173}$$

where m_b in our application is the baryon rest mass of the background matter, Y^{t} and Z^{t} a particle number fraction and a particle mean specific energy, respectively. Note that this assumption is only made for the trapped particle component within a fluid element. The streaming particles, which communicate between fluid elements, keep their detailed spectral information. The measure taken in eq. 2.173 reduces the number of variables to describe the distribution functions of the trapped particles drastically.
We can now rewrite the evolution equation 2.162 for the trapped particle component with an Eulerian time derivative and use the continuity equation to substitute the $d\ln\rho/dt$ term by the velocity divergence,

$$\begin{aligned} \frac{\partial f^{\mathrm{t}}}{c\partial t} &+ \frac{\partial}{r^2\partial r}\left(r^2\frac{v}{c}f^{\mathrm{t}}\right) - \frac{\partial}{r^2\partial r}\left(r^2\frac{v}{c}\right)\frac{\partial\left(E^3 f^{\mathrm{t}}\right)}{3E^2\partial E} \\ &= j - (j+\chi) f^{\mathrm{t}} - \Sigma \; . \end{aligned} \tag{2.174}$$

If we now perform the energy integrals which appear in eq. 2.173 on 2.174, we obtain the following evolution equations for Y^{t} and Z^{t}:

$$\begin{aligned} &\frac{\partial}{\partial t}\left(\rho Y^{\mathrm{t}}\right) + \frac{\partial}{r^2\partial r}\left(r^2 v\rho Y^{\mathrm{t}}\right) \\ &\qquad = m_{\mathrm{b}}\frac{4\pi c}{(hc)^3}\int\left[j - (j+\chi) f^{\mathrm{t}} - \frac{1}{2}\int \Sigma d\mu\right]E^2 dE \; , \end{aligned} \tag{2.175}$$

and

$$\frac{\partial}{\partial t}\left(\rho Z^{\mathrm{t}}\right)+\frac{\partial}{r^2\partial r}\left(r^2 v\rho Z^{\mathrm{t}}\right)+\frac{\partial}{r^2\partial r}\left(r^2 v\right)\frac{\rho Z^{\mathrm{t}}}{3} \\ = m_{\mathrm{b}}\frac{4\pi c}{\left(hc\right)^3}\int\left[j-\left(j+\chi\right)f^{\mathrm{t}}-\Sigma\right]E^3 dE \; . \quad (2.176)$$

The equation for Z^{t} corresponds to an energy equation with a pdV term for the radiation pressure $\rho Z^{\mathrm{t}}/3$ on the left hand side. Moreover, and in analogy to an entropy equation, it can be transformed into a conservative form for the evolution of $\left(\rho Z^{\mathrm{t}}\right)^{3/4}$. Therefore, one can solve the advective part, i.e. the left hand side of eq. 2.176 together with the hydrodynamical conservation law (eq. 2.171) expressed by the following primitive variables:

$$U=\begin{pmatrix}\rho\\ \rho v\\ \rho\left(e+\frac{1}{2}v^2\right)\\ \rho Y_{\mathrm{e}}\\ \rho Y_l^{\mathrm{t}}\\ \left(\rho Z_l^{\mathrm{t}}\right)^{\frac{3}{4}}\end{pmatrix}, \quad F=\begin{pmatrix}v\rho\\ v\rho v+p\\ v\rho\left(e+\frac{1}{2}v^2+\frac{p}{\rho}\right)\\ v\rho Y_{\mathrm{e}}\\ v\rho Y_l^{\mathrm{t}}\\ v\left(\rho Z_l^{\mathrm{t}}\right)^{\frac{3}{4}}\end{pmatrix}, \quad (2.177)$$

where p is the fluid pressure, e the fluid specific internal energy, and Y_{e} the electron fraction. The index l stands for the different species of trapped particles, i.e. the ν_e and $\overline{\nu}_e$ neutrinos in the current implementation.

The distribution function of trapped particles in thermal equilibrium, $f_l^{\mathrm{t}}\left(E\right)=\left\{\exp\left[\beta_l\left(E-\mu_l\right)\right]+1\right\}^{-1}$, has two free parameters β_l and μ_l. Hence, it can be reconstructed in such a way that eq. 2.173 is fulfilled for the new/updated values of Y_l^{t} and Z_l^{t}. Subsequently, the remaining update of the trapped particle distribution in eq. 2.174 is given by

$$\frac{\partial f_l^{\mathrm{t}}}{c\partial t}=j_l-\left(j_l+\chi_l\right)f_l^{\mathrm{t}}-\Sigma_l \; . \quad (2.178)$$

Equation 2.178 also determines the net reaction rates,

$$s_l=j_l-\left(j_l+\chi_l\right)\left(f_l^{\mathrm{t}}+f_l^{\mathrm{s}}\right) \; , \quad (2.179)$$

between matter and the radiation particles, which leads to the following changes of the electron fraction and internal specific energy:

$$\begin{aligned} s_l &= \frac{\partial f_l^{\mathrm{t}}}{c\partial t}+\Sigma_l-\left(j_l+\chi_l\right)\frac{1}{2}\int f_l^{\mathrm{s}}d\mu && (2.180)\\ \frac{\partial Y_{\mathrm{e}}}{c\partial t} &= -\frac{m_{\mathrm{b}}}{\rho}\frac{4\pi c}{\left(hc\right)^3}\int\left(s_{\nu_{\mathrm{e}}}-s_{\bar{\nu}_{\mathrm{e}}}\right)E^2 dE && (2.181)\\ \frac{\partial e}{c\partial t} &= -\frac{m_{\mathrm{b}}}{\rho}\frac{4\pi c}{\left(hc\right)^3}\int\left(s_{\nu_{\mathrm{e}}}+s_{\bar{\nu}_{\mathrm{e}}}\right)E^3 dE \; . && (2.182)\end{aligned}$$

The changes in electron fraction Y_e and specific energy e feed back into the emissivity j and absorptivity χ used in eq. 2.178. Once a consistent solution has been found, eq. 2.178 allows updates of the trapped particle fraction

$$\frac{\partial Y_l^{\mathrm{t}}}{\partial t} = \frac{m_{\mathrm{b}}}{\rho} \frac{4\pi c}{(hc)^3} \int \frac{\partial f_l^{\mathrm{t}}}{\partial t} E^2 dE \ , \tag{2.183}$$

of the trapped particle specific energy

$$\frac{\partial Z_l^{\mathrm{t}}}{\partial t} = \frac{m_{\mathrm{b}}}{\rho} \frac{4\pi c}{(hc)^3} \int \frac{\partial f_l^{\mathrm{t}}}{\partial t} E^3 dE \ , \tag{2.184}$$

and of the matter velocity, which is subject to radiation pressure.

$$\frac{\partial v}{\partial t} = -\frac{1}{\rho} \frac{\partial}{\partial r} \left(\frac{\rho Z_l^{\mathrm{t}}}{3 m_{\mathrm{b}}} \right) \ . \tag{2.185}$$

After updating Y_l^{t}, Z_l^{t} and v, the cycle of updates is completed by the solution of eqs. 2.168 and 2.169 for the distribution function f^{s} for streaming particles based on the sources determined in eqs. 2.178 and 2.165.

IDSA in 3D

So far I have only discussed the IDSA in spherical symmetry. However, the IDSA was in principle designed as a computationally efficient approximation to radiative transfer in multidimensional HD/MHD simulations. Thus, I will now sketch the basic measures required to extend the transport scheme from 1D to 3D. Note that a detailed discussion of the generalization of the IDSA to multi-D applications goes beyond the scope of my PhD thesis. For a partial discussion, I refer the reader to [140], sec. 4. The details about the implementation will follow in Whitehouse et al. (2010, in preparation).

To summarize, one could say that the difference between the 3D and 1D IDSA is only technical – scientifically the schemes are identical. The major difference is given by the fact that the streaming component is treated in spherical symmetry and the trapped component is done in full 3D.

When changing from 1D to 3D, the extension of the state vector U in the equations of hydrodynamics comes quite naturally, and differs from the 1D spherically symmetric one (see eq. 2.177) only by the velocity v, which becomes a vector $\vec{v} = (v_x, v_y, v_z)$. Using $i = 1 \ldots 3$ for the three spatial directions in the momentum equation, the corresponding 3D state vector U and flux vector F read

$$U = \begin{pmatrix} \rho \\ \rho v_i \\ \rho \left(e + \frac{1}{2} v^2 \right) \\ \rho Y_{\mathrm{e}} \\ \rho Y_l^{\mathrm{t}} \\ \left(\rho Z_l^{\mathrm{t}} \right)^{\frac{3}{4}} \end{pmatrix} , \quad F = \begin{pmatrix} \vec{v} \rho \\ \vec{v} \rho v_i + p \\ \vec{v} \rho \left(e + \frac{1}{2} v^2 + \frac{p}{\rho} \right) \\ \vec{v} \rho Y_{\mathrm{e}} \\ \vec{v} \rho Y_l^{\mathrm{t}} \\ \vec{v} \left(\rho Z_l^{\mathrm{t}} \right)^{\frac{3}{4}} \end{pmatrix} . \tag{2.186}$$

This state vector can be evolved by any standard hydrodynamics scheme that solves the multi-dimensional conservation law

$$\frac{\partial}{\partial t} U + \vec{\nabla} \cdot \vec{F} = 0 \, , \tag{2.187}$$

as outlined for example in sec. 2.2.

A more difficult part in the multi-dimensional IDSA is the consistent solution of eqs. 2.165 and 2.178-2.182. The difficulty arises from the non-local scalar

$$\alpha = \vec{\nabla} \cdot \left(\frac{-1}{3\left(j + \chi + \phi\right)} \vec{\nabla} f^{\mathrm{t}} \right) \tag{2.188}$$

in eq. 2.165. All the other equations are local and do not depend on the dimensionality of the problem, except that the integration over the angle cosine, $1/2 \int d\mu$, must be replaced by an integration over the entire solid angle of a sphere, $1/\left(4\pi\right) \int d\Omega$.

In the preliminary 3D IDSA implementation I got provided by S.C. Whitehouse, eq. 2.188 is calculated via f^{t} of the previous time step and update f^{t} locally with eqs. 2.178-2.182. Hence, only the local reactions are implemented implicitly while the diffusion part remains explicit. This approach is only conditionally stable and the time step must be restricted to $\Delta x^2 / \left(2\lambda c\right)$. The relevance of trapped particles diminishes in the transparent regime around $\lambda \sim \Delta x$. Thus, the time step restriction is of a similar order of magnitude as the CFL condition for the particle propagation speed c.

The result of this step determines a partial update of the compositional quantities in U and a spectral diffusion source $\Sigma_l\left(E\right)$ for each particle species l at each grid point. This information is stored for the following updates. The stationary-state solution for the streaming particle component is then in principle based on

$$\Delta\psi \;=\; \frac{1}{4\pi} \int \left[-\left(\hat{j} + \hat{\chi}\right) \hat{f}^{\mathrm{s}} + \hat{\Sigma} \right] d\hat{\Omega} \, , \tag{2.189}$$

which is the extension of eq. (2.168) to the multi-dimensional case. The integration over $d\hat{\Omega}$ is again performed over the solid angle of a sphere. Note that eq. 2.189 must be solved for each energy group and particle species separately. However, all directional information of the streaming particle flux $\vec{\nabla}\psi$ can then be retrieved from the corresponding scalar potential $\psi_l(\hat{E})$.

After the hydrodynamic update according to eq. 2.187, we have to convert the particle flux, $\vec{\nabla}\psi_l(\hat{E})$, into a streaming particle density. For nearly spherical problems such as ours, the simple spherically symmetric ansatz described above currently is applied to obtain an estimate of the flux factor. Once the spectral streaming particle density $1/\left(4\pi\right) \int f_l^{\mathrm{s}}\left(E\right) d\Omega$ has been determined by the quotient of $\vec{\nabla}\psi_l(\hat{E})$ and the flux factor, one cycle of updates in a multidimensional application is concluded, as shown in fig. 2.17, where a schematic view of the IDSA code and flow inside `ELEPHANT` is displayed.

Note that even though the procedure to extend the IDSA from 1D to multi-D was outlined in the pure hydrodynamical case, it is done in the same fashion also for MHD.

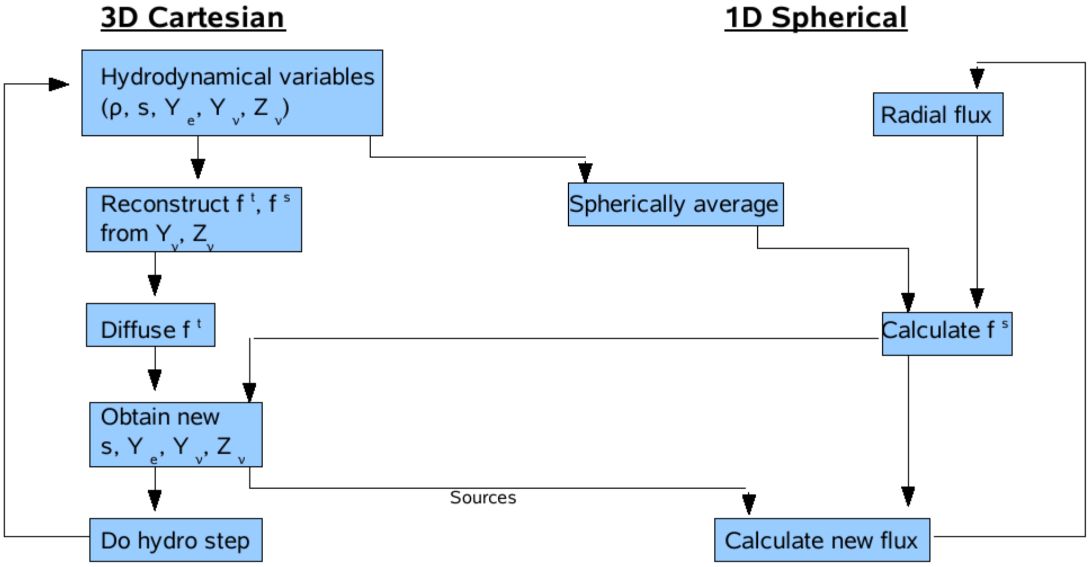

Figure 2.17: Schematic view of the IDSA code and flow inside `ELEPHANT` according to S.C. Whitehouse.

Current reactions implemented in the IDSA

The current implementation of the IDSA includes only electron flavour neutrinos. Their dominant emission and absorption reactions in the postbounce phase are given by electron and positron capture, as outlined in eqs. 2.107 and 2.108. The opacities in our implementation of the IDSA are given by isoenergetic scattering on nucleons and nuclei (eqs. 2.110 and 2.111). Note that all weak interactions are implemented as described in sec. 2.4.1. The thermodynamical state of matter as a function of density, ρ, temperature, T, and electron fraction, Y_{e}, is calculated by the LS EoS [130] or the Shen EoS [215].

In order to resolve the neutrino energy spectrum, we use, as suggested by S. W. Bruenn, 20 geometrically spaced energy zones to span the neutrino energy range between 3 and 300 MeV.

Planned IDSA upgrades

The IDSA includes at present only the dominant reactions relevant to the neutrino transport problem (see [140] for details). Future upgrades will also include contributions from electron-neutrino electron scattering (eq. 2.112). which are indispensable during the collapse phase. This reaction thermalizes the neutrinos very effectively (see, e.g., [37]), which in turn is important because the neutrino mean free paths vary inversely with the square of the neutrino energy ($\lambda \sim \frac{1}{E_{\nu}^{2}}$). Thus, it influences directly the size/mass of the inner core at bounce, which scales roughly proportional to the square of the electron fraction Y_e (and the entropy per baryon) [85]. The size/mass of the inner core in turn is the dynamically relevant quantity for the emission of GWs at core bounce [62]. Moreover, the inclusion of this reaction will

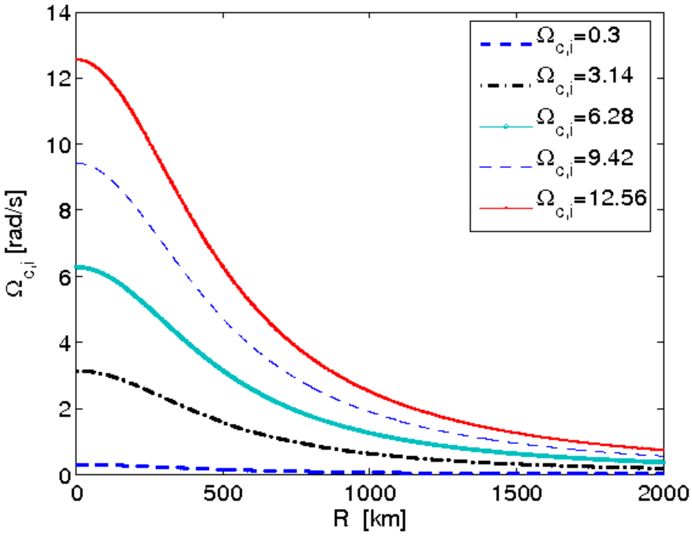

Figure 2.18: Comparison of different precollapse initial rotational configurations, set up according to eq. 2.190. Note that the displayed values of $\Omega_{c,i}$ were applied for models discussed in chap. 3. For the entire model set, I choose $A = 500$ km.

also make the cumbersome switch from the parametrization to the IDSA at bounce obsolete. Finally, there are ongoing efforts (A. Perego) to include μ and τ neutrinos. They are very important for the radial position of the shock wave and to the moment when it stops, before the 'revival' of the stalled shock wave sets in again, and the cooling of the PNS to its final stage as neutron star or black hole (see, e.g., [138,73], and reference therein).

2.5 Presupernova stellar models & initial model configurations

All presupernova stellar models available today stem from Newtonian 1D stellar evolution calculations and hence may not cover all possible states prior to the collapse of a multidimensional star. Therefore, we construct the initial conditions of our simulations by a parametric approach. We employ a solar-metallicity $15M_\odot$ progenitor star of [258]. Angular momentum is added to the presupernova model according to a shell-type constant j (j denotes specific angular momentum) rotation law of [67]:

$$\Omega(r) = \Omega_{i,c} \cdot \frac{A^2}{A^2 + r^2} = \begin{cases} \Omega_{c,i} & \text{for} \quad A \rightarrow \infty \\ \Omega_{c,i} \dfrac{A^2}{r^2} & \text{for} \quad A \rightarrow 0 \end{cases} , \qquad (2.190)$$

where we define $r = \sqrt{x^2 + y^2 + z^2}$ as spherical radius, and (x, y, z) as Cartesian coordinates.

The constant A is the degree of differential rotation that controls the steepness of the angular velocity profile, $\Omega_{i,c}$ the initial central rotation rate, and r is the distance from the origin (see fig. 2.18). Note that for $A \rightarrow \infty$, the rotation becomes uniform. Throughout our entire model set we choose $A = 500$ km as degree of differential rotation.

In order to guarantee a divergence-free initial state, the initial magnetic field configuration was set up employing its definition via the vector potential $\vec{A}$. The components of $\vec{A}$ chosen are

$$\vec{A} = \left(-\frac{B_{pol}}{2} y, \frac{B_{pol}}{2} x, \sqrt{x^2 + y^2} B_{tor} \right) . \tag{2.191}$$

In order to mimic a dipole-like field, we scale the vector potential with density according to the suggestion of M. Liebendörfer as

$$\vec{\tilde{A}} = \sqrt{\frac{\rho}{\rho_{ref}}} \vec{A} . \tag{2.192}$$

Finally, the magnetic field is derived from this vector potential via [105]

$$\vec{B} = \nabla \times \vec{\tilde{A}} . \tag{2.193}$$

The initial toroidal and poloidal components of the magnetic field are specified at a reference density of $\rho_{ref} = 5 \times 10^7 \mathrm{gcm}^{-3}$ according to [93].

3 3D MHD Core-Collapse Simulations: Results I

So this, then, was the kernel of the brute!

Johann Wolfgang von Goethe, Faust I

In this chapter, I will present results from fully self-consistent 3D MHD core-collapse simulations, carried out with `ELEPHANT`.
In the subsequent sections, I will discuss the GW signature of 28 three dimensional models. While presenting the resulting GW patterns, I will pay special attention to possible imprints of different finite temperature EoS, rotation rates, nonaxisymmetric instabilities, magnetic fields and postbounce neutrino transport schemes on the predicted 3D GW signals.
The following papers present the result of this work in condensed form: Scheidegger et al. (2008) [206] and Scheidegger et al. (2010a,b) [208, 210].

3.1 Description of the magnetohydrodynamical models

For the 3D Newtonian ideal MHD core-collapse simulations and their GW signatures presented in this chapter 3, I use the `ELEPHANT` code. However, as a reminder, I will detail here quickly the underlying input physics of the models discussed below.
In this entire section, the gravitational potential is calculated via a spherically symmetric mass integration that includes radial GR corrections (see sec. 2.2.2 and [147]). As for the treatment of the deleptonization during the collapse phase, I apply the simple and computationally efficient Y_e vs. ρ parametrization scheme (see sec. 2.4.2 and [136]. For this I use the results obtained with the `Agile-Boltztran` code [134], including the above-mentioned EoS of Shen et al. [215] and Lattimer-Swesty in all three variations [130], and the electron capture rates from [36]. After core bounce, the neutrino transport is tracked for several models via a partial (i.e. a leakage scheme) or full implementation of the isotropic diffusion source approximation scheme (see sec. 2.4.3 and [140]). The IDSA, decomposes the distribution function f of neutrinos into two components, a trapped component f^t and a streaming component f^s, representing neutrinos of a given species and energy which find the local zone opaque or transparent, respectively. The total distribution function is the sum of the two components, $f = f^t + f^s$. The two components are evolved using separate numerical techniques, coupled by a diffusion source term Σ. The latter converts trapped particles into streaming particles and vice versa. We determine it

from the requirement that the temporal change of f^t has to reproduce the diffusion limit within the limit of a small mean free path. Note that our leakage scheme significantly overestimates the deleptonization in and around the neutrinosphere region, as it neglects any absorption of transported neutrinos by discarding the streaming component ($f^s = 0$). The 3D computational domain consists, for all models, of a central cube of either 600^3 or 1000^3 cells. The grid spacing is chosen to be 1km or 0.6km. The presupernova stellar models stem from Newtonian 1D stellar evolution calculations and hence may not cover all possible states prior to the collapse of a multidimensional star. Therefore I construct the initial conditions of our simulations by a parametric approach, as described in sec. 2.5 above. I employ a solar-metallicity $15M_\odot$ progenitor of [258], and set it into rotation according to a shell-type rotation law of [67] with a shellular quadratic cutoff at 500km radius (see sec. 2.5).

3.2 Model parameters and nomenclature

All my models are named after the combinations of initial central rotation rate, the EoS, and toroidal and poloidal magnetic fields. The first two letters of the model name represent the initial central rotation rate $\Omega_{c,i}$ [rads^{-1}] according to

0	0.3	π	2π	3π	4π
R0	R1	R2	R3	R4	R5

,

the second two letters stand for the applied EoS

LS (K = 180MeV)	LS (K = 220MeV)	LS (K =325 MeV)	Shen
E1	E2	E3	ST

,

while the last two letters assign the order of magnitude of the toroidal and poloidal field strength [G] according to

10^6	10^7	10^9	10^{10}	10^{11}	10^{12}
A	B	C	D	E	F

.

The subscript L and $IDSA$ denotes simulations which were carried out with the leakage scheme or the ‘complete’ IDSA; and whenever the grid spacing is chosen to be not 1km, but 0.6km, this is denoted with a subscript HR, standing for *high resolution.* Some of the values I adopt as rotation rate and magnetic fields correspond to those suggested in [93]. However, I point out that some of the initial rotation rates ($\Omega_{c,i} \gtrsim \pi{\cdot}\text{rads}^{-1}$) and magnetic fields ($B \gtrsim 10^{10}$G) are larger and stronger than current predictions from stellar evolution calculations. I computed these models in order to cover a wide parameter space for our three-dimensional models with neutrino transport approximations.

3.3 Compute requirements

Pure MHD simulations (including the approximate treatment of deleptonization during the collapse phase) require about $15'000 - 20'000$ CPUh per run on CSCS's

Table 3.1: Summary of initial conditions of non- and slowly rotating models [a]

Model	$\Omega_{c,i}$ [rads^{-1}]	β_i	β_b	EoS	$\rho_b[\frac{g}{cm^3}]$	$B_{tor,i}$[G]	$B_{pol,i}$[G]	$E_m/\vert W\vert_b$	$E_m/\vert W\vert_f$
R0E1CA	0	0	0	E1	4.39×10^{14}	5×10^9	1×10^6	1.8×10^{-9}	3.8×10^{-8}
R0E1CA$_{IDSA}$	0	0	0	E1	4.34×10^{14}	5×10^9	1×10^6	-	-
R0E3CA	0	0	0	E3	4.17×10^{14}	5×10^9	1×10^6	1.8×10^{-9}	3.1×10^{-8}
R0STCA	0	0	0	ST	3.38×10^{14}	5×10^9	1×10^6	1.7×10^{-9}	3.3×10^{-8}
R1E1CA	0.3	0.59×10^{-5}	1.7×10^{-4}	E1	4.53×10^{14}	5×10^9	1×10^6	1.7×10^{-9}	3.4×10^{-8}
R1E1CA$_{HR}$	0.3	0.59×10^{-5}	1.7×10^{-4}	E1	4.36×10^{14}	5×10^9	1×10^6	-	-
R1E3CA	0.3	0.59×10^{-5}	1.7×10^{-4}	E3	4.17×10^{14}	5×10^9	1×10^6	1.7×10^{-9}	3.6×10^{-8}
R1E1DB	0.3	0.59×10^{-5}	1.7×10^{-4}	E1	4.53×10^{14}	5×10^{10}	1×10^7	1.7×10^{-7}	3.0×10^{-6}
R1STCA	0.3	0.59×10^{-5}	1.7×10^{-4}	ST	3.38×10^{14}	5×10^9	1×10^6	1.7×10^{-9}	3.2×10^{-8}
R1E1CA$_L$	0.3	0.59×10^{-5}	1.8×10^{-4}	E1	4.38×10^{14}	5×10^9	1×10^6	6.1×10^{-9}	1.2×10^{-7}

[a] The subscript i stands for *initial*, b for *bounce*, while f stands for $final$. ρ_b is the maximum central density at the time of core bounce. $B_{pol,i}$ and $B_{tor,i}$ abbreviate the initially imposed toroidal and poloidal magnetic fields, whereas $E_m/|W|$ stands for the ratio of magnetic to gravitational energy.

Rosa cluster [1] when pushed to $\sim$ 100ms after bounce. As soon as the full IDSA or the leakage scheme is switched on, this number multiplies by a factor of $\sim$ 10. Each of these runs require about 300 GB of storage space. However, this number grows at a pace of $\sim$ 150GB per $\sim$ 100ms of physical simulation time after core bounce, depending of course also on the rate at which data is written out.

3.4 Non- or slowly rotating core collapse

The non- and slowly rotating models' initial conditions and similar relevant quantities are summarized in tab. 3.1, whilst the GW data is listed in tab. 3.2.

3.4.1 General remarks

Non- and slowly rotating progenitors ($\Omega_{c,i} = 0 \ldots 0.3$rads^{-1} in our model set) all undergo quasi-spherically symmetric core collapse. As the emission of GWs intrinsically depends on dynamical processes that deviate from spherical symmetry, the collapse phase in my models (that neglect inhomogenities in the progenitor star) therefore does not provide any kind of signal, as shown in fig. 3.1 for $t - t_b < 0$. However, subsequent pressure-dominated core bounce, where the collapse is halted due to the stiffening of the EoS at nuclear density $\rho_{nuc} \approx 2 \times 10^{14}$gcm^{-3}, launches a shock wave that ploughs through the infalling material, leaving behind

---

[1] Swiss Supercomputing Centre CSCS; URL: www.cscs.ch

Table 3.2: Summary of GW related quantities of non- and slowly rotating models

Model	t_f[ms]	$E_{GW}[M_\odot c^2]$	dir.	$\lvert A_{+,b,max}\rvert$	$\lvert A_{\times,b,max}\rvert$	$\lvert A_{+,pb,max}\rvert$	$\lvert A_{\times,pb,max}\rvert$
R0E1CA	130.8	2.15×10^{-11}	I	3	< 1	3	< 1
			II	2	< 1	5	1
R0E1CA$_{IDSA}$	81.7	1.22×10^{-11}	I	3	< 1	4	2
			II	2	< 1	3	1
R0E3CA	103.9	5.72×10^{-11}	I	2	< 1	10	< 1
			II	2	< 1	8	< 1
R0STCA	70.3	1.35×10^{-11}	I	3	< 1	4	< 1
			II	1	< 1	3	< 1
[a] R1E1CA	112.8	1.36×10^{-10}	I	3	< 1	16	7
			II	3	<1	15	1
R1E1CA$_{HR}$	25.6	2.42×10^{-10}	I	1	< 1	12	6
			II	<1	<1	25	2
R1E3CA	130.4	1.43×10^{-10}	I	2	< 1	10	5
			II	3	< 1	17	< 1
R1E1DB	112.8	1.24×10^{-10}	I	3	< 1	12	6
			II	3	< 1	15	2
R1STCA	45.8	2.01×10^{-11}	I	2	<1	3	1
			II	2	<1	6	<1
R1E1CA$_L$	92.9	1.04×10^{-10}	I	3	< 1	4	2
			II	2	<1	10	1

[a] t_f is the time after core bounce when the simulation was stopped. E_{GW} is the total energy released in gravitational radiation. I present the maximum amplitudes at different stages of their time-evolution in polar (I) and equatorial (II) direction. The subscripts *b* and *pb* stand for bounce and postbounce.

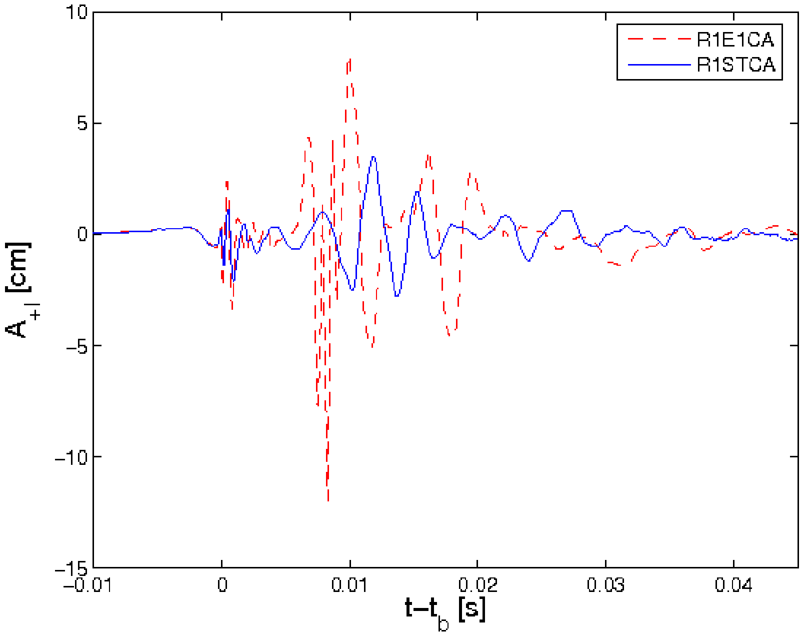

Figure 3.1: Time evolution of the GW amplitude A_{+I} from the slowly rotating models R1STCA (solid line) and R1E1CA (dashed line). Since convection is a stochastic process, the GW amplitudes are rather insensitive to the location of the observer. Hence, I display only one representative polarisation.

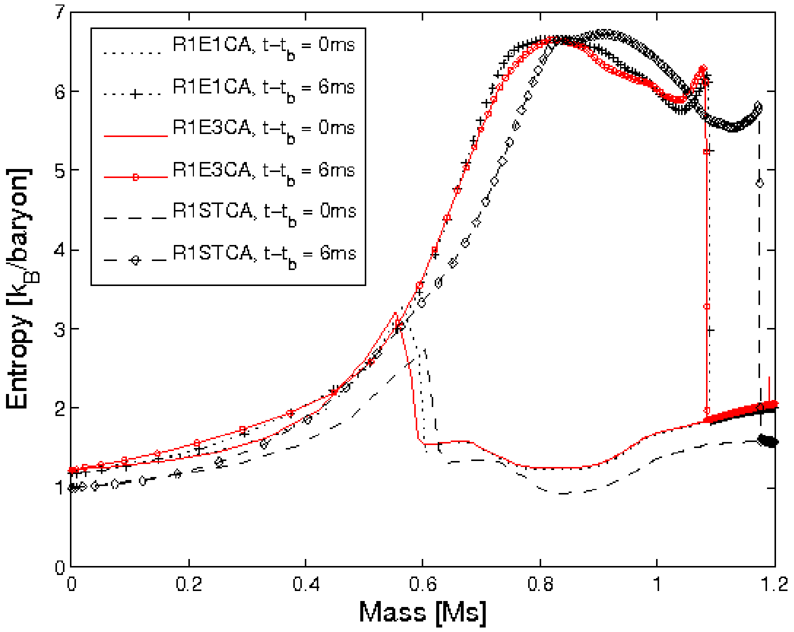

Figure 3.2: Spherically averaged entropy profiles from the slowly rotating models R1E1CA (red solid line), R1E3CA (black dotted line) and R1STCA (black dashed line) at bounce. The second entropy time slice is chosen to be approximately at the onset of the GW signal from prompt convection.

a negative entropy gradient that induces so-called 'prompt' convective activity (see, e.g. [145, 41, 62, 149, 174, 210, 208]). The GW burst which is accompanied by such aspherities starts several ms after bounce when convective overturn starts to be effective. The criterion for convective instability (the 'Ledoux condition') is generally expressed as [127, 251]

$$\left(\frac{\partial\rho}{\partial Y_e}\right)_{P,s}\left(\frac{\partial Y_e}{\partial r}\right)+\left(\frac{\partial\rho}{\partial s}\right)_{P,Y_e}\left(\frac{\partial s}{\partial r}\right)>0\,, \tag{3.1}$$

where Y_e, ρ, r and s are electron fraction, density, stellar radius and entropy per baryon respectively. Thermodynamic consistency requires $(\partial\rho/\partial s)_{Y_e,P} < 0$, which implies that a negative entropy gradient always acts in a destabilizing manner. Additionally, the neutronization burst, occurring some $\sim$ 5ms after bounce, causes a negative lepton gradient at the edge of the PNS which further drives convection (cf. fig. 13 of [221], or [41, 56]). Note that convection is be weakened in the rotational plane by positive specific angular momentum gradients in rotating cores [66].

3.4.2 Models without deleptonization in the postbounce phase: Effects of the EoS and magnetic fields on the GW signature

During the early postbounce stage ($t-t_b \lesssim 20-30$ms), prompt convective motion is predominantly driven by a negative entropy gradient, as pointed out by e.g. [210,208]

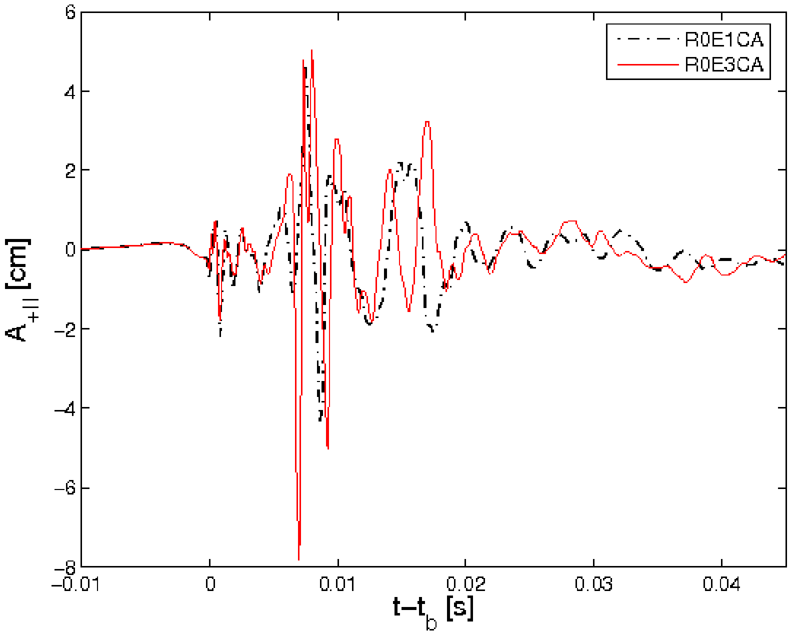

Figure 3.3: Time evolution of the GW amplitude $A_{+\mathrm{II}}$ from the non-rotating models R0E1CA (dashed) and R0E3CA (solid line).

(see also [62, 149, 174]). The GW burst to be associated with prompt convection sets in $\sim$ 6ms after bounce in models based on the LS EoS, generally $\sim 2-3$ms before the same feature occurs in the corresponding simulations using the Shen EoS, as indicated in fig. 3.1. The reason for this behaviour is that the shock wave in the 'Shen'-models carries more energy compared to those in models using a LS EoS, since the initial energy that is imparted to the shock scales roughly as $\propto Y_e^{10/3}$ (see [37], with references therein). Therefore, the shock wave stalls at slightly later times at larger radii (see fig. 3.2), and the conditions for convective activity are delayed compared to the LS runs. Note that the convective overturn causes a smoothing of the negative entropy gradient. As a result, the GW amplitude quickly decays ($t \gtrsim$ 30ms after bounce) and is not revived during the later evolution of the models without deleptonization in the postbounce phase, as displayed in figs. 3.1 and 3.3. Simulations that incorporate the Shen EoS return up to a factor of 2 smaller maximum amplitudes compared to their counterparts, as can be deduced from fig. 3.1 and Table 3.2.

I also find that the GWs from simulations which were carried out with the stiff E3 show no significant deviations from those computed with E1 (see tab. 3.2 and fig. 3.3). The minor deviations of the GWs are entirely due to the stochastic nature of convection. The waveform spectra from the LS models cover a broad frequency band ranging from $\sim 150-500$Hz, as displayed in fig. 3.4. The spectral peak of the Shen models is shifted somewhat to lower frequencies, covering a range from $\sim 150-350$Hz (see fig. 3.4). When comparing the energy E_{GW} which is emitted during the first 30ms after bounce from the LS models to that of the corresponding Shen models, I find the latter models emit less energy (see tab. 3.2). This discrepancy is due to

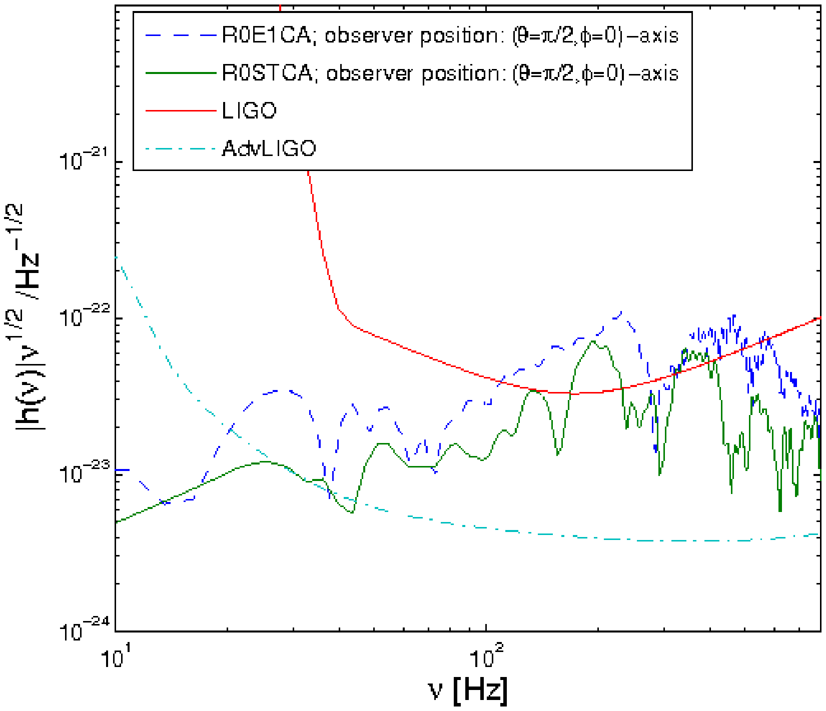

Figure 3.4: Spectral energy distribution from the models R0E1CA (dashed line) and R0STCA (solid line) for a spectator in the equatorial plane at a distance of 10kpc compared with the LIGO strain sensitivity (Shoemaker 2007, private communication) and the planned performance of Advanced LIGO. Optimal orientation between source and detector is assumed.

the lower emission at higher frequency $\nu \gtrsim 350$Hz in the Shen models and the fact that the emitted energy $dE_{GW}/d\nu$ is proportional to ν^2. Moreover I find that slow rotation (rotation rate R1) in enough to lead a deformation of the PNS. This can be quantified by considering e. g. a density cut at $\rho = 10^{11}$gcm^{-3}, which is just inside the convectively unstable region. For the slowly rotating model R1E1CA, this point is located at a radial distance of 80km along the polar axis at 20ms after bounce. However, in the equatorial plane, the same position is reached one radial grid zone further out relative to the origin due to the action of centrifugal forces. The short time variation in the quadrupole due to rotation combines with that of prompt convection and together they lead to somewhat stronger GW emission in the slowly rotating case compared to the non-rotating model set. This effect is strongest for the GW amplitude $\mathrm{A}_{+\mathrm{II}}$, which is the ‘axisymmetric’ ($l = 2, m = 0$) component of the wave field. Despite this feature, the frequency content of models which only differ in rotation rate, stays practically unaltered. I found the key controlling factors that govern the GW emission from prompt convection to be the i) radial location of the convectively unstable zones and ii) the related characteristic dynamical timescales involved, for which we use as a rough estimate

$$t_{dyn} \sim \Delta_r/\overline{c_s} \; , \tag{3.2}$$

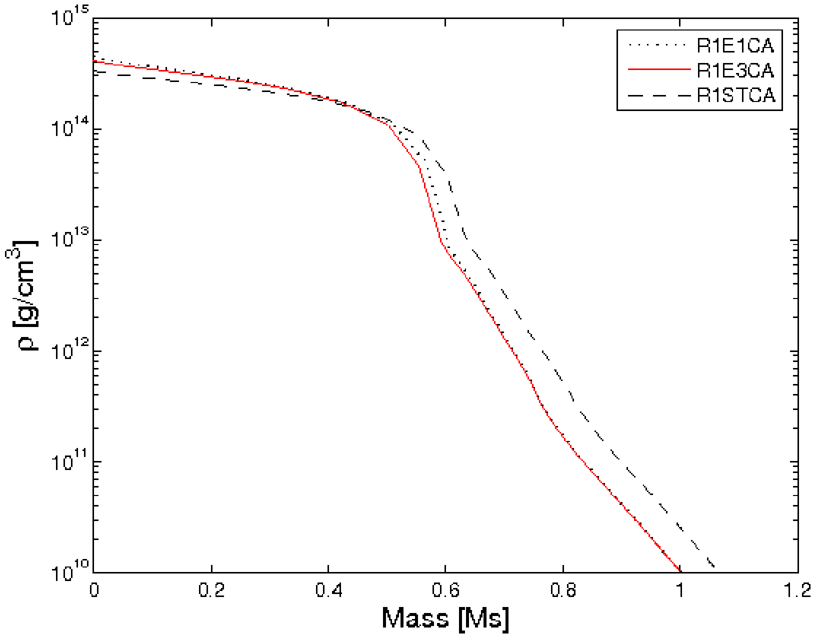

Figure 3.5: Spherically averaged density profiles from models R1E1CA (dotted line), R1E3CA (full line) and R1STCA (dashed line) at core bounce ($t - t_b = 0$).

where

$$\overline{c_s} = 1/\Delta_r \int_r c_s(r)dr \tag{3.3}$$

is the radially averaged sound speed of a convectively unstable layer with a radial extension of Δ_r (Christian D. Ott 2009, private communication). Note that both i) and ii) are implicitly determined by the applied EoS, being responsible e.g. for the local speed of sound and the radial PNS density profile. Our core-collapse simulations that use a version of the LS EoS (E1 or E3) show at core bounce maximum central densities up to $\sim$ 25% higher than the corresponding models that apply the Shen EoS (see tab.3.1). Moreover, the LS-models possess a PNS which is more strongly condensed in central regions and has a steeper density gradient further out. The densities of e.g. R1E1CA and R1STCA intersect at $\sim 0.5M_\odot$ ($\sim$ 8km), as displayed in fig. 3.5. In addition, models using the E1 show somewhat higher central densities compared to the ones applying the stiffer E3 variant, and densities of e.g. R0E1CA and R0E3CA cross at $\sim$ 7km. Nevertheless these two variants of the LS EoS differ only in their compressibility. The radial structures resemble each other strongly, unlike to the models carried out using the Shen EoS, as shown in fig. 3.5. Hence, the particular similarity in the GW characteristics of LS runs (see fig. 3.3) is not unexpected since the region which is convectively unstable is restricted to roughly the same radial and density regimes ($R \approx$ 30-70km, $\rho \approx 10^{11} - 1.1 \times 10^{12}$ gcm^{-3}) and therefore bound to the same dynamical timescale t_{dyn} and its corresponding frequency band. For the Shen models on the other hand the region of negative entropy gradient, whose boundaries are radially constrained by $R \approx$ 60-

90km, contains considerably less matter than its LS analogues. This explains the smaller GW amplitudes. A narrower density spread ($\rho \approx 7 \cdot 10^{10} - 1.2 \times 10^{11}$ gcm^{-3}) in the unstable region leads to a more restricted peak frequency band at lower values (see fig. 3.2).

However, as was pointed out by [174], 'prompt' convection depends not on the negative entropy gradient alone, but also on numerical seed perturbations which are introduced by the choice of the computational grid. Hence, in order to test the dependence of my findings on the spatial resolution, we carried out model R1E1CA$_{HR}$. This better resolved simulation shows considerably smaller seed perturbations around $t - t_b \sim 0$, as grid alignment effects are better suppressed at core bounce; hence prompt convection is much weaker and a smaller GW amplitude ($\sim$ 50%) is emitted, as shown in fig. 3.9. However, better numerical resolution also leads to less numerical dissipation in the system, which eases the dynamical effects that follow. Thus, we find considerably stronger GW emission for $\sim$ 10ms $\lesssim t \lesssim$ 20ms in R1E1CA$_{HR}$ compared to the 1km resolved models, as indicated in fig.3.9.

Computing the SNRs I find that all the simulations discussed above lie just below the detector limits of LIGO if I assume them to be located at a Galactic distance of 10kpc. Their single-detector optimal-orientation SNR is just a little above unity. However, for a successful detection, a SNR of at least 7 to 8 is necessary. Note that the SNRs of models with different EoS do not differ much at this stage since all share a similar spectral energy distribution within the window of LIGO's maximum sensitivity. The current detector sensitivity does not allow for the detection of the high frequency tail of the LS models. Fortunately, for planned future detectors such as the Advanced LIGO facility, things change dramatically. As a direct consequence, these new detectors would permit the distinction between the prompt convection GW signal from the LS and Shen EoS, since the full spectral information would be available. However, I find it impossible to discriminate between the different LS EoS variants. Hence, my simulations indicate that the GW signature depends more strongly on the asymmetry energy than the compressibility parameter of the EoS.

These results are partly different from those previously published. Recently, [149] as well as [174] reported to observe GWs from prompt convection in state-of-the-art 2D simulations which were launched from similar initial conditions as mine, namely the same progenitor star and the soft variant of the LS EoS (K=180MeV). Whilst the extracted GW amplitudes from early prompt convection of [149] (cf. their model M15LS-2D) are in rough agreement with my results, the spectrum of their wave train peaks at considerably lower frequencies, namely around about $\sim$ 100Hz. I suppose that this discrepancy is due mainly to different radial locations of the unstable regions and consequently the encompassed amount of overturning matter. [174] computed two models with different resolution. While one of their models (s15WW95) in particular fits our results well in all characteristic GW features, namely the size of amplitudes, band of emission and the amount of emitted energy, the better resolved model (s15WW95HR) shows that convection is much weaker due to less seed perturbation and hence the GW signal and the total amount of emitted energy are considerably lower.

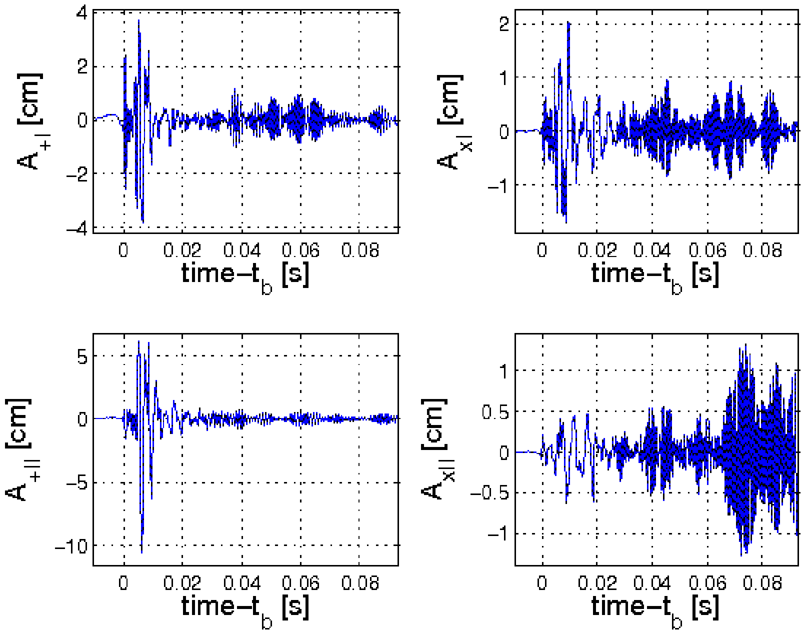

Figure 3.6: Model R1E1CA$_L$'s time evolution of the quadrupole amplitudes A$_{+\mathrm{I}}$, A$_{\mathrm{xI}}$, A$_{+\mathrm{II}}$, and A$_{\mathrm{xII}}$.

Finally, I find that imposing initial magnetic fields ten times as strong as the values suggested in [93] does not influence the model dynamics and therefore the GW signal at all, as can be deduced from tab. 3.2 by a comparison of models R1E1CA and R1E1DB.

3.4.3 Model with deleptonization in the postbounce phase

Due to the absence of accurate postbounce neutrino transport, it is unclear how reliably the models discussed in the previous subsection predict the GW signals from the early postbounce period. As a first step to address this question, we carried out one computationally expensive simulation, model R1E1CA$_L$ [2], that includes the emission of neutrinos after bounce but neglects neutrino heating, which becomes relevant at $t - t_b \gtrsim 50$ms. The absence of the latter makes it impossible for this model to track the long-term postbounce neutrino-driven convection. However, in comparison with purely MHD models, the inclusion of neutrino leakage makes it possible to distinguish effects on the GW signal due to entropy and lepton gradient driven convection.

A detailed comparison of model R1E1CA$_L$ with its purely MHD counterpart R1E1CA shows that both follow a similar dynamical behaviour until about 20ms after bounce. Asphericities leading to GW emission are predominantly driven by entropy- and not lepton-induced convection at this supernova stage. Consequently, the wave trains emitted within this early period fit each other qualitatively (cf. figs. 3.1 and 3.6).

---

[2] Note that R1E1CA$_L$ was kindly provided by S.C. Whitehouse.

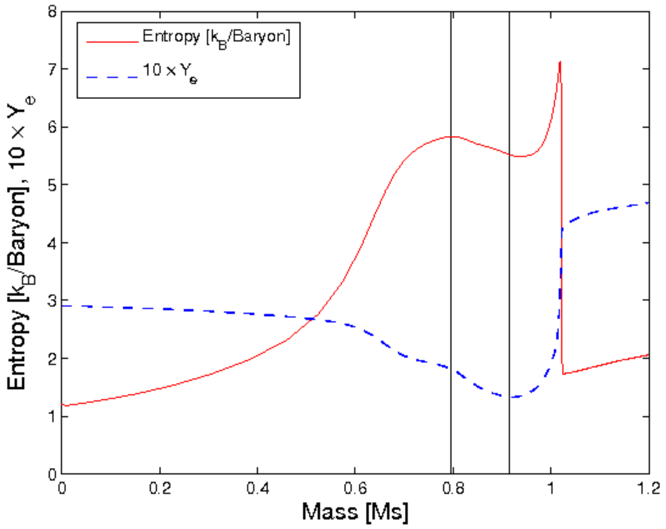

Figure 3.7: Model R1E1CA$_L$'s spherically averaged specific entropy (full line) and 10 × electron fraction Y_e (dashed line) profiles are plotted versus the enclosed mass ∼ 5ms after bounce. The radial position of simultaneous negativ entropy- and lepton gradients are marked by the vertical lines.

However, I find some quantitative deviations: The GWs of R1E1CA$_L$ reach lower maximum values (see tab. 3.2), as the 'Ledoux' unstable region encompasses less mass (see fig. 3.7), and the presence of neutrino cooling leads to a more rapid smoothing of the entropy gradient compared to the models discussed in the previous subsection. Since overturning matter in the top layers of the PNS has the same radial position, densities and dynamical timescales as in model R1E1CA, these models have similar GW spectra, peaking between $\sim 150 - 500$Hz (cf. figs. 3.4 and 3.8). Therefore the physically simpler models still provide reasonably accurate GW predictions in frequency space until about 20ms after bounce, although the amplitudes are overestimated a few ×10% (cf. figs. 3.1 and 3.6). Model R1E1CA$_L$'s later postbounce evolution ($t \gtrsim$ 20ms) differs strongly compared to its purely hydrodynamical counterpart R1E1CA. A negative radial lepton gradient, caused by the neutronization burst and subsequent deleptonization, drives convection inside the lower layers of the PNS [56] at a radial position of ∼ 10-30km and a density range of $\sim 10^{12} - 10^{14}$gcm^{-3} and therefore now causes the entire GW emission. The cooling PNS contracts with time, which causes the convective zones to migrate towards smaller radii and shrink. However, I point out that our leakage scheme overestimates the neutrino cooling processes, as shown in fig. 2.15. Hence, this mechanism proceeds too quickly for model R1E1CA$_L$ (Christian D. Ott 2009, private communication). The PNS convection exhibits GW emission of roughly $\sim 0.5 - 1$cm amplitude, as can be seen in fig. 3.6 ($t \gtrsim$ 20ms). The corresponding spectral distribution is shown in fig. 3.8. A broad peak arises between $\sim 700 - 1200$Hz and reflects the dynamical timescale t_{dyn} of the violent overturn activity of a millisecond scale inside the PNS. The model's SNR for LIGO at 10kpc is around unity again. The high-frequency tail of the spectrum ($\gtrsim$ 700Hz), which is present due to PNS

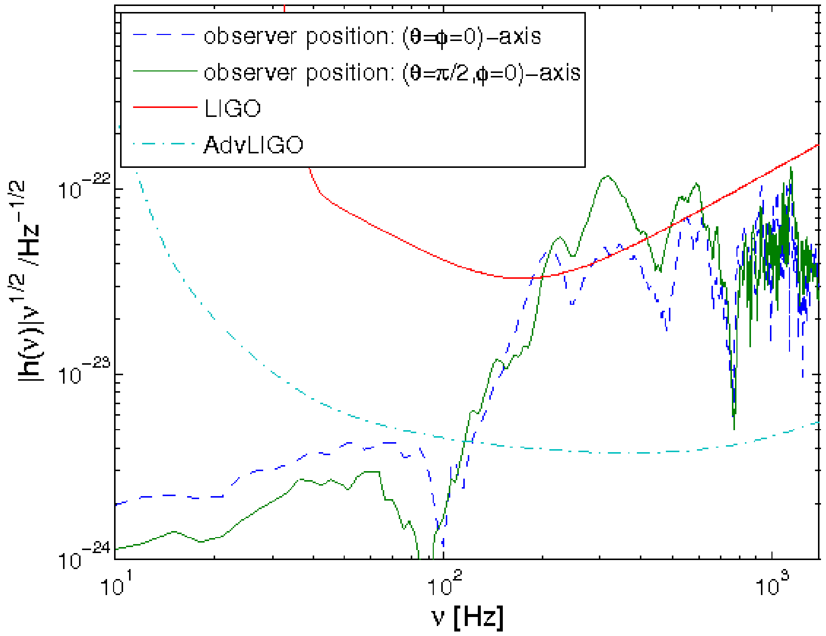

Figure 3.8: Model R1E1CA$_L$'s spectral energy distribution of the GW signals at a distance of 10kpc. Note that the spectrum interval from $\sim 150-500$Hz is caused by prompt convective activity, while the higher modes result from lepton gradient driven postbounce PNS convection.

convection, cannot contribute to the SNR as it lies below the current detector sensitivity. My computed GW strains for PNS convection agree roughly in amplitude with the ones found by Ott in [174] for axisymmetric MGFLD models. However, the amount of released energy emitted is found to be about one order of magnitude higher compared to his simulations. This discrepancy is most likely due to the lower average frequency content of the GWs in Ott's model ($\sim$ 350Hz; see his fig. 7), as $dE_{GW}/df \propto \nu^2$. I suppose the reason for this mismatch to be the different radial location of the convectively unstable region and thus the different related dynamical timescale t_{dyn}. I will prove this statement in section 3.4.4 below.

3.4.4 Model with IDSA in the postbounce phase

As a second step studying the influence of spectral neutrino transport on the stochastic matter dynamics in the early supernova stages ($t \lesssim$ 100ms after bounce), without having other different physical parameters interfering, we carried out R0E1CA$_{IDSA}$ [3] (incorporates both neutrino cooling and heating), which permits comparisons with its 'model counterparts' R0E1CA (purely hydrodynamical postbounce evolution), R1E1CA$_L$ (includes a leakage scheme).
A detailed comparison of these three models shows that all of them follow a similar dynamical behaviour until about 20ms after bounce. At this stage, aspherities lead-

---

[3] Note that R0E1CA$_{IDSA}$ was kindly provided by S.C. Whitehouse.

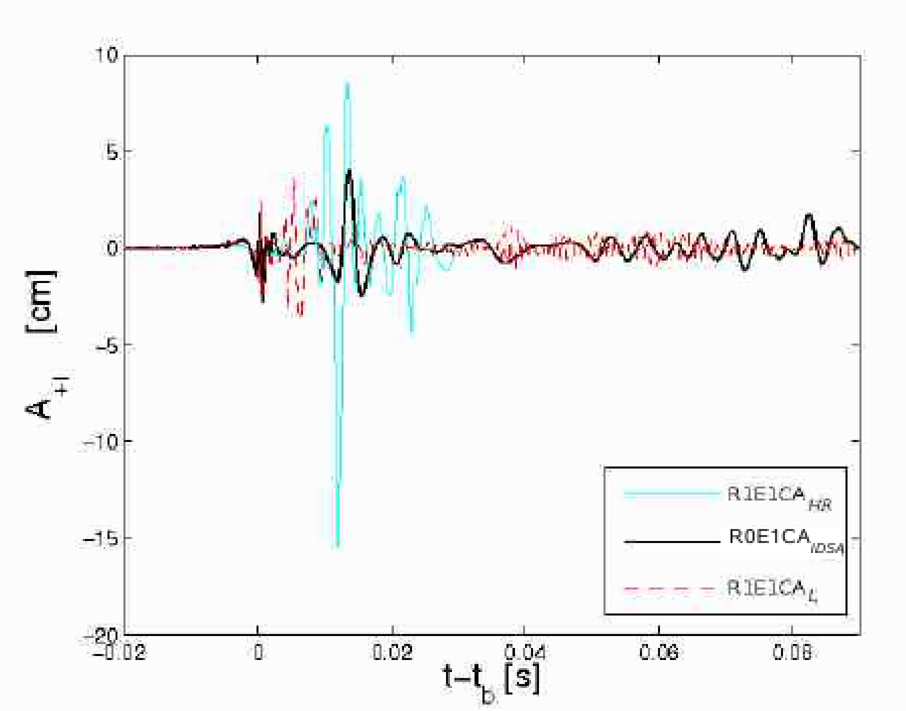

Figure 3.9: Time evolution of the GW + polarization for a spectator located at the polar axis (Models R1E1CA$_{HR}$, R0E1CA$_{IDSA}$ and R1E1CA$_{L}$).

ing to GW emission are predominantly driven by the negative entropy gradient and not by the lepton gradient, as already found in subsection 3.4.3 when comparing the purely 'hydrodynamical' model with the 'leakage' model. Hence, the wave trains of all three reference models, which are based on stochastic processes, fit each other relatively well both in amplitude (several cm) and spectra ($\sim 150-500$Hz).

The three representative simulation results of R0E1CA$_{IDSA}$, R0E1CA and R1E1CA$_{L}$ diverge strongly in the later postbounce evolution ($t \gtrsim 20$ms). As pointed out previously, convective overturn causes, a smoothing of the entropy gradient. As a result, the GW amplitude in the hydrodynamical model R0E1CA quickly decays ($t \lesssim 30$ms after bounce) and is not revived during the later evolution. On the other hand, the negative radial lepton gradient (see figs. 3.11 and 2.15 which is caused by the neutronization burst and the subsequent deleptonization, modelled only in R1E1CA$_{L}$ and R0E1CA$_{IDSA}$, now starts to drive convection inside the PNS.

For the latter models, the PNS convection [56] exhibits similar maximum amplitudes of ~1-2cm (see fig. 3.9), while differing strongly from each other in the corresponding spectra, as displayed in fig. 3.10. R1E1CA$_{L}$'s spectrum peaks between ~600 - 1000Hz, while R0E1CA$_{IDSA}$'s frequency band peaks at values as low as ~100Hz. This affects the total energy E_{GW} emitted ($\mathcal{O}(10^{-10})M_{\odot}c^2$ vs. $\mathcal{O}(10^{-11})M_{\odot}c^2$; see tab. 3.2), being one order of magnitude higher for R1E1AC$_{L}$ due to $dE_{GW}/df \propto f^2$. I found the key controlling factor of this behaviour again to be the radial location of the convectively unstable zones and the related dynamical timescales t_{dyn} involved (cf. eq. 3.2). If I apply typical numbers from the models R0E1CA$_{IDSA}$

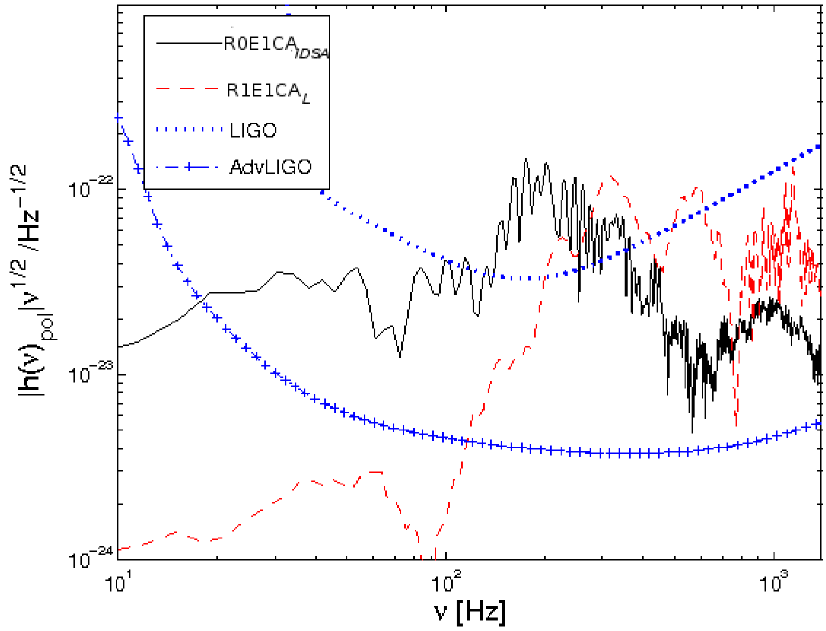

Figure 3.10: Spectral energy distribution of models R0E1CA$_{IDSA}$ and R1E1CA$_L$ for a spectator located at the polar axis and at a distance of 10kpc, compared with the LIGO strain sensitivity and the planned performance of Advanced LIGO. Optimal orientation between source and detector is assumed.

and R1E1CA$_L$, I confirm the values obtained. Furthermore, our leakage scheme significantly overestimates neutrino cooling processes, as shown in fig. 2.15. There, the convectively unstable layer is extended to radii above nuclear densities, where matter is still opaque for neutrinos and where the local speed of sound assumes values far larger than in the case of model R0E1CA$_{IDSA}$. Hence, the dynamical timescale of R1E1CA$_L$ is considerably shorter and the spectral distribution is peaked at higher values. When comparing the results found for model R0E1CA$_{IDSA}$ with a recent 2D study of [149], where they carried out one simulation (cf. their model M15LS-2D) with comparable input physics (same $15M_\odot$ progenitor; same underlying finite-temperature EoS) and a very sophisticated neutrino transport scheme, I find very good agreement both in the amplitudes and frequencies. Hence I conclude that the primary ingredient for supernova simulations which attempt a quantitative prediction of GWs from 'prompt' and early PNS convection ($t \lesssim 100$ms after bounce) is the accurate radial location and size of convectively unstable layers. It defines the dynamical behaviour and timescale of overturning matter in this early supernova stage.

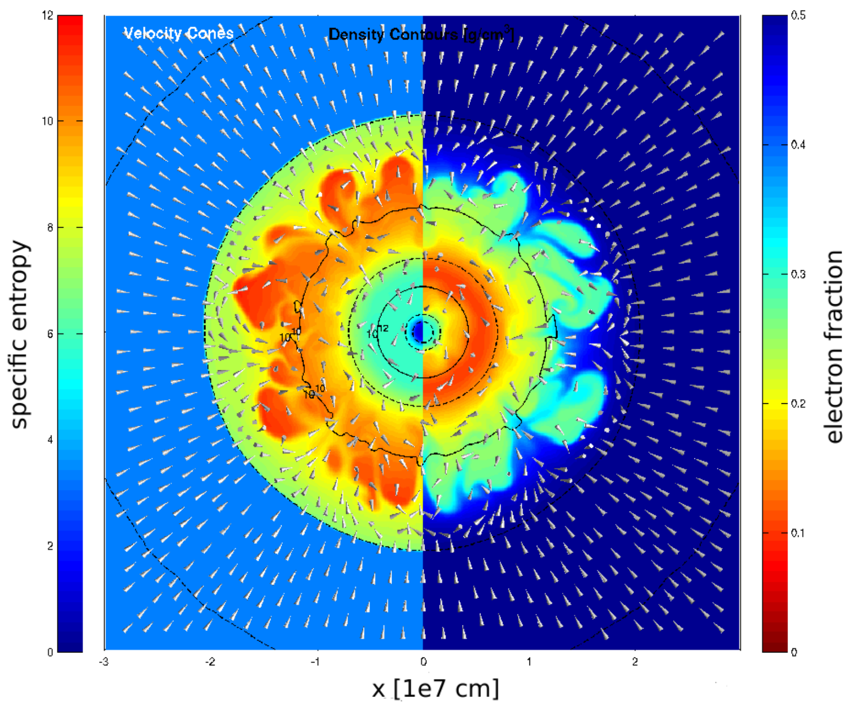

Figure 3.11: Model R0E1CA$_{IDSA}$'s specific entropy distribution [k$_B$/baryon] (left side) and electron fraction Y_e (right side) 50ms after core bounce. The innermost 600^2km^2 in the x-y plane are displayed. The entropy colour bar scales from 0 (blue) to 12 (red). The Y_e colour bar accounts for values from 0 (red) to 0.5 (blue).

3.5 Rapidly rotating core collapse

The rapidly rotating models' initial conditions, similar relevant quantities and GW data are summarized in tabs. 3.3, 3.4 and 3.5.

3.5.1 Core bounce: Effects of the rotation rate on the GW signature

Rapidly rotating progenitors ($\Omega_{c,i} = \pi \ldots 4\pi$rads^{-1} in my model set) undergo different core-collapse dynamics compared to the previously discussed non- and slowly rotating models. Conservation of angular momentum in combination with contraction leads to a massive spin-up and hence oblate deformation of the core. The collapse is halted either by pure stiffening of the EoS above nuclear saturation density, or, if rotation is sufficiently strong, by a combination of the centrifugal and nuclear forces. The abrupt slowdown of axisymmetrically-arranged and quickly rotating bulk matter gives rise to rapid temporal variations in the quadrupole tensor, resulting in the emission of GWs (see fig. 3.12). Note that the core remains essentially axisymmetric during collapse and early postbounce times ($t - t_b \lesssim 10$ms), as already pointed out in [179, 180]. Within the chosen parameter space of the rota-

Table 3.3: Summary of initial conditions of rapidly rotating core collapse [a]

Model	$\Omega_{c,i}$ [rads^{-1}]	β_i	β_b	EoS	$\rho_b[\frac{g}{cm^3}]$	$B_{tor,i}$[G]	$B_{pol,i}$[G]	$E_m/\vert W\vert_b$	$E_m/\vert W\vert_f$
R2E1AC	π	0.64×10^{-3}	1.6×10^{-2}	E1	4.27×10^{14}	1×10^{6}	1×10^{9}	6.5×10^{-9}	1.27×10^{-5}
R2E3AC	π	0.64×10^{-3}	1.6×10^{-2}	E3	4.00×10^{14}	1×10^{6}	5×10^{9}	6.4×10^{-9}	5.1×10^{-6}
R2STAC	π	0.64×10^{-3}	1.6×10^{-2}	ST	3.30×10^{14}	1×10^{6}	5×10^{9}	6.4×10^{-9}	3.6×10^{-6}
R3E1AC	2π	0.26×10^{-2}	5.2×10^{-2}	E1	3.80×10^{14}	1×10^{6}	5×10^{9}	8.0×10^{-9}	6.7×10^{-6}
R3E2AC	2π	0.26×10^{-2}	5.1×10^{-2}	E2	3.65×10^{14}	1×10^{6}	5×10^{9}	8.9×10^{-9}	7.2×10^{-6}
R3E3AC	2π	0.26×10^{-2}	5.1×10^{-2}	E3	3.64×10^{14}	1×10^{6}	5×10^{9}	9.0×10^{-9}	5.8×10^{-6}
R3STAC	2π	0.26×10^{-2}	5.1×10^{-2}	ST	3.01×10^{14}	1×10^{6}	5×10^{9}	8.9×10^{-9}	4.7×10^{-6}
R3E1CA	2π	0.26×10^{-2}	5.2×10^{-2}	E1	3.82×10^{14}	5×10^{9}	1×10^{6}	3.1×10^{-9}	1.4×10^{-8}
R3E1DB	2π	0.26×10^{-2}	5.2×10^{-2}	E1	3.81×10^{14}	5×10^{10}	1×10^{7}	3.1×10^{-7}	1.6×10^{-6}
R3E1AC$_L$	2π	0.26×10^{-2}	5.1×10^{-2}	E1	3.65×10^{14}	1×10^{6}	5×10^{9}	8.7×10^{-9}	8.6×10^{-5}
R4E1AC	3π	0.57×10^{-2}	8.6×10^{-2}	E1	3.22×10^{14}	1×10^{6}	5×10^{9}	1.2×10^{-8}	1.3×10^{-5}
R4STAC	3π	0.57×10^{-2}	9.0×10^{-2}	ST	2.69×10^{14}	1×10^{6}	5×10^{9}	1.5×10^{-8}	1.4×10^{-5}
R4E1EC	3π	0.57×10^{-2}	8.6×10^{-2}	E1	3.22×10^{14}	1×10^{11}	5×10^{9}	2.4×10^{-8}	1.3×10^{-5}
R4E1FC	3π	0.57×10^{-2}	8.6×10^{-2}	E1	3.19×10^{14}	1×10^{12}	5×10^{9}	1.3×10^{-4}	1.3×10^{-4}
R4E1FC$_L$	3π	0.57×10^{-2}	8.7×10^{-2}	E1	3.14×10^{14}	1×10^{12}	5×10^{9}	1.3×10^{-4}	2.0×10^{-4}
R4E1CF	3π	0.57×10^{-2}	8.2×10^{-2}	E1	3.22×10^{14}	5×10^{9}	1×10^{12}	5.8×10^{-4}	5.9×10^{-3}
R5E1AC	4π	1.02×10^{-2}	10.2×10^{-2}	E1	2.47×10^{14}	1×10^{6}	5×10^{9}	1.3×10^{-8}	1.2×10^{-5}

[a] The subscript i stands for *initial*, b for *bounce*, while f stands for $final$. ρ_b is the maximum central density at the time of core bounce. $B_{pol,i}$ and $B_{tor,i}$ abbreviate the initially imposed toroidal and poloidal magnetic fields, whereas $E_m/|W|$ stands for the ratio of magnetic to gravitational energy. The subscript L denotes models which were carried out with the leakage scheme.

tion rate, all my models exhibit a so-called type I GW burst ([261]; see fig. 3.13) around core bounce, no matter what the initial choice of the EoS or the magnetic field configuration is. This was previously also found by [62] in 2D GR simulations without magnetic fields.

The question now arises as to what kind of information could possibly be delivered from a quasi-axisymmetric type I GW burst, since it is a priori unclear how degenerate it is with respect to the model parameters such as the EoS, rotation rate and so forth. This was already investigated in great detail by [62] who performed an extensive set of 2D GR core-collapse simulations. Our 3D results show the same systematics: the negative peak amplitude $|h|_{max,b} \equiv \mathrm{A}_{+\mathrm{II}}/\mathrm{R}$ scales about linearly with β_b for models up to a moderately rapid rotation ($\beta_b \lesssim 10\%$, see fig. 3.14).

The Fourier transforms of the bounce wave trains (± 5ms relative to core bounce) show for most models in the indicated parameter range a spectrum with a narrow

Table 3.4: Summary of GW related quantities of rapidly rotating core collapse

Model	t_f[ms]	$E_{GW}[M_\odot c^2]$	dir.	$\|A_{+,b,max}\|$	$\|A_{\times,b,max}\|$	$\|A_{+,pb,max}\|$	$\|A_{\times,pb,max}\|$	$f_b[Hz]$	$f_{TW}[Hz]$
R2E1AC	127.3	5.52×10^{-9}	I	2	2	6	5	-	-
			II	105	<1	1	3	841	-
R2E3AC	106.4	5.31×10^{-9}	I	2	2	4	4	-	-
			II	104	<1	1	< 1	803	-
R2STAC	64.0	7.62×10^{-9}	I	3	3	6	6	-	-
			II	133	<1	2	1	680	-
R3E1AC	62.5	5.58×10^{-8}	I	2	1	15	16	-	725
			II	393	< 1	10	2	880	-
R3E2AC	45.5	6.53×10^{-8}	I	2	1	11	13	-	-
			II	409	< 1	5	3	882	-
R3E3AC	57.5	6.44×10^{-8}	I	2	2	6	9	-	-
			II	409	< 1	6	3	891	-
R3STAC	50.2	1.05×10^{-7}	I	5	4	9	11	-	935
			II	526	< 1	5	3	854	-
R3E1CA	69.4	8.05×10^{-8}	I	3	3	9	9	-	-
			II	426	< 1	5	3	897	-
R3E1DB	62.7	7.76×10^{-8}	I	8	8	13	11	-	-
			II	425	< 1	8	3	886	-
R3E1AC$_L$	196.7	2.14×10^{-7}	I	1	1	136	136	-	909
			II	437	< 1	70	9	909	-
R4E1AC	98.7	7.74×10^{-8}	I	1	< 1	37	37	-	662
			II	512	< 1	20	6	385	-
R4STAC	67.2	1.91×10^{-7}	I	2	1	102	109	-	902
			II	536	< 1	53	3	396	-
R4E1EC	100.8	7.51×10^{-8}	I	1	1	25	20	-	611
			II	492	< 1	15	7	866	-
R4E1FC	80.1	7.29×10^{-8}	I	< 1	< 1	16	19	-	828
			II	516	< 1	9	3	859	-
R4E1FC$_L$	97.6	3.42×10^{-7}	I	2	1	316	298	-	673
			II	536	< 1	157	6	485	-
R4E1CF	19.1	6.50×10^{-8}	I	1	1	4	4	-	-
			II	518	< 1	ring-down	2	370	-
R5E1AC	93.2	1.20×10^{-8}	I	1	1	18	18	-	727
			II	238	< 1	10	11	317	-

[a] t_f is the time after core bounce when the simulation was stopped. E_{GW} is the total energy released in gravitational radiation. We present the maximum amplitudes at different stages of their time-evolution in polar (I) and equatorial (II) direction. The subscripts b and pb stand for bounce and postbounce. f_b denotes the peak frequency of the GW burst at bounce, while f_{TW} stands for the spectral peak from the narrow band emission caused by a low $T/|W|$ instability.

bandwidth, peaking around $\sim 800 - 900$Hz (see tab. 3.4 and fig. 3.15). Moreover, with growing rotation rate, prompt convective overturn in the rotational plane is suppressed by the influence of positive angular momentum gradients. This effect was first pointed out by [66] and is known as the Solberg-Høiland instability criterion.

The outcome of my 3D models confirms the statement of [62] that two parameters are essential for the behaviour of the GW amplitude around $t - t_b = 0$, namely the mass of the inner core at bounce, which I denote as $M_{ic,b}$, and the initial central rotation rate $\Omega_{c,i}$. Over the parameter range covered by my models, β_b is a strictly monotonic function of the initial central angular velocity $\Omega_{c,i}$, as displayed in fig. 3.16. The mass of the inner core $M_{ic,b}$ is linked to β_b via its dependence on $\Omega_{c,i}$ (see fig. 3.16). The positive mass offset of the inner core (which is approximately constant for all rotational configurations) that occurs when switching from E1 to ST is interpreted as follows: in a static initial configuration, the mass of the inner core is

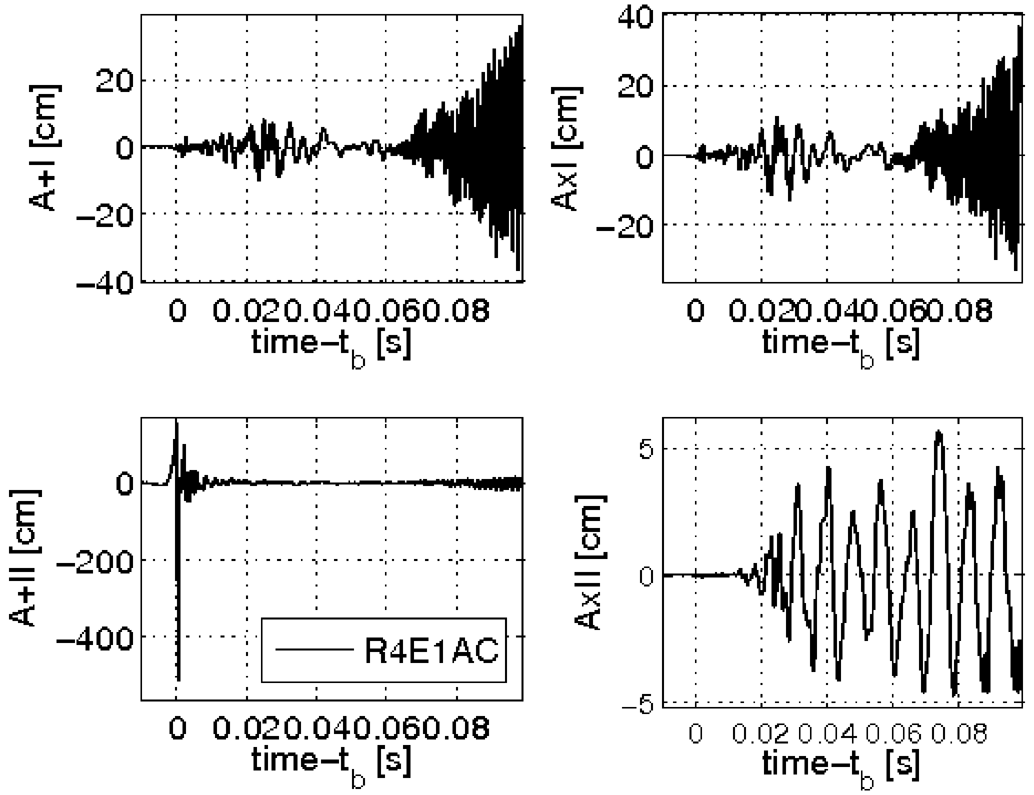

Figure 3.12: Time evolution of the quadrupole amplitudes $A_{+\mathrm{I}}$, A_{xI}, $A_{+\mathrm{II}}$, and A_{xII} for model R4E1AC. Note that The amplitudes for the three directions and polarizations, A+I, A_{xI}, $A_{+\mathrm{II}}$, are not very sensitive to rotation and show a similar size of several centimetres. Apparently, they initially couple only weakly to rotationally induced large-scale asymmetries in the mass-energy distribution. The only GW amplitude that is strongly correlated to axisymmetric rotation at the time of core bounce turns out to be $A_{+\mathrm{II}}$ in the $\theta = \pi/2$, $\phi = 0$-direction, as previously stated by [179, 206].

proportional to the square of the electron fraction Y_e and the entropy per baryon [85]. As the minimum of $Y_e(\rho)$ for E1 appears at ~ 0.276 compared to ~ 0.293 for the Shen EoS (see fig. 2.13), I attribute the mass difference primarily to this relative difference, and secondarily to changes in the specific entropy which occurs as the LS EoS permits more efficient electron capture. However, note that I may overestimate the spread of the inner core mass $M_{ic,b}$ in dependence with rotation compared to simulations which are carried out with full neutrino transport (Thomas Janka 2009, private communication). The stronger the rotation becomes (at $\Omega_{c,i} \gtrsim 3\pi$), the more centrifugal forces start to play a dominant role, slowing down the entire dynamics of the collapse and causing the core to rebound at sub- or just above supra-nuclear matter densities. The imprint of such behaviour is found in the GW signature by a smaller maximum amplitude and lower peak frequency compared to slower rotating

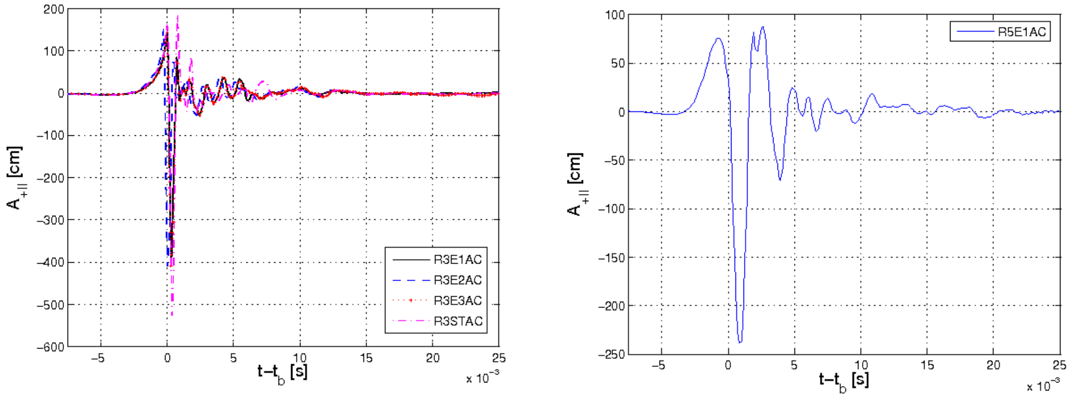

Figure 3.13: **Left panel:** Time evolution of the GW amplitude A_{+II} of the models R3E1AC (solid line), R3E2AC (dashed line), R3E3AC (dotted line), and R3STAC (dashed-dotted line). **Right panel:** Model R5E1AC's GW amplitude A_{+II}.

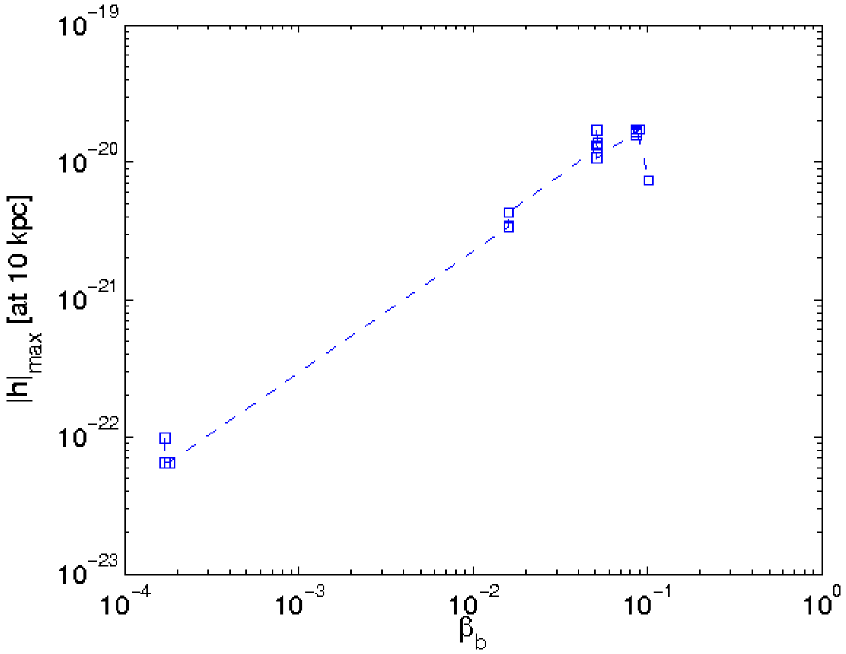

Figure 3.14: Summary of all model's dimensionless peak gravitational wave amplitude $|h|_{max,b}$ at a distance of 10kpc and at core bounce versus the rotation rate β_b. While $|h|_{max,b}$ scales roughly linearly with β_b for rotation rates $\beta_b \lesssim 10\%$, the growing centrifugal force reduces $|h|_{max,b}$ for $\beta_b \gtrsim 10\%$.

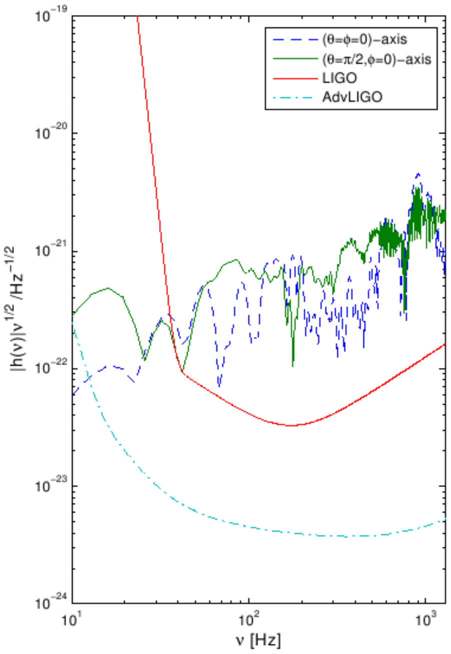

Figure 3.15: Spectral energy distribution of the rotational model R3E1AC's GW signal at a distance of 10 kpc in comparison with the present LIGO strain sensitivity and the possible performance of Advanced LIGO (broadband tuning). The dashed lines show the GW signal for an observer on the rotational axis of the source, the solid lines show the GW signal for an observer in the equatorial plane. Note that the the frequency peak of the latter at ∼ 900 Hz is due to the GW signal from core bounce.

models, as shown in fig. 3.13 and tab. 3.4. Similar to [62], I also find that h_{max} depends sensitively on the competition of both the amount of imposed quadrupolar deformation due to rotation, and on the other hand on the average density level in the for GW emission dynamically relevant region of the inner core. The density in the central region of the PNS is lowered considerably by centrifugal forces, however, no longer compensated by a prominent quadrupolar deformation which results from rapid rotation. The 'optimal' configuration for strong GW emission is now overshot, causing a smaller maximum amplitude and a lower peak frequency. Our findings stand in very good qualitative agreement with [62], who recently performed a large set of 2D core-collapse simulations in GR, with nearly identical microphysical input, but without magnetic fields. However, there are some quantitative differences. For our models that undergo a pressure-dominated bounce, we find spectra which peak on average some 100-150Hz higher than the models in [62]. It has been shown by Dimmelmeier (2007, private communication) that the difference stems from the fact that fully relativistic calculations shift the GW bounce spectrum to lower frequencies in comparison to the ones using an effective, spherically symmetric gravitational potential, as displayed in fig. 3.17. Furthermore, for comparable precollapse rotational configurations, our models return higher peak GW values. We suspect the size of the inner core to be the major cause of this difference. The mass of the inner core

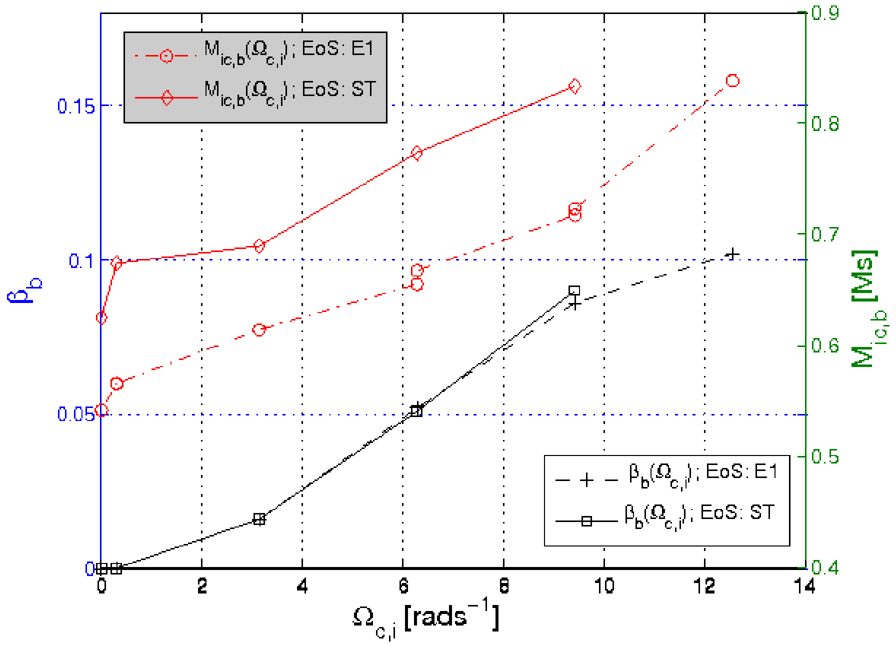

Figure 3.16: Precollapse central angular velocity $\Omega_{c,i}$ versus the rotation rate β_b or the mass of the inner core $M_{ic,b}$ at core bounce for models run with the E1 or ST EoS. We define the mass of the inner core as the mass enclosed by the entropy maximum at core-bounce, i.e. the unshocked region.

for all our simulations is roughly $\sim 0.1 M_\odot$ bigger than the ones of [62]. If we take into account that we are using different electron capture rates ([36] versus [128,98]), I consider the mismatch to be understood, as updated rates cause the mass of the inner core in my models to shrink.

Core bounce: Effects of magnetic fields on the GW signature

The presence of magnetic fields in our models slows down the accretion of angular momentum onto the PNS via field winding. For example, the poloidal field's stress acts on fluid particles moving in the x-y plane in a direction opposing the motion, leading to a deceleration. Thus, while the GW signal from the initially 'weakly' magnetized model R4E1AC is already strongly affected by centrifugal forces at bounce (the frequency peak at bounce is at $\sim$ 385Hz, while the central angular velocity is $\Omega_{c,b} \sim 6200 \text{rads}^{-1}$), the initially more strongly magnetized but otherwise comparable model R4E1FC still undergoes a pressure dominated bounce with a frequency peak at $\sim$860Hz and a central angular velocity of $\Omega_{c,b} \sim 5600 \text{rads}^{-1}$. Note that this effect only gets prominent for initial magnetic fields that are by two orders of magnitude stronger than suggested by [93]. I will discuss the issue of strong magnetic fields in more detail in sec. 3.5.7.

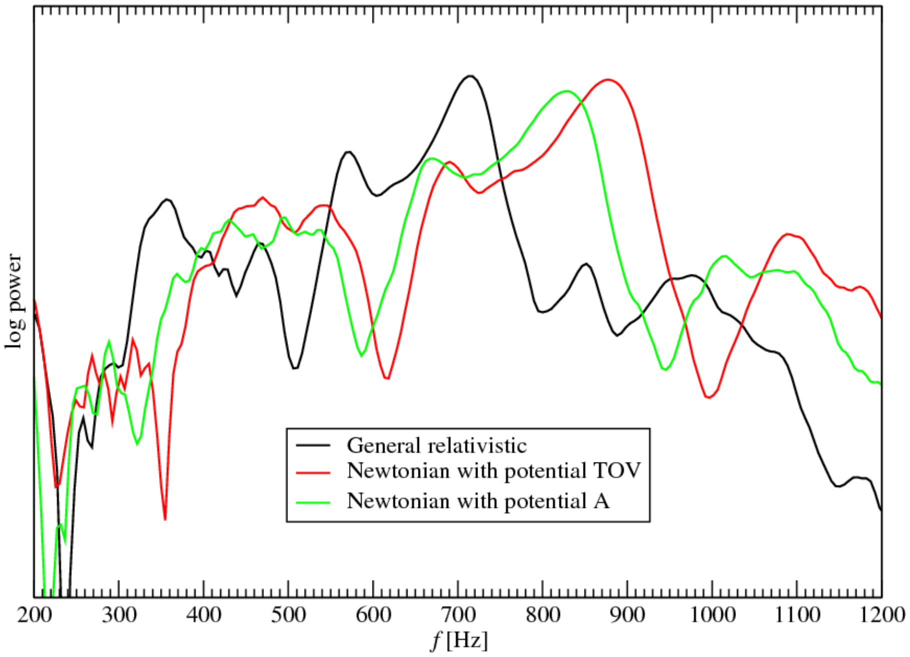

Figure 3.17: Comparison of spectral energy distribution of axisymmetic models with a similar set-up as model R3E1AC. The black line represents a general relativistic calculation, while the green and the red profiles were extracted from simulations with variations of the effective, GR-corrected potential [147] I apply in my simulations. The figure is courtesy of H. Dimmelmeier.

3.5.2 Core bounce: Effects of the EoS on the GW signature

In order to understand the dependence of the GW burst at bounce on the EoS, I repeated several simulations, changing only the EoS while keeping the other parameters fixed. The most prominent change occurs when switching from E1 to ST. Applying the latter EoS in our models leads to systematically larger absolute GW amplitudes at lower frequencies compared to their counterparts, as shown in tab. 3.4 and the left panel of fig. 3.13. This was also observed e.g. by [122], where the two EoS were compared. The shift to lower frequencies can be explained by the fact that the typical timescale of the GW burst at bounce is given by the free-fall timescale $\tau_{dyn} \sim 1/\sqrt{G\overline{\rho}_{ic}}$, where $\overline{\rho}_{ic}$ is the mean density of the inner core. Since E1 leads to substantially higher central densities at core bounce compared to ST in simulations that are not dominated by centrifugal forces, the spectral peak of the GW signal is shifted to higher frequencies. The maximum GW burst amplitude depends on the dynamical timescale, the mass of the inner core as well as on the global density distribution inside the core, as pointed out e.g. by [122,62]. The dimensionless GW amplitude is roughly proportional to M_{ic}, divided by the square of the dynamical timescale ($h \propto M_{ic}/\tau_{dyn}^2$). Hence, it scales approximately linearly with density. This implies that one could expect higher GW peak amplitudes from the more compact cores in the case of E1. However, since models using E1 are slightly more compact in central regions, they exhibit lower densities in the outer layers. This is displayed

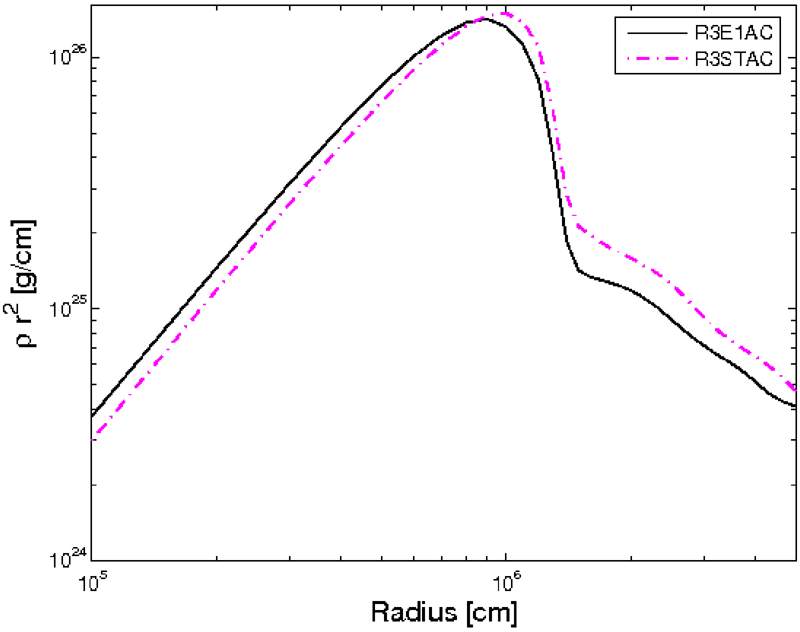

Figure 3.18: Radial profiles of the weighted density ρr^2 of the spherically averaged data at time $t = 0$ relative to core bounce for model R3E1AC and its opposing model R3STAC.

in fig. 3.5. Following the reasoning of [62], I display the quantity ρr^2 in fig. 3.18, which is the essential quantity in the integrand of the quadrupole GW formula (see eq. 1.59). From this plot it is apparent that models run with E1 have higher ρr^2 at small radii, ST yields higher values at intermediate and large radii. Due to their larger volume, these regions contribute more to the total quadrupole integral. For fast rotators ($\Omega_{c,i} \gtrsim 3\pi$), centrifugal forces start to play a dominant role, as already previously observed by [62]. Here, the relative difference between the GW signatures of models run with two EoS decreases, since in the regime of lower densities, the EoS do not differ significantly. When comparing, e.g., model R3E1AC with R3STAC, the absolute size of the burst amplitudes vary roughly 25%, whereas for R4E1AC and R4STAC they only differ by $\sim 4\%$ (see tab. 3.4). In summary I state that it seems very difficult to reveal information about the two different EoS by considering the GW signature from core bounce alone. For models run with either the LS or the Shen EoS and all other parameters being indentical, the differences brought about by the EoS are clearly distinguishable. However, since a small variation in one of the other parameters can easily have a similar effect as the EoS change, it will be nearly impossible to constrain the nuclear EoS in the general case.

When changing the LS compressibility from K=180MeV to K=220MeV or K=375MeV, the features of the collapse dynamics and the corresponding GW emission remain practically unaltered, as displayed in the left panel of fig. 3.13. The only notable difference occurs in the vicinity of core bounce at the center of the PNS: models run with the softest version of the LS EoS (E1) allow the core to bounce at slightly higher central density compared to E2 and E3 (see tab. 3.1). At the same time, models run with E1 exhibit lower densities at larger radii compared to cases where E2 or E3 was applied (see fig. 3.5). However, since the differences in the radial density profiles are relatively low, these effects cancel each other out if we consider again the quantity ρr^2. This leads to GW amplitudes of similar size and frequencies.

3.5.3 Gravitational waves from the nonaxisymmetric rotational instability: General remarks

Rotating proto-neutron stars can be subject to non-axisymmetric rotational instabilities in situations when $T/|W|_{dyn} = \beta$ exceeds a certain critical value. Since the growing instabilities carry the object's spheroidal- into a triaxial configuration with a time-dependent quadrupole moment, strong GW emission is to be expected. The best understood type of instability is the classical dynamical bar mode rotational instability with a threshold value of $\beta_{dyn} \sim 27\%$. However, strong evidence was found by [62] that it is unlikely that the PNS reaches rotation rates required for it to become unstable during the core-collapse and the early postbounce phase of the iron core. Another possibility is the secular instability, triggered at moderately high $\beta_{sec} \sim 14\%$ if a dissipative mechanism is present. It grows on the relatively slow dissipative timescale of the order of a second [228]. Since none of my models reach such high β-values, both instabilities cannot play any role in my simulations.

However, recent work, some of which has been carried out in idealized setups and assumptions [217, 199, 200, 243, 183, 51] and later also in more self-consistent core-collapse simulations [180, 179, 206], suggests that a differentially rotating PNS can become dynamically unstable at $T/|W|$-values as low as $\sim 1\%$. Today this so-called low '$T/|W|$' instability is interpreted as being a resonance phenomenon [243]. The underlying mechanism is suspected to be the amplification of azimuthal (non-axisymmetric) modes at *co-rotation points*, where the pattern speed $\sigma_p = \sigma/m$ of the unstable mode matches the local angular velocity, ($\propto \exp[i(\sigma t - m\Phi)]$) where σ is the mode's eigenfrequency. The PNS is differentially rotating outside a radius of $\sim$ 10km, as displayed in fig. 3.19. This differential rotation provides a reservoir of shear energy which may be tapped by the instability. The latter leads to spiral waves, as displayed in fig. 3.20, which transfer angular momentum outwards (see, e.g., [143]).

Note that this entire phenomenon appears to be closely related to the Papaloizou-Pringle instability which occurs in accretion discs around a central gravitating body [184].

The gravitational wave morphology resulting from the nonaxisymmetric process generally shows narrow-band and highly periodic signals which persist until the end of my simulations. This is shown in fig. 3.21 and the upper panels of fig. 3.25.

Bearing in mind that the effectively measured GW amplitude scales with the number of GW cycles N as $h_{\text{eff}} \propto h\sqrt{N}$ [233] and that it could last for several hundreds of ms as our simulations suggest, the chances of being able to detect such a kind of signal are enhanced compared e.g. to the short duration burst signal at bounce, as one can see in fig. 3.22. In the lower panels of fig. 3.25 the normalized mode amplitudes of the models R3E1AC$_L$ and R4E1FC$_L$ are plotted in order to follow the behaviour

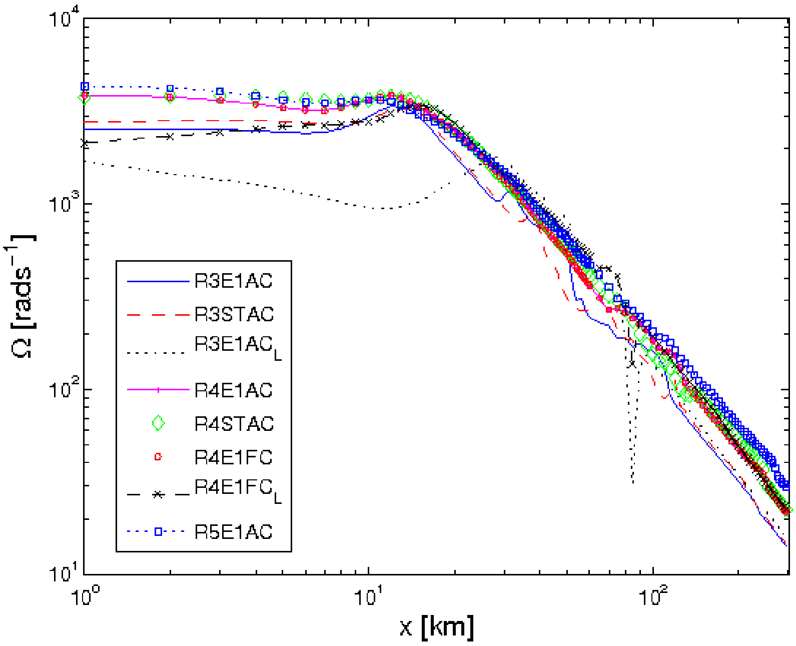

Figure 3.19: Angular velocity profile along the positive x-axis for different models at 10ms after bounce. Note that the hump in the angular velocity profile at about $\sim$ 11km seems to be a generic feature, caused by accreting material with rather high specific angular momentum which accumulates on the nuclear density region of the PNS, as discussed in [178]. It is most pronounced in models with an initial rotation rate $\lesssim$ R3 and gets flatter for high initial rotation rates.

of unstable modes. We generally find modes with density wave numbers $m = 1, 2, 3$ being triggered, with the $m = 1$ or $m = 2$ as the overall dominant ones, depending on the individual model. Furthermore, note that all modes have the same pattern speed, as previously observed by [180, 179, 206]. In fig. 3.20, the upper panels of vorticity plots show nicely a two-armed $m = 2$ spiral pattern, while the middle plot of the lower panel mainly shows the same for a $m = 1$ mode, as we expect from a mode analysis of the corresponding model R4E1FC$_L$ presented in fig. 3.25. After the early linear growth phase, the modes saturate due to Kelvin-Helmholtz shear instabilities, which break the spirals apart in the outer layers, as displayed in fig. 3.20 and previously observed and discussed in e.g. [51]. Note the close relation between the $m = 2$ bar mode and the emission of GWs. The growth and saturation of this mode is imprinted on the GWs emitted. As soon as it exceeds the Cartesian $m = 4$ noise background, strong GW emission at a frequency corresponding to twice the $m = 2$ pattern speed along the pole emerges, with the + and × polarizations shifted by a quarter cycle, as one could expect from GWs emitted by a spinning bar.

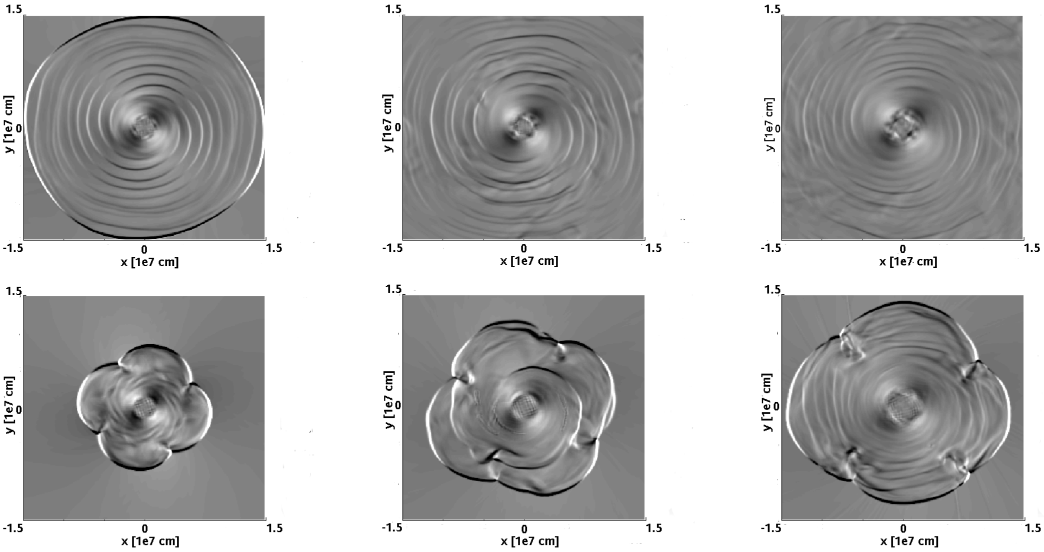

Figure 3.20: Snapshots of the vorticity's z-component $\vec{w_z} = (\nabla\times\vec{v})_z$ in the equatorial plane for models R4STAC (upper panels, $t - t_b = 10, 29, 63$ms) and R4E1FC$_L$ (lower panels, $t - t_b = 10, 29, 54$ms) at three representative instants of their evolution. The innermost 300^2km^2 are displayed, and the colour is encoded in units of [s^{-1}], ranging from -5000 (white) to 5000 (black). The upper panels of vorticity plots show nicely a two-armed $m = 2$ spiral pattern, while the middle plot of the lower panel mainly shows the same for a $m = 1$ mode.

3.5.4 Models without deleptonization in the postbounce phase: Effects of the EoS and magnetic fields on the GW signature from the low T/|W| instability

We now turn to a more detailed discussion of individual simulations. When comparing models that were carried out with the Shen and the LS (E1) EoS, we find that the 'Shen' models emit GWs at significantly higher frequencies than their LS counterparts. This result is a consequence of the fact that the specific angular momentum, which scales as $j_z \propto \rho\omega_z$, is roughly preserved on a mass shell [114]: The innermost part of the PNS in 'Shen' simulations, which rotates in nearly perfect solid body rotation at the pattern speed (see fig. 3.23), has lower density in this radial region. Hence the central rotation rate must in turn be higher to fulfill the conservation law. As an example, we compare the models R3E1AC and R3STAC in detail. While R3E1AC rotates at $t - t_b = 10$ms with a central rotation rate of $\omega_{R3E1AC} \sim 2300$rads^{-1} and has a central density $\rho_{R3STAC} \sim 3.38\times10^{14}$gcm^{-3}, R3STAC revolves with the values of $\omega_{R3STAC} \sim 2800$ rads^{-1} and $\rho_{R3E1AC} \sim 2.63 \times 10^{14}$gcm^{-3}, as displayed in fig. 3.23. Doing the maths, the ratios of $\omega_{R3E1AC}/\omega_{R3STAC}$ to $\rho_{R3STAC}/\rho_{R3STAC}$ are about the same. I also state that the dynamical instability in the 'Shen' cases grows generically faster than in the LS simulations, as shown in fig. 3.21.

I generally observe a slower growth of the T/|W| unstable modes in situations where we applied stronger initial poloidal than toroidal magnetic fields. Although such

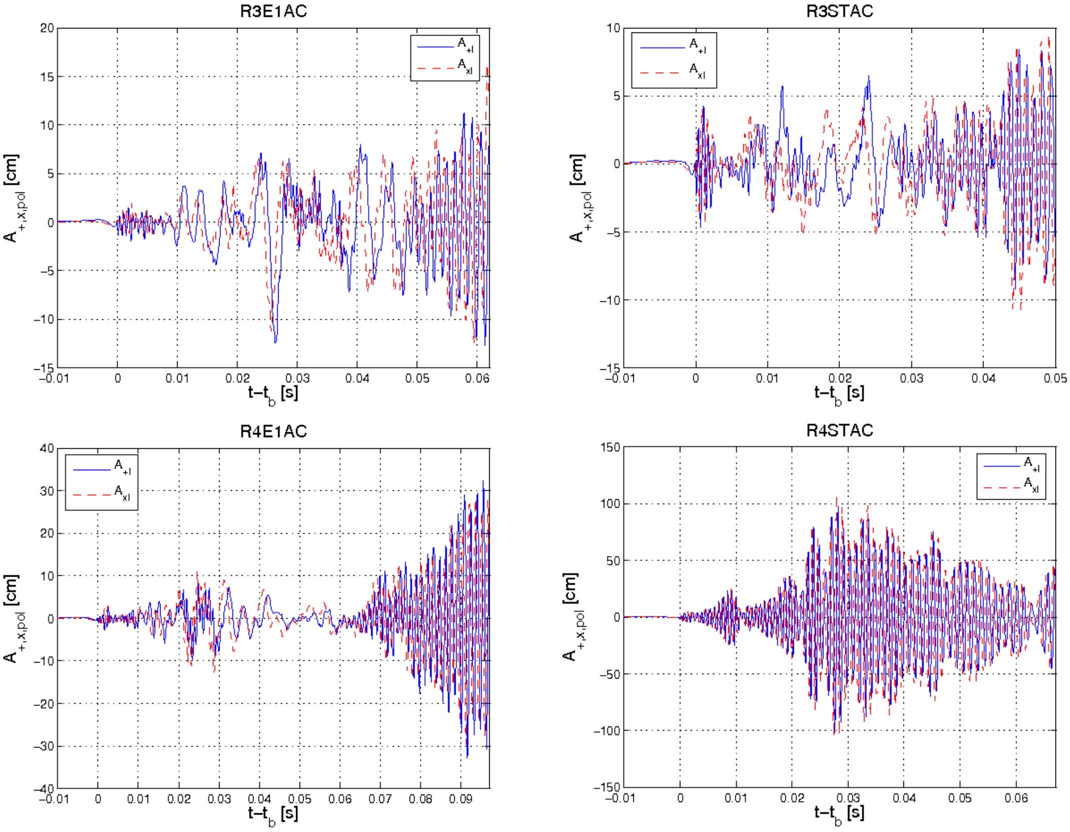

Figure 3.21: The upper left panel shows the time evolution of the GW amplitudes A_+ and $A_\times$ of model R3E1AC emitted along the polar axis. The upper right displays the same for model R3STAC. The lower two panels contain the same information for R4E1AC and R4STAC from left to right. Note that A_+ and $A_\times$ oscillate at the same frequency, phase shifted by $\pi/2$.

magnetic fields ($B_{pol,i} > B_{tor,i}$) may not be motivated by stellar evolution calculations [93], it is still important to study their effects. Model R3E1AC for example starts to emit strong GWs due to the low $T/|W|$ instability around $\sim$ 50ms after bounce, while model R3E1DB does not within the duration of the simulation, which we followed until $\sim$ 65ms after bounce (note, however, that the latter model shows strong growth of the m=1,2,3 modes although GW emission due to the low $T/|W|$ had not set in yet). The poloidal fields are able to suppress the dynamical instability for some time as they slow down the spin-up of the PNS. The detailed discussion of this issue is postponed to sec. 3.5.7.

Centrifugal forces set a limit to the maximum frequency of the GW signal in similar fashion to the situation at core bounce. As discussed in the previous subsection, the limit is somewhere around $\sim$ 935Hz (which is twice the pattern speed!). The faster the initial rotation rate, the stronger the influence of centrifugal forces, which slow down the advection of angular momentum onto the PNS in the postbounce phase. The result is a slower central rotation rate, a lower pattern speed and thus GW emission at lower frequencies. Beside these semi-quantitative statements which allow for the distinction of the simulations' input physics by its GW signature on a

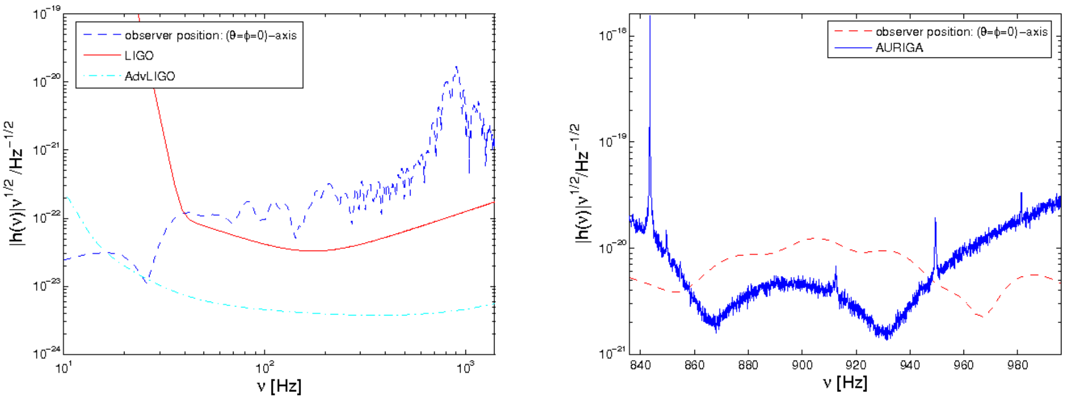

Figure 3.22: Model R4STCA's spectral energy distribution of the GW signal from a low T/|W| instability, emitted along the polar axis at a distance of 10kpc, evaluated for LIGO, Advanced LIGO (left panel) and the AURIGA detector [5] (right panel). Note that the excellent sensitivity of resonant detectors within their 'narrow' bandwith makes them suitable for specialized searches such as a for GWs from so-called low T/|W| instabilities [243].

model-to-model basis, where only one parameter is varied while keeping the others fixed, it is in general very difficult to discern effects of individual features of the input physics in a GW signal that cannot unambiguously be attributed to a specific model. The degeneracy in the simulation results is large with respect to the rotation rate, the magnetic fields and the underlying EoS.

3.5.5 Lower limit

One important question in the context of the low T/|W| instabilities is the following: which is the minimal β value required in self-consistent core-collapse simulation to trigger the onset of the instability? This is important to know, since most stars which undergo a core collapse rotate only slowly [92]; therefore, the higher this value is, the more unlikely it becomes for this to occur in nature. Furthermore, it was pointed out by [62] that even fast rotating PNS can never accrete enough angular momentum to reach the β_{dyn} value required for the onset of the classical bar mode instability.

From tab. 3.4 it becomes obvious that all models with an initial rotation rate of at least R3 ($\beta_b \sim 5.2\%$) sooner or later become low-β dynamically unstable in this particular parameter set, while models run with R2 ($\beta_b \sim 1.6\%$) do not. Hence, the upper limit for the onset of the instability must lie somewhere in between. However, this parameter band is still not very indicative due to its width. Therefore, I carried out two additional simulations A and B, where I systematically changed the rotation rate while keeping the other model parameters fixed as in model R3E1AC. Some initial parameters and the GW relevant quantities are summarized in tab. 3.5.

The minimal $T/|W|$ value we found with the aid of the two extra models to trigger the instability was $\beta_b \sim 2.3\%$ at core bounce (model R3), which is considerably lower

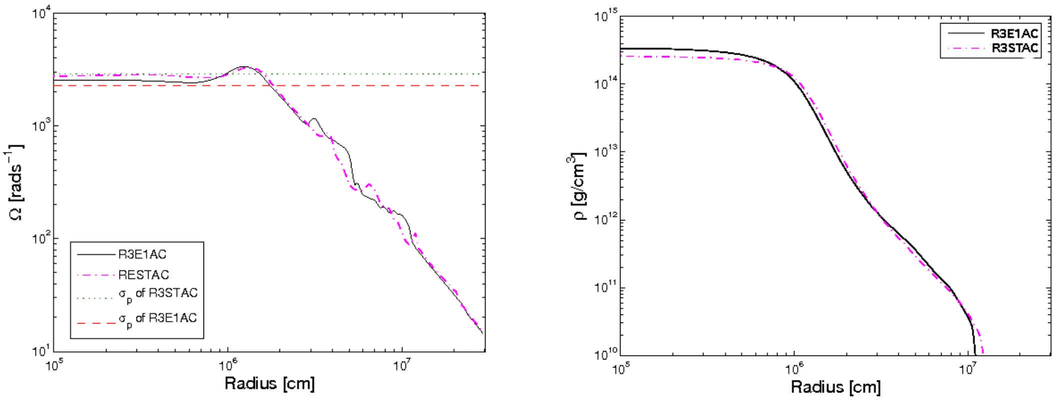

Figure 3.23: **Left panel:** angular velocity profile at $t - t_b \approx 10$ms along the positive x-axis for the models R3E1AC and R3STAC. The pattern speeds of the corresponding simulations are indicated by horizontal lines. **Right panel:** spherically averaged radial density profiles at the same particular time.

Table 3.5: Summary of initial conditions and GW relevant quantities in context with the low β instability.

[a] Model	$\Omega_{c,i}$[rads^{-1}]	β_i	β_b	$\rho_{c,b}[10^{14}gcm^{-3}]$	f_{TW}	$E_{GW}[10^{-9}M_{\odot}c^2]$	t_f[ms]
A	3.93	$1.0{\cdot}10^{-3}$	$2.3 \cdot 10^{-2}$	4.16	670	14	106
B	4.71	$1.4{\cdot}10^{-3}$	$3.2 \cdot 10^{-2}$	4.04	615	35	64

[a] Summary of the models' initial conditions and GW related quantities. $\Omega_{c,i}$ is the precollapse central angular velocity, while $\beta = T/|W|$ is the ratio of rotational to gravitational energy. $\rho_{c,b}$ is the maximum central density at the time of core bounce. E_{GW} is the energy emitted as GWs. f_{TW} [Hz] stands for the spectral peak from the narrow band emission caused by a low $T/|W|$ instability. t_f is the time after core bounce when the simulation was stopped.

than seen in previous studies ([179] found $\beta_b \sim 9\%$, while [206] found $\beta_b \sim 5\%$).

3.5.6 Models with deleptonization during the postbounce phase

The improved input physics of the two leakage models R3E1AC$_L$ and R4E1FC$_L$ allows us to address the question how the inclusion of deleptonization in the postbounce phase quantitatively alters the GW signal of our 3D MHD models. While the results show qualitative agreement with our earlier findings, they clearly deviate in quantitative terms. As the most striking feature, these models show $5 - 10\times$ bigger maximum GW amplitudes due to the nonaxisymmetric dynamics compared to their counterparts that neglect neutrino cooling, as one can see in tab. 3.2 or when comparing fig. 3.21 with fig. 3.25. This suggests that the treatment of postbounce neutrino cooling plays an important role when it comes to the quantitative forecast of GW signals from a low β instability. The neutrino cooling during the postbounce phase leads to a more condensed PNS with a shorter dynamical timescale compared to the purely hydrodynamical treatment, as shown in fig. 3.24. This in turn is

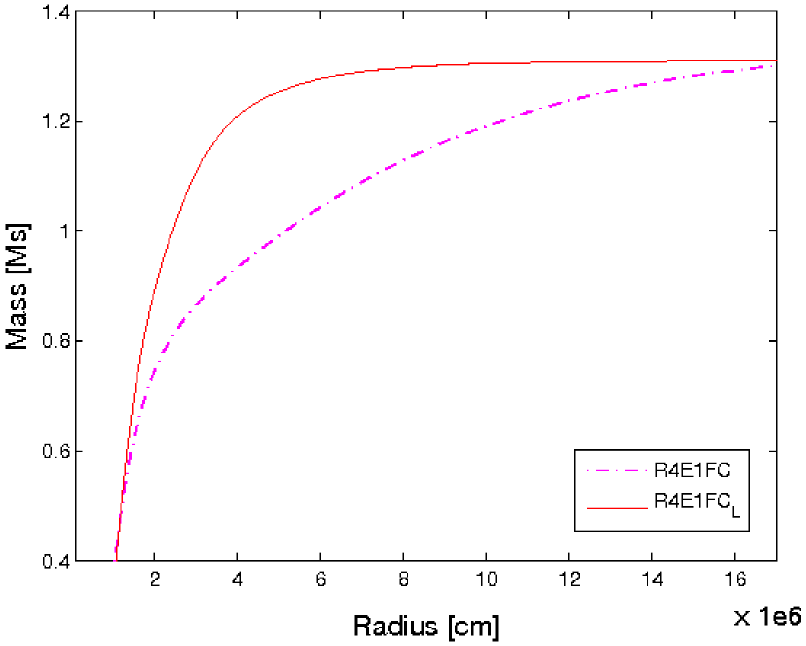

Figure 3.24: Enclosed mass $[M_\odot]$ as a function of radius for models R4E1FC and R4E1FC$_L$ at $t - t_b \approx 25$ ms, which explains the strong GW emission of the latter model.

directly reflected in the dynamical evolution: The shock wave stalls at considerably smaller radii and becomes more quickly unstable to azimuthal fluid modes (see fig. 3.20). Since there is much more matter in the unstable region of these models, the unstable modes grow faster and the triggered spiral density waves cause the emission of much more powerful GWs.

We close this subsection by pointing out that previous core-collapse computations by [180,179,206] show both qualitative and quantitative agreement with the ones presented in the previous subsection as they incorporate nearly identical microphysics. However, they mismatch on a quantitative scale with R3E1AC$_L$ and R4E1FC$_L$ due to the absence of the postbounce neutrino treatment. We point out that our leakage scheme overestimates the compactification of the PNS due to neutrino cooling. The 'reality' for the strength of GW emission therefore should lie between the results from the pure MHD and the leakage treatment. I also want to point out that another limitation which might affect the absolute values of the GW signature from a $T/|W|$ dynamical instability is the grid resolution. Our choice of a uniform grid leads to more than sufficient resolution at the stalled shock, but may underresolve the surface of the PNS. For example, [51] showed that resolution can have a significant effect on the instability's developement and its GW signal.

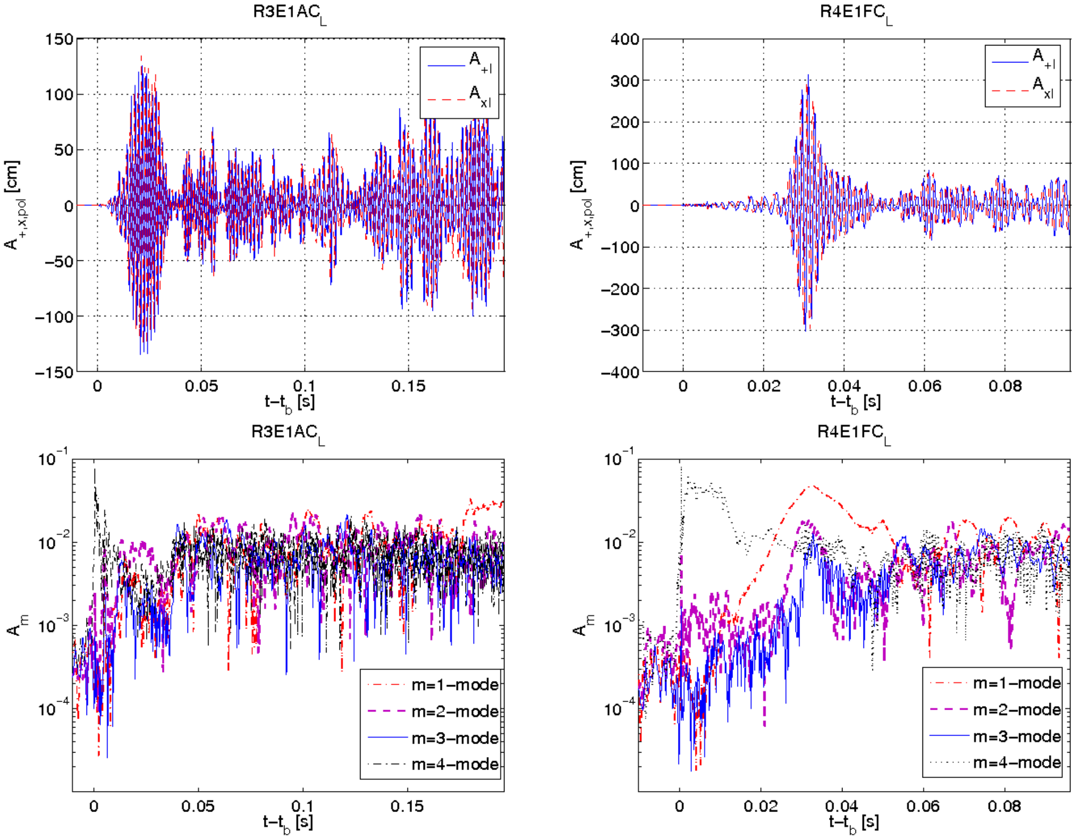

Figure 3.25: The upper left panel displays the emission of the A_+ and the $A_\times$-amplitude along the polar axis for model R3E1AC$_L$. The upper right panel displays the same for model R4E1FC$_L$. The lower two panels show for the same models as above the normalized mode amplitudes A_m for $m = 1, 2, 3, 4$ extracted at a radius of 25km.

3.5.7 The influence of strong magnetic fields on the gravitational wave signature

In the previous three subsections we have shown that the core-collapse dynamics and thus the GW signal of initially weakly or moderately strong magnetized stellar cores ($\lesssim 10^{11}$ G) is hardly affected by magnetic fields. However, in the case of strong initial fields ($\sim 10^{12}$ G) things change dramatically. The combined action of flux-freezing, field winding [151] and also of the magneto-rotational instability MRI [24] generally may lead to growth of magnetic fields by many orders of magnitude to values where the magnetic pressure becomes comparable to matter pressure. This, in turn, triggers a collimated, bipolar jet-explosion (see, e.g., [43], and references therein) by converting magnetic energy into kinetic energy. However, with our current grid setup we are unable to resolve exponential growth triggered by the MRI [68]; the initial magnetic fields are amplified solely by compression during the infall phase and by magnetic winding.

Magnetically-driven explosions are of interest for the prediction of GWs for two reasons. Firstly, the bipolar outflow of matter results in a ‘memory effect’ [233]

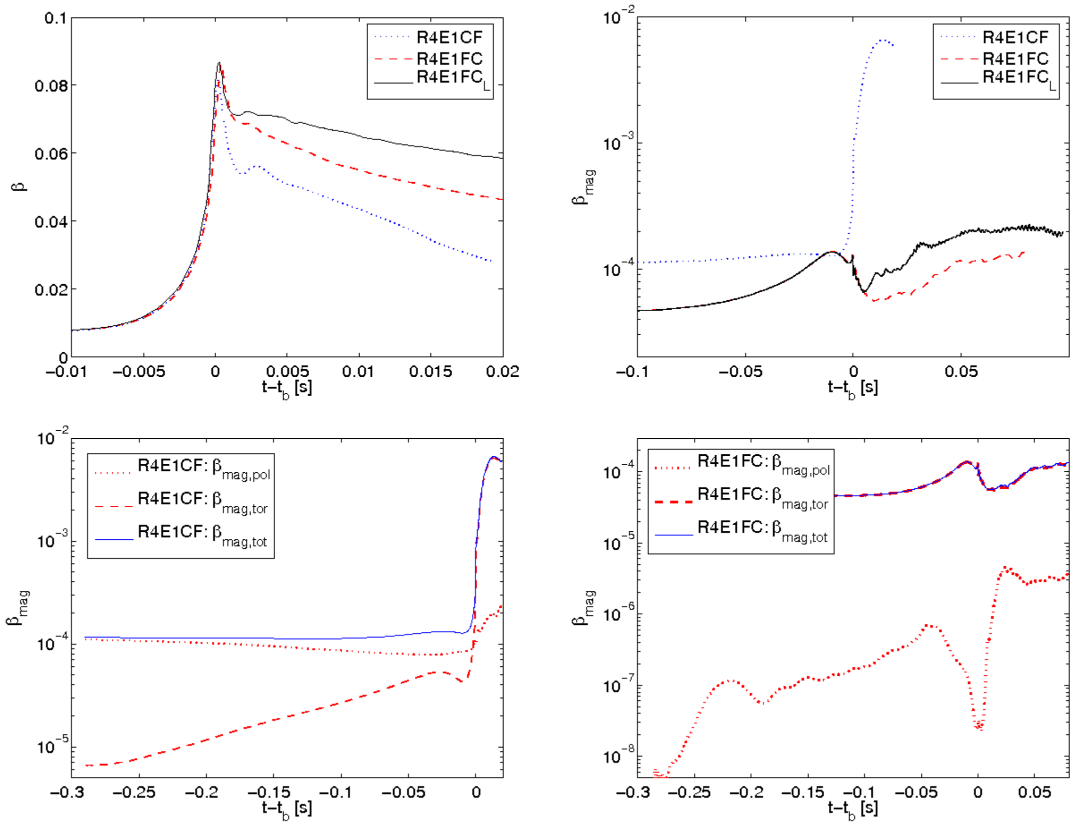

Figure 3.26: The upper left panel shows the first 20ms of the time evolution of the rotational energy parameter $\beta = T/|W|$ of models R4E1CF, R4E1FC and R4E1FC$_L$. The upper right panel displays the time evolution of the magnetic energy parameter β_{mag} for the same models. The small hump in the β_{mag} profiles at $t - t_b = 0$, best visible for R4E1FC and R4E1FC$_L$, stems from the fact that field compression scales as $B \propto \rho^{2/3}$. When the core overshoots its equilibrium position at bounce and re-expands, the density decreases temporarily, which in turn is reflected in the energy density of the magnetic field. The lower left panel shows the evolution of the magnetic parameter $\beta_{tor,mag}$, $\beta_{pol,mag}$ and the total β_{mag} for R4E1CF, the lower right displays the same quantities for R4E1FC.

in the GW signature, as observed e.g. by [170, 218]. As the out-stream of matter usually happens along the rotational axis, the amplitude $A_{+\mathrm{II}}$ will grow over time, scaling as $A_{+\mathrm{II}} \propto 2mv_z^2$, where the ejected mass m increases constantly in the early stage of a magneto-rotational supernova. Secondly, the GW amplitude of these (not necessarily) realistic models is also affected passively by strong magnetic fields, as they rise during collapse and early postbounce phase to values as high as $\sim 10^{16-17}$G. The magnetic energy density may provide sizeable contributions to the overall amplitude, as estimated approximately by the following formula (cf. [122],

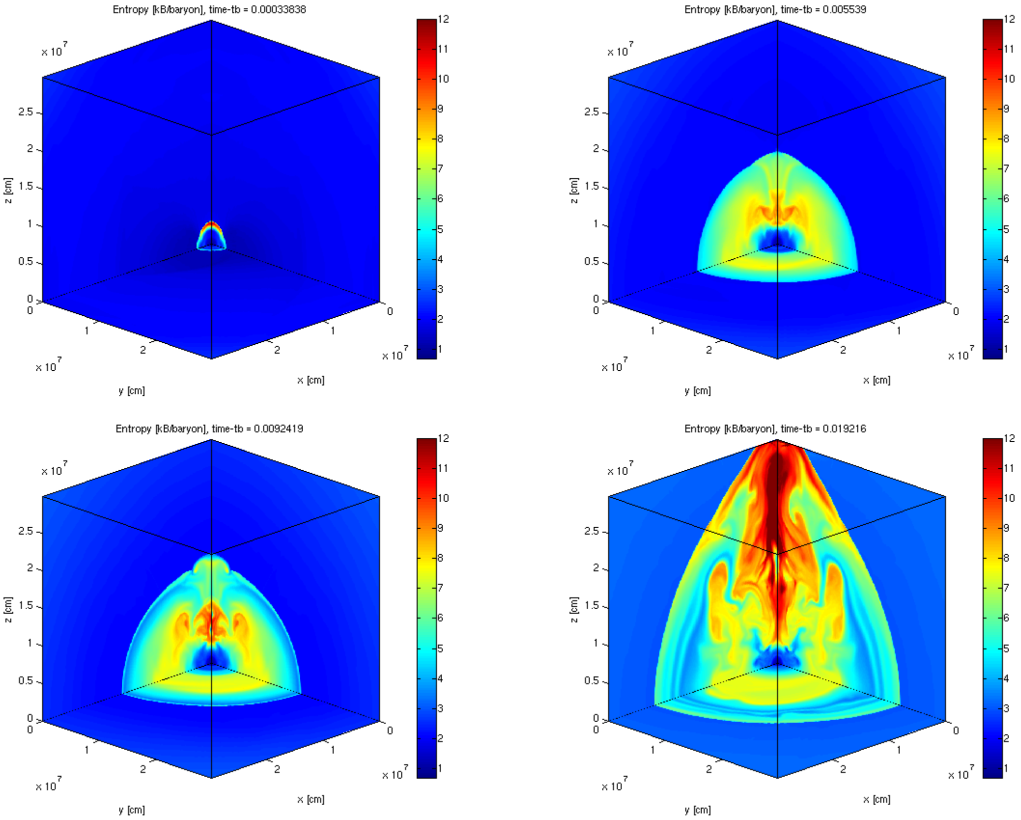
Entropy [kB/baryon], time-tb = 0.00033838

Entropy [kB/baryon], time-tb = 0.005539

Entropy [kB/baryon], time-tb = 0.0092419

Entropy [kB/baryon], time-tb = 0.019216

Figure 3.27: Snapshot of model R4E1CF's entropy distribution in the first octant at representative instants of its evolution. The innermost 300^3km^3 are displayed ($t - t_b = 0.4, 5, 9.2, 19.2$ms, going from the upper left to the lower right).

eq. 22):

$$\eta_{mag} = \frac{\frac{B_c^2}{8\pi}}{\rho_c c^2} \sim 10\% \left(\frac{B_c}{\text{several} \times 10^{17}\text{G}} \right)^2 \left(\frac{\rho_c}{10^{13}\text{gcm}^{-3}} \right)^{-1}, \tag{3.4}$$

where B_c and ρ_c stand for the central values of the magnetic field and density. If magnetic contributions become significant it is necessary to include them in eq. 1.68, which then turns into eq. 1.72.

For the purpose of studying the effect of very strong magnetic fields on the GW signal in 3D, we carried out three runs: R4E1CF, R4E1FC and a leakage model R4E1FC$_L$. In order to overcome the technically challenging simulation of magnetic field growth through small-scale [171] or long-term processes, we applied initial configurations which may not be realized in nature, but can deliver the formation of jets in a similar way as natural field growth would.

Model R4E1CF, which was set up with very strong initial poloidal fields (see tab. 3.1), shows a typical behaviour for a magneto-rotational core collapse followed by a jet-like explosion. Field compression during the collapse phase strongly amplifies both the toroidal- and poloidal magnetic fields, since flux-freezing in stellar collapse guarantees the B-field to scale as $B \sim \rho^{2/3}$. Note that we evaluate *toroidal* and

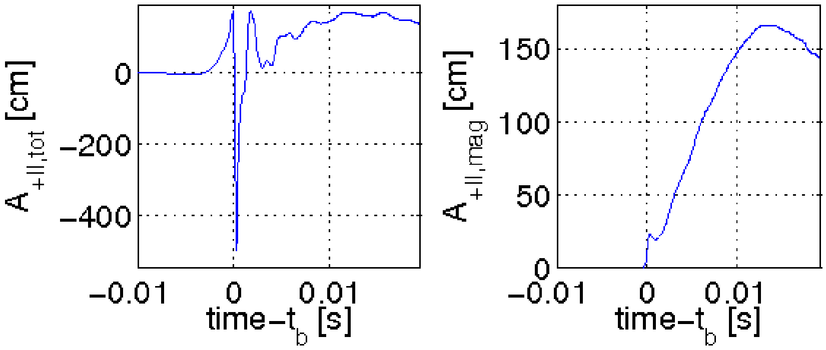

Figure 3.28: Model R4E1CF's time evolution of the *total* quadrupole amplitude $\mathrm{A}_{+\mathrm{II,tot}}$ (left panel) and its contributions from the magnetic field $\mathrm{A}_{+\mathrm{II,mag}}$ (right panel).

poloidal magnetic field components as:

$$B_{tor} = \sqrt{B_x^2 + B_y^2} \tag{3.5}$$

$$B_{pol} = B_z \ . \tag{3.6}$$

Furthermore, the toroidal field is built up by tapping the magnetic energy contained in the poloidal component of the field trough winding, whilst the poloidal field component grows only little during the postbounce phase by the action of meridional motions in the core as shown in the lower left panel of fig. 3.26. In turn, the generated hoop stresses grow fast to reach high values near the polar region, and the ratio of magnetic to matter to fluid pressure reaches ~ 1 (see fig. 3.29).
A bipolar, collimated jet explosion is launched, quickly leaving the computational domain (see fig. 3.27).
Another remarkable feature is that, in contrast to weakly magnetized models, magnetic breaking efficiently decelerates the inner core by redistributing angular momentum [151]. This is shown in the upper left panel of fig. 3.26. Note that model R4E1FC slows down at a higher rate than R4E1FC$_L$ as its fluid can re-expand to larger radii due to the absence of neutrino cooling. The GW signal is displayed in fig. 3.28. In order to distinguish the different contributions to the total GW amplitude $h_{ij,tot}^{TT}$, we split the magnetic and fluid part in the following way:

$$h_{ij,tot}^{TT} = h_{ij,matter}^{TT} + h_{ij,mag}^{TT} \ . \tag{3.7}$$

Around core bounce, the structure of the GW signal is very similar to that of less magnetized cores, exhibiting a clear type I signature. However, shortly after bounce we observe a growing, slowly time-varying offset of $A_{+\mathrm{II}}$ relative to the horizontal axis compared to ring-down oscillations of the weakly-magnetized simulations. There are two reasons for this behaviour. Firstly, the magnetic contribution $A_{+\mathrm{II,mag}}$ to the total GW amplitude grows strongly as magnetic forces act on the core.
Secondly, as we have explained earlier in this subsection, matter-outflow along the z-axis also contributes to the signal. This behaviour was already observed by [170] in

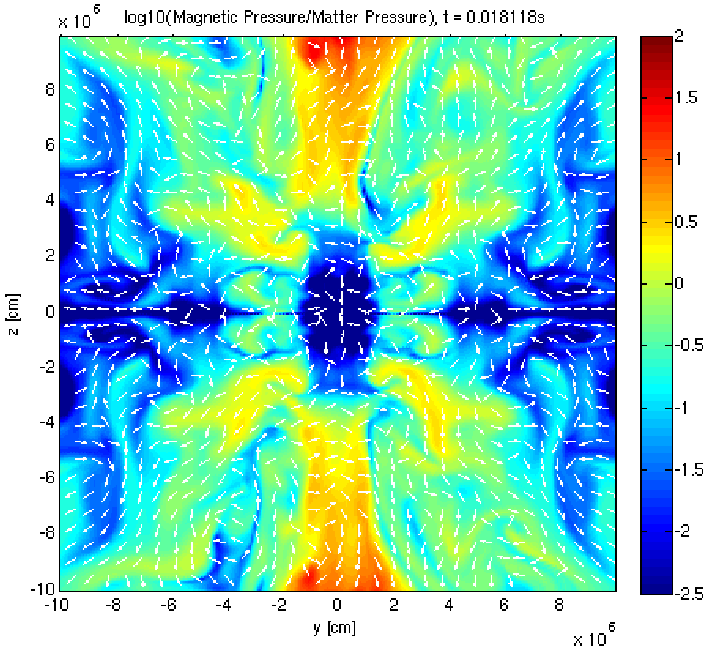

Figure 3.29: Ratio of magnetic- to matter pressure of model R4E1CF in the x-y plane, 18ms after core bounce. The innermost $100^2\mathrm{km}^2$ are displayed.

axisymmetric simulations and its characteristical GW amplitude was named '*type IV* signal' [170]. The contribution of the magnetic amplitudes shrinks with the onset of the jet. The emerging matter gains its kinetic energy by tapping the energy stored in the magnetic field, which causes a drop in β_{mag} and hence also in $A_{+\mathrm{II,mag}}$, as can be seen in figs. 3.26 and 3.28 at about $t - t_b \approx 10$ms. The non-axisymmetric amplitudes are negligible compared to the axisymmetric part of the wave train (see tab. 3.2) and the result of some prompt convective motions and complicated time-variations in the postbounce magnetic field configuration. However, even if a Galactic supernova was optimally orientated for the detection of a type IV signal, it is still questionable whether we could distinguish it in early stages from an ordinary type I signal. The characteristic offset of this particular signal type was suggested e.g. by [170] to be a valid measure of aspherity of the ongoing supernova explosion. However, since the memory effect in the amplitude appears on the long timescale of several times 10ms, it would be out of the LIGO band. The planned space-based DECIGO instrument [113] could make it possible to track the low frequency contribution of such a GW signal in the future.

We point out that at the onset of jet formation around $t - t_b \approx 10$ms, the absolute value of the magnetic field in the polar region at the edge of the PNS is $\sim 10^{16}$G, which translates into a mildly relativistic fast Alfvén speed. Additionally, the velocity of the ejected matter accelerates up to radial velocities of $\sim 0.1c$ when leaving the boundary of our computational domain. These two points challenge the Newtonian treatment of the dynamics in our scheme and suggest the use of a special- or general- relativistic code for the further evolution of the jet dynamics.

Models R4E1FC and R4E1FC$_L$ show a very different dynamical outcome. For these

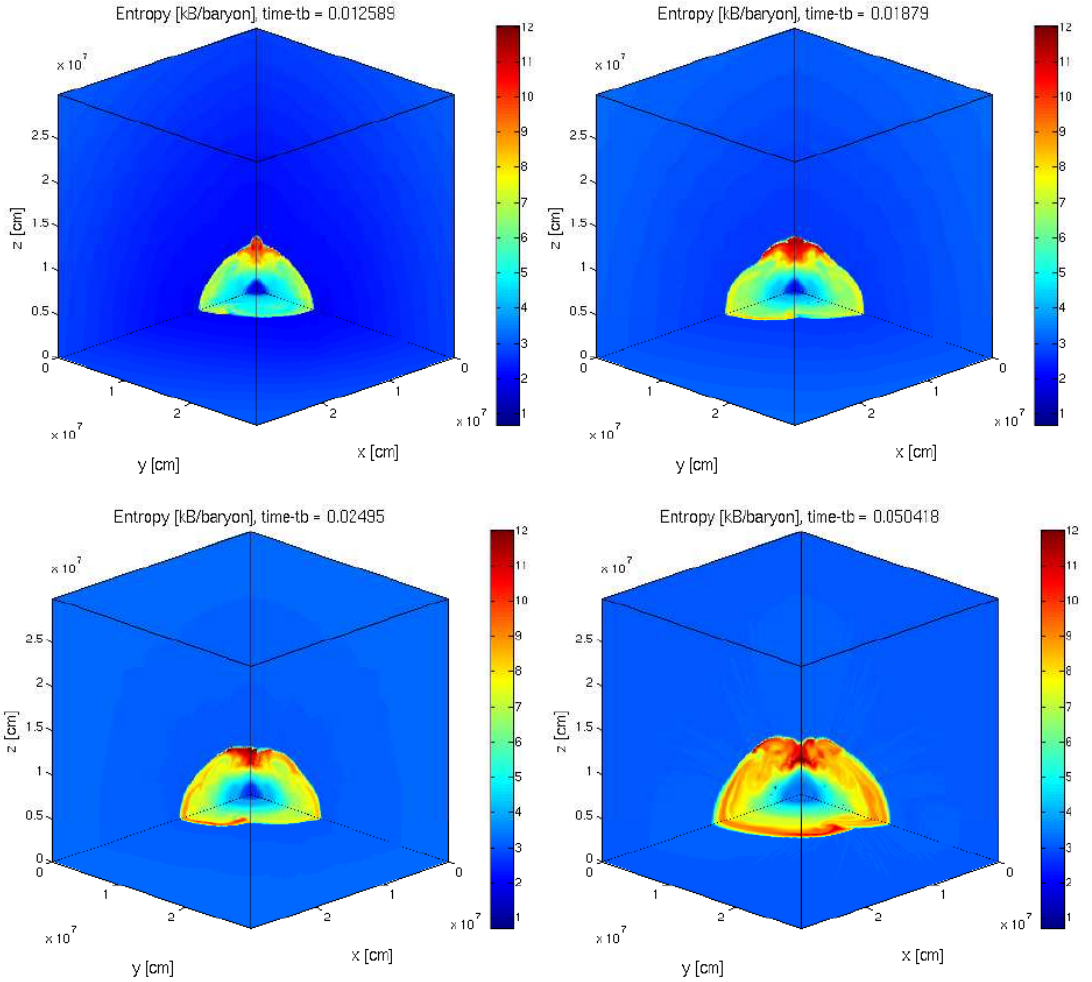

Figure 3.30: Snapshots of model R4E1FC$_L$'s entropy distribution in the first octant at four representative instants of its evolution ($t - t_b = 12.6, 18.7, 25, 50.4$ms, going from the upper left to the lower right). The innermost 300^3km^3 are displayed.

two simulations, we assumed the initial toroidal field to be 10^3 times the values of the poloidal field, as suggested from stellar evolution calculations by [93]. During collapse the magnetic field components primarily grow due to compression as one can see in the lower right panel of fig. 3.26. Right after bounce, the strong toroidal fields in both models cause the onset of a jet, as one can see in the left panel of fig. 3.30. However, surprisingly and in contrast to the previously discussed models, or simulations from [122] where they applied similar initial conditions and obtained jet explosions in 2D, the wind-up of the poloidal- into the toroidal field does not occur efficiently enough. The spiral wave of the standing accretion shock instability (SASI; see, e.g. [34]), which forms at the same time, hinders and delays the growth of a jet, as displayed in the right panel of fig. 3.30. We interpret this phenomenon as follows: matter can easily slip along, but not move perpendicular to the magnetic field. In the x-y plane, the poloidal field's stress acts on matter in the opposite direction of the fluid motion. This is also reflected in the upper left panel of fig.

3.26. It displays clearly that the magnetic forces are not capable of slowing down the inner core in case of strong initial toroidal fields as effectively as the poloidal ones that are anchored in the outer stellar layers. Since models R4E1FC and R4E1FC$_L$ have relatively weak initial poloidal magnetic fields, the fluid, which rotates around the z-axis, can develop nearly unhindered instabilities. The developing spiral waves then successfully counteract the formation of a jet-like explosion by turning matter aside the pole (see fig. 3.30), where the magnetic hoop stresses are strongest (and in axisymmetry most probably would be able to launch a jet at this stage of the simulation). This finding has very recently been confirmed by [125] in 3D GRMHD, but without taking a nuclear EoS or neutrino transport into account.

This corresponds also to my observation from the last subsection where we stated that the low $T/|W|$ instability grows slower in the presence of dominant poloidal fields, because they cause stresses that act against the spiral instabilities. However, further discussion of this phenomenon is beyond the scope of my Thesis and will be investigated in a subsequent study.

The resulting GW signals consequently show a type I signal at core bounce, subsequently followed by a low β instability (see the right panels of fig. 3.25). Although the GW contributions due to magnetic stresses in model R4E1FC$_L$ show qualitatively the same features as the ones from model R4E1CF, they are smaller and dominated by the hydrodynamics part of the amplitude (e. g., $A_{+\mathrm{II,mag}} \sim$ 10cm vs. $A_{+\mathrm{II,matter}}$ $\sim$150cm at 30ms after bounce).

4 3D MHD Core-Collapse Simulations: Results II

> *'It's a dangerous business, Frodo, going out of your door,' he used to say. 'You step into the road, and if you don't keep your feet, there is no telling where you might be swept off to.'*
>
> John Ronald Reuel Tolkien, The Lord of the Rings

Since a CCSN does not proceed in an entirely spherically symmetric way due to reasons outlined in chap. 3, direction-dependent gradients of the gravitational potential are likely to emerge in 3D simulations. This in turn is reflected in non-uniform matter accelerations (cf. sec. 2.2 and eqs. 2.51 ff.), leading to a slightly modified temporal outcome of numerical simulations where the dimensionality of the gravitational potential is varied while keeping the other parameters fixed.

In this chapter, I investigate the influence of axisymmetric (2D) and 3D potentials (cf. sec. 2.2.2) on the the resulting GW signature of rotating stellar core collapse. This will allow us to probe the robustness of GW predictions obtained by simulations which employ the computationally considerably 'cheaper' 1D approach (see chap. 3).

4.1 Description of the magnetohydrodynamical models

For the CCSNe simulations and their GW signatures presented in this chap. 4, I employ the `ELEPHANT` code (see chap. 2). In this entire section, the *multidimensional* gravitational potentials are calculated via methods described in sec. 2.2.2. The monopole term of the resulting gravitational potential is always GR-corrected according to eq. 2.60 and [147]. As for the treatment of the deleptonization during the collapse phase, I apply the Y_e vs. ρ parametrization scheme [136]. For this I use the results obtained with the `Agile-Boltztran` code [134], including the Lattimer-Swesty EoS (K=180 MeV) [130] and the electron capture rates from [36] (see sec. 2.4 for more details). The 3D computational domain consists of 600^3 zones with an equidistant grid spacing of 1km. The models are named after the conventions described in chap. 3. The subscripts $2d$ and $3d2d$ denote simulations which were carried out either with an axisymmetric (2D) or a 3D Poisson solver for gravity. For the latter, axisymmetric boundary conditions were assumed (cf. fig. 4.3).

The models' initial conditions and similar relevant quantities are summarized in tab.

Table 4.1: Summary of initial conditions of rapidly rotating models [a]

Model	$\Omega_{c,i}$ [rads^{-1}]	β_i	β_b	EoS	$\rho_b[\frac{g}{cm^3}]$	$B_{tor,i}$[G]	$B_{pol,i}$[G]	$E_m/\lvert W\rvert_b$	$E_m/\lvert W\rvert_f$
R2E1AC$_{2d}$	π	0.64×10^{-3}	1.6×10^{-2}	E1	4.27×10^{14}	1×10^6	5×10^9	6.9×10^{-9}	5.7×10^{-6}
R2E1AC$_{3d2d}$	π	0.64×10^{-3}	1.6×10^{-2}	E1	4.15×10^{14}	1×10^6	5×10^9	7.8×10^{-9}	5.8×10^{-6}
R3E1AC$_{2d}$	2π	0.26×10^{-2}	4.9×10^{-2}	E1	3.82×10^{14}	1×10^6	5×10^9	9.8×10^{-9}	9.6×10^{-6}
R3E1AC$_{3d2d}$	2π	0.26×10^{-2}	4.8×10^{-2}	E1	3.66×10^{14}	1×10^6	5×10^9	9.9×10^{-9}	1.4×10^{-5}

[a] The subscript i stands for *initial*, b for *bounce*, while f stands for $final$. ρ_b is the maximum central density at the time of core bounce. $B_{pol,i}$ and $B_{tor,i}$ abbreviate the initially imposed toroidal and poloidal magnetic fields, whereas $E_m/|W|$ stands for the ratio of magnetic to gravitational energy.

Table 4.2: Summary of GW related quantities of rapidly rotating models [a]

Model	t_f[ms]	$E_{GW}[M_\odot c^2]$	dir.	$\lvert A_{+,b,max}\rvert$	$\lvert A_{\times,b,max}\rvert$	$\lvert A_{+,pb,max}\rvert$	$\lvert A_{\times,pb,max}\rvert$	$f_b[Hz]$	$f_{TW}[Hz]$
R2E1AC$_{2d}$	72.4	9.71×10^{-9}	I	2	2	9	10	-	-
			II	159	< 1	2	2	867	-
R2E1AC$_{3d2d}$	60.5	8.18×10^{-9}	I	2	1	8	9	-	-
			II	145	< 1	2	2	896	-
R3E1AC$_{2d}$	60.2	9.49×10^{-8}	I	1	1	24	25	-	745
			II	512	< 1	13	3	958	-
R3E1AC$_{3d2d}$	67.0	7.31×10^{-8}	I	2	< 1	26	25	-	721
			II	489	< 1	15	4	930	-

[a] t_f is the time after core bounce when the simulation was stopped. E_{GW} is the total energy released in gravitational radiation. I present the maximum amplitudes at different stages of their time-evolution in polar (I) and equatorial (II) direction. The subscripts b and pb stand for bounce and postbounce. f_b denotes the peak frequency of the GW burst at bounce, while f_{TW} stands for the spectral peak from the narrow band emission caused by a low $T/|W|$ instability.

4.1, whilst the GW data is listed in tab. 4.2.

4.2 Axisymmetric (2D) gravity

In order to investigate the influence of an axisymmetric gravitational potential (see sec. 2.2.2) on the resulting GW signal, I carried out two rapidly rotating models, denoted R2E1AC$_{2d}$ and R3E1AC$_{2d}$. The ‘pure’ hydrodynamical treatment of the postbounce phase and the comparison with models which were carried out with 1D gravity allows for a clear distinction of features which are caused by 2D gravity without having other physical parameters interfering.

The aforementioned models undergo typical SN dynamics affiliated with rapidly rotating core collapse (see sec. 3.5 for a detailed discussion). In consequence, they qualitatively show the same GW signatures both in signal shape and frequency band compared to their reference models with spherically symmetric gravity, i.e. a type I signal at core bounce, followed by GW emission due to a low $T/|W|$ instability in the early postbounce phase (only R3E1AC$_{2d}$).

However, the 2D treatment of gravity alters the CCSN dynamics considerably quan-

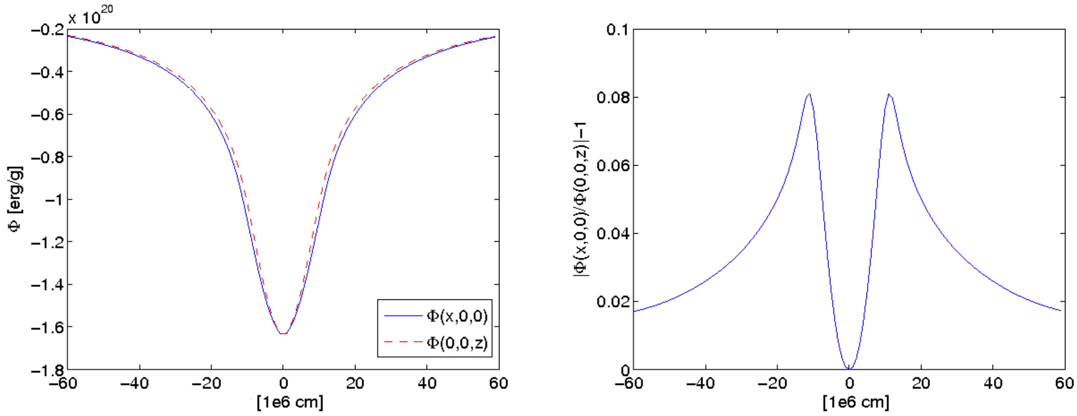

Figure 4.1: **Left panel:** Comparison of the gravitational potential Φ of the rotating model R3E1AC$_{2d}$ along the x- and z-axis ($y = z = 0$ or $x = y = 0$) at core bounce ($t - t_b = 0$). Note that the gravitational potential along the x- and y-axis is equal due to axisymmetry. **Right panel:** Relative difference $|\Phi(x, 0, 0)/\Phi(0, 0, z)| - 1$.

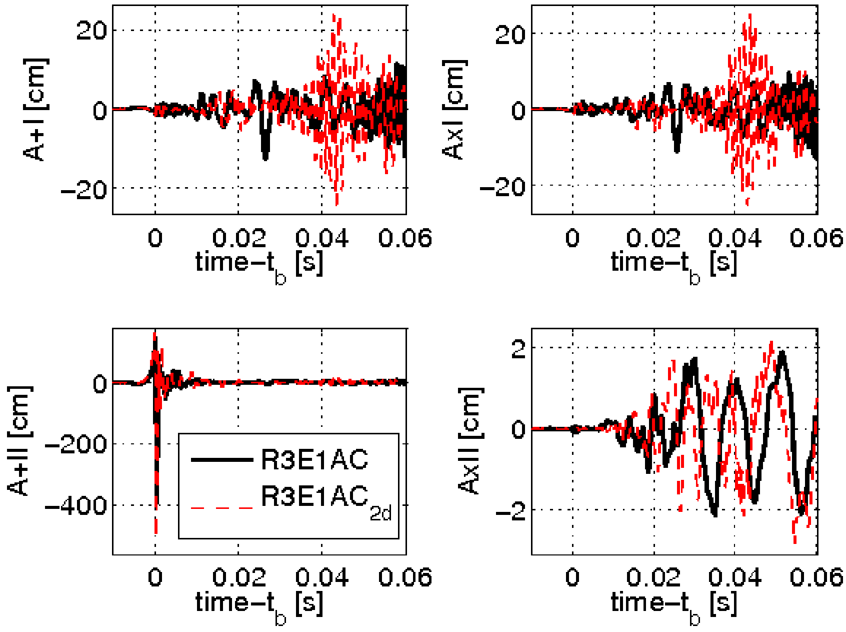

Figure 4.2: Time evolution of the quadrupole amplitudes $A_{+\mathrm{I}}$, A_{xI}, $A_{+\mathrm{II}}$, and A_{xII} for the rapidly rotating models R3E1AC and R3E1AC$_{2d}$. Note that the GW amplitudes of R3E1AC$_{2d}$ at core bounce ($A_{+\mathrm{II}}$) and due to the low $T/|W|$ instability ($A_{+\mathrm{I}}$, A_{xI}) are considerably larger compared to R3E1AC.

titatively and thus also the resulting GW signature. I will now outline the most prominent features.

The axisymmetric acceleration of the fluid due to gravity – a steeper gradient of Φ along the polar $z-$axis compared to the x-y plane for radii $\lesssim$ 20km (see the left panel of fig. 4.1) – leads to stronger centrifugal forces (β_b of R3E1AC$_{2d}$ is 4.9% compared to model R1E1AC's β_b of 5.2%). This causes a somewhat more oblate configuration of the PNS around bounce and the early postbounce phase compared to models which were run with a monopolar approach for gravity. This in direct consequence results in considerably stronger GW emission at core bounce, with an enhancement of the maximum amplitude of $\sim 20\% - 30\%$ (see fig. 4.2 and tab. 4.2) compared to the reference models with 1D gravity (see tab. 3.4).

Because the type I GW signal from core bounce is purely axisymmetric (see sec. 3.5, and references therein) and as the underlying input physics of the model is 'complete', I consider the trend found here as robust. This finding therefore indicates that an axisymmetric treatment of gravity, which comes along with an increase of $\sim 5\%$ of CPU time spent, is a necessity for future, quantitative GW predictions of type I signals at core bounce.

Significant differences also occur for the GW signal from the low $T/|W|$ instability when comparing R3E1AC$_{2d}$ with R3E1AC. The axisymmetric treatment of gravity can account better for spiral structures. This in turn leads to a faster growth of unstable modes (see eq. 1.82 and sec. 3.5.3) to more prominent values, causing i) an earlier onset of the GW emission and ii) maximum amplitudes up to a factor of 2 larger in model R3E1AC$_{2d}$ compared to its reference R3E1AC (see the upper panels of fig. 4.2).

However, a more decisive assessment of the reliability of the above findings can only be reached via reference calculations which consider gravity in full 3D. As a next step, I therefore carried out comparative models with full 3D treatment of gravity (see sec. 2.2.2) within the innermost zones.

4.3 3D gravity

Motivated by the findings of sec. 4.2 and in order to investigate the trends found there, I carried out two more simulations (R2E1AC$_{3d2d}$, R3E1AC$_{3d2d}$) which incorporate a full 3D treatment of gravity (see sec. 2.2.2) within the innermost 80^3 km^3. The boundary conditions are provided by the adjacent axisymmetric solution of the Poisson equation (see fig. 4.3). Inside this domain, the 3D Poisson equation is solved via the the direct sparse matrix method described in sec. 2.2.2 (cf. fig. 4.3). With this setup, the *total* treatment of gravity consumes about $\sim 10\%$ of the CPU time spent. As the innermost central cube contains $\sim 99\%$ of the total mass treated in my simulations, it makes the dominant contributions to the overall gravitational potential.

During the collapse and the early postbounce phase ($t - t_b \lesssim 20 - 30$ms), the hydrodynamical evolution of models R2E1AC$_{3d2d}$ and R3E1AC$_{3d2d}$ is purely axisymmetric and therefore fits nearly perfectly – apart from stochastic deviations due to the finite accuracy of numerical simulations (cf. sec. 2.2) – the behaviour of the reference models R2E1AC$_{2d}$ and R3E1AC$_{2d}$ (see sec. 4.2), as displayed in the upper panels of fig. 4.5. In consequence, the GW signal from models run with 3D gravity also show a $\sim 20 - 30\%$ enhanced peak amplitude at core bounce compared to models which incorporate only 1D gravity due to the same reasons already outlined in sec.

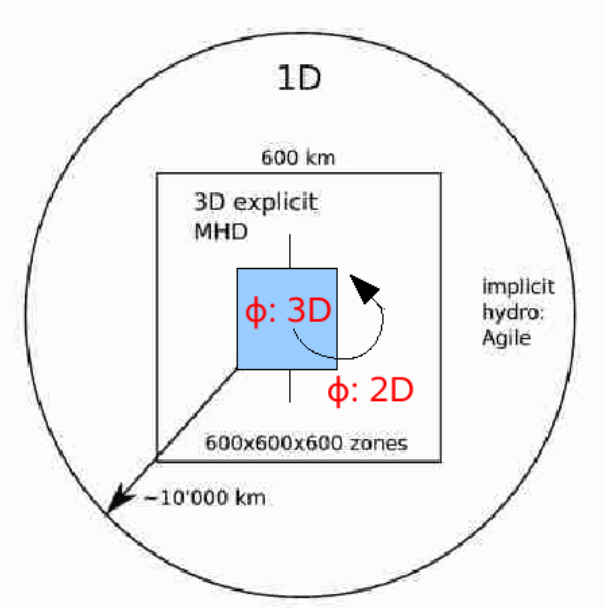

Figure 4.3: Schematic description of the code set-up when 3D gravity is taken into account: the 3D computational domain is embedded in a larger spherically symmetric domain. The axisymmetric gravitational potential $\Phi(r, z)$ provides the boundary conditions for the central cube of 80^3 zones size, where gravity is treated in full 3D.

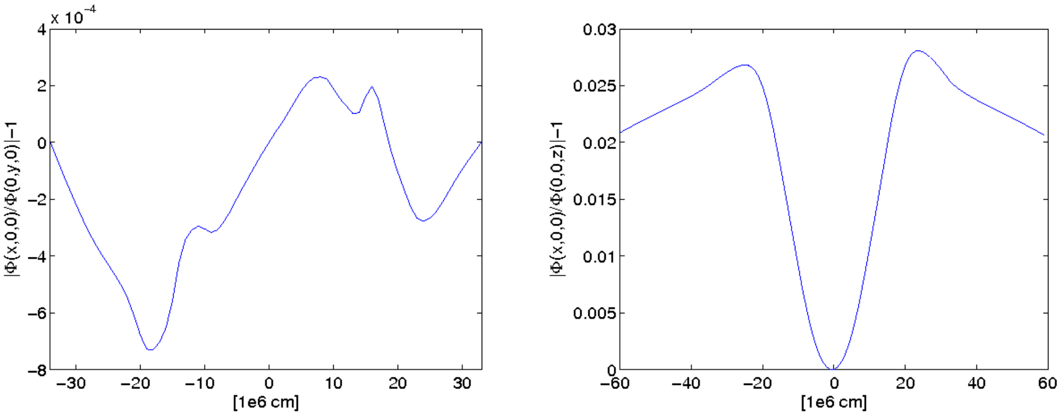

Figure 4.4: Comparison of the gravitational potential Φ of the rotating model R3E1AC$_{3d2d}$ along the x-, y- and z-axis at 67ms after core bounce. **Left panel:** Relative difference $|\Phi(x, 0, 0)/\Phi(0, y, 0)| - 1$. **Right panel:** Relative difference $|\Phi(x, 0, 0)/\Phi(0, 0, z)| - 1$.

4.2 (see the lower left panel of fig. 4.6 and tab. 4.2).

The later postbounce phase ($t - t_b \gtrsim$ 30ms) of each of the models R2E1AC$_{3d2d}$ and R3E1AC$_{3d2d}$ shows a significantly different dynamical evolution compared to their counterparts R2E1AC$_{2d}$ and R3E1AC$_{2d}$. Emerging local inhomogenities in the density distribution combined with a 3D treatment of gravity allow for nonaxisymmetric accelerations of the fluid (see fig. 4.5) which in turn lead to the breaking

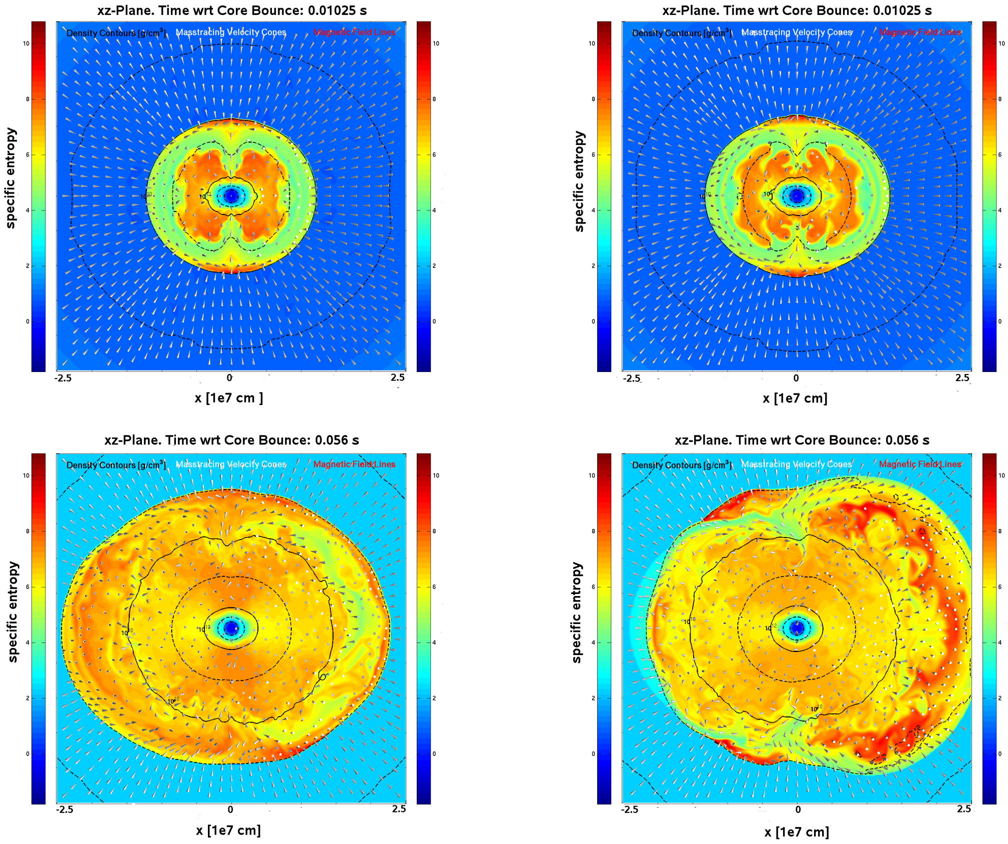

Figure 4.5: Comparison of model R3E1AC$_{2d}$'s (left panels) and R3E1AC$_{3d2d}$'s (right panels) specific entropy [k$_B$/baryon] profiles at different instances of time. The upper panels display snapshots at 10ms, the lower panels at 56ms after bounce. The innermost 500^{2}km^2 in the x-z plane are displayed. The entropy color bar scales from 0 (blue) to 10 (red).

of the axisymmetric configuration (see the lower panels of fig. 4.2). These central, nonaxisymmetric perturbations then propagate outwards and become dynamically relevant in the regime of the stalled shock ($R \gtrsim$ 200km, $\rho \lesssim 10^{10}$[g/cm^3]), as shown in the lower right panel of fig. 4.2.

The latter finding implies that both a spherically symmetric and an axisymmetric treatment of gravity are too restrictive for a quantitative description of the post-bounce dynamics of rapidly rotating CCSN models.

In agreement with sec. 4.2, again only one model (R3E1AC$_{3d2d}$) emits GWs due to the low $T/|W|$ instability. It can be deduced from the upper panels of fig. 4.6 and tab. 4.2 that the GW characteristics of this model fit those of model R3E1AC$_{2d}$ surprisingly well, even though their dynamical evolutions diverge vastly.

This phenomenon can be explained by the fact that the dominant contributions to the GW amplitudes are usually emitted at radii $R \lesssim$ 30km in my models. In this central region, the rotation rate is highest (cf. fig. 3.19) and the centrifugal forces, which carry the PNS into an oblate, axisymmetric deformation, are at their strongest. Therefore, the dynamics of the PNS region which is relevant to the

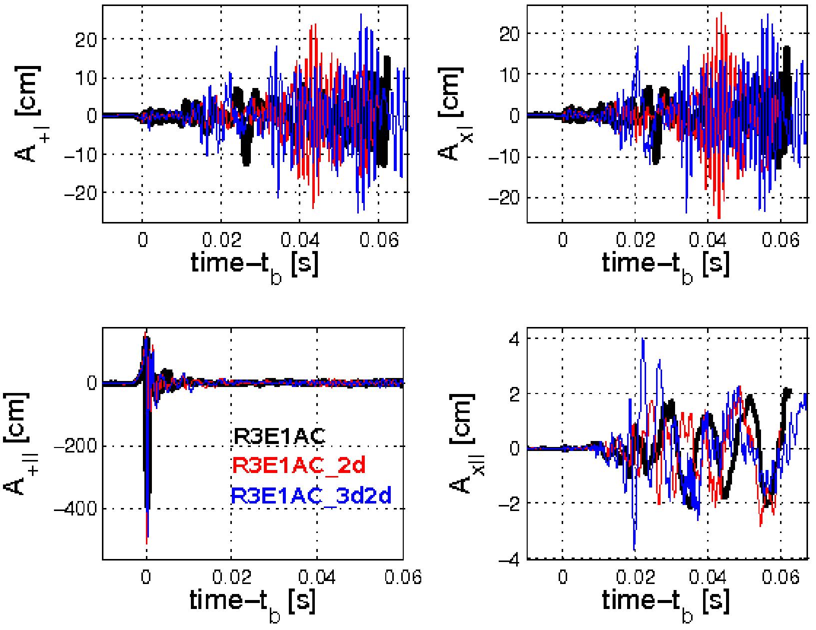

Figure 4.6: Time evolution of the quadrupole amplitudes $A_{+\mathrm{I}}$, A_{xI}, $A_{+\mathrm{II}}$, and A_{xII} for the rapidly rotating models R3E1AC, R3E1AC$_{2d}$ and R3E1AC$_{3d2d}$. Note that the GW amplitudes of R3E1AC$_{2d}$ and R3E1AC$_{3d2d}$ at core bounce ($A_{+\mathrm{II}}$) and due to the low $T/|W|$ instability ($A_{+\mathrm{I}}$, A_{xI}) are considerably larger compared to R3E1AC.

GW emission process is sufficiently well captured by an axisymmetric gravitational potential, even though the evolution of model R3E1AC$_{3d2d}$ clearly deviates in the outer layers from axisymmetry.

I therefore conclude that the inclusion of 3D gravity in my rapidly rotating models is not an option, but a necessity for the quantitative outcome of the simulations. However, the computationally cheaper treatment of gravity in axisymmetry still might be an option if one is only interested in the GW signature and not in the overall dynamics.

As next steps, I plan i) to enlarge the size of the central domain where gravity is treated in 3D, and ii) to implement gravity in a way which is dependent on the centre of mass and not on the computational origin.

Point i) is important in order to investigate in further detail the dynamical relevance of gravity with respect to the overall supernova evolution and the SASI (see, e.g. [34]). Point ii) will enable us to examine in a fully self-consistent way if core g-modes really play a crucial role in the CCSN explosion mechanism, as has been found so far only by Burrows [45, 46]. However, these steps go beyond the scope of this dissertation and will be addressed in subsequent work.


WHAT YOU BROUGHT TO SEMINAR AND WHAT IT SAYS ABOUT YOU:
Stuff to take notes: First year. Foolishly thinks he'll ever need notes again.
Reading material: Third year. Just here for show.
Didn't bring anything: ABD/Postdoc. Has nothing better to do.
Laptop: Young Assistant Professor. Working on three proposals at the same time.
Playing with latest Gadget/Gizmo: Full Professor. Loooves new toys.
tap tap
JORGE CHAM © 2008
WWW.PHDCOMICS.COM

5 Summary and Conclusions

> *Nunc agam modice nec longius progrediar quam me mea fides et causa ipsa coget.*
>
> Cicero, Pro Caelio

Gravitational wave astronomy may soon become a reality and will allow humankind to address questions about many different astrophysical objects that are hidden from electromagnetic detection. Within the past few years, the first generation of the ground-based GW detectors LIGO (USA), VIRGO (Italy), GEO600 (Germany), and TAMA (Japan) have got very close to or even reached design sensitivity and have collected partially coincident data, as discussed by [14]. Lately, the two 4km LIGO detectors were upgraded to sensitivities increased by a factor of 2-3 (enhanced LIGO, see [191]) and resumed observations in 2009. Upgrades of the three LIGO interferometers and VIRGO are expected to be completed by 2014 and will increase the observable volume by a factor of ~ 1000.

Operating at such a high level of precision, GW detectors should be sensitive to many different sources such as compact binary coalescence from black holes and neutron stars up to distances of several 100 megaparsecs, but might also very likely produce the first detections of, e.g., black-hole and neutron star mergers, and neutron star normal mode oscillations [39].

Ever since the first attempts to detect gravitational waves, core-collapse supernovae have been deemed prime candidates of GWs for earth-based detectors. Their GWs could provide us access to the electromagnetically hidden compact inner core of some such cataclysmic events, supplying us with valuable information about e.g., the angular momentum distribution and the baryonic equation of state, both of which are uncertain. Furthermore, they might even help constrain theoretically predicted SN mechanisms [174]. However, GW astronomy strongly depends on the extensive data processing of detector output on the basis of reliable GW estimates, which have only recently become feasible due to the emerging power of supercomputers. Moreover, the parameter space of possible initial conditions of stellar core collapse is huge since many progenitor configurations are possible at the onset of collapse.

In this dissertation, I reported on the dependences of the 3D GW form of the early postbounce phase ($t \lesssim 200$ ms) upon a variety of these conditions. For unmodelled burst analysis techiques [14], which must be applied for GWs from CCSN, partial information on wave forms is already useful, e.g. typical waveform features, approximate spectra and the type of polarization and burst duration.

With my model series containing more than 30 three-dimensional MHD core-collapse supernova simulations, I have tried to probe the GW signature with respect to different nuclear equations of state, rotation rates, poloidal and toroidal magnetic fields, multidimensional Poisson solvers for the gravitational potential, and postbounce neutrino transport approximations.

Similar to the findings of e.g. [145, 62, 149, 174, 209], my results show that in the case of non- and slowly rotating models the GWs emitted during the first 20ms after bounce are predominantly due to entropy-driven ‘prompt’ convection that is caused by the presence of a negative radial entropy gradient. It turns out that the crucial parameter to study this stochastic phenomenon is the choice of the spatial resolution and not the inclusion of a neutrino transport scheme. This parameter has a twofold effect: Firstly, it governs the influence of numerical noise, since a better resolution leads to lower numerical seed perturbations and thus smaller grid alignment effects. Therefore, the GW amplitude at core bounce is smaller for higher spatial resolution. Secondly, it enhances the ability to follow dynamical features, as better numerical resolution causes less numerical dissipation in the system, which eases the dynamical effects which follow, leading to larger GW amplitudes after the core bounce compared to less resolved models.

Furthermore, I could show in simulations without deleptonization in the postbounce phase that the waveforms obtained from this early stage of a supernova explosion contain indirect information about the underlying EoS. Due to different radial locations of the convectively unstable region and the amount of matter it contains, I was able to distinguish the LS EoS from that of Shen. While the LS EoS leads to GW emission in a frequency band peaking between $\sim 150 - 500$Hz, the spectrum of the models using the Shen EoS is restricted to roughly $\sim 150 - 350$Hz. However, LIGO’s current sensitivity makes it impossible to see the high-frequency component of the LS models. Thus, a distinction between the two EoS is currently not possible. Nevertheless, planned upgrades of the interferometers in the near future should enable the discrimination between the prompt convection GW signal of the LS and the Shen EoS. We also found minor deviations in the GW characteristics for simulations which were carried out with different compressibility versions of the LS EoS. However, the differences in the frequency domain of the GW signal are negligibly small and thus not likely to be constrained by observation.

The lepton-driven convection is the central engine for the later dynamical postbounce evolution of the PNS ($t \gtrsim 20$ms) and hence the GW emission. My findings and comparisons with state-of-the-art 2D simulations of [149] suggest that the radial location and size of the convectively unstable layers are the key controlling factors for the outcome of the GW prediction, as they define the timescale and the dynamical behaviour of the overturning matter. Here I find a large sensitivity to the numerical approach of the neutrino transport scheme.

In my set of models, simulations with a precollapse core angular velocity within the parameter range of $\Omega_{c,i} = \pi \ldots 4\pi \cdot \mathrm{rads}^{-1}$ undergo a rotational core collapse. The models all exhibit a so-called type I GW burst at core bounce. As the most important outcome, our 3D MHD models could confirm the recent findings of [62] that the purely axisymmetric ($l = 2, m = 0$) peak amplitude scales approximatively linearly with the rotation rate β_b at core bounce ($|h_{max}| \propto \beta_b$) for $\beta_b \lesssim 10\%$, while the Fourier-transform of the bounce wave trains for most models in the indicated parameter range align around a spectral peak of $\sim 800 - 900$Hz. However, for very fast initial rotation rates of $\Omega_{c,i} \gtrsim 3\pi \cdot \mathrm{rads}^{-1}$, centrifugal forces significantly decelerate collapse and core bounce. The longer timescale and the weakened spin-up of the core due to the action of centrifugal forces leads generically to a decrease of the peak amplitude and a broadened spectral peak at lower frequencies. Furthermore, our results indicate that the particular choice of the nuclear EoS has little influence on the GW signal from rotational core bounce. These findings are in good qualitative agreement with the ones [62] derived from axisymmetric models.

In my rotational core-collapse simulations, nonaxisymmetric dynamics develops for models with a rotation rate of $\beta_b \gtrsim 2.3\%$ at core bounce. Beyond this value, which is considerably lower than found in previous studies (e.g. [179,206]), all models become subject to the 'low $T/|W|$' instability of dominant m=1 or m=2 character within several ms after bounce, depending on the individual model. This nonaxisymmetric dynamical shear instability leads to prolonged narrow-band GW emission at a frequency of twice the rotation rate of the innermost part of the PNS which rotates as a solid body. The fact that the effectively measured GW amplitude scales with the number of GW cycles N as $h_{eff} \propto h\sqrt{N}$ suggests that the detection of such a signal is tremendously enhanced compared to, e.g., the short-lived GW bursts from core bounce, and would allow us to probe the rotational state of the PNS over a long period. However, I point out that such a mechanism only operates if the progenitor is rotating much faster than predicted for most stars by stellar evolution calculations [93]. I also find that centrifugal forces set a limit to the maximum frequency of this periodic GW signal somewhere around ~ 935Hz as they suppress the inward advection of angular momentum. Besides that, I point out that GWs from a low $T/|W|$ instability are highly degenerate with respect to initial rotation rate, EoS, and magnetic fields. Thus, it is very difficult to extract individual features of the input physics from the GW signal that can clearly be attributed to the initial conditions of a progenitor. Rapidly rotating models that include the postbounce neutrino physics at a qualitative level reproduce the previous findings. However, the GW signatures from these more advanced models show huge quantitative deviations from the ones that treat the postbounce phase purely hydrodynamically. As the neutrino cooling during the postbounce phase leads to a more condensed PNS, the unstable regions contain considerably more mass, which then results in 5 to 10 times larger GW amplitudes.

My simulations show that the impact of magnetic fields on the overall supernova dynamics is generally small in cores with relatively weak precollapse fields (B $<$ 10^{11}G). Nevertheless, if I impose very strong and probably unrealistic initial poloidal magnetic fields ($\sim 10^{12}$G), the combined action of flux-freezing and field winding allows the toroidal field component to grow over many orders of magnitude to values where the magnetic pressure can trigger a jet-like explosion along the poles. The bipolar outflow of matter then causes a type IV GW signal. However, if I assume a strong initial toroidal magnetic field, the onset of a jet is effectively suppressed by the fast growing spiral waves of the SASI. This finding stands in contradiction to 2D simulations, where similar configurations led to 'jet'-like explosions, as e.g. in [122]. Thus, in simulations where the toroidal component of the magnetic field dominates over the poloidal one, the magnetic contributions to the GW signal are dominated by the hydrodynamical part of the amplitude. This effect is even stronger in simulations with a deleptonization scheme in the postbounce phase.

The major limitation in most of the simulations I have presented in this thesis lies in the monopole treatment of gravity, since it cannot account for spiral structures, which could be reflected in GWs. In order to investigate the sensitivity of the GW signatures with respect to multidimensional approaches for gravity, I implemented axisymmetric (2D) and 3D Poisson solvers for the gravitational potential. My first studies indicate that in the case of rapidly rotating models with a 2D gravitational potential, the axisymmetric acceleration of the fluid due to gravity leads to a somewhat more oblate configuration of the PNS around core bounce and the early postbounce phase compared to models which were run with a spherically symmetric approach for gravity. This in direct consequence causes considerably stronger GW emission at core bounce with an enhancement of the maximum amplitude of $\sim 20\% - 30\%$ compared to the reference models with 1D gravity. Moreover, significant differences also occur for the GW signal from the low $T/|W|$ instability. Since the axisymmetric treatment of gravity can account better for spiral structures, this in turn leads to a faster growth of unstable modes to more prominent values, causing an earlier onset of the GW emission, and maximum amplitudes up to a factor of 2 larger compared to the reference models with 1D gravity. In case of rapidly rotating models which implement gravity in 3D, I could confirm the trends found with respect to GW emission in simulations which treat the gravitational potential in axisymmetry. This is due to the fact that in my models, the dominant contributions to the GW amplitudes are emitted at radii $R < 30$km, where the predominant deformation of the PNS is of axisymmetric nature. Moreover, I also could show that the postbounce dynamics occuring in the outer layers ($R \gtrsim 200$km) of models run with 3D gravity deviates vastly from the ones run with a 1D or 2D potential. The latter finding implies that both spherically symmetric and axisymmetric treatments of gravity are too restrictive for a quantitative description of the overall postbounce evolution of rapidly rotating CCSN models.

At present, the IDSA includes only the dominant reactions relevant to the neutrino transport problem (see [140] and sec. 2.4.3 for details). Future upgrades will also include contributions from electron-neutrino scattering, which are indispensable during the collapse phase. The inclusion of this reaction will also make the cumbersome switch of the neutrino parametrization scheme to the IDSA at bounce obsolete. Finally, the Basel supernova group is working on the inclusion of μ and τ neutrinos, which are very important for the cooling of the PNS to its final stage as neutron star.

In future work, I plan to focus on aspects of the late postbounce ($t \gtrsim 200$ ms) GW signature from 3D MHD CCSN simulations. From today's point of view, hardly anything is known about the 3D GW signal from this SN stage. Moreover, I will carry on working on the implementation of the IDSA into the general relativistic hydrodynamics codes of Ott et al. [172, 12, 182] (see Appendix A) in order to contribute on a long-term perspective to the first $\{3 + 1\}$ GR and GRMHD simulations of stellar core collapse with postbounce neutrino radiation transport. At densities and velocities encountered in stellar collapse, the inclusion of general relativistic effects is not an optional model sophistication but a necessity for quantitatively reliable GW estimates. Moreover, such simulations are also indispensable to unravel questions of modern astrophysics other than the supernova problem, for example the SN-GRB connection.

Being allowed to contribute to the very active field of GW research in the course of my PhD studies has been a priviledge. I hope that my humble work will help encourage and further research and discoveries in this fascinating field of astrophysics.

A 1DGR & IDSA

> *Und es ist eine grosse Lust aufgekommen, die Ursache aller Dinge zu erforschen: warum der Stein fällt, wenn man ihn loslässt, und wie er steigt, wenn man ihn hochwirft. Jeden Tag wird etwas gefunden. Selbst die Hundertjährigen lassen sich noch von den Jungen ins Ohr schreien, was Neues entdeckt wurde.*
> *Da ist schon viel gefunden, aber da ist mehr, was noch gefunden werden kann. Und so gibt es wieder zu tun für neue Geschlechter.*
>
> Bertold Brecht, Leben des Galilei

At densities and velocities encountered in stellar collapse, the inclusion of general relativistic effects is not an optional model sophistication, but a necessity for quantitatively reliable results, as outlined earlier in this thesis (see sec. 1.8). However, multi-dimensional simulations in conformally-flat (CFC; see [59], and references therein) or full GR (see, e.g., [213, 60]) traditionally relied on simple analytic EoS and polytropic initial models and thus neglect crucial neutrino effects due to restrictions of computational power.

Only recently have the first 2D [61, 62, 163] and 3D [179, 180] GR core-collapse simulations become available that employ a microphysical EoS and neutrino transport to a certain extent. However, while Dimmelmeier et al. [61, 62] and Ott et al. [179, 180] had to restrict themselves to a state-of-the-art nuclear EoS and approximate treatment of deleptonization in the collapse phase (see sec. 2.4, and [136]), only Müller et al. [163] have succeded so far in implementing a sophisticated radiative transport scheme, the 'ray-by-ray plus' of [41], in the 2D CFC framework of [61, 62].

The IDSA on the other hand allows for an efficient way of including spectral neutrino transport in multidimensional GR frameworks. In order to address this task, I have recently started to collaborate with C. D. Ott and E. O'Connor from CALTECH to work on the implementation of the IDSA into their general relativistic hydrodynamics codes [172, 12, 182].

As a first step, I am currently working on the implementation of the IDSA into their spherically symmetric open-source code `1DGR`. Afterwards, the goal is to get the IDSA running in the framework of the $\{3+1\}$ GR code. Note that the original routines of the 1D IDSA were kindly provided by Matthias Liebendörfer. They serve me as starting point for the required adjustment to the `1DGR`.

Below, I will give a short overview of the principles of the spherically symmetric GR hydrodynamics code `1DGR` and the way how the IDSA is included. Note, however, that I will go neither into the details of derivations nor the implementation of the code. This goes beyond the scope of this thesis and can be found in [172]. Following

O'Connor & Ott [172], I will assume spacelike signature $(-,+,+,+)$ and, unless mentioned otherwise, use units of $G = c = M_\odot = 1$. Greek (Latin) indices run through all (spatial) coordinates.

A.1 Merging `1DGR` & IDSA: hydrodynamics and curvature equations

The unification of space and time into spacetime is central to general relativity (see sec. 1.3, and references therein). However, for a numerical treatment, it is more desirable to reverse this unification and recast GR into a so-called '3+1' formulation, in which a time coordinate is explicitly split from three spatial coordinates, i.e., the four-dimensional spacetime is 'carved-up' into a family of three-dimensional spatial 'slices'. For a complete introduction to the subject, I refer to the review of Baumgarte & Shapiro [28], and references therein.

According to the 3+1 decomposition of Einstein's equations, the invariant line element is written with the objects α (lapse), β^i (shift), and γ_{ij}, keeping the line element [28]

$$ds^2 = g_{\mu\nu}dx^\mu dx^\nu = -(\alpha - \beta_i\beta^i)dt^2 + 2\beta_i dx^i dt + \gamma_{ij}dx^i dx^j \; . \tag{A.1}$$

The *Eulerian* `1DGR` code of O'Connor & Ott [172] follows [87, 197] who formulate the 3+1 GR curvature and hydrodynamics equations in radial-gauge, polar-slicing (RGPS) coordinates. In these coordinates, $\beta^i = 0 \; \forall i$, $g_{\mu\nu} = diag(-\alpha^2, X^2, r^2, r^2\sin^2\theta)$, the three-metric $\gamma_{ij} = diag(X^2, r^2, r^2\sin^2\theta)$, and hence

$$ds^2 = -\alpha(r,t)^2 dt^2 + X(r,t)^2 dr^2 + r^2 d\Omega^2 \; , \tag{A.2}$$

where α and X can be written more conveniently as functions of a metric potential, $\Phi(r,t)$, and the enclosed gravitational mass $M_{\mathrm{grav}}(r,t) = m(r,t)$,

$$\alpha(r,t) = \exp\left[\Phi(r,t)\right] \;\text{ and }\; X(r,t) = \left(1 - \frac{2m(r,t)}{r}\right)^{-1/2} \; . \tag{A.3}$$

Note that the RGPS is nothing more than a generalization of the well-known Schwarzschild metric to the non-vacuum and non-static case [87].
The equations describing the evolution of matter are the expression of the *local conservation* of baryon number

$$\nabla_\mu J^\mu = 0 \; , \tag{A.4}$$

and the *local conservation* of energy momentum

$$\nabla_\mu T^{\mu\nu} = 0 \; . \tag{A.5}$$

For the current J^μ and the stress-energy tensor $T^{\mu\nu}$, perfect fluid is assumed, where

$$T^{\mu\nu} = \rho h u^\mu u^\nu + P g^{\mu\nu} \quad \text{and} \quad J^\mu = \rho u^\mu \,. \tag{A.6}$$

Here, ∇_μ is the covariant derivative, ρ is the rest-mass density, p is the pressure, and h is the specific enthalpy defined by $h = 1 + \epsilon + p/\rho$, where ϵ is the specific internal energy. u^μ is the four-velocity of the fluid and is equal to $[W/\alpha, Wv^r, 0, 0]$. $W = \alpha u^0 = \alpha u^t = (1-v^2)^{-1/2}$ is the Lorentz factor. The 'physical' velocity $v = Xv^r$ represents the fluid velocity relative to an observer at rest in the coordinate frame.

With the above coordinate conditions and the following set of conserved, unknown variables,

$$\begin{aligned} D &= \alpha X J^t = X\rho W \ , \\ DY_e &= \alpha X Y_e J^t = X\rho W Y_e \ , \\ S^r &= \alpha X T^{tr} = \rho h W^2 v \ , \\ \tau &= \alpha^2 T^{tt} - D = \rho h W^2 - P - D \ , \end{aligned} \tag{A.7}$$

the general relativistic evolution equations can be written as a system of conservation laws (with sources):

$$\partial_t \vec{U} + \frac{1}{r^2}\partial_r \left[\frac{\alpha r^2}{X}\vec{F}\right] = \vec{\mathcal{S}} \,, \tag{A.8}$$

where $\vec{U}$ is the set of conserved variables, $\vec{F}$ is their flux vector, and $\vec{\mathcal{S}}$ is the vector containing gravitational, geometric, and neutrino-matter interaction sources and sinks. Note that the conserved variables are functions of the primitive variables ρ, Y_e, ϵ, v, and P.

In spherically symmetric coordinates, the flux $\vec{F}$ is given by $\vec{F} = [Dv, DY_e v, S^r v + P, S^r - Dv]$ and the sources and sinks are given by

$$\begin{aligned} \vec{\mathcal{S}} = \ & \Big[0, R^\nu_{Y_e}, (S^r v - \tau - D)\alpha X \left(8\pi r P + \tfrac{m}{r^2}\right) + \alpha P X \tfrac{m}{r^2} \\ & + \tfrac{2\alpha P}{Xr} + Q^{\nu,\mathrm{E}}_{S^r} + Q^{\nu,\mathrm{M}}_{S^r}, Q^{\nu,\mathrm{E}}_{\tau} + Q^{\nu,\mathrm{M}}_{\tau}\Big] \ . \end{aligned} \tag{A.9}$$

The source and sink terms $R^\nu_{Y_e}, Q^{\nu,\mathrm{E}}_{S^r}, Q^{\nu,\mathrm{M}}_{S^r}, Q^{\nu,\mathrm{E}}_{\tau}$, and $Q^{\nu,\mathrm{M}}_{\tau}$ are associated with a neutrino leakage scheme (see [172], sec. 4). Note, however, that the terms from the leakage scheme are mentioned here only for the sake of consistency with [172]; they are not of direct relevance for our case and thus may be set to zero. The IDSA handles their physics internally (see sec. 2.4.3).

In order to lump together the hydrodynamics of `1DGR` with the IDSA, I follow the description given in sec. 2.4. The advective part of the IDSA is, in analogy to eq. 2.177, added to eq. A.8. However, since we are in a GR framework, the conserved variables of the advective part of the IDSA (cf. eq. 2.177) must be casted into a general-relativistic form. They read

$$DY_l^t \quad \text{and} \quad (DZ_l^t)^{\frac{3}{4}} \; , \tag{A.10}$$

with the corresponding fluxes

$$DY_l^t v \quad \text{and} \quad (DZ_l^t)^{\frac{3}{4}} v \; . \tag{A.11}$$

The rest – the inhomogeneous parts of the IDSA such as changes in Y_e and internal specific energy – is handled according to sec. 2.4.3 in an operator-splitted manner.

The above system of equations A.8 is closed by an EoS (see sec. 2.3) and the Einstein equation, which furnish conditions on the quantities $m(r,t)$ and $\Phi(r,t)$ [87]. The equation for the gravitational mass needed for determining the metric coefficient $X(r,t)$ of A.3 is derived from the Hamiltonian constraint equation [28] and reads

$$m(r,t) = 4\pi \int_0^r (\rho h W^2 - P + \tau_m^\nu) r'^2 dr' \; . \tag{A.12}$$

τ_m^ν is the contribution to the gravitational mass from the energy and pressure of trapped neutrinos (see sec. 2.4), and given by [172]

$$\tau_m^\nu = (4W^2 - 1) P_\nu \; . \tag{A.13}$$

The expression for the metric potential $\Phi(r,t)$ is determined by the momentum constraints, which take into account the polar slicing condition that imposes $\mathrm{tr}\,[K] = K_r{}^r$, where K_{ij} is the extrinsic curvature tensor (see, e.g., [87]):

$$\Phi(r,t) = \int_0^r X^2 \left[\frac{m(r',t)}{r'^2} + 4\pi r' (\rho h W^2 v^2 + P + \tau_\Phi^\nu) \right] dr' + \Phi_0 \; . \tag{A.14}$$

In analogy to eq. A.12, τ_Φ^ν takes into account the effect trapped neutrinos and reads [172]

$$\tau_\Phi^\nu = (4W^2 v^2 + 1) P_\nu \; . \tag{A.15}$$

Φ_0 is a constant of integration and is chosen such that $\Phi(r,t)$ matches at the star's surface ($r = R_\star$) to the Schwarzschild metric,

$$\Phi(R_\star, t) = \ln\left[\alpha(R_\star, t)\right] = \frac{1}{2} \ln \left[1 - \frac{2m(R_\star, t)}{R_\star} \right] . \tag{A.16}$$

For numerical details about the temporal update of eqs. A.8, I refer to [172].
Note, however, that after the update of the variables $D, DY_e, S^r, DY_l^t, (DZ_l^t)^{\frac{3}{4}}$ and τ, the primitive variables $\rho, DY_e, v, P(\rho, \epsilon, Y_e)$ must be extracted since they are needed for the next timestep. In the general case, the primitive variables (with the exception of Y_e, Y_l^t and Z_l^t) cannot be expressed algebraically in terms of the conserved variables. Hence, an iterative approach is employed in `1DGR`, which makes an initial guess using P_{old} from the previous timestep,

$$v = \frac{S^r}{\tau + D + P_{old}} \ , \quad \rho = \frac{D}{XW} \ , \quad \epsilon = \frac{\tau + D + P_{old}(1 - W^2)}{\rho W^2} - 1 \ , \qquad \text{(A.17)}$$

where X can be calculated from the conserved variables $\rho h W^2 - P = \tau + D$. W is calculated from the estimate of v. Then, a call to the EoS gives a new pressure. This process is iterated using a Newton-Raphson method until convergence [172].

List of Figures

List of Tables

B List of Publications

2010: *Neutrino Radiation-Hydrodynamics:*
General Relativistic versus Multidimensional Supernova Simulations
M. Liebendörfer, T. Fischer, M. Hempel, R. Käppeli, G. Pagliara, A. Perego,
I. Sagert, J. Schaffner-Bielich, **S. Scheidegger**,
F.-K. Thielemann, S.C. Whitehouse
Progress of Theoretical Physics Supplement, 2010, 186, 87-92

Gravitational waves from supernova matter
S. Scheidegger, S.C. Whitehouse, R. Käppeli, M. Liebendörfer
Class. Quantum Grav. 27 (2010) 114101

The influence of model parameters on the prediction of gravitational wave signal from stellar core collapse
S. Scheidegger, R. Käppeli, S.C. Whitehouse, T. Fischer, M. Liebendörfer
Astronomy & Astrophysics **514** (2010), A51+

2009 *FISH: A 3D parallel MHD code for astrophysical applications*
R. Käppeli, S.C. Whitehouse, **S. Scheidegger**, U.-L. Pen, M. Liebendörfer
submitted to the *The Astrophysical Journal Supplement*, arXiv:0910.2854

Supernovae as Nuclear and Particle Physics Laboratories
M. Liebendörfer, T. Fischer, M. Hempel, A. Mezzacappa, G. Pagliara, I. Sagert,
J. Schaffner-Bielich, **S. Scheidegger**, F.-K. Thielemann, S. C. Whitehouse
Nuclear Physics A, Volume 827, Issue 1-4, pp. 573-578c

2008: *Nuclear physics in core-collapse supernovae*
M. Liebendörfer, T. Fischer, C. Fröhlich, R. W. Hix, K. Langanke,
G. Martinez-Pinedo, A. Mezzacappa, **S. Scheidegger**,
F.-K. Thielemann and S.C. Whitehouse
New Astronomy Reviews **52** Issue 7-10, pp. 373-376

Gravitational waves from 3D MHD core collapse simulations
S. Scheidegger, T. Fischer, S.C. Whitehouse, M. Liebendörfer
Astronomy & Astrophysics **490**, Issue 1, pp. 231-241

C Curriculum vitæ

Simon Urs Scheidegger

Date of Birth: October 15, 1982
Citizenship: Swiss

Research interests

Gravitational waves, core-collapse supernovae, computational magnetohydrodynamics, the physics of compact stars, high performance computing.

Academic education

October 2010	Ph.D. summa cum laude in Theoretical Physics, Basel University Supervisors: Prof. Dr. M. Liebendörfer, Prof. Dr. F-K. Thielemann External expert: PD Dr. J. Novak (LUTH, Meudon)
2007 - 2010	Ph.D. student, Department of Physics, Basel University
Since 2007	Member of the European Graduate School Basel-Graz-Tübingen: *'Hadrons in vacuum, in nuclei and stars'*
May 2007	M.Sc. summa cum laude in Physics, Basel University Thesis title: *'Computing gravitational waves from core-collapse supernovae'* Supervisor: Prof. Dr. M. Liebendörfer. Examination topic: *'General relativity, advanced quantum mechanics and quantum field theory'* Examiners: Prof. Dr. D. Trautmann, PD Dr. K. Hencken

2005 - 2007	Master student, Department of Physics, Basel University
Fall 2005	B.Sc. in Physics, Basel University (Marks: 5.7 out of 6.0)
2002 - 2005	Bachelor student, Department of Physics, Basel University
January 2002	High school Graduation: Matura Type B (12* subjects, including Latin & modern languages)
1994 - 2002	Gymnasium (Grammar school) at Kantonsschule Solothurn
1989 - 1994	Elementary school, Solothurn

During my studies I heard lectures by the following persons:
Prof. Dr. G. Baur, Prof. Dr. B. Binggeli, Prof. Dr. C. Bruder, Dr. H. Burkhart, PD Dr. A. A'Campo-Neuen, Prof. Dr. O. Gerhard, Prof. Dr. S. Goedecker, Prof. Dr. H.-J. Güntherodt, Prof. Dr. M. Grote, PD Dr K. Hencken, Prof. Dr. H.-J. Hug, Prof. Dr. H.-C. Im Hof, PD Dr. J. Jourdan, Prof. Dr. B. Krusche, Prof. Dr. M. Liebendörfer, Prof. Dr. D. Loss, Prof. Dr. D. Masser Prof. Dr. E. Meyer, Prof. Dr. E. Parlow, PD Dr. T. Rauscher, PD Dr. D. Rohe, Prof. Dr. H. Schierenbeck, Prof. Dr. C. Schönenberger, Prof. Dr. I. Sick, PD Dr. D. Simko Prof. Dr. F.-K. Thielemann, Prof. Dr. D. Trautmann, Prof. Dr. M. Weber

Languages

German (native), English (fluent), French (good), Latin (written)

Bibliography

[1] http://geo600.aei.mpg.de/.

[2] http://lisa.nasa.gov/.

[3] http://public.web.cern.ch/public/.

[4] http://tamago.mtk.nao.ac.jp/.

[5] http://www.auriga.lnl.infn.it/.

[6] http://www.bnl.gov/rhic/.

[7] http://www.ego-gw.it/.

[8] http://www.gravity.uwa.edu.au/.

[9] http://www.gsi.de/fair/.

[10] http://www.ligo.caltech.edu/.

[11] http://www.roma1.infn.it./rog/.

[12] http://www.whiskycode.org/.

[13] J Abadie et al. All-sky search for gravitational-wave bursts in the first joint LIGO-GEO-Virgo run. Phys. Rev. D, 81(10):102001–+, May 2010.

[14] B. P. Abbott et al. LIGO: the Laser Interferometer Gravitational-Wave Observatory. *Reports on Progress in Physics*, 72(7):076901–+, July 2009.

[15] E. B. Abdikamalov, C. D. Ott, L. Rezzolla, L. Dessart, H. Dimmelmeier, A. Marek, and H.-T. Janka. Axisymmetric general relativistic simulations of the accretion-induced collapse of white dwarfs. Phys. Rev. D, 81(4):044012–+, February 2010.

[16] A. Abramovici, W. E. Althouse, R. W. P. Drever, Y. Gursel, S. Kawamura, F. J. Raab, D. Shoemaker, L. Sievers, R. E. Spero, and K. S. Thorne. LIGO - The Laser Interferometer Gravitational-Wave Observatory. *Science*, 256:325–333, April 1992.

[17] F. Acernese, M. Alshourbagy, P. Amico, F. Antonucci, S. Aoudia, K. G. Arun, P. Astone, S. Avino, L. Baggio, G. Ballardin, F. Barone, L. Barsotti, M. Barsuglia, T. S. Bauer, S. Bigotta, S. Birindelli, M. A. Bizouard, C. Boccara, F. Bondu, L. Bosi, S. Braccini, C. Bradaschia, A. Brillet, V. Brisson, D. Buskulic, G. Cagnoli, E. Calloni, E. Campagna, F. Carbognani, F. Cavalier, R. Cavalieri, G. Cella, E. Cesarini, E. Chassande-Mottin, S. Chatterji, F. Cleva, E. Coccia, C. Corda, A. Corsi, F. Cottone, J.-P. Coulon, E. Cuoco, S. D'Antonio, A. Dari, V. Dattilo, M. Davier, R. De Rosa, M. DelPrete, L. Di Fiore, A. Di Lieto, M. D. P. Emilio, A. Di Virgilio, M. Evans, V. Fafone, I. Ferrante, F. Fidecaro, I. Fiori, R. Flaminio, J.-D. Fournier, S. Frasca, F. Frasconi, L. Gammaitoni, F. Garufi, E. Genin, A. Gennai, A. Giazotto, V. Granata, C. Greverie, D. Grosjean, G. Guidi, S. Hamdani, S. Hebri, H. Heitmann, P. Hello, D. Huet, P. La Penna, M. Laval, N. Leroy, N. Letendre, B. Lopez, M. Lorenzini, V. Loriette, G. Losurdo, J.-M. Mackowski, E. Majorana, N. Man, M. Mantovani, F. Marchesoni, F. Marion, J. Marque, F. Martelli, A. Masserot, F. Menzinger, L. Milano, Y. Minenkov, M. Mohan, J. Moreau, N. Morgado, S. Mosca, B. Mours, I. Neri, F. Nocera, G. Pagliaroli, C. Palomba, F. Paoletti, S. Pardi, A. Pasqualetti, R. Passaquieti, D. Passuello, F. Piergiovanni, L. Pinard, R. Poggiani, M. Punturo, P. Puppo, O. Rabaste, P. Rapagnani, T. Regimbau, A. Remillieux, F. Ricci, I. Ricciardi, A. Rocchi, L. Rolland, R. Romano, P. Ruggi, D. Sentenac, S. Solimeno, B. L. Swinkels, R. Terenzi, A. Toncelli, M. Tonelli, E. Tournefier, F. Travasso, G. Vajente, J. F. J. van den Brand, S. van der Putten, D. Verkindt, F. Vetrano, A. Viceré, J.-Y. Vinet, H. Vocca, and M. Yvert. Virgo status. *Classical and Quantum Gravity*, 25(18):184001–+, September 2008.

[18] H. M. Antia. *Numerical Methods for Scientists and Engineers.* Birkhäuser, 2002.

[19] W. D. Arnett. Neutrino escape, nuclear dissociation, and core collapse and/or explosion. *apj*, 263:L55–L57, December 1982.

[20] P. Aufmuth and K. Danzmann. Gravitational wave detectors. *New Journal of Physics*, 7:202–+, September 2005.

[21] W. Baade and F. Zwicky. Cosmic rays from super-novae. *Proceedings of the National Academy of Science*, 20:259–263, 1934.

[22] W. Baade and F. Zwicky. On Super-novae. *Proceedings of the National Academy of Science*, 20:254–259, May 1934.

[23] L. Baggio et al. A joint search for gravitational wave bursts with AURIGA and LIGO. *Classical and Quantum Gravity*, 25(9):095004–+, May 2008.

[24] S. A. Balbus and J. F. Hawley. Instability, turbulence, and enhanced transport in accretion disks. *Reviews of Modern Physics*, 70:1–53, January 1998.

[25] Gabriele Jost Barbara Chapman and Ruud van der Pas. *Using OpenMP - Portable Shared Memory Parallel Programming.* MIT Press, 2007.

[26] M. R. Bate. The dependence of star formation on initial conditions and molecular cloud structure. MNRAS, 397:232–248, July 2009.

[27] Yuri K. Batygin. Accuracy and efficiency of 2d and 3d fast poisson solvers for space charge field calculations of intense beam. In *Proc of EPAC, 1998*, 1998.

[28] T. W. Baumgarte and S. L. Shapiro. Numerical relativity and compact binaries. Phys. Rep., 376:41–131, March 2003.

[29] H. A. Bethe. Supernova mechanisms. *Rev. Mod. Phys.*, 62:801–866, 1990.

[30] H. A. Bethe and J. R. Wilson. Revival of a stalled supernova shock by neutrino heating. ApJ, 295:14–23, August 1985.

[31] H. Billing, K. Maischberger, A. Ruediger, R. Schilling, L. Schnupp, and W. Winkler. An argon laser interferometer for the detection of gravitational radiation. *Journal of Physics E Scientific Instruments*, 12:1043–1050, November 1979.

[32] L. Blanchet, T. Damour, and G. Schaefer. Post-Newtonian hydrodynamics and post-Newtonian gravitational wave generation for numerical relativity. MNRAS, 242:289–305, January 1990.

[33] J. M. Blondin and A. Mezzacappa. Pulsar spins from an instability in the accretion shock of supernovae. Nature, 445:58–60, January 2007.

[34] J. M. Blondin, A. Mezzacappa, and C. DeMarino. Stability of Standing Accretion Shocks, with an Eye toward Core-Collapse Supernovae. *apj*, 584:971–980, February 2003.

[35] Christoph Scholz Frank Zetsche Bogdan Povh, Klaus Rith. *Teilchen und Kerne. Eine Einführung in die physikalischen Konzepte*. Springer Verlag, Berlin, Heidelberg, New York, 1999.

[36] S. W. Bruenn. Stellar core collapse - Numerical model and infall epoch. ApJS, 58:771–841, August 1985.

[37] S. W. Bruenn. Stellar core collapse: Numerical model and infall epoch. *apjsup*, 58:771–841, August 1985.

[38] S. W. Bruenn, K. R. De Nisco, and A. Mezzacappa. General Relativistic Effects in the Core Collapse Supernova Mechanism. *apj*, 560:326–338, October 2001.

[39] Bernard F. Schutz B.S. Sathyaprakash. Physics, astrophysics and cosmology with gravitational waves. *Living Reviews in Relativity*, 12(2), 2009.

[40] R. Buras, H.-T. Janka, M. Rampp, and K. Kifonidis. Two-dimensional hydrodynamic core-collapse supernova simulations with spectral neutrino transport. II. Models for different progenitor stars. *Astronomy & Astrophysics* , 457:281–308, October 2006.

[41] R. Buras, M. Rampp, H.-T. Janka, and K. Kifonidis. Two-dimensional hydrodynamic core-collapse supernova simulations with spectral neutrino transport. I. Numerical method and results for a 15 Mȯ star. *aap*, 447:1049–1092, March 2006.

[42] A. Burrows. Supernova neutrinos. ApJ, 334:891–908, November 1988.

[43] A. Burrows, L. Dessart, E. Livne, C. D. Ott, and J. Murphy. Simulations of Magnetically Driven Supernova and Hypernova Explosions in the Context of Rapid Rotation. ApJ, 664:416–434, July 2007.

[44] A. Burrows, W. B. Hubbard, J. I. Lunine, and J. Liebert. The theory of brown dwarfs and extrasolar giant planets. *Reviews of Modern Physics*, 73:719–765, July 2001.

[45] A. Burrows, E. Livne, L. Dessart, C. D. Ott, and J. Murphy. A New Mechanism for Core-Collapse Supernova Explosions. ApJ, 640:878–890, April 2006.

[46] A. Burrows, E. Livne, L. Dessart, C. D. Ott, and J. Murphy. Features of the Acoustic Mechanism of Core-Collapse Supernova Explosions. ApJ, 655:416–433, January 2007.

[47] Adam Burrows. Supernova explosions in the universe. *Nature*, 403:727–733, 2000.

[48] J. B. Camp and N. J. Cornish. Gravitational wave astronomy. *Ann. Rev. Nuc. Part. Sci.*, 54:525–577, 2004.

[49] E. Cappellaro, R. Evans, and M. Turatto. A new determination of supernova rates and a comparison with indicators for galactic star formation. *Astronomy & Astrophysics* , 351:459–466, November 1999.

[50] J. I. Castor. Radiative Transfer in Spherically Symmetric Flows. ApJ, 178:779–792, December 1972.

[51] P. Cerdá-Durán, V. Quilis, and J. A. Font. AMR simulations of the low T/—W— bar-mode instability of neutron stars. *Computer Physics Communications*, 177:288–297, August 2007.

[52] J. Chadwick. Possible existence of a neutron. *Nature*, 129:312, 1932.

[53] Kimberly C.B. New Chris L. Fryer. Gravitational waves from gravitational collapse. *Living Reviews in Relativity*, 6(2), 2003.

[54] D. H. Clark and F. R. Stephenson. The historical supernovae. pages 355–370, November 1982.

[55] S. A. Colgate and R. H. White. The hydrodynamic behavior of supernovae explosions. *apj*, 143:626, March 1966.

[56] L. Dessart, A. Burrows, E. Livne, and C. D. Ott. Multidimensional Radiation/Hydrodynamic Simulations of Proto-Neutron Star Convection. ApJ, 645:534–550, July 2006.

[57] L. Dessart, A. Burrows, C. D. Ott, E. Livne, S.-Y. Yoon, and N. Langer. Multidimensional Simulations of the Accretion-induced Collapse of White Dwarfs to Neutron Stars. *apj*, 644:1063–1084, June 2006.

[58] R. Diehl, H. Halloin, K. Kretschmer, G. G. Lichti, V. Schönfelder, A. W. Strong, A. von Kienlin, W. Wang, P. Jean, J. Knödlseder, J.-P. Roques, G. Weidenspointner, S. Schanne, D. H. Hartmann, C. Winkler, and C. Wunderer. Radioactive 26 Al from massive stars in the Galaxy. Nature, 439:45–47, January 2006.

[59] H. Dimmelmeier, J. A. Font, and E. Müller. Relativistic simulations of rotational core collapse II. Collapse dynamics and gravitational radiation. *Astronomy & Astrophysics* , 393:523–542, October 2002.

[60] H. Dimmelmeier, J. Novak, J. A. Font, J. M. Ibáñez, and E. Müller. Combining spectral and shock-capturing methods: A new numerical approach for 3D relativistic core collapse simulations. Phys. Rev. D, 71(6):064023–+, March 2005.

[61] H. Dimmelmeier, C. D. Ott, H.-T. Janka, A. Marek, and E. Müller. Generic Gravitational-Wave Signals from the Collapse of Rotating Stellar Cores. *Physical Review Letters*, 98(25):251101–+, June 2007.

[62] H. Dimmelmeier, C. D. Ott, A. Marek, and H.-T. Janka. Gravitational wave burst signal from core collapse of rotating stars. Phys. Rev. D, 78(6):064056–+, September 2008.

[63] A. Einstein. Die feldgleichungen der gravitation. *Preuss. Akad. Wiss. Berlin, Sitzber.*, page 844, 1915.

[64] A. Einstein. Zur allgemeinen relativitätstheorie. *Preuss. Akad. Wiss. Berlin, Sitzber.*, page 778, 1915.

[65] A. Einstein. Über Gravitationswellen. *Sitzungsberichte der Königlich Preußischen Akademie der Wissenschaften (Berlin), Seite 154-167.*, pages 154–167, 1918.

[66] A. S. Endal and S. Sofia. The evolution of rotating stars. II - Calculations with time-dependent redistribution of angular momentum for 7- and 10-solar-mass stars. ApJ, 220:279–290, February 1978.

[67] Y. Eriguchi and E. Mueller. A general computational method for obtaining equilibria of self-gravitating and rotating gases. *Astronomy & Astrophysics* , 146:260–268, May 1985.

[68] Z. B. Etienne, Y. T. Liu, and S. L. Shapiro. General relativistic simulations of slowly and differentially rotating magnetized neutron stars. Phys. Rev. D, 74(4):044030–+, August 2006.

[69] C. R. Evans and J. F. Hawley. Simulation of magnetohydrodynamic flows - A constrained transport method. ApJ, 332:659–677, September 1988.

[70] A. V. Filippenko. Optical Spectra of Supernovae. *Astronomy*, 35:309–355, 1997.

[71] L. S. Finn and C. R. Evans. Determining gravitational radiation from Newtonian self-gravitating systems. ApJ, 351:588–600, March 1990.

[72] T. Fischer. *Neutrino radiation hydrodynamics in hot and dense nu- clear matter and the role of microphysics in simulations of massive stars,.* PhD thesis, University of Basel, Department of Physics, 2009.

[73] T. Fischer, S. C. Whitehouse, A. Mezzacappa, F. -. Thielemann, and M. Liebendörfer. Protoneutron star evolution and the neutrino driven wind in general relativistic neutrino radiation hydrodynamics simulations. *ArXiv e-prints*, August 2009.

[74] T. Fischer, S. C. Whitehouse, A. Mezzacappa, F.-K. Thielemann, and M. Liebendörfer. The neutrino signal from protoneutron star accretion and black hole formation. *Astronomy & Astrophysics* , 499:1–15, May 2009.

[75] É. É. Flanagan and S. A. Hughes. Measuring gravitational waves from binary black hole coalescences. I. Signal to noise for inspiral, merger, and ringdown. Phys. Rev. D, 57:4535–4565, April 1998.

[76] É. É. Flanagan and S. A. Hughes. The basics of gravitational wave theory. *New Journal of Physics*, 7:204–+, September 2005.

[77] Otto Forster. *Analysis 1.* Vieweg, 1999.

[78] C. Fröhlich, G. Martínez-Pinedo, M. Liebendörfer, F.-K. Thielemann, E. Bravo, W. R. Hix, K. Langanke, and N. T. Zinner. Neutrino-Induced Nucleosynthesis of A¿64 Nuclei: The νp Process. *Physical Review Letters*, 96(14):142502–+, April 2006.

[79] C. L. Fryer and M. S. Warren. The Collapse of Rotating Massive Stars in Three Dimensions. *apj*, 601:391–404, January 2004.

[80] G. M. Fuller, W. A. Fowler, and M. J. Newman. Stellar weak interaction rates for intermediate-mass nuclei. ii - a = 21 to a = 60. 252:715, 1982.

[81] N. A. Gentile, M. B. Aufderheide, G. J. Mathews, F. D. Swesty, and G. M. Fuller. The QCD phase transition and supernova core collapse. ApJ, 414:701–711, September 1993.

[82] M. E. Gertsenshtein and V. I. Pustovoit. *Sov. Phys. JETP*, 16:433, 1963.

[83] B. Giacomazzo, L. Rezzolla, and L. Baiotti. Can magnetic fields be detected during the inspiral of binary neutron stars? MNRAS, 399:L164–L168, October 2009.

[84] S. K. Godunov. A difference scheme for numerical solution of discontinuous solution of hydrodynamic equations. *Mat. Sb. (N.S.)*, 47:271–306, 1959.

[85] P. Goldreich and S. V. Weber. Homologously collapsing stellar cores. *apj*, 238:991–997, June 1980.

[86] H. Goldstein. Classical mechanics. 1950.

[87] E. Gourgoulhon. Simple equations for general relativistic hydrodynamics in spherical symmetry applied to neutron star collapse. *Astronomy & Astrophysics* , 252:651–663, December 1991.

[88] P. Grandclément, S. Bonazzola, E. Gourgoulhon, and J.-A. Marck. A Multidomain Spectral Method for Scalar and Vectorial Poisson Equations with Noncompact Sources. *Journal of Computational Physics*, 170:231–260, June 2001.

[89] N. J. Hammer, H.-T. Janka, and E. Müller. Three-dimensional Simulations of Mixing Instabilities in Supernova Explosions. ApJ, 714:1371–1385, May 2010.

[90] M. Hamuy. Observed and Physical Properties of Core-Collapse Supernovae. 582:905–914, January 2003.

[91] A. Heger, C. L. Fryer, S. E. Woosley, N. Langer, and D. H. Hartmann. How Massive Single Stars End Their Life. ApJ, 591:288–300, July 2003.

[92] A. Heger, S. E. Woosley, and H. C. Spruit. Presupernova Evolution of Differentially Rotating Massive Stars Including Magnetic Fields. ApJ, 626:350–363, June 2005.

[93] A. Heger, S. E. Woosley, and H. C Spruit. Presupernova Evolution of Differentially Rotating Massive Stars Including Magnetic Fields. *apj*, 626:350–363, June 2005.

[94] M. Herant, W. Benz, W. R. Hix, C. L. Fryer, and S. A. Colgate. Inside the supernova: A powerful convective engine. 435:339–361, November 1994.

[95] W. Hillebrandt. An exploding 10 solar mass star - A model for the Crab supernova. *Astronomy & Astrophysics* , 110:L3–L6, June 1982.

[96] K. Hirata, T. Kajita, M. Koshiba, M. Nakahata, and Y. Oyama. Observation of a neutrino burst from the supernova sn1987a. *prl*, 58:1490–1493, April 1987.

[97] K. S. Hirata, T. Kajita, M. Koshiba, M. Nakahata, Y. Oyama, N. Sato, A. Suzuki, M. Takita, Y. Totsuka, T. Kifune, T. Suda, K. Takahashi, T. Tanimori, K. Miyano, M. Yamada, E. W. Beier, L. R. Feldscher, W. Frati, S. B. Kim, A. K. Mann, F. M. Newcomer, R. van Berg, W. Zhang, and B. G. Cortez. Observation in the Kamiokande-II detector of the neutrino burst from supernova SN1987A. Phys. Rev. D, 38:448–458, July 1988.

[98] W. R. Hix, O. E. Messer, A. Mezzacappa, M. Liebendörfer, J. Sampaio, K. Langanke, D. J. Dean, and G. Martínez-Pinedo. Consequences of Nuclear Electron Capture in Core Collapse Supernovae. *Physical Review Letters*, 91(20):201102–+, November 2003.

[99] W. R. Hix, O. E. B. Messer, A. Mezzacappa, M. Liebendörfer, J. Sampaio, K. Langanke, D. J. Dean, and G. Martínez-Pinedo. Questing for the grail: The consequences of nuclear electron capture in core collapse supernovae. 91, 2003.

[100] C. J. Horowitz. Weak magnetism for antineutrinos in supernovae. *prd*, 65, 2002.

[101] R. A. Hulse and J. H. Taylor. Discovery of a pulsar in a binary system. ApJ, 195:L51–L53, January 1975.

[102] J. Ira Thorpe. LISA long-arm interferometry. *Classical and Quantum Gravity*, 27(8):084008–+, April 2010.

[103] N. Itoh. Ion-ion correlation effect on freedman's neutrino opacity. *Progress of Theoretical Physics*, 54:1580–1581, November 1975.

[104] W. Iwakami, K. Kotake, N. Ohnishi, S. Yamada, and K. Sawada. Three-Dimensional Simulations of Standing Accretion Shock Instability in Core-Collapse Supernovae. ApJ, 678:1207–1222, May 2008.

[105] John David Jackson. *Classical Electrodynamics*. John Wiley & Sons, Inc., 1998.

[106] H.-T. Janka, K. Langanke, A. Marek, G. Martínez-Pinedo, and B. Müller. Theory of core-collapse supernovae. Phys. Rep., 442:38–74, April 2007.

[107] H.-Th. Janka and E. Müller. Neutrino heating, convection, and the mechanism of type-ii supernova explosions. *aa*, 306:167, 1996.

[108] Sheila Rowan Jim Hough. Gravitational wave detection by interferometry (ground and space). *Living Reviews in Relativity*, 3(3), 2000.

[109] S. Jin and Z. Xin. The relaxation schemes for systems of conservation laws in arbitrary space dimensions. *Commun. Pure Appl.Math.*, 48:235, 1995.

[110] D.C. Barnes J.U Brackbill. The effect of nonzero on the numerical solution of the magnetohydrodynamics equations. *J.Comput.Phys.*, 35:426–430, 1980.

[111] R. Kaeppeli, S. C. Whitehouse, S. Scheidegger, U. -. Pen, and M. Liebendoerfer. FISH: A 3D parallel MHD code for astrophysical applications. *ArXiv e-prints*, October 2009.

[112] R. Käppeli. Introduction to hydrodynamics (skript zur vorlesung "hydrodynamik: Einführung in das programmieren paralleler computer in fortran"). Master's thesis, University of Basel, 2007.

[113] S. Kawamura, T. Nakamura, M. Ando, N. Seto, K. Tsubono, K. Numata, R. Takahashi, S. Nagano, T. Ishikawa, M. Musha, K.-i. Ueda, T. Sato, M. Hosokawa, K. Agatsuma, T. Akutsu, K.-s. Aoyanagi, K. Arai, A. Araya, H. Asada, Y. Aso, T. Chiba, T. Ebisuzaki, Y. Eriguchi, M.-K. Fujimoto, M. Fukushima, T. Futamase, K. Ganzu, T. Harada, T. Hashimoto, K. Hayama, W. Hikida, Y. Himemoto, H. Hirabayashi, T. Hiramatsu, K. Ichiki, T. Ikegami, K. T. Inoue, K. Ioka, K. Ishidoshiro, Y. Itoh, S. Kamagasako, N. Kanda, N. Kawashima, H. Kirihara, K. Kiuchi, S. Kobayashi, K. Kohri, Y. Kojima, K. Kokeyama, Y. Kozai, H. Kudoh, H. Kunimori, K. Kuroda, K.-i. Maeda, H. Matsuhara, Y. Mino, O. Miyakawa, S. Miyoki, H. Mizusawa, T. Morisawa, S. Mukohyama, I. Naito, N. Nakagawa, K. Nakamura, H. Nakano, K. Nakao, A. Nishizawa, Y. Niwa, C. Nozawa, M. Ohashi, N. Ohishi, M. Ohkawa, A. Okutomi, K. Oohara, N. Sago, M. Saijo, M. Sakagami, S. Sakata, M. Sasaki, S. Sato, M. Shibata, H. Shinkai, K. Somiya, H. Sotani, N. Sugiyama, H. Tagoshi, T. Takahashi, H. Takahashi, R. Takahashi, T. Takano, T. Tanaka, K. Taniguchi, A. Taruya, H. Tashiro, M. Tokunari, S. Tsujikawa, Y. Tsunesada, K. Yamamoto, T. Yamazaki, J. Yokoyama, C.-M. Yoo, S. Yoshida, and T. Yoshino. The Japanese space gravitational wave antenna-DECIGO. *Classical and Quantum Gravity*, 23:125–+, April 2006.

[114] W. Keil, H.-T. Janka, and E. Mueller. Ledoux Convection in Protoneutron Stars—A Clue to Supernova Nucleosynthesis? ApJ, 473:L111+, December 1996.

[115] F. S. Kitaura, H.-T. Janka, and W. Hillebrandt. Explosions of O-Ne-Mg cores, the Crab supernova, and subluminous type II-P supernovae. *Astronomy & Astrophysics* , 450:345–350, April 2006.

[116] K. Kotake, W. Iwakami, N. Ohnishi, and S. Yamada. Ray-Tracing Analysis of Anisotropic Neutrino Radiation for Estimating Gravitational Waves in Core-Collapse Supernovae. ApJ, 704:951–963, October 2009.

[117] K. Kotake, W. Iwakami, N. Ohnishi, and S. Yamada. Stochastic Nature of Gravitational Waves from Supernova Explosions with Standing Accretion Shock Instability. ApJ, 697:L133–L136, June 2009.

[118] K. Kotake, N. Ohnishi, and S. Yamada. Gravitational Radiation from Standing Accretion Shock Instability in Core-Collapse Supernovae. ApJ, 655:406–415, January 2007.

[119] K. Kotake, K. Sato, and K. Takahashi. Explosion mechanism, neutrino burst and gravitational wave in core-collapse supernovae. *Reports of Progress in Physics*, 69:971–1143, 2006.

[120] K. Kotake, H. Sawai, S. Yamada, and K. Sato. Magnetorotational effects on anisotropic neutrino emission and convection in core-collapse supernovae. *apj*, 608:391–404, June 2004.

[121] K. Kotake, S. Yamada, and K. Sato. Gravitational radiation from axisymmetric rotational core collapse. *prd*, 68(4):044023–+, August 2003.

[122] K. Kotake, S. Yamada, K. Sato, K. Sumiyoshi, H. Ono, and H. Suzuki. Gravitational radiation from rotational core collapse: Effects of magnetic fields and realistic equations of state. *prd*, 69(12):124004–+, June 2004.

[123] P. Kroupa. The Initial Mass Function of Stars: Evidence for Uniformity in Variable Systems. *Science*, 295:82–91, January 2002.

[124] Russell M. Kulsrud. *Plasma Physics for Astrophysics*. Princeton University Press, 2004.

[125] T. Kuroda and H. Umeda. Three Dimensional Magneto Hydrodynamical Simulations of Gravitational Collapse of a 15Msun Star. *ArXiv e-prints*, August 2010.

[126] L. D. Landau and E. M. Lifshitz. *Klassische Feldtheorie*. Verlag Harri Deutsch, 12., überarbeitete Auflage, 1947.

[127] L. D. Landau and E. M. Lifshitz. *Fluid mechanics*. Course of theoretical physics, Oxford: Pergamon Press, 1959.

[128] K. Langanke, G. Martínez-Pinedo, O. E. B. Messer, J. M. Sampaio, D. J. Dean, W. R. Hix, A. Mezzacappa, M. Liebendörfer, H.-Th. Janka, and M. Rampp. Electron capture rates on nuclei and implications for stellar core collapse. *prl*, 90, 2003.

[129] K. Langanke, G. Martínez-Pinedo, J. M. Sampaio, D. J. Dean, W. R. Hix, O. E. Messer, A. Mezzacappa, M. Liebendörfer, H.-T. Janka, and M. Rampp. Electron Capture Rates on Nuclei and Implications for Stellar Core Collapse. *Physical Review Letters*, 90(24):241102–+, June 2003.

[130] J. M. Lattimer and F. D. Swesty. A generalized equation of state for hot, dense matter. *Nucl. Phys. A*, 535:331–376, December 1991.

[131] J. M. Leblanc and J. R. Wilson. A Numerical Example of the Collapse of a Rotating Magnetized Star. *apj*, 161:541–+, August 1970.

[132] D. C. Leonard, A. V. Filippenko, M. Ganeshalingam, F. J. D. Serduke, W. Li, B. J. Swift, A. Gal-Yam, R. J. Foley, D. B. Fox, S. Park, J. L. Hoffman, and D. S. Wong. A non-spherical core in the explosion of supernova SN 2004dj. Nature, 440:505–507, March 2006.

[133] M. Liebendörfer, O. E. B. Messer, A. Mezzacappa, S. W. Bruenn, C. Y. Cardall, and F.-K. Thielemann. A Finite Difference Representation of Neutrino Radiation Hydrodynamics in Spherically Symmetric General Relativistic Spacetime. 150:263–316, January 2004.

[134] M. Liebendörfer, M. Rampp, H.-T. Janka, and A. Mezzacappa. Supernova Simulations with Boltzmann Neutrino Transport: A Comparison of Methods. *apj*, 620:840–860, February 2005.

[135] M. Liebendörfer, S. Rosswog, and F. Thielemann. An Adaptive Grid, Implicit Code for Spherically Symmetric, General Relativistic Hydrodynamics in Comoving Coordinates. *apjsup*, 141:229–246, July 2002.

[136] M. Liebendörfer. A Simple Parameterization of the Consequences of Deleptonization for Simulations of Stellar Core Collapse. *apj*, 633:1042–1051, November 2005.

[137] M. Liebendörfer, T. Fischer, M. Hempel, A. Mezzacappa, G. Pagliara, I. Sagert, J. Schaffner-Bielich, S. Scheidegger, F.-K. Thielemann, and S. C. Whitehouse. Supernovae as Nuclear and Particle Physics Laboratories. *Nuclear Physics A*, 827:573–578, August 2009.

[138] M. Liebendörfer, A. Mezzacappa, F.-K. Thielemann, O. E. B. Messer, W. R. Hix, and S. W. Bruenn. Probing the gravitational well: No supernova explosion in spherical symmetry with general relativistic boltzmann neutrino transport. *prd*, 63, 2001.

[139] M. Liebendörfer, U.-L. Pen, and C. Thompson. Efficient approximations of neutrino physics for three-dimensional simulations of stellar core collapse. In *International Symposium on Nuclear Astrophysics - Nuclei in the Cosmos*, volume (NIC-IX), page 132, 2006.

[140] M. Liebendörfer, S. C. Whitehouse, and T. Fischer. The Isotropic Diffusion Source Approximation for Supernova Neutrino Transport. ApJ, 698:1174–1190, June 2009.

[141] Matthias Liebendorfer, Ue-Li Pen, and Christopher Thompson. Efficient approximations of neutrino physics for three- dimensional simulations of stellar core collapse. *PoS*, NIC-IX:132, 2006.

[142] Duncan R. Lorimer. Binary and millisecond pulsars at the new millennium. *Living Reviews in Relativity*, 4(5), 2001.

[143] R. V. E. Lovelace, H. Li, S. A. Colgate, and A. F. Nelson. Rossby Wave Instability of Keplerian Accretion Disks. ApJ, 513:805–810, March 1999.

[144] H. Lück, M. Hewitson, P. Ajith, B. Allen, P. Aufmuth, C. Aulbert, S. Babak, R. Balasubramanian, B. W. Barr, S. Berukoff, A. Bunkowski, G. Cagnoli,

C. A. Cantley, M. M. Casey, S. Chelkowski, Y. Chen, D. Churches, T. Cokelaer, C. N. Colacino, D. R. M. Crooks, C. Cutler, K. Danzmann, R. J. Dupuis, E. Elliffe, C. Fallnich, A. Franzen, A. Freise, I. Gholami, S. Goßler, A. Grant, H. Grote, S. Grunewald, J. Harms, B. Hage, G. Heinzel, I. S. Heng, A. Hepstonstall, M. Heurs, S. Hild, J. Hough, Y. Itoh, G. Jones, R. Jones, S. H. Huttner, K. Kötter, B. Krishnan, P. Kwee, M. Luna, B. Machenschalk, M. Malec, R. A. Mercer, T. Meier, C. Messenger, S. Mohanty, K. Mossavi, S. Mukherjee, P. Murray, G. P. Newton, M. A. Papa, M. Perreur-Lloyd, M. Pitkin, M. V. Plissi, R. Prix, V. Quetschke, V. Re, T. Regimbau, H. Rehbein, S. Reid, L. Ribichini, D. I. Robertson, N. A. Robertson, C. Robinson, J. D. Romano, S. Rowan, A. Rüdiger, B. S. Sathyaprakash, R. Schilling, R. Schnabel, B. F. Schutz, F. Seifert, A. M. Sintes, J. R. Smith, P. H. Sneddon, K. A. Strain, I. Taylor, R. Taylor, A. Thüring, C. Ungarelli, H. Vahlbruch, A. Vecchio, J. Veitch, H. Ward, U. Weiland, H. Welling, L. Wen, P. Williams, B. Willke, W. Winkler, G. Woan, and R. Zhu. Status of the GEO600 detector. *Classical and Quantum Gravity*, 23:71–+, April 2006.

[145] E. Müller, M. Rampp, R. Buras, H.-T. Janka, and D. H. Shoemaker. Toward Gravitational Wave Signals from Realistic Core-Collapse Supernova Models. *apj*, 603:221–230, March 2004.

[146] Andre Maeder. *Physics, Formation and Evolution of Rotating Stars.* Astronomy and Astrophysics Library, 2008.

[147] A. Marek, H. Dimmelmeier, H.-T. Janka, E. Müller, and R. Buras. Exploring the relativistic regime with Newtonian hydrodynamics: an improved effective gravitational potential for supernova simulations. *aap*, 445:273–289, January 2006.

[148] A. Marek and H.-T. Janka. Delayed Neutrino-Driven Supernova Explosions Aided by the Standing Accretion-Shock Instability. ApJ, 694:664–696, March 2009.

[149] A. Marek, H.-T. Janka, and E. Müller. Equation-of-state dependent features in shock-oscillation modulated neutrino and gravitational-wave signals from supernovae. *Astronomy & Astrophysics* , 496:475–494, March 2009.

[150] G. Martínez-Pinedo, M. Liebendörfer, and D. Frekers. Nuclear Input for Core-collapse Models. *Nuc. Phys. A, in press*, December 2006.

[151] D. L. Meier, R. I. Epstein, W. D. Arnett, and D. N. Schramm. Magnetohydrodynamic phenomena in collapsing stellar cores. ApJ, 204:869–878, March 1976.

[152] A. Mezzacappa. The Core Collapse Supernova Mechanism: Current Models, Gaps, and the Road Ahead. In M. Turatto, S. Benetti, L. Zampieri, and W. Shea, editors, *ASP Conf. Ser. 342: 1604-2004: Supernovae as Cosmological Lighthouses*, pages 175–+, December 2005.

[153] A. Mezzacappa and S. W. Bruenn. A numerical method for solving the neutrino Boltzmann equation coupled to spherically symmetric stellar core collapse. 405:669–684, March 1993.

[154] A. Mezzacappa and S. W. Bruenn. Type II supernovae and Boltzmann neutrino transport - The infall phase. 405:637–668, March 1993.

[155] D. Mihalas and B. Weibel Mihalas. *Foundations of radiation hydrodynamics.* Dover, 1984.

[156] H. Mikami, Y. Sato, T. Matsumoto, and T. Hanawa. Three-dimensional Magnetohydrodynamical Simulations of a Core-Collapse Supernova. ApJ, 683:357–374, August 2008.

[157] C. W. Misner, K. S. Thorne, and J. A. Wheeler. *Gravitation.* San Francisco: W.H. Freeman and Co., 1973, 1973.

[158] R. Moenchmeyer, G. Schaefer, E. Mueller, and R. E. Kates. Gravitational waves from the collapse of rotating stellar cores. *Astronomy & Astrophysics* , 246:417–440, June 1991.

[159] G. E. Moss, L. R. Miller, and R. L. Forward. Photon-noise-limited laser transducer for gravitational antenna. Appl. Opt., 10:2495–2498, 1971.

[160] E. Mueller. Gravitational radiation from collapsing rotating stellar cores. *Astronomy & Astrophysics* , 114:53–59, October 1982.

[161] E. Mueller and H.-T. Janka. Gravitational radiation from convective instabilities in Type II supernova explosions. *Astronomy & Astrophysics* , 317:140–163, January 1997.

[162] B. Müller, H. Dimmelmeier, and E. Müller. Exploring the relativistic regime with Newtonian hydrodynamics. II. An effective gravitational potential for rapid rotation. *Astronomy & Astrophysics* , 489:301–314, October 2008.

[163] B. Müller, H.-T. Janka, and H. Dimmelmeier. A New Multi-dimensional General Relativistic Neutrino Hydrodynamic Code for Core-collapse Supernovae. I. Method and Code Tests in Spherical Symmetry. ApJS, 189:104–133, July 2010.

[164] J. W. Murphy and A. Burrows. Criteria for Core-Collapse Supernova Explosions by the Neutrino Mechanism. ApJ, 688:1159–1175, December 2008.

[165] J. W. Murphy, C. D. Ott, and A. Burrows. A Model for Gravitational Wave Emission from Neutrino-Driven Core-Collapse Supernovae. ApJ, 707:1173–1190, December 2009.

[166] K. Nakazato, K. Sumiyoshi, and S. Yamada. Astrophysical implications of equation of state for hadron-quark mixed phase: Compact stars and stellar collapses. Phys. Rev. D, 77(10):103006–+, May 2008.

[167] Pawel Haensel Nicolas Chamel. Physics of neutron star crusts. *Living Reviews in Relativity*, 11(10), 2008.

[168] A. Waechter O. Schenk and M. Hagemann. Matching-based preprocessing algorithms to the solution of saddle-point problems in large-scale nonconvex interior-point optimization. *Journal of Computational Optimization and Applications*, 36(2-3):321–341, 2007.

[169] M. Bollhoefer O. Schenk and R. Roemer. On large-scale diagonalization techniques for the anderson model of localization. featured sigest paper in the siam review selected "on the basis of its exceptional interest to the entire siam community. *SIAM Review*, 50:91–112, 2008.

[170] M. Obergaulinger, M. A. Aloy, and E. Müller. Axisymmetric simulations of magneto-rotational core collapse: dynamics and gravitational wave signal. *aap*, 450:1107–1134, May 2006.

[171] M. Obergaulinger, P. Cerdá-Durán, E. Müller, and M. A. Aloy. Semi-global simulations of the magneto-rotational instability in core collapse supernovae. *Astronomy & Astrophysics* , 498:241–271, April 2009.

[172] E. O'Connor and C. D. Ott. A new open-source code for spherically symmetric stellar collapse to neutron stars and black holes. *Classical and Quantum Gravity*, 27(11):114103–+, June 2010.

[173] K.I. Oohara, T. Nakamura, and M. Shiabata. A Way to 3D Numerical Relativity. *Progress of theoretical physics supplement No. 128, 1997*, 128:183–249, 1997.

[174] C. D Ott. TOPICAL REVIEW: The gravitational-wave signature of core-collapse supernovae. *Classical and Quantum Gravity*, 26(6):063001–+, March 2009.

[175] C. D. Ott, A. Burrows, L. Dessart, and E. Livne. A New Mechanism for Gravitational-Wave Emission in Core-Collapse Supernovae. *Physical Review Letters*, 96(20):201102–+, May 2006.

[176] C. D. Ott, A. Burrows, L. Dessart, and E. Livne. Two-Dimensional Multiangle, Multigroup Neutrino Radiation-Hydrodynamic Simulations of Postbounce Supernova Cores. ApJ, 685:1069–1088, October 2008.

[177] C. D. Ott, A. Burrows, E. Livne, and R. Walder. Gravitational Waves from Axisymmetric, Rotating Stellar Core Collapse. 600:834–864, January 2004.

[178] C. D. Ott, A. Burrows, T. A. Thompson, E. Livne, and R. Walder. The Spin Periods and Rotational Profiles of Neutron Stars at Birth. ApJS, 164:130–155, May 2006.

[179] C. D. Ott, H. Dimmelmeier, A. Marek, H.-T. Janka, I. Hawke, B. Zink, and E. Schnetter. 3D Collapse of Rotating Stellar Iron Cores in General Relativity Including Deleptonization and a Nuclear Equation of State. *Physical Review Letters*, 98(26):261101–+, June 2007.

[180] C. D. Ott, H. Dimmelmeier, A. Marek, H.-T. Janka, B. Zink, I. Hawke, and E. Schnetter. Rotating collapse of stellar iron cores in general relativity. *Classical and Quantum Gravity*, 24:139–+, June 2007.

[181] C. D. Ott, S. Ou, J. E. Tohline, and A. Burrows. One-armed Spiral Instability in a Low-T/—W— Postbounce Supernova Core. ApJ, 625:L119–L122, June 2005.

[182] Christian D. Ott. *Stellar Iron Core Collapse in 3+1 General Relativity and The Gravitational Wave Signature of Core-Collapse Supernovae.* PhD thesis, AEI, 2007.

[183] S. Ou and J. E. Tohline. Unexpected Dynamical Instabilities in Differentially Rotating Neutron Stars. ApJ, 651:1068–1078, November 2006.

[184] J. C. B. Papaloizou and J. E. Pringle. The dynamical stability of differentially rotating discs. II. MNRAS, 213:799–820, April 1985.

[185] U.-L. Pen, P. Arras, and S. Wong. A Free, Fast, Simple, and Efficient Total Variation Diminishing Magnetohydrodynamic Code. ApJS, 149:447–455, December 2003.

[186] S. Perlmutter, G. Aldering, G. Goldhaber, R. A. Knop, P. Nugent, P. G. Castro, S. Deustua, S. Fabbro, A. Goobar, D. E. Groom, I. M. Hook, A. G. Kim, M. Y. Kim, J. C. Lee, N. J. Nunes, R. Pain, C. R. Pennypacker, R. Quimby, C. Lidman, R. S. Ellis, M. Irwin, R. G. McMahon, P. Ruiz-Lapuente, N. Walton, B. Schaefer, B. J. Boyle, A. V. Filippenko, T. Matheson, A. S. Fruchter, N. Panagia, H. J. M. Newberg, and W. J. Couch. Measurements of Omega and Lambda from 42 High-Redshift Supernovae. 517:565–586, June 1999.

[187] M. E. Peskin and D. V. Schroeder. *An Introduction to Quantum Field Theory.* Westview Press, 1995.

[188] Jrme Novak Philippe Grandclment. Spectral methods for numerical relativity. *Living Reviews in Relativity*, 12(1), 2009.

[189] W. H. Press, S. A. Teukolsky, W. T. Vetterling, and B. P. Flannery. *Numerical recipes in FORTRAN. The art of scientific computing.* Cambridge: University Press, —c1992, 2nd ed., 1992.

[190] Alfio Quarteroni. *Numerical Methods for Differential Problems.* Springer, 2009.

[191] S. Waldman R. Adhikari, P. Fritschel. Enhanced ligo. Technical report, Caltech, MIT (http://www.ligo.caltech.edu/docs/T/T060156-01.pdf), 2006.

[192] H. Lewy R. Courant, K. Friedrichs. Über die partiellen differenzengleichungen der mathematischen physik. *Mathematische Annalen*, 100:32, 1928.

[193] S.C. Whitehouse M. Liebendörfer R. Käppeli, S. Scheidegger. Approximate riemann solvers corrected for garvitationally induced source terms, in prep. *Comput. Phys.*, 2010.

[194] G[eorg] G. Raffelt. Mu- and tau- neutrino spectra formation in supernovae. *apj*, 561:890–914, November 2001.

[195] M. Rampp, E. Muüller, and M. Ruffert. Simulations of non-axisymmetric rotational core collapse. *Astronomy & Astrophysics* , 332:969–983, 1998.

[196] P. Rhodes. Fermi-dirac functions of integral order. *Proc. Royal Soc. A*, 204:396–405, 1950.

[197] J. V. Romero, J. M. A. Ibanez, J. M. A. Marti, and J. A. Miralles. A New Spherically Symmetric General Relativistic Hydrodynamical Code. ApJ, 462:839–+, May 1996.

[198] I. Sagert, T. Fischer, M. Hempel, G. Pagliara, J. Schaffner-Bielich, A. Mezzacappa, F.-K. Thielemann, and M. Liebendörfer. Signals of the QCD Phase Transition in Core-Collapse Supernovae. *Physical Review Letters*, 102(8):081101–+, February 2009.

[199] M. Saijo, T. W. Baumgarte, and S. L. Shapiro. One-armed Spiral Instability in Differentially Rotating Stars. ApJ, 595:352–364, September 2003.

[200] M. Saijo and S. Yoshida. Low T/—W— dynamical instabilities in differentially rotating stars: Diagnosis with canonical angular momentum. In *Albert Einstein Century International Conference*, volume 861 of *American Institute of Physics Conference Series*, pages 728–735, November 2006.

[201] P. R. Saulson. *Fundamentals of interferometric gravitational wave detectors.* 1994.

[202] G. Schaller, D. Schaerer, G. Meynet, and A. Maeder. New grids of stellar models from 0.8 to 120 solar masses at Z = 0.020 and Z = 0.001. A&AS, 96:269–331, December 1992.

[203] L. Scheck, H.-T. Janka, T. Foglizzo, and K. Kifonidis. Multidimensional supernova simulations with approximative neutrino transport. II. Convection and the advective-acoustic cycle in the supernova core. *Astronomy & Astrophysics* , 477:931–952, January 2008.

[204] L. Scheck, T. Plewa, H.-T. Janka, K. Kifonidis, and E. Müller. Pulsar Recoil by Large-Scale Anisotropies in Supernova Explosions. *Physical Review Letters*, 92(1):011103–+, January 2004.

[205] S. Scheidegger. Computing gravitational waves from core-collapse supernovae. Master's thesis, University of Basel, 2007.

[206] S. Scheidegger, T. Fischer, S. C. Whitehouse, and M. Liebendörfer. Gravitational waves from 3D MHD core collapse simulations. *Astronomy & Astrophysics* , 490:231–241, October 2008.

[207] S. Scheidegger, R. Kaeppeli, S. C. Whitehouse, T. Fischer, and M. Liebendoerfer. The influence of model parameters on the prediction of gravitational wave signals from stellar core collapse. *ArXiv e-prints*, January 2010.

[208] S. Scheidegger, R. Käppeli, S. C. Whitehouse, T. Fischer, and M. Liebendörfer. The influence of model parameters on the prediction of gravitational wave signals from stellar core collapse. *Astronomy & Astrophysics* , 514:A51+, May 2010.

[209] S. Scheidegger, S. C. Whitehouse, R. Kaeppeli, and M. Liebendoerfer. Gravitational waves from supernova matter. *ArXiv e-prints*, December 2009.

[210] S. Scheidegger, S. C. Whitehouse, R. Käppeli, and M. Liebendörfer. Gravitational waves from supernova matter. *Classical and Quantum Gravity*, 27(11):114101–+, June 2010.

[211] O. Schenk and K. Gärtner. Solving unsymmetric sparse systems of linear equations with pardiso. *Journal of Future Generation Computer Systems*, 20(3):475–487, 2004.

[212] O. Schenk and K. Gärtner. On fast factorization pivoting methods for symmetric indefinite systems. *Elec. Trans. Numer. Anal.*, 23:158–179, 2006.

[213] Y.-I. Sekiguchi and M. Shibata. New criterion for direct black hole formation in rapidly rotating stellar collapse. Phys. Rev. D, 70(8):084005–+, October 2004.

[214] S. L. Shapiro and S. A. Teukolsky. *Black Holes White Dwarfs and Neutron Stars: The Physics of Compact Objects.* Wiley-Interscience, New York, 1983.

[215] H. Shen, H. Toki, K. Oyamatsu, and K. Sumiyoshi. Relativistic equation of state of nuclear matter for supernova and neutron star. *Nucl. Phys. A*, 637:435–450, July 1998.

[216] H. Shen, H. Toki, K. Oyamatsu, and K. Sumiyoshi. Relativistic Equation of State of Nuclear Matter for Supernova Explosion. *Prog. Theor. Phys.*, 100:1013–1031, November 1998.

[217] M. Shibata, S. Karino, and Y. Eriguchi. Dynamical instability of differentially rotating stars. MNRAS, 334:L27–L31, August 2002.

[218] M. Shibata, Y. T. Liu, S. L. Shapiro, and B. C. Stephens. Magnetorotational collapse of massive stellar cores to neutron stars: Simulations in full general relativity. Phys. Rev. D, 74(10):104026–+, November 2006.

[219] M. Shibata and Y.-I. Sekiguchi. Gravitational waves from axisymmetrically oscillating neutron stars in general relativistic simulations. Phys. Rev. D, 68(10):104020–+, November 2003.

[220] G. Strang. On the construction and comparison of difference schemes. *SIAM J. Num. Anal.*, 5:506–517, 1968.

[221] K. Sumiyoshi, H. Suzuki, S. Yamada, and H. Toki. Properties of a relativistic equation of state for collapse-driven supernovae. *Nucl. Phys. A*, A730:227–251, 2004.

[222] K. Sumiyoshi, S. Yamada, and H. Suzuki. Dynamics and Neutrino Signal of Black Hole Formation in Nonrotating Failed Supernovae. II. Progenitor Dependence. ApJ, 688:1176–1185, December 2008.

[223] Y. Suwa, T. Takiwaki, K. Kotake, and K. Sato. Gravitational Wave Background from Population III Stars. ApJ, 665:L43–L46, August 2007.

[224] F. D. Swesty and E. S. Myra. A Numerical Algorithm for Modeling Multigroup Neutrino-Radiation Hydrodynamics in Two Spatial Dimensions. ApJS, 181:1–52, March 2009.

[225] M. Takahara and K. Sato. Phase Transitions in the Newly-Born Neutron Star and Neutrino Emissionsfrom SN1987A. *Progress of Theoretical Physics*, 80:861–867, November 1988.

[226] R. Takahashi and the TAMA Collaboration. Status of TAMA300. *Classical and Quantum Gravity*, 21:403–+, March 2004.

[227] T. Takiwaki, K. Kotake, and K. Sato. Special Relativistic Simulations of Magnetically Dominated Jets in Collapsing Massive Stars. ApJ, 691:1360–1379, February 2009.

[228] J.-L. Tassoul. *Theory of rotating stars.* 1978.

[229] T. A. Thompson and A. Burrows. Neutrino processes in supernovae and the physics of protoneutron star winds. *Nucl. Phys. A*, 688:377c–381c, 2001.

[230] T. A. Thompson, A. Burrows, and J. E. Horvath. μ and τ neutrino thermalization and production in supernovae: Processes and time scales. *prc*, 62, August 2000.

[231] T. A. Thompson, E. Quataert, and A. Burrows. Viscosity and Rotation in Core-Collapse Supernovae. 620:861–877, 2005.

[232] Todd A. Thompson, Adam Burrows, and Philip A. Pinto. Shock breakout in core-collapse supernovae and its neutrino signature. *apj*, 592:434–456, 2003.

[233] K. Thorne. *Three Hundred Years of Gravitation*. Hawking, S. W. and Israel, W., April 1989.

[234] K. S. Thorne. Multipole expansions of gravitational radiation. *Reviews of Modern Physics*, 52:299–340, April 1980.

[235] K. S. Thorne. Gravitational Waves. In E. W. Kolb and R. D. Peccei, editors, *Particle and Nuclear Astrophysics and Cosmology in the Next Millenium*, pages 160–+, 1995.

[236] F. X. Timmes and D. Arnett. The Accuracy, Consistency, and Speed of Five Equations of State for Stellar Hydrodynamics. ApJS, 125:277–294, November 1999.

[237] F. X. Timmes and F. D. Swesty. The Accuracy, Consistency, and Speed of an Electron-Positron Equation of State Based on Table Interpolation of the Helmholtz Free Energy. ApJS, 126:501–516, February 2000.

[238] Eleuterio F. Toro. *Riemann Solvers and Numerical Methods for Fluid Dynamics - A Practical Introduction (2nd Edition)*. Springer - Verlag, 2006.

[239] Manuel Torrilhon. *Zur Numerik der idealen Magnetohydrodynamik*. PhD thesis, ETH Zürich, 2003.

[240] B. J. van Leer. Towards the ultimate consrevative difference scheme: Iv. a new approach to numerical convection. *J. Comput. Phys.*, 23:276, 1977.

[241] B. J. van Leer. Towards the ultimate conservative difference scheme. v - a second-order sequel to godunov's method. *J. Comput. Phys.*, 32:101, 1979.

[242] M. van Veggel. Gravitational wave detectors - broadening their horizon (talk 06 jul 2009 in potsdam, germany/ligo-g0900652-v2). 2009.

[243] A. L. Watts, N. Andersson, and D. I. Jones. The Nature of Low T/—W— Dynamical Instabilities in Differentially Rotating Stars. ApJ, 618:L37–L40, January 2005.

[244] J. Weber. Gravitational Radiation. *Physical Review Letters*, 18:498–501, March 1967.

[245] N. N. Weinberg and E. Quataert. Non-linear saturation of g-modes in proto-neutron stars: quieting the acoustic engine. MNRAS, 387:L64–L68, June 2008.

[246] S. Weinberg. *Gravitation and Cosmology: Principles and Applications of the General Theory of Relativity*. July 1972.

[247] R. Weiss. Electromagetically coupled broadband gravitational antenna. *Quarterly Progress Report, Research Laboratory of Electronics, MIT*, 105:54, 1972.

[248] S. E. Whitcomb. Ground-based gravitational-wave detection: now and future. *Classical and Quantum Gravity*, 25(11):114013–+, June 2008.

[249] Anthony Skjellum William Gropp, Ewing Lusk. *Using MPI.* MIT Press, 1999.

[250] J. R. Wilson. In J. Centrella, J. LeBlanc, and R. Bowers, editors, *Relativistic Astrophysics*, page 422. Jones and Bartlett, 1985.

[251] J. R. Wilson and R. W. Mayle. Convection in core collapse supernovae. Phys. Rep., 163:63–77, 1988.

[252] S. Woosley and T. Janka. The physics of core-collapse supernovae. *Nature Physics*, 1:147–154, December 2005.

[253] S. E. Woosley. Gamma-ray bursts from stellar mass accretion disks around black holes. ApJ, 405:273–277, March 1993.

[254] S. E. Woosley and J. S. Bloom. The Supernova Gamma-Ray Burst Connection. *Astronomy*, 44:507–556, September 2006.

[255] S. E. Woosley, A. Heger, and T. A. Weaver. The evolution and explosion of massive stars. 74:1015–1071, October 2002.

[256] S. E. Woosley, A. Heger, and T. A. Weaver. The evolution and explosion of massive stars. *Reviews of Modern Physics*, 74:1015–1071, November 2002.

[257] S. E. Woosley and T. A. Weaver. The physics of supernova explosions. *Astronomy*, 24:205–253, 1986.

[258] S. E. Woosley and T. A. Weaver. The evolution and explosion of massive stars. ii. explosion hydrodynamics and nucleosynthesis. *apjsup*, 101:181, 1995.

[259] A. Yahil. Self-similar stellar collapse. 265:1047–1055, February 1983.

[260] W. R. Yueh and J. R. Buchler. Neutrino transport in supernova models/ SN method. ApJ, 217:565–577, October 1977.

[261] T. Zwerger and E. Mueller. Dynamics and gravitational wave signature of axisymmetric rotational core collapse. *Astronomy & Astrophysics* , 320:209–227, April 1997.

[262] F. Zwicky. On Collapsed Neutron Stars. ApJ, 88:522–525, November 1938.